Dynamics and Signatures of an Emergent Gauge Field

Doctoral thesis
for
the award of the doctoral degree
of the Faculty of Mathematics and Natural Sciences
of the University of Cologne

submitted by

Aprem P. Joy

accepted in the year 2024

Berichterstatter: Prof. Dr. Achim Rosch

Prof. Dr. Simon Trebst

പദാർത്ഥനിരതൻ പ്രകൃതിജഭാവം പരസ്പരാകർഷം;
പ്രാണികുലത്തിൻ പരമാത്മഗുണം പരസ്പരപ്രേമം

All matter, by nature, mutually attract;
the supreme quality of living beings is mutual love.

-Ulloor (Malayalam poet)

Abstract

One of the most profound predictions of modern condensed matter physics is that gauge theories may emerge naturally in the low-energy description of certain solid state systems. This is in stark contrast with particle physics, where gauge theories have to be postulated. Emergent gauge theories often bring with them quasiparticles that carry fractions of a fundamental quantum number, holding the potential to revolutionize quantum technologies.

The paradigmatic Kitaev model, an exactly solvable quantum spin liquid, realizes an emergent static $\mathbb{Z}_2$ gauge field and itinerant Majorana fermions coupled to it. Remarkably, there is a large class of materials that have shown significant promise for realizing this exotic phase of matter. Despite tremendous experimental efforts, a conclusive proof of emergent gauge fields and fractionalized excitations of the Kitaev spin liquid has remained elusive. Any material realizations of this model inevitably contain interactions that break the integrability of the model, and make the gauge fields dynamical. Understanding the properties this dynamical emergent gauge field is crucial for predicting its observable signatures in real materials.

In this thesis, we develop a comprehensive theory of dynamical gauge fields in the Kitaev spin liquid, weakly perturbed away from its integrable limit. We focus on the dynamical properties of the fundamental gauge excitation - the *vison*, dressed by a cloud of Majorana fermions.

Through a controlled perturbation theory, we calculate the dispersion of a single vison, induced by an off-diagonal exchange (Γ) term and an external magnetic field $\boldsymbol{h}$. Our findings reveal that the sign of the Kitaev interaction has a profound influence on the dynamical and topological properties of visons. While they can move efficiently and coherently in the ferromagnetic Kitaev model, their motion in an antiferromagnetic (AFM) Kitaev model is driven by the an incoherent, Majorana-assisted hopping. Remarkably, in the presence of an external magnetic field, visons of the AFM Kitaev model become topological, predicting a novel contribution to the thermal Hall effect. The massless Majorana fermions scatter from the vison's gauge flux in a highly singular manner. Employing a modified Boltzmann formalism to capture this behaviour, we show that it leads to a universal mobility in the low-temperature (T) limit, $\mu(T) = \frac{6\hbar v_m^2}{(k_B T)^2}$, where v_m is the velocity of Majorana fermions.

Motivated by the layered three-dimensional (3D) structure of candidate materials, we investigate the gauge field dynamics in weakly coupled multilayer Kitaev spin liquids. The interplay of novel conservation laws and robust topological constraints prevents single vison motion, leading instead to a variety of dynamic vison-pairs. The conservation laws put strong constraints on the motion of these excitations. Depending on the stacking pattern, inter-layer pairs may exhibit a fully two-dimensional (2D) motion within the layers, or a highly restricted one-dimensional mobility. Intra-layer pairs can, however, move across layers, with the direction of motion determined by the stacking pattern. Furthermore, we show how the anisotropy of Kitaev couplings strongly influences the coherence of interlayer tunnelling.

In the final part, we focus on two experimental signatures of mobile visons: Raman spectroscopy and the thermal Hall effect. Using an effective two-particle model of visons, we calculate the low-energy Raman response of visons in a generic ferromagnetic Kitaev spin liquid. Our results reveal distinct signatures of anyonic statistics in the continuum response and sharp peaks associated with anyon-bound states. Notably, these sharp peaks exhibit a strong sensitivity to the chirality of Raman light, a feature observed in several experiments. Finally, we provide a detailed calculation of the thermal Hall effect resulting from dynamical visons in the antiferromagnetic Kitaev model, discussing its implications for experimental detection.

Table of contents

List of figures

Chapter 1

Introduction

Matter around us exists in an astonishing variety of forms. In classical physics, which governs our everyday experiences, we are most familiar with three distinct phases: solid, liquid, and gas. The air we breathe is a gas, the water we drink is a liquid, and the walls that protect us from nature's elements are made of solids. Despite this variety, modern particle physics reveals a remarkable truth: all matter, from the most delicate vapor to the hardest rock, is ultimately made of the same fundamental building blocks—elementary particles like electrons, quarks, and a few others. But how can this small set of particles give rise to such vastly different forms of matter? The key lies in the way large collections of these particles interact with one another. When grouped together in enormous numbers, they behave collectively in ways that individual particles do not, giving rise to unique properties and behaviours. This presents a new paradigm in our way of understanding the world - *emergence*. Emergent properties are what determine if a mass of particles can form a solid with a rigid structure in one scenario, or the same particles may move freely as a gas or flow smoothly as a liquid. The diversity we observe in the world around us, then, is not due to a difference in fundamental particles, but rather how those particles organize and cooperate on a larger scale.

The traditional framework that largely shaped our understanding of phases and phase transitions was developed by Lev Landau [2]. Symmetry lies at the heart of this tremendously successful paradigm. Different phases are characterized by the system exhibiting different degrees of symmetries. Consider the example of a classical ferromagnet (like a kitchen magnet) in three-dimensions (3D). It can be approximately described by a lattice of spins that interact with their neighbouring spins - two neighbours aligned with each other lower the energy by an amount J. At low temperatures, $T \ll J$, the spins have very low energy and thus prefer to align with its neighbour forming a highly uniform state with all the spins pointing in one single direction in space. This is a high-symmetry, ordered state. As the temperature increases, the spins gain enough energy to deviate from their common direction and start to fluctuate. At very large temperatures, $T \gg J$, the system will have randomly pointing spins, causing the net magnetization (sum of all spin vectors) to be vanishingly small. Landau described such a phase transition using an *order parameter* - a single quantity that distinguishes two different phases. In the case of the ferromagnet, this takes the form of local magnetization $\boldsymbol{m}(\boldsymbol{r})$ which is a sum of spin vectors in a small volume. In the ordered phase, $m(\boldsymbol{r}) \neq 0$ while in the disordered phase $\boldsymbol{m}(\boldsymbol{r}) = 0$. The system is said to undergo a spontaneous symmetry breaking phase transition at a particular temperature, known as the Curie temperature (T_c), as it is cooled from high to low temperatures. This is mathematically described by writing down the free energy of the system, $F[\boldsymbol{m}(\boldsymbol{r})]$, as a simple function of the order parameter consistent with the symmetries of the system. The remarkable success of this prescription has largely shaped our understanding of most equilibrium phenomena.

Given a phase of matter, how does emergent behaviour determine its properties? A classic example is the theory of hydrodynamics, which describes the motion of a fluid in terms of a coarse-grained velocity field while the microscopic description would require keeping tracking track of the molecular motion of 10^{23} (for a drop of water), an impossible task even if we know exactly how to describe it! The hydrodynamical description, expressed by the Navier-Stokes equations beautifully explains a whole range of phenomena we encounter ranging from rocket propulsion to atmospheric modelling. This principle of coarse-graining the microscopic details to understand complex systems in a macroscopic (or emergent) scale also applies to the biological world. In fact, many examples from nature demonstrate the power of collective behaviour. Consider the synchronized movement of a school of fish or a flock of birds in flight—they exhibit coordinated, seemingly intelligent patterns, yet no single fish or bird controls the group. Perhaps the ultimate collective emergent behaviour is life itself.

Wilson [3], Kadanoff [4], Anderson[5], Fischer[6], Wegner[7] and many others translated the idea of coarse-graining into a mathematically rigorous framework known as the *renormalization group* theory. The behaviour of a complex system, at larger scales, is described by what are called fixed points in a parameter space, where the physical properties exhibit universal behaviours despite differences in the microscopic models. Most remarkably, these emergent descriptions can be qualitatively different from the laws that govern a single constituent entity's behaviour. For example, a surfer in the ocean has little use of the quantum mechanical motion of the water molecules but the formation and dynamics of the waves described by hydrodynamics may mean life or death.

Enough with classical physics. Borrowing Feynman's words, there's plenty of room at the bottom. Even in the microscopic world, swarms of particles can come together and interact, giving rise to different phases of matter. However, what distinguishes them from classical phases is the underlying quantum mechanical nature of interactions, thus defining *quantum matter*! A flock of "quantum birds" will naturally behave entirely differently than the classical birds. The question is if we can use the same principles from Landau's framework and renormalization theory to discover emergence in quantum systems. The answer? Yes and No.

For the ‘Yes’ part, an excellent example is the Landau-Ginzburg theory of superconductivity - a fascinating phenomenon where a metal, upon cooling, transitions into a state with zero resistance, essentially possessing charges that can move without friction. Within the metallic phase (‘disordered’ phase), the electrons behave almost as if they do not interact with each other. The dominant sources of friction are the small concentration of impurities or lattice disorder. Landau showed that this collection of interacting electrons in a metal could be described by the notion of a *quasiparticle* - an electron whose properties are only slightly modified by interactions[8]. Mathematically speaking, the quasiparticle is *adiabatically connected* to the electronic degrees of freedom, with its fundamental properties like charge or spin remaining unchanged. However, as the metal is cooled down below the Curie temperature T_c, this description suddenly fails and the system becomes superconducting. Landau along with Vitaly Ginzburg, proposed a theory for superconductivity using a a complex field $\psi(\boldsymbol{r})$ as the order parameter [9]. A free energy expansion in terms of this field could produce a phase transition that describes the superconducting transition phenomenologically. Later, a more microscopic theory by Bardeen-Cooper-Schrieffer (BCS) led to the interpretation of $|\psi(\boldsymbol{r})|^2$ as the local density of electrons that are in the superconducting state [10]. In the ordered phase, the quasiparticles are no longer ‘almost electrons’; they are, in fact quantum superpositions of an electron and its absence (a hole)!

The theory of BCS superconductivity still admits a description in terms of a local order parameter and lies well within the paradigm of spontaneous symmetry breaking. For example, to detect if the system is in the superconducting phase, one only needs access to a small chunk of the system (neglecting superconducting vortices). However, towards the end of the 20th century, a new paradigm of phases and phase transitions beyond the reach of this conventional wisdom emerged - *topological phases of matter* [11]. This rapidly evolving field has unified abstract concepts from mathematical topology and collective phenomena in condensed matter physics, revealing fundamental connections between them.

The first hint of an uncharted territory came from the quantum Hall effect (QHE)[12]. A two-dimensional electronic gas under a strong magnetic field shows a remarkable feature - the Hall conductance of the system displays a plateau as a function of the magnetic field. The value is quantized to integer multiples of a fundamental constant $\frac{e^2}{h}$ where e is the electric charge and h is Planck’s constant. The quantization is so incredibly accurate (to nearly one part in a billion) that it has been used as the standard for electrical resistance. The story only got more intriguing with the observation of the fractional quantum Hall effect (FQHE) where the conductance is quantized to a fraction of $\frac{e^2}{h}$ [13]. And most fascinating, the quasiparticles of this state were found to carry a fraction of the unit electric charge! - an utterly baffling observation considering that the underlying electrons are fundamental particles that cannot be split [14, 15]. Later, it was proposed and observed that these quasiparticles not only carry fractional charge but also carry fractional statistics; that is, they are neither bosons nor fermions [16, 17]. Such bizarre quasiparticles were later found to emerge in a variety of systems, although most of them still remain theoretical.

A recurring and even more profound feature in these fractionalized quantum systems is the presence of *gauge fields*[18]. Gauge fields, a cornerstone of fundamental particle physics, were long believed to be theoretical constructs that had to be postulated rather than emergent. Their natural emergence in the low-energy description of condensed matter systems was, therefore, a profound and unexpected development, with wide-reaching implications. Many topological phases of matter are now understood not through the traditional Landau theory of symmetry breaking, but instead via emergent gauge theories, with quasiparticles resembling those of the standard model of particle physics. They exemplify a new kind of order, *topological order*, where no symmetries are broken and the information about a system's (topological) phase is encoded not locally, but globally. Much like an ant can't tell if its walking on a pretzel or a donut unless it explores the whole object, different topological phases cannot be distinguished by local observables. (Indeed, the ant can tell the difference if it decides to takes a bite.)

For a computer scientist, this may present a different kind of revelation. If we could store information in the topology of such a phase of matter, errors acting locally would have a hard time accessing and changing the bit of information. This is the idea behind *topological quantum computing* [19]. Quantum information can be stored in a non-local manner, such as in two fractions of a single electron's spin. Remarkably, the information remains protected unless the two quasiparticles (or "fractions") are brought back together. To draw a lousy analogy, imagine the two quasiparticles as secret spy agents, each holding a piece of a secret code. No matter how intensively you interrogate one agent, the full code remains protected unless you can get both of them together.

Although well established theoretically, an unambiguous experimental detection of emergent gauge fields and the associated fractional quasiparticles is still lacking. Astonishing progress has been made in FQHE systems although its description in terms of an emergent gauge field still lacks a concrete theoretical and experimental footing [20].

In this context, a remarkable class of systems where gauge fields and fractional quasiparticles naturally emerge has been at the center of attention - *quantum spin liquids*. When quantum fluctuations are strong enough to prevent any kind of magnetic order (e.g. the ferromagnet discussed above), quantum spins may exist in a highly quantum entangled state with the low energy physics described by an emergent gauge field, with “matter” that interacts with it. A wide variety of such states have been proposed across many different systems. However, detecting these states experimentally has proven to be an incredibly challenging task, despite the extensive theoretical groundwork. A major obstacle in this search is the presence of undesirable interactions and disorder inevitable in real materials. These imperfections often push the system away from the ideal parameter regimes predicted by theoretical models, making it difficult to observe the exotic phenomena. Understanding how such perturbations modify the properties and signatures of such theoretically fine-tuned models is extremely crucial in detecting them experimentally as well as engineering them in materials.

Part I

Preliminaries

Chapter 2

Emergent Gauge Fields

2.1 Gauge Theories in Physics

A central pillar of our understanding of the world around is built on gauge theories[21]. The philosophy of this class of field theories is remarkably simple: physical observables must be invariant under certain local transformations, or redundancies in the mathematical description. Let us start with a familiar example - Maxwell's electromagnetism in three dimensions. The physical quantities are the electric and magnetic fields, $\boldsymbol{E}(\boldsymbol{r})$ and $\boldsymbol{B}(\boldsymbol{r})$ respectively. However, the mathematical description uses the language of vector potentials $\boldsymbol{A}(\boldsymbol{r})$ such that the fields, and therefore the Lagrangian, are invariant under the transformation

$$\boldsymbol{A}(\boldsymbol{r}) \to \boldsymbol{A}(\boldsymbol{r}) + \nabla\lambda(\boldsymbol{r}). \tag{2.1}$$

This freedom in choosing the "gauge" offers a redundancy in the description and going from one choice of $\lambda(\boldsymbol{r})$ to another is a *gauge transformation*. It is useful to recall that the electric field $\boldsymbol{E}(\boldsymbol{r})$, the conjugate variable to $\boldsymbol{A}(\boldsymbol{r})$ generates the gauge transformations, much like the momentum operator generating translations in space. Furthermore, if we demand that the state of a system shall be invariant under any gauge transformation, for an arbitrary $\lambda(\boldsymbol{r})$,

$$e^{-i\int \nabla\lambda\cdot\boldsymbol{E}} \left|\psi\right\rangle = e^{i\int \lambda\nabla\cdot\boldsymbol{E}} \left|\psi\right\rangle = \left|\psi\right\rangle, \tag{2.2}$$

we end up with the following *Gauss law*.

$$\nabla \cdot E = 0. \tag{2.3}$$

This rather simple result that gauge redundancy leads to local constraints is a hallmark of gauge theories. A violation of the Gauss law at a point defines a 'defect' of the field, localized in space. Recalling from our experience that this violation, expressed as $\nabla \cdot E = \rho$, is basically the

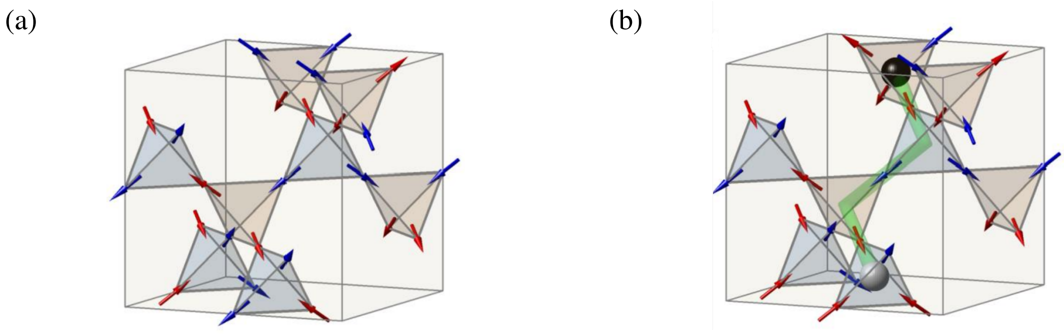

Fig. 2.1 **Spin ice and monopoles in a pyrochlore lattice.** (a.) In a spin ice material, classical spins form a pyrochlore lattice. The ground state is described by the 'two-in two-out' ice rule. (b.) Flipping a spin at a single site breaks the ice rules in two site-sharing tetrahedra. The defective tetrahedra host effective magnetic monopoles (black spheres) which can be separated from each other by sequentially flipping more spins. This realizes an emergent classical magnetostatics with monopoles and Dirac strings (green) connecting them. Figure adapted from Ref. [23]

definition of electric charge, we witness the magic where charges are a natural consequence of the electromagnetic gauge invariance. Beyond electromagnetism, all the other fundamental forces of the standard model were unified by introducing different gauge fields, proving that they are somehow, mysteriously, fundamental in physics. The current framework of particle physics consists of elementary particles like electrons and gauge fields that mediate interactions between them. However, in the late nineties, surprising developments in the (then) rather mundane field of condensed matter physics saw gauge theories emerge naturally, rather than being forced upon the framework!

2.2 Spin Ice: A (classical) Success Story

A remarkable and conceptually simple example of an emergent gauge theory in solid state systems is the spin ice model [22]. In the material $Dy_2Ti_2O_7$, Dy atoms form a pyrochlore lattice (corner-sharing tetrahedra), shown in Fig. 2.1, with their magnetic moments approximated by classical spins. The interaction between spins can be described by an effective nearest neighbour Ising model $\sum_{\langle ij\rangle} J\, S_i S_j$, where the local Ising axis is along the line connecting the centres of tetrahedra sharing the spin. A long-range dipolar interaction is also present in these systems, which we neglect for simplicity. The ground state manifold is described by the collection of spin-states obeying the 'ice rules': every tetrahedron must have two spins pointing inside and two outside ('two-in two-out'). An alert reader may already have spotted the gauge theory lurking behind this emergent local constraint. At temperature scales below the Ising exchange strength, thermal fluctuations will dominantly mix states within this large ground state manifold.

Let us now connect the centres of adjacent tetrahedra to form a diamond lattice whose links now hold an Ising variable: the spins of the original lattice. Fluctuations within the ground state manifold will involve flipping these variables such that the ice rules remain intact. It is easy to see that such transformations will trace out closed loops of flipped link variables. This picture now resembles a lot the electromagnetic theory we saw earlier. To make this connection more apparent, let us call these variables ‘ magnetic’ vector field. Closed loops of this magnetic field lines form a defining property of the emergent magnetostatics. The ice rule corresponds to the Gauss law of this gauge theory, roughly speaking, a discrete version of Maxwell’s theory. Once we allow for defects (violation of the ice rule), something fascinating happens, magnetic monopoles emerge!

Consider flipping a single spin. This violates the Gauss law in two tetrahedra sharing the flipped spin. Such a pair of point defects form a source and a sink for the magnetic field lines, thus defining the emergent monopoles. Importantly, the pair (monopole and anti-monopole) can be separated by further spin flips without any extra energy cost making a single monopole the true elementary excitation of the system. Spin ice materials have been instrumental in helping us tame the concept of emergent gauge fields in condensed matter to some extent. Remarkably, several experiments have conclusively established this physics [24]. The most striking among them are the thermal quench experiments which observed a characteristic slow relaxation timescale, consistent with a physical picture of diffusion and annihilation of magnetic monopoles.[25, 26]

It is important to emphasize that spin ice is a purely classical system where the gauge fields are in fact observable quantities; they are real classical spins. In this sense it is qualitatively different from what we are concerned with in this thesis. Our focus will be on quantum systems where the emergent gauge fields are indeed a redundancy in the description and only the defects (gauge excitations) have a physical meaning. Adding quantum effects naturally takes us to the notion of a quantum spin liquid, a central theme of this thesis. Indeed, Ross *et al.* [27] showed that strong quantum effects can turn a classical spin ice into a quantum spin liquid with an emergent quantum electrodynamics, featuring quantum coherent excitations such as emergent magnetic and electric monopoles, as well as a gapless ‘photon’.

2.3 Quantum Spin Liquids and Fractionalization

While the story of spin ice is rather recent (early 2000s), the idea that quantum fluctuations may prevent the ordering of a magnet all the way down to absolute zero was already around since the 1970s. Anderson pioneered the notion of a phase of matter where the quantum spins are strongly entangled with each other and therefore exist in a macroscopic superposition state [28]. Much like we saw how a spin flip splits into two magnetic monopoles in the spin ice, a spin

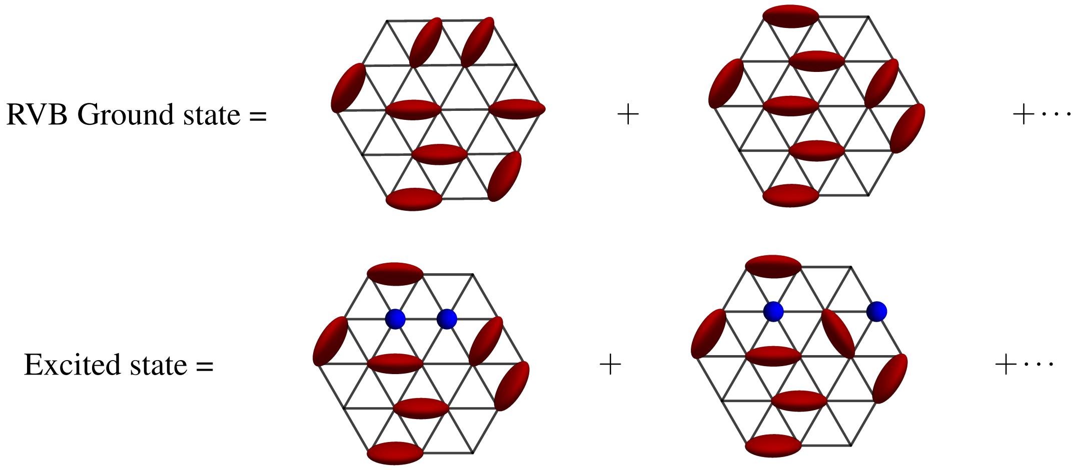

Fig. 2.2 **Resonating valence bond spin liquid and fractional spinons**. Spins on a triangular lattice form an EPR pair with its neighbour (red ellipsoids). The quantum state is a superposition of all possible pairings. (b.) Breaking a pair creates two unpaired spin-half excitations called spinons (blue spheres), that are deconfined and can hop around freely.

flip in such a quantum liquid state also splits into quasiparticles called *spinons*, but this time they are truly quantum objects that are entangled with each other. This exemplifies the idea of a collective phenomenon where the fundamental excitations carry a fraction of the quantum numbers of its constituents, an archetypal example being the fractional quantum Hall effect [29].

Consider a triangular lattice of spin-$\frac{1}{2}$ moments as shown in Fig. 2.2. One can imagine a state where the spins that share a link form an entangled EPR pair state, given by $|\uparrow\downarrow\rangle + |\downarrow\uparrow\rangle$ (represented by the red ellipses). Due to quantum fluctuations, different pairings can mix and the system can exist in a massive superposition state as shown schematically in Fig. 2.2. This defines what is called a resonating valence bond state (RVB), first proposed by Anderson as a variational ansatz [28]. There is no magnetization in the system and no symmetries are broken.

However, excitations on top of this state are well defined. Breaking an entangled pair will result in two unpaired modes carrying spin-$\frac{1}{2}$ quantum number (blue spheres) - spinons. Just like the monopoles we encountered before, this locally created pair can move independently, far from each other by rearranging the pairing bonds making a single spinon a well-defined and localized quasiparticle. However, unlike the monoples that always carry a 'Dirac string' of flipped spins connecting it to its anti-monopole pair, the spinons have no strings attached (pun intended); whatever connects them is completely unobservable. This is the essence of fractionalization in a quantum spin liquid. While in an ordered state, the elementary excitations must always carry an integer spin (e.g. magnons), they may carry only a fraction of it in a spin liquid. This is perhaps the most definitive statement and experimentally relevant feature of a quantum spin liquid. Absence of magnetic order is merely a guidepost, but detecting fractional quasiparticles is the smoking-gun sign of a quantum spin liquid.

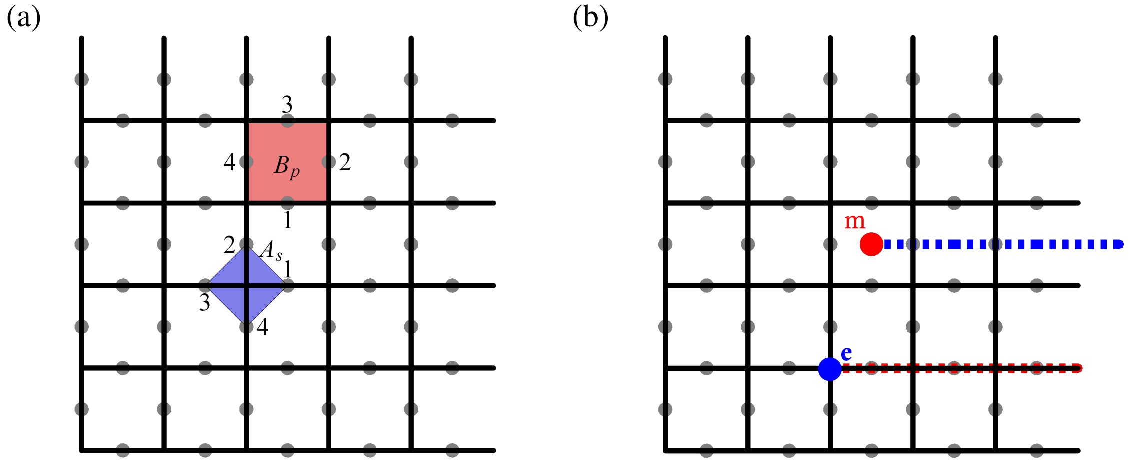

Fig. 2.3 **Toric code and gauge theory.** (a.) Grey dots at the centres of each edge are spin-1/2 degrees of freedom. The Hamiltonian is made of two types of operators, $\hat{A}_s$, defined as the product of σ^x around a vertex (blue) and $\hat{B}_p$ defined as the product of σ^z around a square plaquette (red). (b.) $B_p = -1$ and $A_x = -1$ at a single vertex or plaquette respectively constitute an elementary excitation of the Toric code. Flipping a semi-infinite chain of σ^z (σ^x) along the blue (red) dashed line creates a single m (e) particle.

How do all of this connect to gauge theories though? Does such a liquid like state with a macroscopically entangled ground state emerge naturally from a Hamiltonian? A paradigmatic model was invented by Alexei Kitaev in 2003 that naturally answers these questions in a remarkably elegant manner: The Toric code, a predecessor of the honeycomb spin liquid [30].

2.4 Toric Code: $\mathbb{Z}_2$ Gauge Theory and Anyons

The model is defined on a square lattice with period boundary conditions where every link (or edge) carries a single spin-$\frac{1}{2}$ degree of freedom. The Hamiltonian is defined as

$$H^{TC} = -J_A \sum_s \hat{A}_s - J_B \sum_s \hat{B}_p, \tag{2.4}$$

where the *vertex* operator $\hat{A}_s$ is defined on every vertex labelled by s, and *plaquette* operator $\hat{B}_p$ is defined on every square plaquette p as follows.

$$\hat{A}_s = \prod_{j=1}^{4} \sigma^x_{j,s}, \qquad \hat{B}_p = \prod_{i=1}^{4} \sigma^z_{i,s}. \tag{2.5}$$

Here, $\sigma^x_{i,s}$ is the Pauli operator corresponding to the spin-$\frac{1}{2}$ at the link i, connected to the vertex s. Similarly the plaquette operator is defined as the product of σ^z around a square plaquette as shown in Fig. 2.3.

The operators $\hat{B}_p$ and $\hat{A}_s$ all commute with each other:

$$[\hat{B}_p, \hat{B}_{p'}] = 0, \qquad [\hat{A}_s, \hat{A}_{s'}] = 0. \tag{2.6}$$

The commutation of a vertex (plaquette) operator with its neighbouring vertex (plaquette) operator is trivially proven, as they all involve the same spin component. The commutativity of a vertex and its adjacent plaquette operator follows from the fact that they always share two sites with each other. Importantly, every operator in the Hamiltonian is a conserved quantity, and has eigenvalues ± 1 as $\hat{B}_p^2 = \hat{A}_s^2 = 1$. Periodic boundary conditions also impose an extra global conservation law give by

$$\prod_p \hat{B}_p = \prod_s \hat{A}_s = 1 \tag{2.7}$$

Given $J_p = J_s > 0$, the ground state is then given by all the eigenvalues being 1:

$$B(p)\,|\psi\rangle = |\psi\rangle\,\forall p, \qquad A(s)\,|\psi\rangle = |\psi\rangle\,\forall v. \tag{2.8}$$

One can even write down the exact ground state wavefunction of the many body system as

$$|\psi\rangle = \frac{1}{\sqrt{2}} \prod_v (\mathbb{1} + \hat{A}_s)\,|0\cdots 0000\rangle\,. \tag{2.9}$$

The gauge theory is now apparent. Every link hosts a $\mathbb{Z}_2$ gauge field variable. The vertex operator then resembles an electric field while the plaquette operator defines a magnetic field. The condition that all $\hat{B}_p$ operators take eigenvalues 1 is analogous to the Gauss law we encountered in electromagnetism as well as in the spin ice system. Expanding the ground state wavefunction given above, one ends up with a sum of many states of the form $\hat{A}_{s_1}...\hat{A}_{s_n}\,|00...0\rangle$, for arbitrary n. The ground state is thus a superposition of all states where the flipped σ^z eigenvalues are flipped such that they form closed loops in the dual lattice connecting the centers of the squares. An example of such a loop is shown in Fig. 2.4a (blue dashed square). One can transform between different states in this superposition by flipping such closed loops. This defines the gauge transformations! We could have also written the ground state in terms of the $\hat{B}_p$ operators, with the spins in the σ^x basis. In this picture, the loops would be defined in the original lattice. This reflects a fundamental duality between the 'electric' and 'magnetic' fields in this model.

2.4.1 Topological order

Besides the closed loops, there exists another class of conserved quantities in the toric code defined by loops that wind around the torus, similar to the Wilson loops in Wegner's lattice

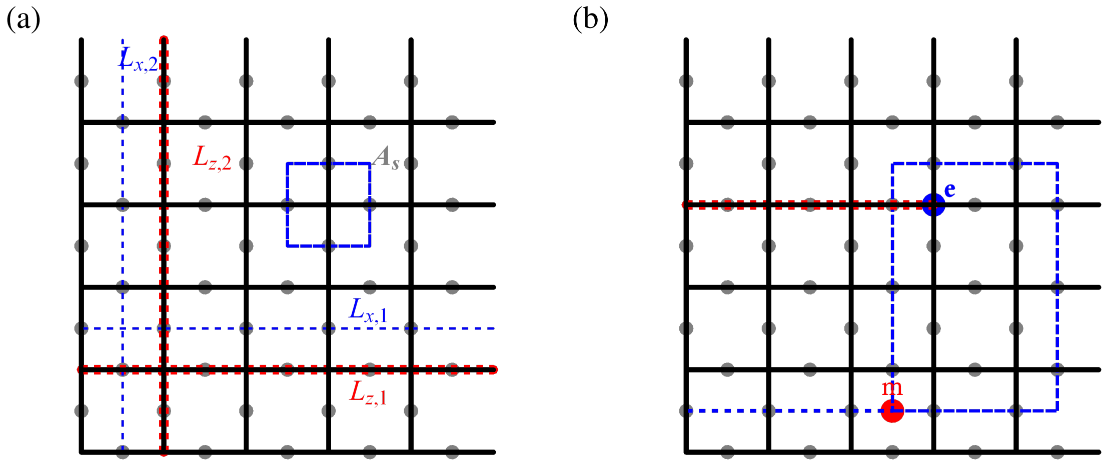

Fig. 2.4 **Topological order and Abelian anyons.** (a.) $L_{x,1}, L_{x,2}, L_{z,1}, L_{z,2}$ defines loops that run around the torus in horizontal and vertical directions. They are conserved quantities of the toric code and determines its topological order. (b.) Taking an m particle around an e particle along the dashed blue loop results in an extra phase of π for total wavefunctions. e and m are abelian anyons with respect to each other.

gauge theory [31]. These are illustrated in Fig. 2.4a defined by $L_{z,1(2)} = \prod_i \sigma_i^z$, where the product is defined along the red line that runs horizontally (vertically) across the whole torus. Similarly, the operator $L_{x,1(2)} = \prod_j \sigma_j^x$, where the product is over the sites crossed by the blue line winding around the torus in the horizontal (vertical) direction. They are conserved quantities with eigenvalues ±1:

$$[L_{x,1}, L_{z,1}] = [L_{x,2}, L_{z,2}] = 0, \qquad \{L_{x,1}, L_{z,2}\} = \{L_{x,2}, L_{z,1}\} = 0. \tag{2.10}$$

These non-trivial loops define the topological order [32] that describes a phase of matter that does not exhibit broken symmetries, characterized by degenerate ground states that cannot be distinguished by any local operator. Earlier, we obtained the ground state of the toric code by assigning to the vertex and plaquette operators eigenvalues 1. However, the eigenvalues of the non-contractible loops still need to be fixed. Using the commutation relations Eq.(2.10), one can think of the four non-trivial loop operators as the Pauli x and z operators of two effective spin-1/2 modes. In the basis of $L_{z,1}$ and $L_{z,2}$ with the eigenvalues denoted by z_1 and z_2 one can define a four-dimensional ground state manifold labelled by $(z_1, z_2) = (1,1), (1,-1), (-1,1), (-1,-1)$. Graphically, $z_1 = -1$ corresponds to a non-trivial loop winding across the torus in the vertical direction. Similarly $z_2 = -1$ defines a loop along the horizontal direction. (See Fig. 2.4). Therefore, if one needs to detect a ground state within the manifold, a global observable has to be checked; no local process is capable of it. Indeed, to flip between two ground states, the non-trivial loops $L_{x,1}$ and $L_{x,2}$ have to be used, just like σ^x flips between the eigenstates of σ^z for a usual spin-half particle.

2.4.2 Abelian anyons

What are the excitations of the toric code? The elementary excitation corresponds to a single vertex or a plaquette operator with eigenvalue -1. In terms of the gauge theory, these can be interpreted as "electric" and "magnetic" charges denoted by e and m. A single $\sigma^x_{v,1}$ acting on the ground state would flip the eigenvalues of two plaquette operators that share the link $(v,1)$, creating a pair of m particles. Similarly, a single $\sigma^z_{p,1}$ would create a pair of e particles at the two vertices connected by the link $(p,1)$. The global conservation law further constraints that, in a toroidal geometry, e and m particles should always come in pairs. However, one can still consider a single isolated excitation by taking its pair far way; infinitely far away in the thermodynamic limit.

Consider two isolated e and m particles, as illustrated in Fig.2.3b. We can apply a sequence of σ^x operators along a closed loop such that the e particle moves in a loop (shown in blue) and comes back to its original position. If this loop encloses the m particle, as shown in Fig.2.4b, the quantum state of the system acquires an extra phase π. This simply arises from the fact that the closed loop intersects the string of σ^x used to create the m particle. The Pauli algebra then enforces a minus sign on the final wavefunction. This observation reveals the *anyonic* nature of e and m particles. Taking an e particle around an m results in the wavefunction acquiring an extra minus sign. An e and an m particle are thus said to be mutual *semions* but two e (or two m) particles are bosons with respect to each other. The excitations of the toric code realizes the simplest class of anyons called *abelian* anyons, where the exchange of two particles results in a U(1) phase. As we will see in the next chapter, more complicated *non-abelian* anyons whose exchange results in a unitary transformation acting on the ground state manifold.

2.4.3 Quantum memory

The toric code is many things. But Kitaev originally proposed it as a model of fault tolerant quantum computation. It is worth discussing this rather important aspect of the model. The degenerate ground state manifold offers an ideal space to store quantum information, protected from errors. The four-fold degenerate space can realize two logical qubits. Since no local processes acting on individual spins can cause a transition between two ground states, (we shall make this argument more quantitative in a moment), there is virtually no errors affecting the logical qubit space. Let us understand this a bit more closely.

Imagine adding a a small Zeeman field term $h\sum_i \sigma^z_i$ to the toric code Hamiltonian. At zero temperature, we prepare the system in one of the ground states, say $z_1 = z_2 = 1$ and turn on the Zeeman field. The perturbation at a single site will create a pair of e particles, raising the energy of the system by $\Delta = 2J_s$. However such creation processes will be exponentially suppressed in temperature by the factor $\sim e^{-\beta\Delta}$, leaving only virtual processes involving creation and annihilation of pairs. For a logical error to occur, one of these virtual processes should involve creating a pair and taking them all the way around the torus only to finally annihilate them. Using perturbation theory, it is straightforward to argue that such a hopping of an e particle around a torus of length L occurs at order h^L. Thus for a weak perturbation to the toric code, $h \ll \Delta$, logical errors are exponentially suppressed in system size as well as the energy gap. Equivalently, the energy splitting between the different ground states of a perturbed toric code decreases exponentially with the system size. This excited the hope of a robust quantum memory - a holy grail of quantum computing. However, it turns out that, although the toric code is resilient to a coherent noise source like the Zeeman field above, it is totally fragile towards incoherent error sources like a finite temperature bath. At a finite temperature, the topological order and consequently the ground state degeneracy are destroyed [33, 34].

2.5 Experimental Evidence of Quantum Spin Liquids

The natural question arises: are these exotic macroscopic quantum states possible to be realized in real systems? Anderson's original proposal of an RVB ground state was explored in several triangular lattice antiferromagnets. However, it was later shown that a simple triangular antiferromagnet in fact orders in a 120° Nèel state. Follow up works claimed that adding a weak next-nearest exchange induces a spin liqiud phase in a narrow parameter range. Experimental search for possible realizations of spin liquids in magnetic materials have not provided any smoking-gun evidence for a true spin liquid state. However, theoretical insights have been helpful in developing a general recipe to guide our search - magnetic *frustration* and quantum fluctuations in spin (or effective spin)-$\frac{1}{2}$ systems. Frustration refers to the inability of spins to align with each other due to competing interactions. This could be naturally induced by the lattice geometry, or by tailored Hamiltonians that enhance quantum fluctuations. According to conventional wisdom, low dimensionality should also enhance quantum effects, bringing 2D (or quasi 2D) materials to the forefront of this research.

In particular, Kagome and triangular lattices due to their frustrating geometry have received tremendous attention. As a popular example for a triangular lattice system, κ-(BEDT-TTF)$_2$Cu$_2$(CN)$_3$, a 2D organic salt, was studied using NMR (nucear magnetic resonance) which suggested a lack of magnetic ordering and gapless spinon-like degrees of freedom [35]. In other materials within the class of 2D organic salts, metallic thermal conductivity ($\kappa \propto T$) at low temperatures was observed in some samples which may suggest the presence of a Fermi surface of charge neutral spinons [36]. However, the existence of such a spinon-Fermi surface even lacks a solid theoretical foundation at moment. Extensive experimental efforts were aimed at Herbertsmithite (ZnCu$_3$(OH)$_6$Cl$_2$) as a potential spin liquid material due to its Kagome geometry. No long range order was found in this system and neutron scattering experiments observed a broad continuum of excitations[37]. However, the explanation of this in terms of novel fractionalized excitations are strongly contested by other descriptions based on disorder or impurity spins[38, 39]. These two examples certainly do not exhaust this rich field teeming with numerous candidate materials.

2.6 Aim and Outline

Despite the astounding progress in the field, there is a pressing need for an unambiguous experimental detection of a quantum spin liquid and emergent gauge fields. Ending the dearth of solvable models, Kitaev, in his seminal paper [40] introduced an exactly solvable spin model hosting a spin liquid in its ground state. Needless to say, the model has been studied extensively and several exciting properties both relevant to experiments and theory have been extracted. Another theoretical milestone was achieved when Jackeli and Khaliullin [41] demonstrated that the Kitaev model can indeed be realized in naturally occurring materials. A half-quantized thermal Hall effect, the smoking-gun evidence of the Kitaev spin liquid was reported in the material $\alpha - \mathrm{RuCl}_3$[42, 43]. This has ignited an overwhelming excitement across the field. Although a conclusive reproduction of this result is still awaited, it is arguably the closest we have ever come to realizing a true quantum spin liquid with emergent gauge fields.

However, the nature of the emergent gauge theory in these systems remains poorly understood due to the strong interaction between the gauge fields and matter fermions. Understanding the dynamics of Z_2 gauge theories with gapless matter in general has been a long standing problem. In this thesis we aim to take a crucial step towards bridging this gap between an idealized model and its material realization. They central objective is to characterize the dynamical properties of the emergent gauge field, when perturbations arising from real materials and external fields are present. The main protagonists will be *visons*, the elementary excitations of the emergent gauge theory.

In Chapter 3, I will introduce Kitaev's exactly solvable model and describe how an emergent gauge theory coupled to matter fermions emerges in this model. A brief discussion of material candidates that can potentially realize this model will be discussed, particularly focusing on the material $\alpha - \mathrm{RuCl}_3$. This will set up the main questions we explore in this thesis. In Chapter 4, quantum dynamics of a single vison due to material relevant perturbations and an external magnetic field will be investigated. Chapter 5 deals with the finite temperature effects on vison motion, arising from the surrounding gapless matter fermions. In Chapter 6, we will investigate the effects arising from the layered three-dimensional structure of materials on the emergent gauge field. In Part III, we will present two major experimental signatures: Raman spectroscopy (Chapter 7) and the thermal Hall effect (Chapter 8). We will end with an overarching summary and a brief outlook towards future directions.

Chapter 3

The Kitaev Spin Liquid

In this chapter, we introduce the honeycomb model proposed by Kitaev [40]. We will review the original solution using the Majorana representation, with an emphasis on the emergent gauge field excitations - visons. This will help us grasp the fractionalized nature of quasiparticles in the spin liquid phase. A thorough understanding of this *pure* Kitaev model will form the foundation for the remaining chapters, where we add realistic perturbations to the model, destroying its exact solubility.

3.1 The Model

The Kitaev model is defined on a honeycomb lattice of spins. Interaction between spins are described by the Hamiltonian

Kitaev Hamiltonian

$$H = K_x \sum_{\langle ij \rangle_x} \sigma_i^x \sigma_j^x + K_y \sum_{\langle ij \rangle_y} \sigma_i^y \sigma_j^y + K_z \sum_{\langle ij \rangle_z} \sigma_i^z \sigma_j^z, \tag{3.1}$$

where $\gamma = x, y, z$. This defines three types of bonds on the honeycomb lattice, shown in three different colours in Fig. 3.1. Two spins that share a red coloured bond, denoted by $\langle ij \rangle_z$, interact with each other through the z component of the spin. Similar definitions follow for blue (x-type) and green (y-type) bonds. Due to the non-commuting property of the three types of interactions on a single site, the model has what is called *exchange frustration*.

The Kitaev model is exactly solvable due to the presence of an extensive number of conserved quantities: the plaquette operators, defined as the product of Kitaev terms ($\sigma_i^\alpha \sigma_j^\alpha$)

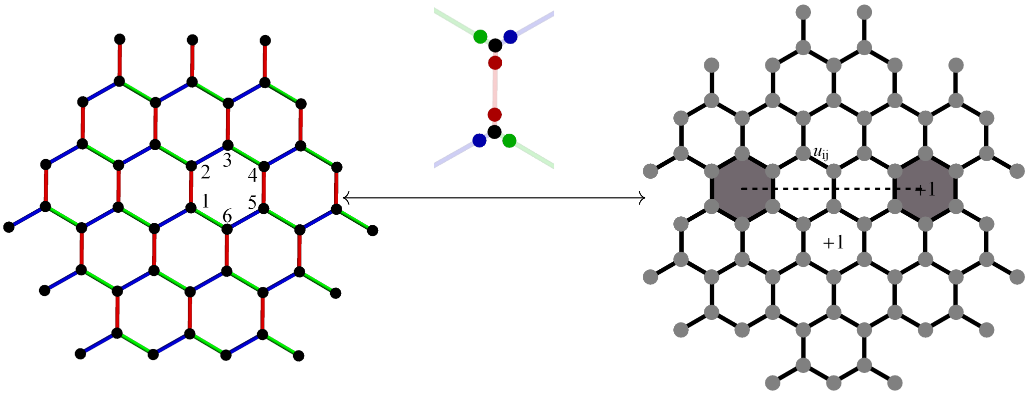

Fig. 3.1 **Kitaev honeycomb model and the emergent gauge theory** Kitaev model defined on a honeycomb lattice of spins. The spin interactions $\sigma_i^\alpha \sigma_j^\alpha$ depends on the type of link $\langle ij \rangle$ connecting them. $\alpha = x\,(\text{blue}), y\,(\text{green}), z\,(\text{red})$. Spin-Majorana mapping is illustrated above the arrow. Majorana fermions of four kinds c_i (black), b^x (blue), b^y (green) and b^z (red) are introduced on each site to rewrite the spin operators as $\sigma_i^\alpha = i b_i^\alpha c_i$. The model on the right has the c Majoranas hopping on the honeycomb lattice coupled to a $\mathbb{Z}_2$ gauge field formed by $u_{\langle ij \rangle}$. The shaded plaquettes correspond to the fluxes of the gauge field - visons.

around an elementary hexagon, indexed by p. For example,

$$W_1 = \sigma_1^z \sigma_2^z \sigma_2^x \sigma_3^x \sigma_3^y \sigma_4^y \sigma_4^z \sigma_5^z \sigma_5^x \sigma_6^x \sigma_6^y \sigma_2^y = \sigma_1^x \sigma_2^y \sigma_3^z \sigma_4^x \sigma_5^y \sigma_6^z \tag{3.2}$$

as shown in Fig. 3.1. Importantly, these operators are localized on the hexagons and have eigenvalues $w_p = \pm 1$. The conservation law is then expressed as

$$[H, W_p] = 0, \qquad [W_p, W_{p'}] = 0. \tag{3.3}$$

This implies that the eigenstates of the spin model can be separated into sectors labelled by a set of eigenvalues of all W_p operators. As we shall see shortly, Kitaev's exact solution gives a beautiful physical interpretation to these objects in terms of exotic quasiparticles of the model, completely different in nature from the underlying spins.

To solve the model, we start out by mapping every spin to four *Majorana* fermions, b^x, b^y, b^z, c. These obey the fermionic commutation relations, and are their own antiparticles: $c = c^\dagger$, $b^\alpha = b^{\alpha\dagger}$. The spin operators are written as,

$$\sigma_j^x = i b_j^x c_j, \qquad \sigma_j^y = i b_j^y c_j, \qquad \sigma_j^z = i b_j^z c_j. \tag{3.4}$$

This is shown schematically in Fig.3.1. The Hamiltonian becomes

$$H = -\sum_{\langle ij \rangle_\gamma} K^\gamma i \hat{u}_{ij}^\gamma c_i c_j, \tag{3.5}$$

where we introduced a 'bond operator' $\hat{u}^{\gamma}_{ij} = ib^{\gamma}_{i}b^{\gamma}_{j}$, for a link of type γ, that connects site $i \in A$ and $j \in B$, where A and B are the two sub-lattices of the honeycomb lattice. Operators $\hat{u}^{\gamma}_{ij}$ takes eigenvalues $u_{ij} = \pm 1$. Most importantly, they commute with the Hamiltonian, as well as with each other:

$$[H, \hat{u}^{\gamma}_{ij}] = 0, \qquad [\hat{u}^{\gamma}_{ij}, u^{\alpha}_{kl}] = 0. \tag{3.6}$$

The conserved quantities, plaquette operators $\hat{W}_p$, of the original spin model now become local *flux* operators of the gauge theory.

$$\hat{W}_p = \prod_{<ij>_{\alpha} \in \hexagon} \hat{u}^{\alpha}_{ij} \tag{3.7}$$

Introduction of fermions on each site naturally leads to a doubling of the Hilbert space (two complex fermions can be fromed out of four Majoranas). More precisely, while the original spin model has a Hilbert space dimension of 2^N, the enlarged (fermionic) Hilbert space has dimension 2^{2N}. This implies that half of the fermionic states must be *unphysical* and should not affect observables. This is enforced by an operation which would project any unphysical state to zero. Such a *projector*, $\hat{P}_i$, can be defined as

$$\hat{P} = \prod_{i} \frac{(1 + \hat{D}_i)}{2}, \text{ with} \qquad \hat{D}_i = b^x_i b^y_i b^z_i c_i. \tag{3.8}$$

The projector acts on a state in the fermionic Hilbert space as follows.

$$\hat{P}\left|\psi\right\rangle = \left|\psi_{ph}\right\rangle, \qquad \left|\psi\right\rangle \in \mathscr{H} \qquad \left|\psi_{ph}\right\rangle \in \mathscr{H}_{spin}. \tag{3.9}$$

Thus, a physical state can be defined by the following condition:

$$\hat{D}_i \left|\psi_{ph}\right\rangle = \left|\psi_{ph}\right\rangle \qquad \forall \quad i. \tag{3.10}$$

Making the gauge fields explicit, the spin Hamiltonian can now be written as

$\mathbb{Z}_2$ Gauge theory with matter

$$H = -iK_x \sum_{<ij>_x} u^x_{ij} c_i c_j - iK_y \sum_{<ij>_y} u^y_{ij} c_i c_j - iK_z \sum_{<ij>_z} u^z_{ij} c_i c_j \tag{3.11}$$

where $u_{\langle ij \rangle} = \pm 1$.

3.2 Solving the model

For any given configuration of the gauge field, $\mathscr{G} = \{u_{\langle ij\rangle}\}$, the Hamiltonian is reduced to a simple model of fermions hopping on a honeycomb lattice, with the signs of the hopping rate specified by the gauge field value on the corresponding link. In matrix form,

$$H = \frac{i}{2}\begin{pmatrix} c^A & c^B \end{pmatrix}\begin{pmatrix} 0 & M \\ -M^T & 0 \end{pmatrix}\begin{pmatrix} c^A \\ c^B \end{pmatrix} \tag{3.12}$$

where $c^A = (c^A_1, c^A_2, ..., c^A_N)$ and M is a $N \times N$ matrix where N is the number of unit cells. Here, we introduce a slight change of notation to label the sublattice degrees of freedom by A and B.

The absence of diagonal elements simply implies that there is no hopping between the same sublattice sites. In his original work, Kitaev showed that an external magnetic field, $\boldsymbol{h} = \frac{h}{\sqrt{3}}(1,1,1)$, induces a next-nearest neighbour hopping term $\kappa \sim \frac{h_x h_y h_z}{K^2}$. We will review this in the following sections. Therefore, in general, if time reversal symmetry is broken, the general form of the Majorana Hamiltonian is

$$H = \frac{i}{2}\begin{pmatrix} c^A & c^B \end{pmatrix}\begin{pmatrix} D & M \\ -M^T & -D \end{pmatrix}\begin{pmatrix} c^A \\ c^B \end{pmatrix}. \tag{3.13}$$

It is convenient to combine pairs of Majoranas into complex fermions to convert the Hamiltonian into the familiar Bogoliubov-de-Gennes (BdG) form [44],

$$H = \frac{1}{2}\begin{pmatrix} f^\dagger & f \end{pmatrix}\begin{pmatrix} \xi & \Delta \\ \Delta^\dagger & -\xi^T \end{pmatrix}\begin{pmatrix} f \\ f^\dagger \end{pmatrix}, \tag{3.14}$$

where the complex fermions are defined on a z-bond (chosen to be the unit cell), at position $\boldsymbol{r}$:

$$f_{\boldsymbol{r}} = \frac{1}{2}(c_i + i c_j), \qquad f^\dagger_{\boldsymbol{r}} = \frac{1}{2}(c_i - i c_j). \tag{3.15}$$

The parameters of the Hamiltonian are given by

$$\xi = M + M^T, \qquad \Delta = M^T - M + i\,2D. \tag{3.16}$$

The BdG Hamiltonian can be diagonalized by a Bogoliubov transformation T, to obtain the energy spectrum and eigenstates, with

$$T^\dagger H T = \begin{pmatrix} -E & 0 \\ 0 & E \end{pmatrix}, \tag{3.17}$$

where E is an $N \times N$ diagonal matrix with the energy levels $\varepsilon_i = E_{ii}$. The eigenmodes, or the Bogoliubov quasiparticles, are given by operators a, defined by

$$\begin{pmatrix} X^* & Y^* \\ Y & X \end{pmatrix} \begin{pmatrix} f \\ f^\dagger \end{pmatrix} = \begin{pmatrix} a \\ a^\dagger \end{pmatrix}. \tag{3.18}$$

The many-body ground state is then given by the Bogoliubov vacuum $|0\rangle$, defined by $a|0\rangle = 0$, and energy -$\frac{1}{2}\sum_{i=1}^{N} \varepsilon_i$. The spectrum is symmetric with respect to zero, reflecting the particle hole symmetry of the model.

3.2.1 Many-body wavefunctions

The Hamiltonian given by Eq.(3.14), for a given gauge configuration $\mathscr{G}$, has the same form as a that of superconductor in the BCS formalism [45]. The ground state wavefunction can be thus mapped to the corresponding BCS vacuum, denoted by $|M(\mathscr{G})\rangle$. Using the Bogoliubov transformation T, and the resulting eigenmodes a_n, this can be expressed in the so called Thouless form [46](or Onishi formula in nuclear physics) as

BCS ground state

$$|M(\mathscr{G})\rangle = \sqrt{\det(X)} \exp\left\{ -\frac{Z_{mn}}{2} a_m^\dagger a_n^\dagger \right\} |0_f\rangle, \tag{3.19}$$

where we have defined the matrix

$$Z = X^{*-1} Y^*. \tag{3.20}$$

Here, $|0_f\rangle$ denotes the vacuum state for the f fermions, defined by $f_i |0_f\rangle = 0$, for any i.

An important caveat is the following. By definition, Eq.(3.19) assumes that the f fermion vacuum and the BCS vacuum are non-orthogonal to each other. The BCS wavefunction is built as a superposition of states with even number of eigenmodes a on top of $|0_f\rangle$. However, for certain gauge configurations, the parities of f and a fermions are opposite to each other, resulting in $\det(X) = 0$. The total fermionic parity, of χ and c, is a gauge invariant quantity and follows the following relation.

$$(-1)^{N_\chi + N_f} = -\det(Q)(-1)^{N_a} \prod_{\langle ij \rangle} u_{ij}. \tag{3.21}$$

where N_a is the total number of eigenmodes occupied (for ground state, it is zero) and Q is defined using the Bogoliubov matrices [47, 48]. $\det\{Q\}$ takes values ± 1. This implies,

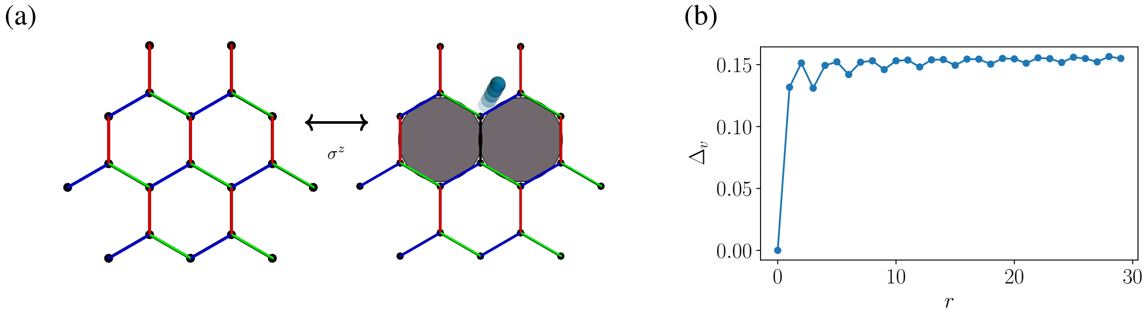

Fig. 3.2 **Fractionalization of a spin.** In the Kitaev model, a single spin flip, e.g. σ^z, flips a pair of localized gauge field excitations, visons (shaded hexagons), and creates an itinerant Majorana fermion (blue sphere). (b). The energy cost per vison, Δ_v, as a function of the separation r between a pair. The value saturates to the $\Delta_v^0 \approx 0.15|K|$ implying that the visons are deconfined.

depending on the gauge configuration and $\det\{Q\}$, the parity of f fermions and that of the eigenmodes a has to be different from each other for the state to be physical. See Ref.[47] for further details. In the next chapter, we will show how to circumvent this complication by using appropriate gauge transformations, as well as by carefully choosing basis states that are non-orthogonal to the BCS wavefunctions we are interested in.

3.3 Emergent Gauge Theory

The doubling of Hilbert space obviously introduces redundancy in the description of the system, a defining feature of gauge theories in physics. Let us explore this connection in detail. Starting from the fermionic Hamiltonian, one can replace the bond operators $\hat{u}_{ij}^{\gamma}$ with their eigenvalues ± 1 as they commute with the Hamiltonian. This defines a $\mathbb{Z}_2$ degree of freedom that lives on each bond of the honeycomb lattice forming the emergent gauge field. The c Majorana fermions form the *matter* degrees of freedom. The gauge-matter coupling takes the form of a Peierls' factor attached to the hopping terms where the phase takes values of 0 or π.

For a fixed pattern of u_{ij}^{γ} (fixed gauge) the Hamiltonian is purely fermionic with only quadratic terms and can be diagonalized to obtain the eigenvalues and eigenstates. Therefore, for a system of N spins, each of the $2^{\frac{3N}{2}}$ patterns results in a free fermion problem. We can then use the projector $\hat{P}$ to obtain the physical states. This is what makes the Kitaev model exactly soluble.

3.3.1 Visons

In particle physics where gauge theories are more fundamental, excitations of the gauge field carry the *gauge charge* and mediate interactions between matter particles, much like the photon of the electromagnetic field. These excitations define the physical degrees of freedom of the gauge theory and are gauge invariant objects. What are the analogous excitations of our emergent $\mathbb{Z}_2$ gauge field? (Recall our discussion in Chapter 2.) To answer this, let us create a local excitation by flipping the value of a single gauge variable u_{ij}^{γ}, while all the others are set to $+1$. This flips the eigenvalues of two plaquette operators that share the flipped bond, costing an extra energy of $\Delta_{2v} \approx 0.26\,|K|$, on top of ground state. If we flip a chain of u_{ij}^{γ} such that one end of the chain is at the boundary, we have created a single $W_p = -1$. This costs an energy $\approx \frac{\Delta_{2v}}{2}$, which is, most importantly, finite. The W_p operators that are localized on the plaquettes thus represent the elementary physical degrees of freedom of the gauge field. Flipping w_p from $+1$ to -1 creates a localized excitation at the plaquette p. Such an excitation of a $\mathbb{Z}_2$ gauge field is called a *vison*. [1]

The above described process can be then interpreted as creating a pair of visons locally, and taking one of them to the system's boundary, resulting in an isolated vison in the bulk. Importantly, a single vison is a localized quasiparticle with a finite energy $E_v^0 \approx 0.15\,|K|$ (we assume $K_x = K_y = K_z = K$ for simplicity). This property, known as *deconfinement*, is crucial for the emergence and stability of a gauge theory and fractional quasiparticles. A locally created excitation splits into two (or more) quasiparticles, which can be infinitely separated with a finite energy cost. Fig. 3.2b shows the energy of a system of two visons, as a function of their separation. The numerically obtained plot clearly shows that in the limit of large separation, the energy saturates to a finite value. The oscillating behaviour arises from finite size effects, enhanced by the gapless nature of Majoranas.

3.3.2 Gauge transformation

Consider the action of $\hat{D}_i$, defined in Eq. (3.8), on a given configuration of u_{ij}^{γ}. It flips the signs of all the gauge links that are connected to the site i, while leaving the plaquette operators W_p (visons) unaffected.

$$\{\hat{D}_i, \hat{u}_{ij}^{\gamma}\} = 0, \qquad [\hat{D}_i, \hat{W}_p] = 0. \tag{3.22}$$

The operator $\hat{D}_i$ hence defines a gauge transformation; it changes the gauge configuration but does not affect the physical degree of freedom of the gauge field. A subtle caveat here is that the gauge transformation here also affects the matter sector in a non-trivial way, as obvious from Eq. (3.8). The projection operator $\hat{P}$ implements nothing but an average over all gauge configuration acting on a given state. This is, in general, necessary to obtain physical observables after doing calculations in a fixed gauge, much like in classical electromagnetism.

---

[1] The name 'vison' was coined by Senthil and Fischer in Ref. [49] as it corresponds to a vortex configuration of a $\mathbb{Z}_2$ field. Within their theory of electron fractionalization, the vison is a remnant of an unpaired $hc/2e$ BCS vortex of high-T_c superconductor.

An important feature of the emergent gauge field in the Kitaev model is its static nature. The visons, once created, are completely localized, a consequence of Eq.(3.3). In other words, visons are infinitely massive quasiparticles of this model.

3.4 Bond Fermions

To facilitate calculations using the exact wavefunctions, it is convenient to form complex fermions out of the b Majoranas [50]:

$$\chi_{\langle ij\rangle_\alpha} = \frac{1}{2}(b_i^\alpha + i b_j^\alpha), \qquad \chi^\dagger_{\langle ij\rangle_\alpha} = \frac{1}{2}(b_i^\alpha - i b_j^\alpha), \tag{3.23}$$

where $\boldsymbol{r}$ denotes the position vector of a unit cell (the center of a z link). The Z_2 gauge variables on each link can now be expressed as the number parity of the corresponding χ fermions:

$$\hat{u}_{ij}^\alpha = 2\chi^\dagger_{\langle ij\rangle_\alpha}\chi_{\langle ij\rangle_\alpha} - 1. \tag{3.24}$$

In other words, the Z_2 gauge variables can be interpreted as the occupation number of fermionic modes that live on the links. where '$+$' is for the sublattice A and '$-$'for B. We can now use this framework to describe how a spin *fractionalizes* in the Kitaev model. The spin operator becomes

$$\sigma_i^\alpha = \frac{i}{2}(\chi^\dagger_{\langle ij\rangle_\alpha} + \chi_{\langle ij\rangle_\alpha})c_i \qquad \sigma_j^\alpha = -\frac{1}{2}(\chi^\dagger_{\langle ij\rangle_\alpha} - \chi_{\langle ij\rangle_\alpha})c_j, \tag{3.25}$$

where $i \in A$ and $j \in B$. We call the space of χ fermions as the *gauge sector*, while the f fermions constitute the *matter sector*.

A generic eigenstate of the model can be written as a direct product of states in the gauge and matter sector:

$$|\Phi(\{R_1, R_2, ..\})\rangle = \hat{P}\,|\{R_1, R_2, ..\}, \mathscr{G}\rangle\,|M(\mathscr{G})\rangle\,, \tag{3.26}$$

where $\{R_1, R_2, ..\}$ specify the positions of the visons, and $|M(\mathscr{G})\rangle$ represents the many-body wavefunction of the matter Majoranas in the presence of the visons, all expressed in the fixed gauge field configuration $\mathscr{G}$. The action of spin operator on the ground state is now clear: it changes the χ fermion occupation on the corresponding bond creating a pair of visons and simultaneously introduces a free Majorana fermion which now propagates in the new vison-pair potential.

We note that $\mathscr{G}$ already fixes the vison positions making Eq. (3.26) redundant. Nevertheless, we stick with it so as to get a more intuitive understanding while working with multiple vison sectors.

3.5 Physical States and Projection

While calculating physical quantities that are gauge invariant, it is imperative that we use the projection operation. Let us see how to numerically implement the projector on a finite size system. Although the infinite sum over gauge configuration may seem an insurmountable problem, Pedrocchi, Chesi and Loss [47] showed that it is possible to implement the projection operator on a finite size system by relating it to fermionic parities.

The projection operator can be factorized as a product of operators $\hat{P}'-$ sum of gauge transformations that change the local bond fermion occupation numbers in unique ways, and $(1+D_0)$, a global gauge transformation that does not change the link variables for a system with periodic boundary conditions[47, 51]:

$$\begin{aligned}\hat{P} &= \frac{1+\sum_i \hat{D}_i + \sum_{i,j}\hat{D}_i\hat{D}_j + \ldots + \prod_i \hat{D}_i}{2^{2N}} \\ &= \hat{P}'\frac{(1+\prod_i \hat{D}_i)}{2} = \hat{P}'\frac{1+(-1)^{\theta+N_\chi+N_f}}{2}.\end{aligned} \tag{3.27}$$

Importantly, the second equality shows that the operator $(1+D_0) = (1+\prod_i \hat{D}_i)$ is ultimately related to the parity of total number of bond and matter fermions. The factor $\theta = M+L_1+L_2$ will be chosen to be even for the rest of the work, where L_1 and L_2 are the linear dimensions of the system and M is a factor that depends on how the periodic boundary is implemented. The projection operation can thus be understood as follows. Any state with an odd number parity of fermions is an unphysical state, which is annihilated during the projection, while a state with even fermionic number parity is transformed into a superposition of (non-equivalent) gauge transformed states within the same flux sector.

3.6 Ground State

What is the ground state of the model? Since visons cost finite energy, one would expect the ground state to be in the zero vison sector. However, we should not forget that the visons can act like scattering potentials for the Majoranas, possibly leading to lower energy states. Due to a theorem by Lieb [52, 53], it turns out that the ground state is indeed vison free, for the Kitaev model. Recall that we still have the freedom to choose a gauge configuration. The energy levels are gauge invariant, observable quantities. The most convenient choice is to set all gauge

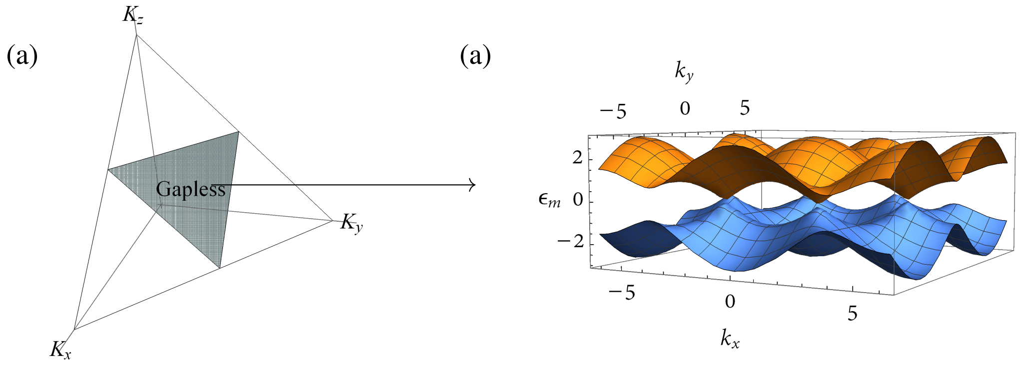

Fig. 3.3 **Ground state phase diagram and Dirac fermions**. The Kitaev model features a gapless spin liquid near the isotropic point $K_x = K_y = K_z$ where the Majorana fermions have a linear band touching, as sketched in (b). The spectrum obtains a (trivial) gap for sufficiently strong anisotropy of the Kitaev couplings (unshaded triangles). The corners of the large triangle correspond to the Toric code limit, where one of the couplings is much stronger than the others. The focus of this thesis is the gapless phase where, vison-Majorana interactions are important.

variables u_{ij}^{γ} to $+1$, leading to a translationally invariant Hamiltonian, written in momentum space as

$$H = \frac{1}{2}\begin{pmatrix} f_{\boldsymbol{k}}^{\dagger} & f_{-\boldsymbol{k}} \end{pmatrix}\begin{pmatrix} \xi_{\boldsymbol{k}} & \Delta_{\boldsymbol{k}} \\ \Delta_{\boldsymbol{k}}^{\dagger} & -\xi_{\boldsymbol{k}} \end{pmatrix}\begin{pmatrix} f_{\boldsymbol{k}} \\ f_{-\boldsymbol{k}}^{\dagger} \end{pmatrix}, \tag{3.28}$$

where $\Delta_{\boldsymbol{k}} = i\,\mathrm{Im}\{F(\boldsymbol{k})\}$, and $\xi(\boldsymbol{k}) = \mathrm{Re}\{F(\boldsymbol{k})\}$, which are in turn defined by $F(\boldsymbol{k}) = \sum_{\alpha} K_{\alpha} e^{i\boldsymbol{k}\cdot\boldsymbol{\delta}_{\alpha}}$ The hopping vectors, for the lattice shown in Fig. 3.1 are given by $\boldsymbol{\delta}_x = \boldsymbol{n}_1 = (\frac{1}{2}, \frac{\sqrt{3}}{2})$, $\boldsymbol{\delta}_y = \boldsymbol{n}_2 = (-\frac{1}{2}, \frac{\sqrt{3}}{2})$ and $\boldsymbol{\delta}_z = (0,0)$. Diagonalising the Hamiltonian thus gives the energy dispersion of the matter fermions:

$$\varepsilon_m(\boldsymbol{k}) = \pm|f(\boldsymbol{k})| = \pm|2(K_z + K_x e^{\boldsymbol{k}\cdot\boldsymbol{n}_1} + K_y e^{\boldsymbol{k}\cdot\boldsymbol{n}_2})|. \tag{3.29}$$

Phase Diagram. The band structure reveals an interesting feature; the spectrum become gapless ($\varepsilon(\boldsymbol{k}) = 0$) when K_x, K_y and K_z obey the following inequalities.

$$|K_x| \leq |K_y| + |K_z|, \qquad |K_y| \leq |K_x| + |K_z|, \qquad |K_z| \leq |K_x| + |K_y|. \tag{3.30}$$

Translating this into a phase diagram as shown in Fig. 3.3 shows two different phases - gapless and gapped. Without going into the details, let us summarize the main features of these two phases. The gapped phase exists for sufficiently strong anisotropies of the Kitaev couplings, and are adiabatically connected to the Toric code phase discussed in Chapter 2. The visons in this phase come in two variants - e and m. They are abelian *anyons* (semions) with respect to each other but bosons with respect to themselves. In the rest of this thesis, we shall not discuss this phase but focus on the gapless phase. However, the dynamics of anyons in the toric code can also be quantitatively studied using the methods developed in this thesis.

Dirac Equation. As shown in the Fig. 3.3, near the isotropic point ($K_x = K_y = K_z = K$), there are two unique points in the Majorana Brillouin zone, called Dirac points K_+ and K_-, where the bands touch linearly.

$$K_- = 2\pi(-1/3, 1/\sqrt{3}), \qquad K_+ = 2\pi(1/3, 1/\sqrt{3}).$$

In the complex fermion language, the two points can be combined into a single Dirac point $\boldsymbol{K}$ since $f_{\boldsymbol{k}} = f_{-\boldsymbol{k}}$. In the vicinity of the Dirac point, the Hamiltonian can be a expanded in the leading order to obtain a relativistic Dirac equation. With $\boldsymbol{q} = (q_x, q_y) = \boldsymbol{k} - \boldsymbol{K}$,

Massless Majorana fermions

$$h_K(\boldsymbol{q}) = v_m \begin{pmatrix} 0 & q_x + iq_y \\ q_x - iq_y & 0 \end{pmatrix}, \tag{3.31}$$

where the Majorana velocity $v_m = \frac{\sqrt{3}K}{2}$.

3.7 Chiral Spin Liquid

The model described by Eq.(3.1) is time reversal invariant. An external magnetic field, for example, can break this symmetry. Kitaev, in his original work, showed that a weak Zeeman term can open a gap in the Majorana spectrum and transform the gapless phase into a *chiral spin liquid* (KCSL). Let us consider a field oriented in the $[111]$ direction:

$$H_h = \frac{1}{\sqrt{3}}(h_x\, \sigma_i^x + h_y\, \sigma_i^y + h_z\, \sigma_i^z). \tag{3.32}$$

At first order in perturbation theory, H_h creates a pair of visons and cost energy Δ_{2v}^0, taking the system out of its ground state. At second order, the Majorana hopping rates get a trivial correction from terms of the following form.

$$\delta h_M^{(2)} \sim h_\alpha^2 \frac{\langle 0|\, \sigma_i^\alpha \sigma_i^\alpha \,|0\rangle}{\Delta_{2v}^0} \sim \frac{h_\alpha^2}{|K|} i c_i c_j \tag{3.33}$$

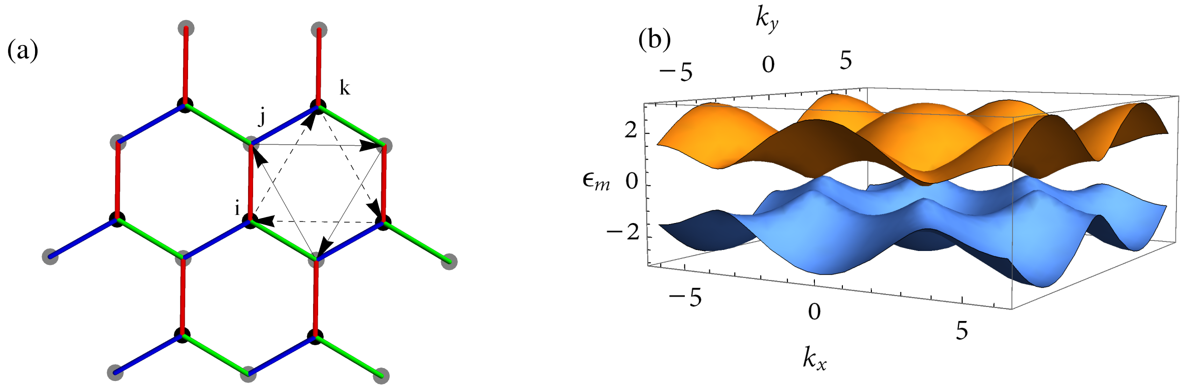

Fig. 3.4 **Field-induced chiral spin liquid phase.** A weak [111] magnetic field induces a hopping between the same sublattice shown by the arrows A-A hopping - dashed arrows, B-B hopping - solid arrows. This opens up a topological gap in the Majorana spectrum, as shown in (b), driving the system into a chiral spin liquid phase.

Here, i and j should be nearest neighbours on an α type bond, necessary to annihilate the visons created by each other. Most importantly, second order perturbation effects do not break time reversal symmetry. At third order, however, non-trivial contributions arise. Consider the following term in perturbation theory,

$$\delta h_M^{(3)} \sim h_x h_y h_z \frac{\langle 0|\, \sigma_i^x \sigma_j^y \sigma_k^z \,|0\rangle}{(\Delta_{2v}^0)^2} \sim \frac{h_x h_y h_z}{K^2} u_{ij} u_{jk} i c_i c_k. \tag{3.34}$$

See Fig. 3.4 for definitions of the indices. This leads to a hopping between the same sublattice sites, given by $t_{AA} = -t_{BB} = \kappa u_{ij} u_{jk}$. (Note the similarity of the effective Hamiltonian to the well-known Haldane model [54] of Chern insulators.) This term also breaks time reversal symmetry, and ultimately opens up a gap in the Majorana spectrum at the Dirac point. It is instructive to see this in the low energy Dirac description. The Dirac equation now obtains a *mass* term $m = 6\sqrt{3}\,\kappa$:

$$h_K(\boldsymbol{q}) = v_m \begin{pmatrix} m & q_x + i q_y \\ q_x - i q_y & -m \end{pmatrix}. \tag{3.35}$$

The energy eigenvalues are given by

$$\varepsilon_{\boldsymbol{q}} \approx \sqrt{v_m^2 q^2 + m^2}. \tag{3.36}$$

The band structure is shown in Fig. 3.4b.

Furthermore, the fermion bands obtain a finite *Chern number*, signalling that they are in a chiral topological phase.

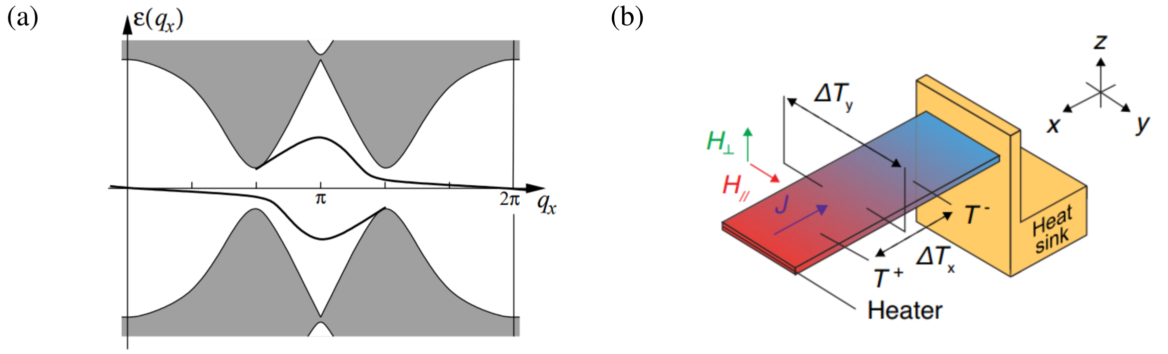

Fig. 3.5 **Majorana edge modes and thermal Hall signature**. (a) In a finite sized sample of a chiral Kitaev spin liquid, a topologically protected chiral edge mode of Majorana fermions (inside the bulk gap) emerge at the boundary (shaded-bulk bands). Figure adapted from Ref. [40] with permission. (b) A typical thermal Hall experimental setup. One edge of the sample is at a higher temperature than the other (T^+ and T^-), while a heat current $\boldsymbol{J}$ is injected. The transverse temperature gradient ΔT_y is measured. Figure adapted from Ref. [55].

Chern number. Now is perhaps a good point to make a short detour into the notion of topological bands. Consider a two-band system, described by the Dirac equation with a mass term, as in Eq. (3.35). This can be expressed using Pauli matrices denoted by τ as

$$h_{\boldsymbol{K}} = \tilde{\boldsymbol{h}} \cdot \boldsymbol{\tau}, \tag{3.37}$$

where $\boldsymbol{\tau} = (\tau^x, \tau^y, \tau^z)$ and $\tilde{\boldsymbol{h}} = (q_x, q_y, m)$. This realizes a mapping from the momentum space to a unit sphere spanned by the unit vector $\hat{\tilde{\boldsymbol{h}}}$. The Berry curvature $\Omega(\boldsymbol{q})$ of the bands are defined by

$$\Omega_{n\boldsymbol{k}} = \hat{\tilde{\boldsymbol{h}}} \cdot \left(\frac{\partial \hat{\tilde{\boldsymbol{h}}}}{\partial q_x} \times \frac{\partial \hat{\tilde{\boldsymbol{h}}}}{\partial q_y} \right). \tag{3.38}$$

Strikingly, the integral of the Berry curvature over the entire Brillouin zone is an integer, known as the Chern invariant ν.

Majorana Chern number

$$\nu_n = \frac{1}{4\pi} \int_{1BZ} d\boldsymbol{k}\, \Omega_{n\boldsymbol{k}} = \mathrm{sgn}(m) \tag{3.39}$$

The Chern invariant has a pivotal role in the modern field of topological phases in condensed matter physics. What are the physical consequences of this?

3.7.1 Edge modes and thermal Hall Effect

For the Majorana fermions of the Kitaev model, the bands carry Chern numbers ± 1, with its sign determined by the magnetic field orientation. A profound consequence of Chern bands is the quantum Hall effect (QHE). However, an important distinction from the QHE of electrons is that the fermions of the spin liquid are not electrically charged. They are neutral, emergent quasiparticles in an insulator. Therefore, one has to look for heat transport instead of electrical transport to see the the Hall effect.

In a typical thermal Hall experiment (THE), the sample is placed in a magnetic field and a temperature gradient $\Delta_x T$ is applied by coupling one end of the sample to a heat bath, along the x axis. Simultaneously, a heat current $\boldsymbol{J}$ is injected along the x axis. An induced temperature gradient $\Delta_y T$ along the y axis between the two edges is then measured.

This gives the thermal Hall resistivity through the relation $\rho_{xy} = \Delta_y T/J$. Using the longitudinal resistivity $\rho_{xx} = \Delta_x T/J$, one can invert the resistivity tensor to obtain the corresponding Hall conductivity

$$\kappa_{xy} = \frac{\rho_{xy}}{\rho_{xy}^2 + \rho_{xx}^2}. \tag{3.40}$$

There are several approaches to calculating κ_{xy} of fermion system. The edge modes of the chiral spin liquids offer an intuitive picture for this which we shall outline now.

Solving the Majorana Hamiltonian Eq.(3.13) on a finite sized lattice with boundaries, one can show that a set of modes appear inside the gap Δ_m. The dispersion of this band depends on the details of the edge. However, crucially, this mode is chiral - it propagates in only one direction. It is also robust against any backscattering from disorder and hence carries all the energy at low temperatures. The energy current due to this propagating mode can be calculated for an arbitrary dispersion. For simplicity let us assume the bulk gap is infinite. The edge mode dispersion obeys the relations $\varepsilon(-q) = -\varepsilon(q)$ and $\varepsilon(q \to \pm\infty) \to \pm\infty$. The energy current is then given by

$$I = \int_{\varepsilon(q)>0} n(q)\varepsilon(q)\frac{d\varepsilon}{dq}\frac{dq}{2\pi} = \frac{\pi}{24}T^2. \tag{3.41}$$

This result is quantized and universal for a given temperature. The thermal Hall conductivity defined as the derivative of the energy current with respect to temperature gives

Half-quantized thermal Hall effect

$$\kappa_{xy} = \frac{\nu}{2}\kappa_0 \tag{3.42}$$

where $\kappa_0 = \frac{\pi k_B^2}{6\hbar}$ is the fundamental unit of conductance. This half-quantization is predicted to be a definitive signature of the chiral spin liquid.

It is worth mentioning that in real materials, the dominant heat carriers are phonons. They provide a finite κ_{xx} unlike what is assumed in the pure spin model with a bulk gap. This leads to an interplay between acoustic phonons and Majorana edge modes. Surprisingly, it was shown independently by Winkler and Rosch [56] and Ye et. al. [57] that coupling to the phonons is not (completely) detrimental and in fact necessary to observe the quantization. In Chapter 8, we will comment on the current experimental efforts and present a novel contribution to the THE.

3.8 Anyons

In three-dimensions, particles can be either fermions or bosons, depending on the global phase change, 0 or π respectively, obtained by the wavefunction when positions of the two particles are exchanged. However, it was shown by Leinaas and Myrheim in 1977 [58] that, in two-dimensions, exchange statistics of particles can take a continuum of values. Later Wilczek [59] expanded upon these ideas to emergent quasiparticles, coining the term "anyons" - particles that are neither fermions nor bosons. Today, anyonic quasiparticles have been predicted in a variety of models and experimentally observed in fractional quantum Hall systems [60].

For *abelian* anyons, exchanging two particles, with position vectors $\boldsymbol{r}_2$ and $\boldsymbol{r}_2$, may result in a global phase change of the wavefunction:

Exchange statistics

$$\psi(\boldsymbol{r}_1,\boldsymbol{r}_2) = e^{-i\theta}\psi(\boldsymbol{r}_1,\boldsymbol{r}_2), \tag{3.43}$$

where θ ranges from 0 (bosons) to π (fermions). More complex types, called non-Abelian anyons, have a higher dimensional Hilbert space than just the position space, as in the Abelian case. An exchange of particles can therefore result in non-trivial transformations in this internal space:

$$\Psi(\boldsymbol{r}_1,\boldsymbol{r}_2) = R\,\Psi(\boldsymbol{r}_1,\boldsymbol{r}_2) \tag{3.44}$$

where importantly, Ψ is a multicomponent vector of dimension d, and R is a unitary matrix of the same dimension.

Description of such anyonic systems often uses a gauge theoretical framework. The main idea is to attach a ‘magnetic’ flux of twice the exchange phase to each particle which is otherwise considered to be a boson. An anyon that is transported around another, topologically equivalent to exchanging them twice, acquires the phase, just like an electron travelling around a solenoid in the classic Aharonov-Bohm effect. Besides realizing a fundamentally new phase of matter, anyonic systems offer a revolutionary approach to quantum information processing. Storing information in the internal states of a pair of well separated anyons, for example, can protect it from local noise. The two anyons have to come together for any local operator to access the information.

3.8.1 Ising anyons

Coming back to the Kitaev spin liquid, what is the statistics of a vison in the chiral spin liquid? While the Majorana fermions acquire a mass gap in the chiral phase, visons carry localized Majorana zero modes (MZM). A pair of well separated visons, thus carry a single fermion mode ψ, formed by the two MZMs, with energy $\varepsilon_\psi = 0$. The occupation of this mode determines, what is called, the *superselection sector* of the pair. If the fermion mode is occupied, the pair is said to be in the fermion (ψ) sector, and if its empty, the pair is in the vacuum ($\mathbb{1}$) sector.

When two anyons are brought together, they can annihilate each other (energetic considerations aside) and may release a fermion ψ. This process is called *fusion* and it describes how one may read-out the quantum information encoded in the system. In general, for two anyons, this process is represented as

Fusion rules

$$\sigma \times \sigma = \mathbb{1} + \psi. \tag{3.45}$$

This defines a fusion rule, which describes the possible outcomes of the annihilation of two anyons. In particular, the above equation along with $\mathbb{1} \times \mathbb{1} = \mathbb{1}$ and $\psi \times \psi = \mathbb{1}$ form the full set of fusion rules of *Ising anyons*.

To understand how the exchange of Ising anyons affect the fusion space, it is useful to study a system of four MZMs. The following discussion closely follows Chapter 6 of Ref. [61]. Consider four anyons $\sigma_i, i = 1,2,3,4$ carrying MZMs $\gamma_i, i = 1,2,3,4$ respectively. We can form two complex fermions out of the by choosing any two pairs. Consider two such pairings:

$$z_1 = \gamma_1 + i\gamma_2, \qquad z_2 = \gamma_3 + i\gamma_4 \tag{3.46}$$

and

$$w_1 = \gamma_1 + i\gamma_3, \qquad w_2 = \gamma_2 + i\gamma_4. \tag{3.47}$$

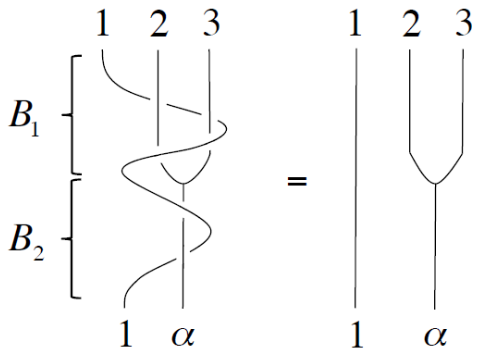

Fig. 3.6 **Braiding of Ising anyons**. A braiding process involving three Ising anyons to extract the topological spin. The process on the left involves braiding γ_1 around γ_2 and γ_3 in a clockwise fashion followed by the fusion of γ_2 and γ_3 to obtain the outcome α. γ_1 is then braided with α in the counter-clockwise direction. This is topologically equivalent to no braiding, as on the right hand side. That is $B_1 B_2 = \mathbb{1}$. Figure taken from Ref. [61].

The corresponding Hilbert spaces are spanned by the states $|n_{z_1} n_{z_2}\rangle$, namely, $|00\rangle_z, |11\rangle_z, |01\rangle_z, |10\rangle_z$, defined similarly for the w fermions. Since the total fermionic parity is a conserved quantity, protected by the Majorana gap (like in a BCS superconductors, where a quasiparticle excitation costs the gap), we can restrict our attention to the subspace spanned by $|00\rangle_z, |11\rangle_z$ and $|00\rangle_w, |11\rangle_w$. Here we assumed that both pairs were created out of the vacuum sector, and hence the fermion modes can be empty. Note that the two basis sets differ only by the exchange of γ_2 and γ_3. It can be proven using the algebra of Majorana operators that the exchange of two Majoranas can be expressed by the following relation.

$$\begin{pmatrix} |00\rangle_w \\ |11\rangle_w \end{pmatrix} = \frac{1}{\sqrt{2}} \begin{pmatrix} -1 & 1 \\ 1 & 1 \end{pmatrix} \begin{pmatrix} |00\rangle_z \\ |11\rangle_z \end{pmatrix}. \tag{3.48}$$

Braiding phase More relevant to us is the braiding phases of Ising anyons. This refers to the effect of exchanging two anyons on the total wavefunction of the system. We consider the same setup as above. One can easily convince themselves that the following operator exchanges γ_2 and γ_3:

$$U_{23} = \frac{e^{i\theta}}{\sqrt{2}} (1 + \gamma_2 \gamma_3), \tag{3.49}$$

where the factor $e^{i\theta}$ corresponds to the abelian part of the transformation. Importantly, if γ_2 and γ_3 are already paired, with a definite parity $i\gamma_2\gamma_3 = \pm 1$, exchanging them will only result in a global phase factor $e^{i(\theta \pm \pi/4)}$. Computing the value of θ is actually not straightforward, as one has to invoke conformal field theoretical (CFT) description of the chiral spin liquid, or the machinery of *unitary modular category* [40]. Here I will present a rather intuitive argument adapted from Ref. [61].

We consider the following processes in sequence, as illustrated in Fig.3.6: (i) γ_1 is braided around γ_2 and γ_3 in a clockwise manner, (ii) γ_2 and γ_3 are then fused into the outcome $\alpha = \psi$ or $\mathbb{1}$, and (iii) γ_1 is then braided around α counter-clockwise. This sequence can be described by

$$B_2 B_1 = U_{\alpha 1} U_{12} U_{13}. \tag{3.50}$$

However, the total braiding process should be equal to identity, as the first and second process are exactly the reverse of each other. We will now assume that exchanging a single MZM and a fermion ψ results in a phase factor i. This is consistent with the fact that exchanging two complex fermions, each composed of two Majorana modes results in a phase $i^2 = -1$. With this assumption,

$$U_{1\alpha} = 1 - 2\psi^{\dagger}\psi = i\gamma_2\gamma_3. \tag{3.51}$$

Therefore $U_{1\alpha} = -1$, if the outcome is a fermion mode, or $+1$ if vacuum. Combining these arguments, we get

$$\mathbb{1} = B_2 B_1 = e^{4\theta}\gamma_2\gamma_3 i\gamma_2\gamma_3 = e^{i(4\theta \mp \pi/2)}. \tag{3.52}$$

This gives the *topological spin* of the Ising anyons

Ising Topological Spin

$$\theta = \pm\frac{\pi}{8}. \tag{3.53}$$

The sign is fixed by the chirality of the system, which is in turn determined by the Chern number ν of the lower Majorana band. A more rigorous calculation of θ from the CFT description results in $\theta = \nu\frac{\pi}{8}$ [40]. Note that exchanging two particles twice is topologically equivalent to looping one around the other. Therefore, taking an Ising anyon around another results in an abelian phase of $\pm\frac{\pi}{4}$ or $\mp\frac{-3\pi}{4}$, if the anyon pair is in the vacuum sector or fermion sector respectively.

3.9 Kitaev Materials

The Kitaev model provided arguably the first concrete theoretical proof that a quantum spin liquid phase can exist and gauge fields naturally emerge. However, the direction-dependent interactions defining the model seemed highly fine-tuned, and its relevance beyond a theoretical breakthrough remained unclear. Surprisingly, a few years later, a seminal paper by Jackeli and Khalliullin [41] proposed that, in certain spin-orbit coupled Mott insulators, such direction dependent spin-spin interactions may naturally dominate the Hamiltonian. This brought the Kitaev model from the theoretical fantasy land to the real world. Let us briefly review this mechanism which ultimately spawned a whole new field of research.

3.9.1 Jackeli-Khaliullin mechanism

The mechanism proposed by Jackeli and Khaliullin (JK) is predicted to occur in certain materials known as Mott insulators. According to the band theory of solids, systems with odd number of electrons per unit cell (half-filled band) should be a metal and even number of electrons should be insulating. However, several materials like transition metal oxides are insulating, despite a partially filled d-band. Mott proposed that this is a result of the strong Coulomb interactions between electrons which essentially suppress their hopping between sites, thus defining a Mott insulator [62].

For the JK mechanism to work, there are three main ingredients. The first is a ligand that induces a crystal-field around the ion carrying the unpaired orbital. Consider the example of a d^5 orbital. When the ligand ions (e.g. Oxygen or Chlorine) form an octahedral cage around the ion, it splits the d^5 band into an empty e_g and a three-fold degenerate t_{2g} states. The second ingredient, spin orbit coupling (SOC), further splits the triply degenerate t_{3g} into an effective angular momentum $j_{\text{eff}} = \frac{1}{2}$ state and two $j_{\text{eff}} = \frac{3}{2}$ multiplets. Jackeli and Khaliullin argued that when the ligands form an octahedral cage around the ion, the coupling between the effective spin-$\frac{1}{2}$ depends sensitively on the geometry of the edge shared by the two ions.

In particular, when the ions-ligand structure are in an idealized edge sharing geometry, the two exchange pathways (as shown in Fig. 3.7b), that would typically give rise to Heisenberg interactions between the spin-$\frac{1}{2}$ moments interfere destructively. The dominant remaining exchange then occurs with the help of a Hund's coupling within the ion orbitals and leads to a highly bond-specific Ising interaction $\sim \frac{t^2 J_H}{U^2} S_i^\alpha S_j^\alpha$. Here $\alpha = x, y, z$ depends on the direction of the edge shared, t is the electron hopping amplitude, J_H is the Hund's coupling and U is the repulsive Coulomb interaction energy. This describes the Kitaev coupling! It is also worth mentioning that such a specific anisotropic interaction was also proposed in the 1982 by Kugel and Khomskii for orbital moments in certain materials[63].

Beyond the above described idealized geometry, including the effects of direct exchange between the ions results in a Heisenberg term to be added to the Kitaev Hamiltonian. The interplay of both direct and ligand-mediated exchange was found to add another term called the symmetric-off diagonal exchange term $\Gamma(S_j^\beta S_i^\gamma + S_i^\beta S_j^\gamma)$ on an α type bond with $\alpha \neq \beta, \gamma$ [65]. This has led to the widely studied $J - K - \Gamma$ model of Kitaev materials [66–68, 64, 69, 70]. In reality, several other non-Kitaev terms, that are allowed by symmetry, will also contribute to the

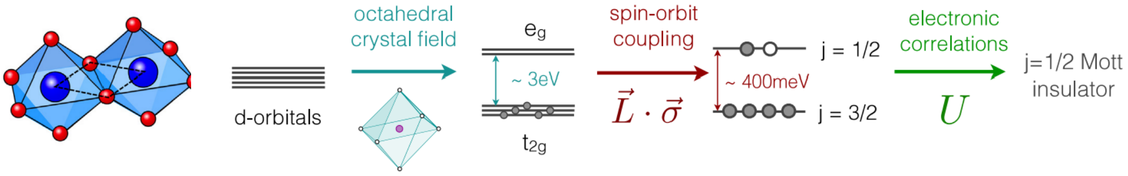

Fig. 3.7 **Jackeli-Khaliullin mechanism in Kitaev materials.** The mechanism operates on a transition metal ion (blue spheres) surrounded by a ligand ion (red spheres) in an octahedral structure. An effective spin-1/2 moment emerges out of the partially filled *d* orbital due to the interplay of crystal-field, spin-orbit coupling and strong electronic correlations. The virtual electron exchange between two ions sharing an edge destructively interfere and helps produce the Kitaev interactions in these materials. Figure adapted from Ref. [64].

Hamiltonian. However, when the Kitaev coupling K is much larger than all the other terms, we expect the system to be in a spin-liquid phase, adiabatically connected to the pure Kitaev model. Such materials are christened *Kitaev materials*[64].

This has led to intense experimental and theoretical efforts to understand and engineer spin liquid phases in a large class of materials [64, 71]. Beyond the JK mechanism, several other ways to engineer Kitaev interactions in materials based on Cobalt (e.g. $Na_2Co_2TeO_6$ and $Na_3Co_2SbO_6$) have been proposed. For a comprehensive review of leading Kitaev material candidates and their theoretical underpinnings, I would refer the reader to Ref.[64] by Trebst and Hickey.

What is the current status of the field? It turns out that almost all the candidate materials order magnetically below some temperature T_N, brutally stomping on the hopes of a spin liquid ground state. Numerous works have proven, through advanced numerical methods that the interplay between Kitaev physics and non-Kitaev terms leads to magnetic order and modifies the experimental signatures of the pure spin liquid [66, 68]. Although the correct values of these couplings for potential Kitaev materials are still under intense debate [72], the Heisenberg and off-diagonal couplings are believed to be the two essential ingredients necessary to capture many of the observed phases in Kitaev materials [70, 65, 73, 74]. This points to the fact that even if Kitaev interactions arise in these materials, the non-Kitaev interactions are probably strong enough to destroy any spin liquid phase.

One may still ask, what about the high temperature phases above T_N? Some of the very first evidences of a possible spin liquid behaviour was found indeed in this regime, where inelastic neutron scattering found a broad continuum of excitations, a necessary (but not sufficient) condition for a fractionalized spin liquid [75]. Raman spectroscopy followed and provided complimentary evidence for such a continuum present [76]. Perhaps the most exciting experimental result came from the group of Matsuda [42, 43], where they observed the half-quantized thermal Hall effect, a smoking gun signature of the Kitaev spin liquid, in $\alpha-RuCl_3$. This result has re-ignited excitement in the field.

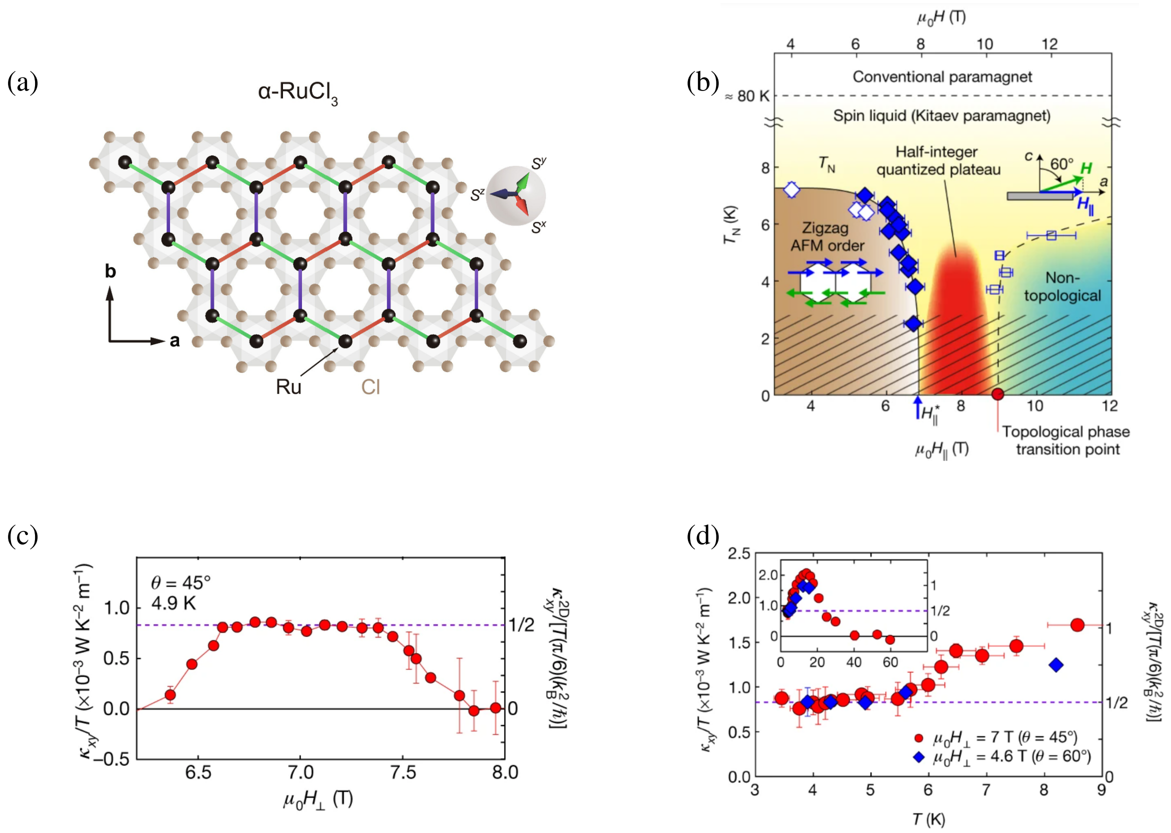

Fig. 3.8 **Crystal structure and Thermal Hall effect of $\alpha-\mathrm{RuCl}_3$.** (a.) $\alpha-\mathrm{RuCl}_3$ is made of honeycomb layers of Ru atoms surrounded by Cl atoms in an octahedral fashion (Figure adapted from Ref. [77]). (b.) Experimentally obtained phase diagram based on thermal Hall effect measurements by Kashara *et al.*[42]. At small magnetic fields, the material magnetically ordered. At high fields, the spins are polarized into a trivial phase. In an intermediate regime (red), a half-quantized thermal Hall effect is observed suggesting a chiral spin liquid phase adiabatically connected to the Kitaev model. At finite temperature, the spin liquid phase persists below the scale of Kitaev interaction K. (c.) Thermal Hall data adapted from Kasahara et.al [42]. A predicted quantization of thermal Hall conductivity is observed between $\sim$ 6.5T - 7.5T. (b.) Thermal Hall conductivity as a function of temperature. Experimental figures (b)-(d) are adapted from Ref. [42] with permission.

3.9.2 The curious case of $\alpha-\mathrm{RuCl}_3$

$\alpha-\mathrm{RuCl}_3$ is composed of weakly coupled layers of honeycomb lattice consisting of $\mathrm{Ru}^{3+}(4d^5)$ ions caged by an octahedron of Cl atoms. The Mott insulating behaviour and the effective spin-half moments in $\alpha-\mathrm{RuCl}_3$ were only discovered in the last decade, first by Plumb et.al. [78]. Hopes of it being an ideal system for the JK mechanism, and a possible spin liquid, were raised. Alas, α-RuCl_3 develops a zig-zag magnetic order below a Néel temperature of approximately 7 K or 14 K depending on its three-dimensional structure. Above the ordering temperature, Raman spectroscopy experiments claimed to have detected the presence of fermionic excitations, unlikely to be present in a trivial paramagnet [76]. However, as mentioned above, a broad continuum of excitations in spectroscopy can also arise from more trivial sources like disorder or interactions.

What if one destroys the magnetic order not by heating the system but by an external magnetic field? Does it immediately transition to a field polarized trivial phase or could we expect an intermediate phase that is adiabatically connected to the Kitaev model? The answer to this question is still under intense debate. The latter is an exciting scenario, but hard to distinguish experimentally from the former. By definition, a quantum spin liquid state does not break symmetry, thus similar to a partially polarized phase. However, there has been a flurry of wide ranging experimental inquiries into this field-induced regime with conflicting results.

In 2018, transport measurements by Kasahara *et al.*[42] provided perhaps the most remarkable and promising evidence for the Kitaev spin liquid phase; a half-quantized thermal Hall conductivity in the field-induced regime ($\sim$ 8T). Exciting this result was, its interpretation required a deeper understanding of thermal transport in a spin liquid material given the presence of phonons that carry most of the heat [56, 57]. This surprisingly revealed that phonons in fact help us to observe the quantization, at least in certain temperature regime. The half-quantization, in its true sense has not been reproduced, although Bruin *et al.* [79] did observe a plateau-like feature. Large non-quantized thermal Hall effect including an oscillatory behaviour has been observed by other groups [80]. Recently, evidence of a planar-thermal Hall effect has been reported in $\alpha-\mathrm{RuCl}_3$[43]. Here, the external field is oriented parallel to the honeycomb plane and the sign of the Hall effect was controlled by the field orientation - two features readily explained by a spin liquid of the Kitaev type. Moreover, recent reports of thermodynamic evidence for closing and re-opening of energy gaps, as a function of magnetic field orientation are also certainly encouraging[81].

However a consistent and conclusive reproduction of these results is absolutely necessary to establish $\alpha-\mathrm{RuCl}_3$ as a true quantum spin liquid material. It is exciting that more materials have been reported to exhibit similar physics as that of $\alpha-\mathrm{RuCl}_3$, making the search for Kitaev spin liquid a very active field.[82]

3.10 Motivation

In this midst of the 'spin liquid or no spin liquid' debate, one could either give up or ask ourselves the question - what if? What if a Kitaev material indeed realizes the spin liquid phase? What would be the nature of its excitations ? How would it be different from the predictions of the pure Kitaev model? For instance, in Ref. [57], it was shown that although a pure Kitaev model is predicted to show a gap in its dynamical response, generic symmetry allowed terms fill this gap and result in a gapless response. It follows from renormalization group arguments that the Majorana fermions, owing to their Dirac nature (linear dispersion) are quite robust to interactions induced by weak non-Kitaev terms [83]. However, a pivotal feature of the Kitaev model, the static nature of the emergent gauge field, is destroyed by any weak perturbation naturally present in a real material. Any realization of a spin liquid that is smoothly connected to the Kitaev model will, therefore, host a dynamical gauge field. Furthermore, the gauge fields will influence most, if not all, experimental quantities related to the spin liquid phase. However, the dynamics of this emergent $\mathbb{Z}_2$ gauge field, strongly interacting with the gapless matter, is largely unexplored. In this thesis, we take a crucial step towards bridging this gap by developing a comprehensive theory of the gauge field excitations, visons, in a generic Kitaev liquid, proposing their experimental signatures.

Part II

Dynamics

Chapter 4

Quantum Dynamics of Visons

Any material realization of the Kitaev spin liquid phase will naturally host a dynamical gauge field coupled to Majorana fermions. How do we describe the dynamics of the elementary gauge field excitations -a single vison-in such a system? Due to its fractional nature, a single vison is a stable quasiparticle which can only decay by annihilating with another vison, making its dynamics fundamentally important.

In this chapter, we develop a controlled perturbative approach to compute the dynamics of visons induced by weak perturbations to the Kitaev model. When the perturbations are weak, the vison gap remains finite, allowing us to study its quasiparticle properties, such as band dispersion and mobility. Consequently, this problem is akin to that of a mobile "impurity" in a gapless fermionic bath. We will obtain an effective single-particle tight-binding model for a vison by calculating its hopping amplitudes using many-body perturbation theory.

We consider the two most relevant non-Kitaev spin-spin interactions as perturbations: an off diagonal exchange term (the Γ term) and a Heisenberg interaction. Together, they form the well-known $J-K-\Gamma$ model [65]. Additionally, we will examine effects of an external magnetic field on the visons. Due to its time-reversal-breaking effects, magnetic fields must be treated rather carefully. In this chapter, we will explore how these perturbation transform the static visons of the pure model into mobile quasiparticles with a band structure.

The hopping amplitudes due the Γ term, in the gapless phase (Section 4.1) were computed, and arguments regarding the Heisenberg perturbation (Section 4.3) were developed during the author's Master thesis [84]. These results are reproduced here to make this thesis self-contained and coherent. The results of this chapter are published in Physical Review X ***12****, 041004 (2022)*[85], *co-authored with Achim Rosch. The numerical data are mostly reproduced from the publication.*

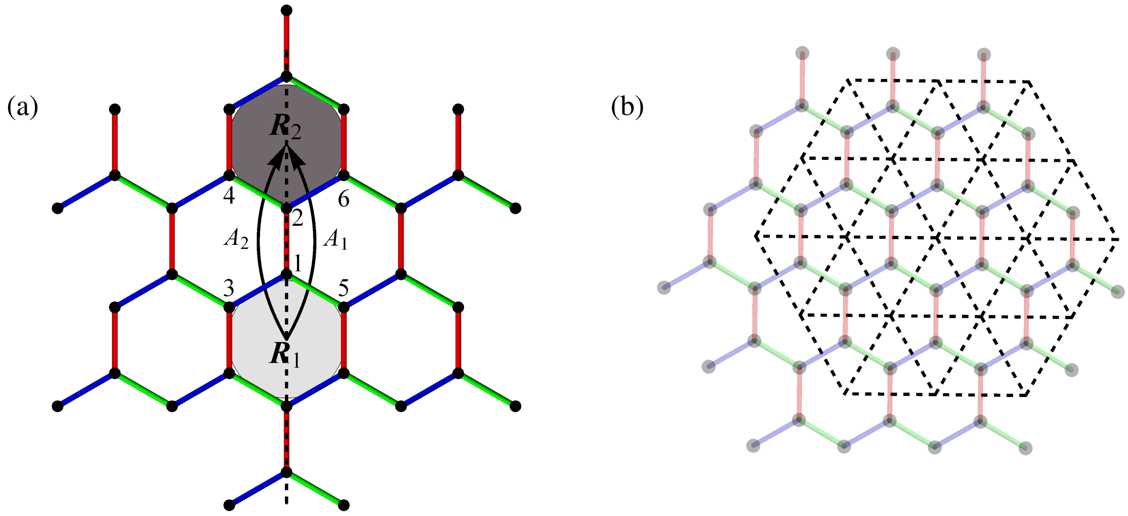

Fig. 4.1 **Vison hopping induced by the Γ term.** (a.) A weak ΔH_Γ on a given bond (shown here for $\langle ij \rangle_z$) has two symmetry related terms that hop a vison from $\boldsymbol{R}_1$ to $\boldsymbol{R}_2$, through two different paths shown by the two arrows. The two processes interfere with each other. (b.) The dual triangular lattice of the honeycomb, on which visons hops around. The Γ term induces a next-nearest-neighbour hopping on this lattice.

4.1 Off-diagonal Exchange

To investigate how perturbations lead to the motion of visons, we start with the off-diagonal symmetric exchange, known as the Γ term. Focusing on this perturbation, we will develop the analytical and computational methods for evaluating vison hopping matrix elements. These can be then used for any generic perturbation that induces vison dynamics.

An off diagonal symmetric exchange interaction is given by

$$\Delta H_\Gamma = \sum_{\substack{\langle ij \rangle_\alpha \\ \alpha \neq \beta \neq \gamma}} (\sigma_i^\beta \sigma_j^\gamma + \sigma_j^\beta \sigma_i^\gamma). \tag{4.1}$$

Let us see how this term makes the visons dynamic. Consider a z bond as shown in Fig. 4.1, where the Γ terms is given by

$$\Delta H_\Gamma^z = \Gamma(\sigma_1^x \sigma_2^y + \sigma_1^y \sigma_2^x). \tag{4.2}$$

Starting with a single vison localized at the plaquette $\boldsymbol{R}_1$, the action of each term in Eq. (4.2) is depicted in Fig. 4.1 using arrows: the vison at $\boldsymbol{R}_1$ hops to $\boldsymbol{R}_2$. Within the gauge theory, the gauge variables on the links crossing the arrows are flipped from $+1$ to -1. Even though both the terms result in the same physical final state, with a vison at $\boldsymbol{R}_2$, there is an important distinction between them in terms of the $\mathbb{Z}_2$ links flipped. The action of the whole term can thus be interpreted as an interference of two paths by which the vison can hop to the same final position. Similar analysis on x and y bonds result in vison hopping along the respective bonds.

We can now calculate using standard degenerate perturbation theory, the matrix elements corresponding to the hopping process. At linear order, the hopping amplitude is given by

$$t_\Gamma = \langle \Phi_0(\boldsymbol{R}_1) | \Delta H^z_\Gamma | \Phi_0(\boldsymbol{R}_2) \rangle \,, \tag{4.3}$$

where the wavefunction $\Phi(\boldsymbol{R}_1)$ is the ground state of the unperturbed system, with a single vison at $\boldsymbol{R}_1$.

The computation of this seemingly harmless quantity is rather complicated due to several factors. The wavefunctions appearing in the expression are the full many-body ground states of the Majorana fermions with a vison, a singular scatterer. Due to the underlying gauge theory, we need to choose a convenient gauge configuration to perform the calculations (a pattern of $u_{\langle ij \rangle}$ compatible with the vison positions) for a given wavefunction. This, in turn, enforces the projection operation Eq. (3.8), that essentially symmetrizes over all gauge transformations. Periodic boundary conditions used in our calculations permit only an even number of visons. To study the hopping of a single vison,therefore, requires to have a pair of visons separated by the maximum possible distance ($L/2$ for a linear system size L), which may lead to strong finite size effects.

4.2 Dressed Visons and Hopping Amplitudes

The above discussion emphasizes, once more, that one should think of the vison as a particle that is *dressed* by a cloud of Majorana fermions scattered by the gauge flux it carries. It is this ‘polaron-like’ particle whose properties we study here.

4.2.1 Spins to fermions

Let us now calculate the matrix elements of the form Eq. (4.3), describing the vison hopping process corresponding to Fig. 4.1. Ground state wavefunction of the unperturbed system can be written as a direct product of the gauge sector, defined in the Fock space of the bond fermions χ, and the BCS wavefunctions of the corresponding matter fermions, following Eq.(3.26). To write down the wavefunction of the gauge sector, we first need to choose a gauge configuration for the initial vison position $\boldsymbol{R}_1$. This is done by flipping the gauge variables $u_{\langle ij \rangle_y}$ along a chain of y bonds, of length $L/2$ in a torus of linear size L, creating two visons separated by a distance $L/2$. This gauge configuration is denoted by $\mathscr{G}_1$. The ground state of such a configuration can be expressed as

$$|\Phi(\boldsymbol{R}_1)\rangle = \hat{P}\prod_{l\in\gamma}\chi_l^\dagger\left|0_\chi\right\rangle|M(\boldsymbol{R}_1,\mathscr{G}_1)\rangle = \hat{P}\,|\boldsymbol{R}_1,\mathscr{G}_1\rangle\,|M(\boldsymbol{R}_1,\mathscr{G}_1)\rangle\,, \tag{4.4}$$

where γ denotes the chain of flipped bonds with a vison at one of its ends, $\boldsymbol{R}_1$. $\left|0_\chi\right\rangle$ denotes the vacuum of the bond fermions, corresponding to the uniform gauge with all $u_{\langle ij\rangle} = +1$. Creating a bond fermion on a link $l = \langle ij\rangle$ flips the value of $u_{\langle ij\rangle}$ from $+1$ to -1.

We start by choosing gauge configurations for the two vison positions, such that the ground states have even matter fermion parity (Eq. (3.27)):

$$|\Phi_0(\boldsymbol{R}_1)\rangle = \hat{P}\prod_{l\in\gamma}\chi_l^\dagger\left|0_\chi\right\rangle|M_0(\boldsymbol{R}_1,\mathscr{G}_1)\rangle = \hat{P}\,|\boldsymbol{R}_1,\mathscr{G}_1\rangle\,|M_0(\boldsymbol{R}_1,\mathscr{G}_1)\rangle\,. \tag{4.5}$$

$$|\Phi_0(\boldsymbol{R}_2)\rangle = \hat{P}\chi_{24}^\dagger\chi_{31}^\dagger\prod_{l\in\gamma}\chi_l^\dagger\left|0_\chi\right\rangle|M_0(\boldsymbol{R}_2,\mathscr{G}_2)\rangle = \hat{P}\,|\boldsymbol{R}_2,\mathscr{G}_2\rangle\,|M_0(\boldsymbol{R}_2,\mathscr{G}_2)\rangle \tag{4.6}$$

Note that we have ignored the second vison in the system as its position is fixed throughout the calculation.

The action of $\chi_{31}^\dagger$ and $\chi_{24}^\dagger$ amounts to moving the bare vison from $\boldsymbol{R}_1$ to $\boldsymbol{R}_2$. The projection operation ensures that the wavefunction is in the physical Hilbert space. Here I show explicitly the expansion of the matrix element in terms of the fermions:

$$\begin{aligned}
\langle\Phi_0(\boldsymbol{R}_1)|\,\Delta H_\Gamma^z\,|\Phi_0(\boldsymbol{R}_2)\rangle &= \Gamma\,\langle M_0(\boldsymbol{R}_1,\mathscr{G}_1)|\,\langle\boldsymbol{R}_1,\mathscr{G}_1|\,(b_2^y b_1^x c_2 c_1 + b_2^x b_1^y c_2 c_1)\hat{P}\,|\boldsymbol{R}_2,\mathscr{G}_2\rangle\,|M_0(\boldsymbol{R}_2,\mathscr{G}_2)\rangle \\
&= \Gamma\,\langle M_0(\boldsymbol{R}_1,\mathscr{G}_1)|\,\langle\boldsymbol{R}_1,\mathscr{G}_1|\,(b_2^y b_1^x c_2 c_1 + b_2^x b_1^y c_2 c_1)\hat{P}'\,|\boldsymbol{R}_2,\mathscr{G}_2\rangle\,|M_0(\boldsymbol{R}_2,\mathscr{G}_2)\rangle \\
&= \Gamma\,\langle M_0(\boldsymbol{R}_1,\mathscr{G}_1)|\,\langle\boldsymbol{R}_1,\mathscr{G}_1|\,(b_2^y b_1^x c_2 c_1 + b_2^x b_1^y c_2 c_1\hat{D}_1\hat{D}_2)\chi_{24}^\dagger\chi_{31}^\dagger\,|\boldsymbol{R}_1,\mathscr{G}_1\rangle\,|M_0(\boldsymbol{R}_2,\mathscr{G}_2)\rangle \\
&= \Gamma\,\langle M_0(\boldsymbol{R}_1,\mathscr{G}_1)|\,\langle\boldsymbol{R}_1,\mathscr{G}_1|\,(b_2^y b_1^x c_2 c_1 + i b_2^y b_1^x \hat{u}_{21})\chi_{24}^\dagger\chi_{31}^\dagger\,|\boldsymbol{R}_1,\mathscr{G}_1\rangle\,|M_0(\boldsymbol{R}_2,\mathscr{G}_2)\rangle\,.
\end{aligned} \tag{4.7}$$

Here, we have used the fact that the ground states have even total fermion parity so that $\hat{P}$ effectively reduces to $\hat{P}'$ (Eq. (3.27)). It can be easily observed that the only term in the expansion of $\hat{P}'$ that gives a non-zero overlap between the two vison sectors is $\hat{D}_1\hat{D}_2$; thus ensuring the second equality. Substituting for $\hat{D}_1$ and $\hat{D}_2$, Eq. (4.7) becomes

$$t_z^\Gamma = \langle\Phi_0(\boldsymbol{R}_1)|\,\Delta H_\Gamma^z\,|\Phi_0(\boldsymbol{R}_2)\rangle = \Gamma\,\langle M_0(\boldsymbol{R}_1,\mathscr{G}_1)|\,(-ic_2c_1 - 1)\,|M_0(\boldsymbol{R}_2,\mathscr{G}_2)\rangle\,. \tag{4.8}$$

Thus we have reduced the calculation of hopping amplitudes to that of calculating matrix elements of fermionic operators in the matter Majorana sector alone. Such fermionic matrix elements can be calculated for large finite size systems as described below.

4.2.2 Majorana matrix elements

We are interested in matrix elements of the form

$$\langle M_0(R_1,\mathscr{G}_1)|\, c_i^A c_j^B \,|M_0(R_2,\mathscr{G}_2)\rangle\,. \tag{4.9}$$

We can derive, using simple fermionic algebra, the expression for matrix elements in terms of the Bogoliubov matrix elements. First, we use the Thouless representation [46] of non-interacting fermionic many-body Slater determinant states introduced in Chapter 3 to express the above quantity in terms of the Bogoliubov matrices. Let a and b be the Bogoliubov quasiparticle operators that diagonalizes the Majorana sector corresponding to the vison positions $\boldsymbol{R}_1$ and $\boldsymbol{R}_2$ respectively (in the chosen gauges), i.e., $a\,|M(\boldsymbol{R}_1,\mathscr{G}_1)\rangle = 0$, $b\,|M(\boldsymbol{R}_2,\mathscr{G}_2)\rangle = 0$.

$$\begin{pmatrix} X_1^* & Y_1^* \\ Y_1 & X_1 \end{pmatrix}\begin{pmatrix} f \\ f^\dagger \end{pmatrix} = \begin{pmatrix} a \\ a^\dagger \end{pmatrix} \qquad \begin{pmatrix} X_2^* & Y_2^* \\ Y_2 & X_2 \end{pmatrix}\begin{pmatrix} f \\ f^\dagger \end{pmatrix} = \begin{pmatrix} b \\ b^\dagger \end{pmatrix}, \tag{4.10}$$

which follows from the Bogoliubov transformation.

The two quasiparticle operators a and b obey the following relation:

$$\Theta\begin{pmatrix} a \\ a^\dagger \end{pmatrix} = \begin{pmatrix} \chi^* & \Sigma^* \\ \Sigma & \chi \end{pmatrix}\begin{pmatrix} a \\ a^\dagger \end{pmatrix} = \begin{pmatrix} b \\ b^\dagger \end{pmatrix}, \tag{4.11}$$

with

$$\chi(R_1,R_2) = Y_2 Y_1^\dagger + X_2 X_1^\dagger, \qquad \Sigma(R_1,R_2) = Y_2 X_1^T + X_2 Y_1^T\,. \tag{4.12}$$

This mapping also leads to the following relation between the ground states.

$$|M_0(\boldsymbol{R}_2,\mathscr{G}_2)\rangle = \sqrt{|\chi|}\exp\left\{-\frac{Z^{12}_{mn}}{2}a_m^\dagger a_n^\dagger\right\}|M_0(\boldsymbol{R}_1,\mathscr{G}_1)\rangle \tag{4.13}$$

where

$$Z^{12} = \chi^{*-1}(R_1,R_2)\Sigma^*(R_1,R_2) \tag{4.14}$$

The magnitude of ground states overlap can now be read off from Eq. (4.14) as $|\sqrt{|\chi|}|$.

However, as discussed briefly in Section 3.2.1, this requires the matter fermionic parity of the two ground states to be the same. This is however not true for all gauge configurations. In such cases, $\det\{\chi\}$ evaluates to zero. But fortunately, this can always be repaired by choosing an appropriate gauge configuration to begin with, since a gauge transformations only conserves the parity of total number of fermions $N_\chi + N_f$, allowing us to modify the parity of the matter fermions (or c Majoranas) while preserving the flux sector. The total fermionic parity for a given state can be calculated following [47, 48]. However, this issue does not appear in the case of Γ induced hopping but poses serious challenge in the case of a Zeeman field.

4.2.3 Overlap of BCS wavefunctions

Although easy to evaluate, the above formula contains no information about the complex phase of the hopping rate, due to the square root operation in Eq. (4.14). As we shall see later, this information is necessary to coherently sum over multiple vison hopping processes which interfere with each other. We turn to nuclear physics for help. A rigorous path integral derivation using doubled Grassmann variables was introduced by Robledo [86], in the context of nuclear matrix-elements. We shall adapt this formalism to our problem, with some subtle modifications as described below.

The key is to choose a 'good' reference vacuum for the Thouless form in Eq. (4.14). The obvious choice would be the vacuum state of the original f fermions defined by $f|0\rangle = 0$. But this turns out to be a bad one, as the matrices χ may be singular leaving Eq. (4.14) itself invalid. Instead, we choose as reference vacuum the ground state corresponding to an arbitrary vison position $\boldsymbol{R}_0 \neq \boldsymbol{R}_1 \neq \boldsymbol{R}_2$. The only constraint that determines the choice of $\boldsymbol{R}_0$ is that all three ground states must have the same fermionic parity, and are not orthogonal to each other.

Let us denote the Bogoliubov quasiparticle operator corresponding to this vison position by d. i.e., $d\,|M(\boldsymbol{R}_0,\mathscr{G}_0)\rangle = d\,|\tilde{0}\rangle = 0$. We can now express the two relevant ground states as

$$|M_0(\boldsymbol{R}_1,\mathscr{G}_1)\rangle = |\sqrt{|\chi(\boldsymbol{R}_0,\boldsymbol{R}_1)|}|\exp\left\{-d^\dagger\frac{Z^{01}}{2}d^\dagger\right\}|M_0(\boldsymbol{R}_0,\mathscr{G}_0)\rangle \tag{4.15a}$$

$$|M_0(\boldsymbol{R}_2,\mathscr{G}_2)\rangle = |\sqrt{|\chi(\boldsymbol{R}_0,\boldsymbol{R}_2)|}|\exp\left\{-d^\dagger\frac{Z^{02}}{2}d^\dagger\right\}|M_0(\boldsymbol{R}_0,\mathscr{G}_0)\rangle\,. \tag{4.15b}$$

The overlap can be calculated by introducing coherent state path integrals and integrating out the Grassmann fields resulting in the final expression. See Appendix A for the detailed derivation.

Pfaffian formula

$$\begin{aligned}&\langle M_0(\boldsymbol{R}_1,\mathscr{G}_1)|M_0(\boldsymbol{R}_2,\mathscr{G}_2)\rangle\\ &= |\sqrt{\det\{\chi(\boldsymbol{R}_0,\boldsymbol{R}_1)\}\det\{\chi(\boldsymbol{R}_0,\boldsymbol{R}_2)\}}|(-1)^{\frac{N(N+1)}{2}}\,\mathrm{Pf}\begin{pmatrix} Z^{02} & -\mathbb{1}\\ \mathbb{1} & -Z^{01}\end{pmatrix}\end{aligned} \tag{4.16}$$

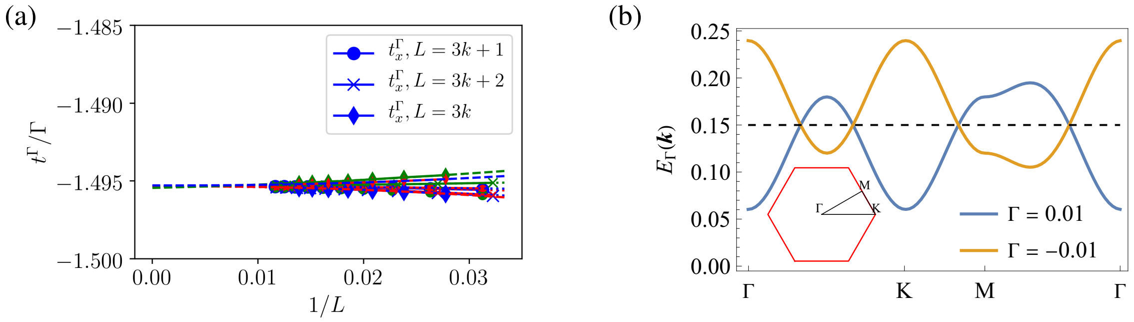

Fig. 4.2 (a) Vison hopping amplitudes linear in Γ for $K=-1$, as function of inverse system size, $L=3k+n$, $k\in\mathbb{N}$, $n=0,1,2$ for a perturbation by a small Γ term (next-nearest neighbour hopping, $\kappa=0$). Color code: blue - t_x^Γ, green - t_y^Γ, red - t_z^Γ where $\zeta=h,\Gamma$. Symbols are used to label different system sizes. The corresponding vison dispersions are shown in (b).

where the Pfaffian is computed for a $2N\times 2N$ anti-symmetric matrix, numerically implemented using the Python package by Wimmer [87].

4.2.4 Results - FM Kitaev model

We first present the hopping amplitudes and the corresponding dispersion for a single vison, induced by the Γ term, when the underlying Kitaev interaction is ferromagnetic ($K<0$, FM Kitaev).

Fig.4.2a shows the hopping amplitude t_Γ calculated as a function of inverse system size L. The finite size effects are negligible and the value extrapolates to

Γ - induced hopping

$$t_\Gamma \approx -1.45\,\Gamma. \tag{4.17}$$

A finite hopping rate in the thermodynamic limit is not *a priori* obvious for mobile heavy particles in a gapless bath. For example, it is well-known that moving an impurity in a Fermi sea results in the famous Anderson orthogonality catastrophe. A strong rearrangement of the Fermi-sea in response to the perturbation leads to a zero overlap between Slater determinants in the thermodynamic limit. However, the vanishing density of states of the Dirac dispersion of the fermions comes to our rescue here.

Assuming a tight-binding model on a triangular lattice with lattice constant $\sqrt{3}a$, where a is the honeycomb lattice constant, we calculate the vison dispersions. For $\Gamma<0$ there are 6 minima located on the lines connecting the Γ and M points. For $\Gamma>0$, the minima of the dispersion are located the Γ and K points. The fact that the Γ and K points are exactly degenerate is an artefact of our leading-order approximation which includes only next-nearest neighbour hopping.

4.2.5 Results - AFM Kitaev model

The hopping matrix element for the antiferromagnetic Kitaev coupling ($K > 0$, AFM Kitaev) evaluates to zero! This reveals a novel interference phenomenon of vison hopping processes related by symmetries as we explain now.

A single vison hopping process induced by $\Delta H_\Gamma^z = \Gamma(\Delta H_1 + \Delta H_2)$ is a sum of two contributions, $t_{ab} = A_1 + A_2$ arising from the two different terms in the Hamiltonian. For instance, on the z-link shown in Fig. 4.1, $\Delta H_1 = \Gamma\sigma_1^x\sigma_2^y$ while $\Delta H_2 = \Gamma\sigma_1^y\sigma_2^x$ These two terms are related by a reflection symmetry (dashed lines in Fig. 4.1), which ensures that $A_1 = \pm A_2$. To fix the sign, we observe that $\langle\Delta H_1 \Delta H_2\rangle = \langle\sigma_1^z\sigma_2^z\rangle$ is negative in the AFM Kitaev model while positive in the FM Kitaev model. This strongly suggests that $A_1 = -A_2$ in the AFM phase as we confirmed numerically by direct evaluation of Eq. (4.3): a destructive interference eliminates the leading vison hopping process.

This however, does not mean that the vison is localized in an AFM Kitaev model with Γ term. Higher orders in perturbation theory may lead to coherent hopping processes which we do not consider here. Instead, we will see how a small magnetic field results in a finite hopping rate even at linear order in Γ. In Chapter 4, we will study how scattering from Majoranas help visons become mobile at finite temperatures.

4.3 Heisenberg Interaction

We now turn to a nearest-neighbour Heisenberg interaction.

$$\Delta H_J = \sum_{\langle ij \rangle} \boldsymbol{\sigma}_i \cdot \boldsymbol{\sigma}_j. \tag{4.18}$$

Starting from the vison-free sector, the action of ΔH_J on a given bond creates four visons around the bond. Therefore, at linear order perturbation analysis like we did for the Γ term, ΔH_J takes the system out of the single vison sector. However, at second order, one can find several terms that realizes the hopping of a vison. A full calculation at second order involves the sum over an extensive number of matrix elements which we do not do here. However, we can argue that all the processes that contribute to the hopping interfere destructively, resulting in a vanishing hopping rate!

Consider a vison hopping across two y-links as shown in Fig 4.3. Let us denote the hopping induced by processes depicted on the left and right side of Fig 4.3 by t_L and t_R. A mirror symmetry maps the processes onto each other. We now repeat the argument used in the main text to discuss the interference of hopping processes induced by Γ or h. By symmetry $t_L = \pm t_R$ and the sign will decide whether there is a destructive interference, $t_L + t_R = 0$, or a constructive interference $t_L + t_R = 2t_L$ of the two terms.

To determine the sign, we can analyze a simplified question and consider the sign of

$$\tilde{t}_{L/R} = \left\langle \Phi^0(\boldsymbol{R}_1) \right| (\Delta H_J \Delta H_J)_{L/R} \left| \Phi^0(\boldsymbol{R}_2) \right\rangle, \tag{4.19}$$

where we denote by $(\Delta H_J \Delta H_J)_{L/R}$ those terms which contribute to the processes on the left/right side of Fig. 4.3 (written below each figure). Although $\tilde{t}_{L/R} \neq t_{L/R}$, the two quantities are expected to have the same symmetry properties.

To map an L process to an R process, we need the information on the flux configuration. The central plaquette in all diagrams in Fig. 4.3 do not carry any flux in the initial and final state. The plaquette operator $\hat{W} = \sigma_1^x \sigma_2^y \sigma_3^z \sigma_4^x \sigma_5^y \sigma_6^z$ has eigenvalue $+1$ (-1) in the absence (presence) of a flux [40]. Thus the following key observation can be made:

$$\left| \Phi^0(\boldsymbol{R}_2) \right\rangle = \hat{W} \left| \Phi^0(\boldsymbol{R}_2) \right\rangle = \sigma_1^x \sigma_2^y \sigma_3^z \sigma_4^x \sigma_5^y \sigma_6^z \left| \Phi^0(\boldsymbol{R}_2) \right\rangle. \tag{4.20}$$

Using this formula and the algebra of Pauli operators it is straightforward to show that

$$\begin{aligned} &\left\langle \Phi^0(\boldsymbol{R}_1) \right| \sigma_1^x \sigma_2^x \sigma_2^z \sigma_3^z \left| \Phi^0(\boldsymbol{R}_2) \right\rangle \\ &\qquad = - \left\langle \Phi^0(\boldsymbol{R}_1) \right| \sigma_6^z \sigma_5^z \sigma_5^x \sigma_4^x \left| \Phi^0(\boldsymbol{R}_2) \right\rangle. \end{aligned} \tag{4.21}$$

Therefore the processes shown in Fig. 4.3a and 4.3b contribute with opposite sign.

A straightforward extension of this argument is not possible for all the other processes shown in Fig. 4.3. But a direct evaluation of $\tilde{t}_L$ and $\tilde{t}_R$ in a finite size system reveals that

$$\tilde{t}_L = -\tilde{t}_R. \tag{4.22}$$

We therefore expect that $t_L = -t_R$ and processes to order J^2 thus cancel by an interference effect independent of the sign of the Kitaev coupling.

A weak Heisenberg coupling is hence expected to contribute only to order J^4 to the dispersion of single visons (as J^3 terms map a single vison to either 3 or 5 visons). Pairs of visons, however, can even hop by processes linear in J as has been shown in Ref. [67].

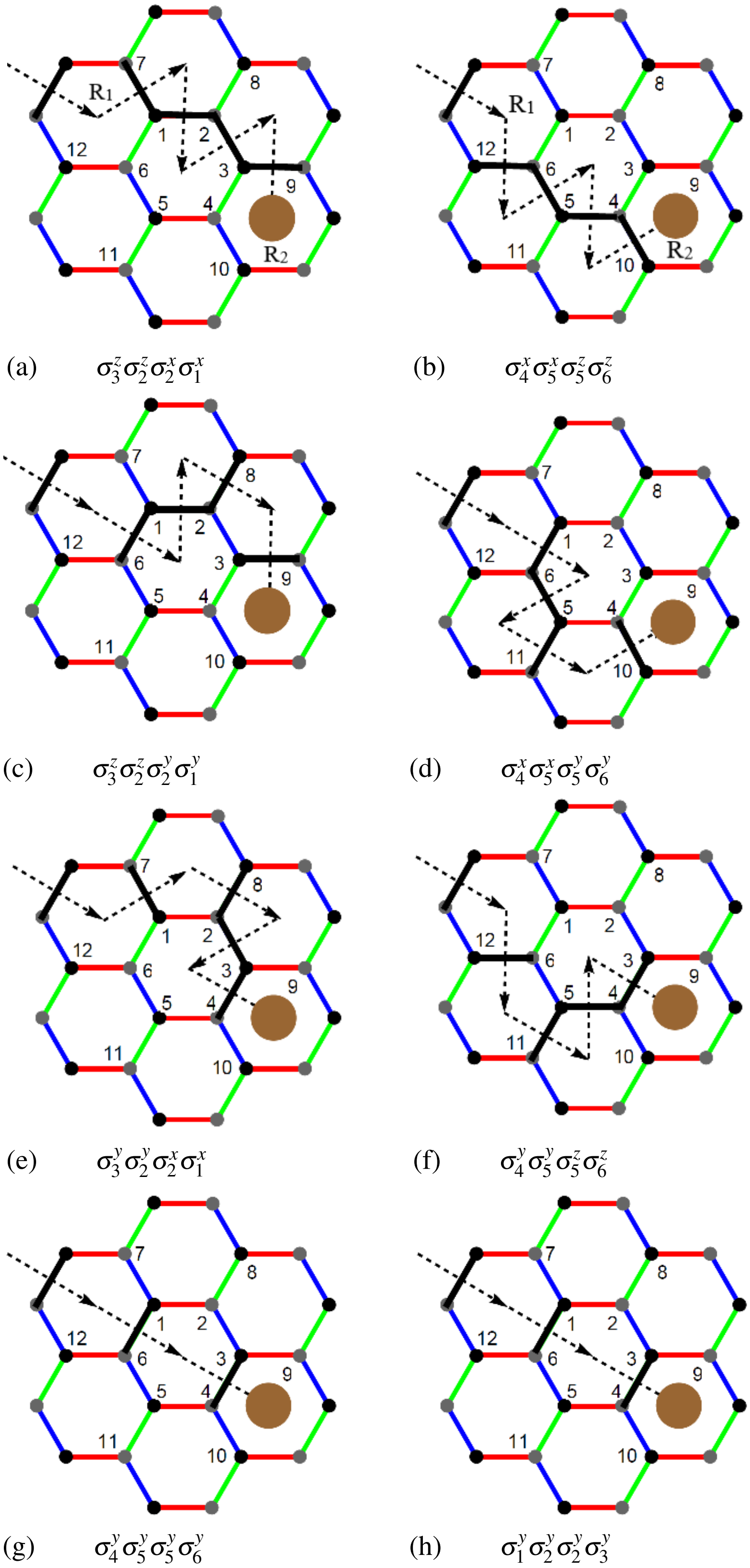

(a) $\sigma_3^z\sigma_2^z\sigma_2^x\sigma_1^x$ (b) $\sigma_4^x\sigma_5^x\sigma_5^z\sigma_6^z$

(c) $\sigma_3^z\sigma_2^z\sigma_2^y\sigma_1^y$ (d) $\sigma_4^x\sigma_5^x\sigma_5^y\sigma_6^y$

(e) $\sigma_3^y\sigma_2^y\sigma_2^x\sigma_1^x$ (f) $\sigma_4^y\sigma_5^y\sigma_5^z\sigma_6^z$

(g) $\sigma_4^y\sigma_5^y\sigma_5^y\sigma_6^y$ (h) $\sigma_1^y\sigma_2^y\sigma_2^y\sigma_3^y$

Fig. 4.3 **Heisenberg interaction.** Eight single-vison hopping processes ($\boldsymbol{R}_1 \rightarrow \boldsymbol{R}_2$) appearing at second order perturbation theory in Heisenberg interaction. All the given processes interfere destructively.

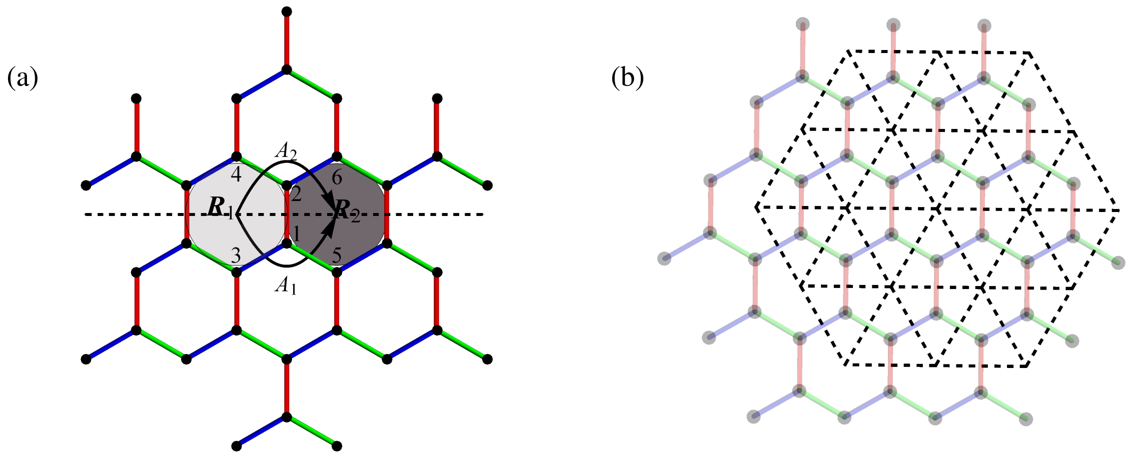

Fig. 4.4 **Vison hopping induced by a magnetic field term.** (a.) The perturbation ΔH_h on a given bond (shown here for $\langle ij\rangle_z$) has two symmetry related terms that hop a vison from $\boldsymbol{R}_1$ to $\boldsymbol{R}_2$ through two different processes. These processes, shown by the two arrows, interfere with each other. (b.) A magnetic field induces a nearest-neighbour hopping on this lattice.

4.4 Effect of a Magnetic Field

An external magnetic field is a distinct perturbation due to its symmetry properties. We consider an external field in the [111] direction. This has two effects: to linear order in h it induces hopping of the visons, to cubic order a gap of size $\Delta_m = 6\sqrt{3}\kappa \sim \frac{h^3}{K^2}$ is opened [40] in the Majorana spectrum (here we assume $\Gamma = 0$). While this scaling suggests that one may neglect the effects of κ to lowest order in perturbation theory, the presence of a Majorana zero mode attached to the vison for $\kappa \neq 0$ (or a quasi-bound state for $\kappa = 0$) makes the analysis more subtle and induces strong finite size effects. [1]

Consider a z bond as shown in Fig. 4.4, where the magnetic field perturbation is $\Delta H_z = \sum_\alpha \frac{h}{\sqrt{3}}(\sigma_1^\alpha + \sigma_2^\alpha)$. Starting with a vison located at $\boldsymbol{R}_1$, the z component of the perturbation induces a hopping across the z bond to $\boldsymbol{R}_2$, while the x and y components hop the vison across the x and y bonds respectively. This defines a triangular lattice for the vison hopping model. The hopping matrix elements are given by

$$t_\alpha^h = \frac{h}{\sqrt{3}} \langle \Phi(\boldsymbol{R}_1)| \left(\sigma_1^\alpha + \sigma_2^\alpha\right) |\Phi(\boldsymbol{R}_2)\rangle \,. \tag{4.23}$$

Using the Majorana representation, and a further gauge transformation for the spin operator (equivalent to rewriting $\sigma^z = -i\sigma^x\sigma^y$) the hopping rate, e.g., for the z component can be written

---

[1] I am sincerely grateful to Chen, Rao and Sodemann for pointing out this numerical artefact which would have otherwise lead to wrong conclusions.

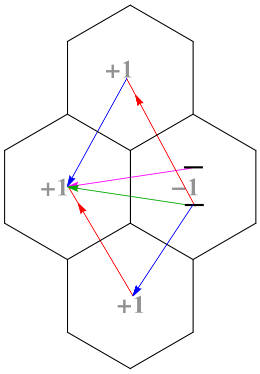

Fig. 4.5 **Parity constraints and physical states.** The pattern of ground-state fermionic parity indicated as +1 (odd) or +1 (even) in the plaquette where the vison is located. This is fixed for a given position of the second vison which is placed on the far left separated by a distance $d_V = L/2$ (not shown in the figure). Here, $L = 34$, $d_V = 14$. For the odd parity case, one needs to calculate the hopping amplitudes to states with a single particle added to the BCS vacuum to stay in the physical Hilbert space. The two levels shown in the odd parity plaquette denote the first two levels of the Majorana spectrum.

as

$$t_z^h = \langle M_0(\boldsymbol{R}_1,\mathscr{G}_1)|\,(-i+c_1c_2)\,|M_0(\boldsymbol{R}_2,\mathscr{G}_2)\rangle\,. \tag{4.24}$$

Parity constraints and reference vacuum The above matrix element is finite only if the states $|M_0(\boldsymbol{R}_1,\mathscr{G}_1)\rangle$ and $|M_0(\boldsymbol{R}_2,\mathscr{G}_2)\rangle$ have the same matter fermionic parity. It turns out that depending on the vison configuration, the physical ground state has an odd fermionic parity. Therefore in such cases, we have to add an extra Majorana mode on top of the vacuum to obtain the true physical state. Therefore one should add an extra Boguliubov particle to the vacuum to get the true physical states. So the physical states in the case of odd parity are given by

$$\left|M_l^{odd}(\boldsymbol{R},\mathscr{G})\right\rangle = \left|\det\left(\chi^{(a)}\right)^{\frac{1}{2}}\right| a_l^\dagger e^{-\frac{1}{2}d^\dagger Z^{(a)} d^\dagger}\left|\tilde{0}\right\rangle, \tag{4.25}$$

where $\left|\tilde{0}\right\rangle$ is an appropriately chosen reference vacuum and χ, Z are the corresponding matrices derived from the Bogoliubov transformation. Quantum number $l = 0$ gives the physical ground state and $l = 1$ gives the first excited state. This results in a pattern of ground-state parities as illustrated in Fig. 4.5, for a given position of the second vison and a fixed gauge configuration (not shown in the figure). While hopping along across the y bond from a plaquette with parity +1 to one with parity -1, one has to calculate the following overlaps for $l = 0$ and $l = 1$:

$$\begin{aligned} t_z^{h(l)} &= \Gamma\left\langle M_l^{odd}(\boldsymbol{R}_1,\mathscr{G}_1)\right|\,\langle\mathscr{G}_1|\,(\sigma_i^z+\sigma_j^z)\,|\mathscr{G}_2\rangle\,|M_0(\boldsymbol{R}_2,\mathscr{G}_2)\rangle \\ &= \Gamma\left\langle M_l^{odd}(\boldsymbol{R}_1,\mathscr{G}_1)\right|\,(ib_i^z c_i + ib_j^z c_j)\hat{P}\,|M_0(\boldsymbol{R}_2,\mathscr{G}_2)\rangle\,. \end{aligned} \tag{4.26}$$

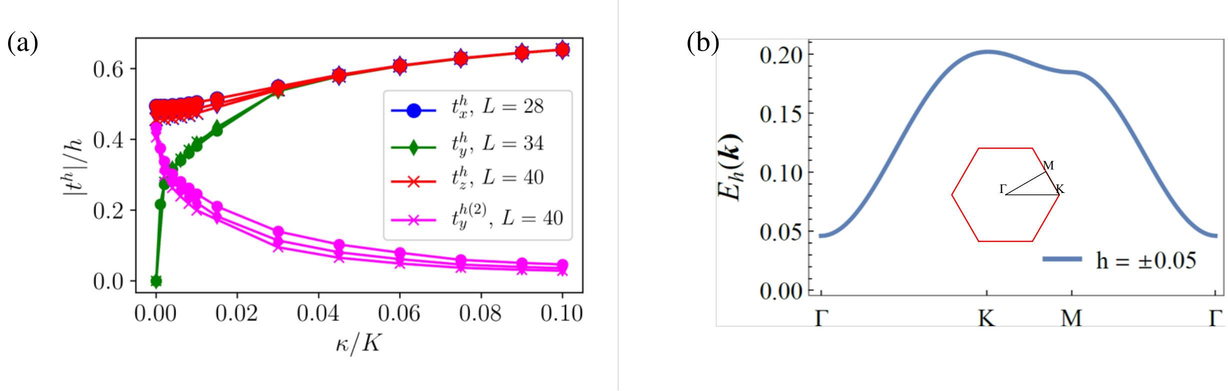

Fig. 4.6 **Field-induced hopping in FM Kitaev model**(a) Vison hopping amplitude (magnitude) induced by a small magnetic field h for $K = -1$ as a function of Majorana mass parameter κ. The magenta plot shows the hopping from a ground-state to an excited state of a nearest neighbour site. Color code: blue - t_x^ζ, green - t_y^ζ, red - t_z^ζ where $\zeta = h, \Gamma$. Symbols are used to label different system sizes. In panel (b) the corresponding vison dispersions is shown

These can be evaluated using the same Pfaffian method as described in Appendix.A.

4.4.1 Results - FM Kitaev

In Fig. 4.6, the hopping amplitudes across the three different bonds are plotted as a function of the Majorana gap parameter κ. We treat κ as an independent parameter to better understand the finite size effects. Besides the ground-state to ground-state hopping rates, it turns out that in the small κ limit one also has to include the hopping to an excited state (with energy $E_V + 2\kappa$ where E_V is the ground state energy of the vison) for certain directions of hopping. Examining Fig. 4.6 a, we can identify two regimes defined by the ratio of two length scales: the distance between the two visons d_V and the extend of the Majorana bound state attached to the vison, $\xi_m \sim v_m/\kappa$. For $d_V \gg \xi_m$ (corresponding to $\kappa > 0.03\,|K|$ in Fig. 4.6 a) one can ignore the hopping to the excited state and one obtains a finite, directionally independent hopping rate of the vison with almost no finite size effects and only a weak dependence on κ. For example, for $|\kappa| = 0.05\,|K|$ we find

$$t_x^h = t_y^h = t_z^h \approx -0.6\,|h|. \tag{4.27}$$

Note that the hopping rate is independent of the sign of h.

In the opposite limit, $d_V \lesssim \xi_m$ (small κ limit in Fig. 4.6a), in contrast, we obtain very large finite size effects and the hopping rates across the y bonds become different from those across the x and z bonds of the Kitaev lattice. This is a consequence of the presence of the second vison which explicitly breaks the rotational symmetries. Furthermore, in the small κ limit one cannot ignore the hopping $t_y^{h(2)}$ to excited states (magenta lines in Fig. 4.6b) across the y bond which becomes much larger than the ground state-to-ground state hopping t_y^h (green line) for $\kappa \to 0$. The case $\kappa = 0$ is special and highly singular ($t_y^h = 0$ and $t_y^{h(2)} \approx t_x^h \approx t_z^h$). As detailed above, in this case, the relative fermionic parity of the states appearing in Eq. (4.23) depends in a non-trivial way on the position of the second vison. Thus certain hopping processes are only allowed if an extra matter Majorana mode is occupied.

This analysis shows that the very notion of a single and independent vison excitation is *not* well defined in the limit when the vison-vison distance d_V is smaller than ξ_m. In this case one cannot formulate a theory of a single vison because the (quasi-) bound Majorana state attached to one vison interacts with neighbouring visons.

In contrast, for $d_V \gg \xi_m$, one can treat a single vison as a well-defined independent particle. Remarkably, our calculation shows that the situation is also different for the Γ perturbation: in this case the single-vison hopping is with high precision independent of the presence of the second vison. This can be traced back to the fact that the Γ term is quadratic in the matter fermions, while the magnetic field is linear, and thus may modify the matter fermion parity. For the Γ perturbation, therefore, it is possible to formulate a theory of single visons even for a gapless Majorana spectrum.

In Fig. 4.6b we show the vison dispersion for $d_V \gg \xi_m$ for a finite gap $m = 0.05\,|K|$ in the Majorana spectrum. Importantly, the vison hopping rates can be chosen to be real. This implies that none of the vison lattice plaquettes enclose a non-trivial flux and the vison bands carry no Chern number. This is, however, not true in the antiferromagnetic model.

4.4.2 AFM Kitaev - Topological vison bands

In the limit of vanishing Majorana gap $\kappa \to 0$, the hopping rate linear in h also evaluates to zero through a similar interference effect as for the Γ term. However, a finite κ breaks the mirror symmetries which lead to this destructive interference. Therefore, both the field-induced hopping rate t^h and the Γ induced rate t^Γ become finite. In Fig. 4.7 a and c, we plot these hopping amplitudes as function of κ for different vison separations ($d_v = L/2$). Here, we can see similar finite size effects as in the FM model (Fig.4.6a), where the second vison breaks the rotation symmetry in the small mass limit. For $d_V \gg \xi$, finite size effects are, however, absent. For $\kappa = 0.05$, for example, we find

$$|t_h| \approx 0.07\,|h|. \tag{4.28}$$

Our numerical data is roughly consistent with

Field-induced hopping

$$|t_h| \approx 0.32\,|h|\sqrt{|\kappa/K|} \tag{4.29}$$

in the regime $d_V \gtrsim \xi$. If one assumes that the Majorana gap arises solely due to the magnetic field, i.e., $\kappa \sim h^3/K^2$, the vison hopping amplitude follows the scaling $t^h \sim |h|^{2.5}$. However, we emphasize that a reliable extraction of the power-law in κ is not possible from our data.

Remarkably, the vison acquires a non-trivial phase when hopping around a triangular loop. The value can be obtained by calculating

$$\arg\left[\langle \boldsymbol{R}_1|\Delta H_h|\boldsymbol{R}_3\rangle\langle \boldsymbol{R}_3|\Delta H_h|\boldsymbol{R}_2\rangle\langle \boldsymbol{R}_2|\Delta H_h|\boldsymbol{R}_1\rangle\right] = -\mathrm{sign}(h)\frac{\pi}{2} \tag{4.30}$$

for three vison sites ordered anticlockwise around a honeycomb site, as shown in the inset of Fig. 4.4c. Thus each triangular vison plaquette (i.e., each site of the original honeycomb lattice) carries a flux of $-\pi/2$ for $h > 0$ ($\frac{\pi}{2}$ for $h < 0$).

Symmetry fractionalization The non-trivial flux in every triangular loop reveals a phenomenon called “translational symmetry fractionalization" that characterizes topological phases enriched by translations [88]. In such systems, translation symmetry of the Hamiltonian is only projectively implemented on its excitations. Here, for the first time, we have shown that the AFM and FM Kitaev models correspond to different symmetry fractionalization realizations although the ground state corresponds to the same chiral spin liquid. [2]

As a consequence, in the AFM model, there is a doubling of the vison unit cell (containing four triangular plaquettes each to obtain a flux of 2π) which results in two vison bands in a reduced Brillouin zone (See Fig. 4.7d). Under the single-vison tight-binding approximation, the band structure is given by

$$H^v(\boldsymbol{p}) = E_0^v \mathbb{1} - \boldsymbol{h}(\boldsymbol{p})\cdot\boldsymbol{\tau}, \qquad \text{where,} \quad \boldsymbol{h}(\boldsymbol{p}) = 2t^h \begin{pmatrix} \sin(\boldsymbol{p}\cdot\boldsymbol{\eta}_1) \\ \cos(\boldsymbol{p}\cdot\boldsymbol{\eta}_2) \\ \sin(\boldsymbol{p}\cdot\boldsymbol{\eta}_3) \end{pmatrix} \tag{4.31}$$

with $\eta_1 = (\frac{1}{2}, \frac{\sqrt{3}}{2})$,$\eta_2 = (\frac{1}{2}, -\frac{\sqrt{3}}{2})$ and $\eta_3 = (1,0)$ are the nearest neighbour vectors of the vison lattice. $\boldsymbol{\tau}$ denotes the Pauli matrices in the sublattice basis (due to the doubled unit cell). The corresponding energies are given by $E^v_{\pm,\boldsymbol{p}} = E^v_0 \pm |\boldsymbol{h}(\boldsymbol{p})|$. We have already seen in Chapter 3 that a pivotal quantity that defines the Hall response of a quasiparticle is the Chern number of its energy bands. As the single vison Hamiltonian given above, Eq. (4.31), is of the form we

---

[2] Parallel to this work, in Phys. Rev. Research 4, 043003, Chen, Rao and Sodemann also obtained results consistent with ours using an exact fermion-flux duality.

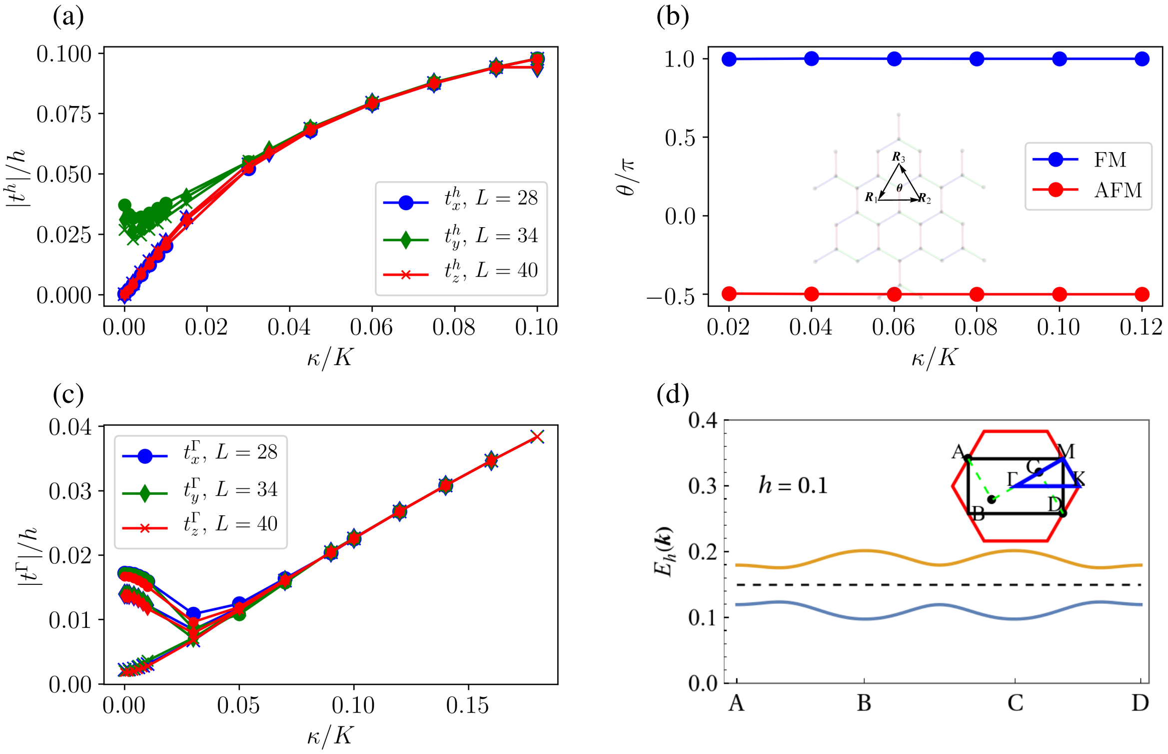

Fig. 4.7 **Hopping in a magnetic field: AFM Kitaev model**: (a) Vison hopping amplitudes for $K = 1$ as function of Majorana gap κ, induced by small magnetic field h for different system sizes. (b) Berry phase θ acquired by a vison while hopping around an elementary triangular loop (inset) for FM v/s AFM Kitaev models. Every triangle carries a flux of π for the FM model but a flux of $-\pi/2$ for the AFM model when $h > 0$. (c.) In the presence of a finite Majorana mass, the vison also obtains a next-nearest-neighbour hopping t^Γ linear in Γ. (d.) Two vison bands with Chern numbers ± 1 emerge ($\Gamma = 0$ in this plot). Inset: The Brillouin zone is halved due to the doubling of the unit cell.

have already encountered in Chapter 3, we can directly compute the Chern number of the vison bands. The Chern number of the lowest band is given by

Vison Chern number

$$C_v = -\mathrm{sgn}(h_x h_y h_z). \tag{4.32}$$

The sign of the Chern number is therefore determined by the sign of the Majorana gap $\Delta_m \sim (h_x h_y h_z)$. This also has profound consequences for the thermal Hall effect experiments in the case of AFM Kitaev materials. This will be discussed in Chapter 8.

Γ induced hopping. As mentioned above, a finite Majorana mass also breaks the destructive interference that suppressed Γ induced hopping. Fig. 4.7c shows this hopping amplitude as a function of κ. From our data, an approximately linear behaviour is obtained:

$$|t_\Gamma| \approx 0.2\Gamma\frac{|\kappa|}{K}. \tag{4.33}$$

Within our perturbative treatment, it is unlikely that this term dominates; for small h and thus small κ, higher-order terms in Γ, $t_\Gamma \sim \Gamma^2$ will dominate, while for larger h, one reaches the regime where $|t_h| > |t_\Gamma|$.

4.5 Instabilities

Stability of the Kitaev spin liquid phase hinges on the finite energy gap of the gauge field excitations. Although the resulting phases are difficult to predict, vison gap closing and the following proliferation of visons will trigger a breakdown of the Kitaev phase. Indeed, this may occur when the vison band touches zero energy, as perturbations grow stronger.

Remarkably, our calculations can already explain an intriguing behaviour of generic Kitaev models seen in numerical studies - an AFM Kitaev model is more stable to Γ interaction and Zeeman terms compared to an FM model[69, 89]. Within our perturbative approach, we found that the hopping amplitudes, and thus the bandwidth of visons are parametrically larger for the FM Kitaev model compared to the AFM model. Several studies have also pointed to the emergence of a gapless U(1)-type spin liquid in an AFM Kitaev model at a critical magnetic field strength. Although our approach here cannot make predictions on such phase transitions, our results do point to qualitatively different vison dynamics in FM and AFM models which may be a good starting point to investigate the nearby phases.

Although single vison gap closing is a prime instability mechanism, it was shown by Zhang *et al.* [67] that a bound pair of visons may also obtain a band structure, and therefore form 'magnon' like bound states which may also drive instabilities. However, it is important to remember that a single vison is an elementary excitation of the gauge theory and is a stable quasiparticle due to its topological nature, whereas a vison-pair can easily decay into the Majorana continuum, leading to a finite lifetime.

In Fig. 4.8, we estimate the critical perturbation strengths for single vison gap closing within our linear order perturbation theory and compare it with the results of Ref. [67]. Furthermore, we also compare the result of the two analytical studies to several numerical works. Let us first discuss the ferromagnetic Kitaev model, believed to be relevant for materials like α-RuCl$_3$ [94–96].

When perturbed by a Γ term, our results suggest that the leading instability arises from the closing of the single-vison gap, see Fig. 9a. Linear order perturbation theory obtains a closing of the gap at values roughly consistent with exact diagonalization (ED) results [69, 90] and a

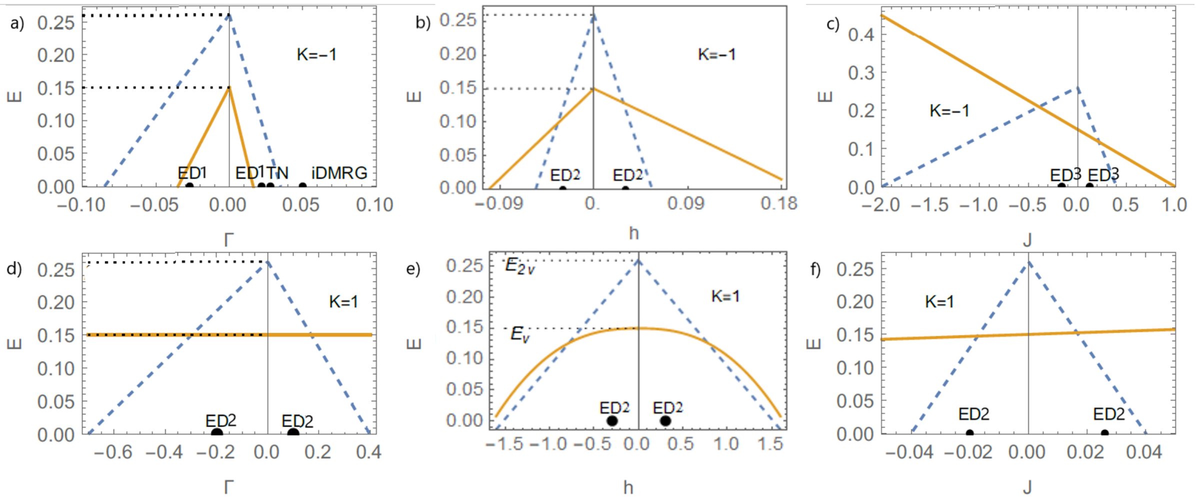

Fig. 4.8 **Vison gap closing instabilities: single vison vs. vison pairs.** Energy gap E, visons and vison pairs, as function of Γ, h and J (solid lines in left, middle, right column) for ferromagnetic (upper panels) and antiferromagnetic (lower panels). In subfigure (e), the vison gap is calculated using the formula Eq. (4.33) which results in a scaling of the form $E_v \propto h^{2.5}$. The dashed line shows the corresponding gap of a vison pair, obtained from Zhang *et al.* [67]. The thick points show numerical predictions for phase boundaries obtained from the exact diagonalization studies of Ref. [69] (ED1), Ref. [90] (ED2) and Ref. [91] (ED3), from a tensor-network based approach [92] (TN) and from an iDMRG study [93].

tensor network calculation [92]. Note, however, that a recent iDMRG study [93] predicts an increased stability of the spin liquid phase.

The situation is very different when one considers perturbations by a magnetic field h, shown in Fig. 4.8b. Already for rather small fields, vison pairs have a lower energy compared to single visons suggesting that the proliferation of vison pairs (or other bound states) may drive the instability. The predicted location of the transition is again roughly consistent with ED studies.

In the antiferromagnetic case, $K > 0$, shown in the lower panel of Fig. 4.8 our theory makes no direct prediction for Γ perturbation as there is no vison hopping to linear order. For the h perturbation, we find that the single vison gap closes at a similar critical field as the vison pair. Although the bare vison pair gap closes at a large field value, well beyond the perturbative limit, Ref.[67] also reported a smaller critical field $\approx 0.5K$ where a transition to a different type of spin liquid phase happens, due to the interplay of Majorana-vison-pair hybridization and their dynamics.

4.6 Summary and Discussion

Given the mounting evidence for Kitaev physics in many materials albeit with several puzzling observations, a better understanding of realistic models is urgently needed. In any real material hosting a spin liquid adiabatically connected to the Kitaev phase, the emergent gauge field will become dynamical and the visons will be mobile. Our analysis is an important first step towards understanding their properties and identifying their signatures.

We used a controlled many-body degenerate perturbation theory to obtain the hopping amplitudes and dispersion of a dressed vison in the presence of experimentally relevant perturbations. Using Kitaev's parton description, we implemented a Pfaffian technique to calculate the overlap of many-body wave functions of Majorana fermions. A crucial step was the careful implementation of the projection operation, necessary to obtain gauge invariant quantities. In this process, a key computational insight was understanding the fermion parity constraints imposed by the projector. This forces one to meticulously choose the reference vacua required to express the Majorana wavefunctions as a BCS state.

Perhaps it is worthwhile to distinguish our work from numerous previous studies on anyon dynamics in *gapped* $\mathbb{Z}_2$ spin liquids[97, 98]. Importantly, due to the surrounding gapless bath of Majoranas, the vison is dressed by a cloud of scattering Majoranas and it is a qualitatively different quasiparticle than the anyons of the toric code. This is most obvious in the gapped chiral phase where the visons are, in fact, Ising anyons. Indeed, we can also straightforwardly extend our calculations to the toric code limit of the Kitaev model by setting $K_z \gg K_x, K_y$.

Even at the level of linear order perturbation theory, a remarkable result was that the AFM and Kitaev models realize profoundly different dynamics for the vison, owing to the coherent interference of vison hopping paths. This immediately offers an intuitive explanation for the stability of the spin liquid as seen in several numerical studies. For example, it has been well established that the AFM Kitaev spin liquid is much more stable with respect to perturbations by Γ and h. This is consistent with the absence of single-vison tunneling linear in Γ or h.

This analysis in turn revealed a more fundamental property - FM and AFM Kitaev models realize two different symmetry fractionalization patterns. While in the FM model, lattice translational symmetry is not fractionalized, it is in an AFM model. In this context, it may be interesting to explore if the proposed emergence of a gapless U(1) spin liquid found only in the AFM model subjected to a magnetic field is related to symmetry fractionalization properties. That said, the destructive interference of vison paths hinges on the mirror symmetries of the model. In a real system, these may be weakly broken, for example $\Gamma^x \neq \Gamma^y$, that may add small corrections to the results obtained here. Intriguingly, under a staggered magnetic field ($\pm\boldsymbol{h}$ for $A(B)$ sublattice), an FM Kitaev model would behave like an AFM model as far as the vison dynamics is concerned. Indeed this is what has been observed in numerical studies [69, 89].

A direct experimental consequence of symmetry fractionalization in the AFM model is an enhanced periodicity in momentum space probed by, e.g., neutron spectroscopy [99]. During such an experiment, a single spin flip may create a pair of visons whose band dispersion is defined on a reduced Brillouin zone. The continuum response will therefore be modulated accordingly with an enhanced periodicity compared to the usual hexagonal Brillouin zone of the honeycomb lattice.

Perhaps one of the most striking results is the emergence of vison Chern bands. This is the first instance, to the best of my knowledge, where visons have been shown to exhibit topological bands and as a result, contribute to thermal Hall effect. A detailed discussion of this novel vison thermal Hall effect is presented in Chapter 8.

We have focused on an isolated vison excitation owing to its gauge charge, assuming a dilute vison density. However, vison-vison and vison-Majorana interactions will become increasingly important when there is a finite density of visons. Indeed, we saw in Section 4.4 that when the vison-vison distance is small the quasi-localized Majorana modes overlap and invalidates a single vison picture. The back-action of a moving vison on the Majoranas is also an interesting problem to be explored.

Chapter 5

Mobility and Diffusion

In the previous chapter, we showed that a single vison, dressed by Majorana fermions obtains a dispersion and therefore a finite effective mass. However, at any finite temperature $T > 0$, thermally excited Majoranas can scatter from visons and qualitatively affect its dynamics. This is what we explore in this chapter. That of a heavy particle interacting with a gapless bath is in fact one of the earliest applications of quantum mechanics to condensed matter systems. A classic example is that of polarons, quasiparticles emergent from the interaction of an electron with the lattice phonons. A moving electrons due to its charge distorts the underlying lattice of ions forming a phonon cloud around it, increasing its effective mass and lowering its mobility. However, even before quantum physics, the motion of a heavy particle in an environment held a special place in classical statistical physics.

The results of this chapter have been published in the article Physical Review X ***12****, 041004 (2022), co-authored by Achim Rosch.*

5.1 The Proverbial Pollen

"*These motions were such as to satisfy me, after frequently repeated observation, that they arose neither from currents in the fluid, nor from its gradual evaporation, but belonged to the particle itself.*" In 1827, the Scottish botanist Robert Brown wrote on his paper on the observation of jiggly random motion of tiny pollen particles suspended in water. Little did he know that this simple observation would go on to prove the existence of atoms. According to Brown, this random motion was unexpected unless the pollen was in some sense "alive". However, it took more than 80 years until Albert Einstein's famous papers published in Annalen der Physik in 1905, a full understanding of this phenomenon, *Brownian motion*, was developed. Einstein argued that the motion must be induced by the bombardment of the water molecules due to their "motions of heat". He not only qualitatively explained Brownian motion but also correctly predicted that such tiny molecular motion induced jiggling of a bigger particle should be easily observable under a microscope. What is striking is that the underlying "invisible" molecules and atoms, though being millions of times lighter that a pollen grain lead to a clearly observable phenomenon in the macroscopic world. It wouldn't be overly dramatic to say that the underlying quantum mechanical motion of particles manifest themselves in the classical world through Brownian motion.

With the classical Brownian motion in the background, let us come back to the vison, something way smaller and more 'quantum' than a pollen grain. In the previous chapter, we learned that the vison has a finite hopping amplitude linear in Γ and magnetic field h in the ferromagnetic Kitaev model. Thus in a generic (perturbed) Kitaev liquid, one should typically expect the visons to be mobile. However, the vison is not alone, it is *dressed* by the background Majorana fermions which have a gapless energy spectrum. This may sound rather dangerous since the motion of such a strong singular scatterer, vison, may potentially excite or scatter strongly from the gapless Majoranas at finite temperature. The situation is slightly different in an AFM model. The hopping vanishes at linear order due to a destructive interference effect. Therefore, we expect motion only at higher orders in perturbations simply due to the fact that the vison conservation law is broken. But here again, there is the possibility that the surrounding gapless Majorana bath may scatter off the vison imparting it some momentum, much like the pollen grain in water. Therefore, it is important to understand the effects arising from dissipation and fluctuations due to the surrounding gapless matter fermions (i) to determine if the vison is actually a well defined and coherent quasiparticle and (ii) fully characterize the finite temperature dynamics. In this chapter, we answer these questions quantitatively by computing the mobility μ_v, or equivalently, the diffusion constant D_v, of a vison.

Mobility of a particle characterizes its response to an applied force $\boldsymbol{F}$ through the following relation

$$\langle \boldsymbol{v} \rangle = \mu \boldsymbol{F}. \tag{5.1}$$

where v is the velocity of the particle, and the $\langle . \rangle$ imply averaging with respect to the distribution function. The diffusion constant is related to mobility through the Einstein relation

$$D = \mu k_B T. \tag{5.2}$$

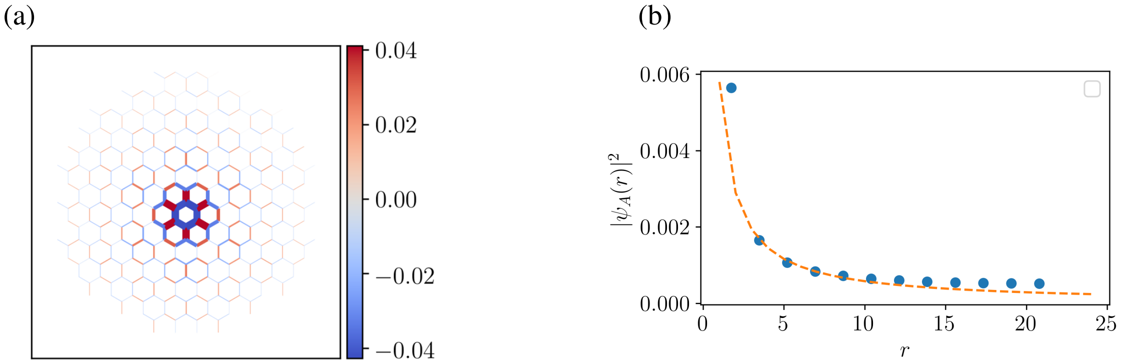

Fig. 5.1 **Visualizing a vison.** (a.) Distortion in the spin-spin correlations $\langle \sigma^\alpha \sigma^\alpha \rangle_v - \langle \sigma^\alpha \sigma^\alpha \rangle_0$, induced by a static vison located at the center. Thickness of the links represents the magnitude of the distortion. Subscript v indicates that expectation value is calculated with respect to the ground state with a vison at the origin. (b.) In the gapless phase, a vison induces a quasilocalized mode with a weakly diverging wavefunction near the center $\psi(r) \sim r^{-\frac{1}{2}}$. Probability amplitude of the sub-lattice A component of this mode is plotted and fit to a power law $\sim r^{-1}$ (dashed line).

5.2 Vison-Majorana Scattering

Before we dive into the calculation of mobility, let us remind ourselves how a vison scatters the surrounding Majorana fermions. We will use the low energy Dirac Hamiltonian to formulate this question as a standard scattering problem. Majorana fermions see a single vison as a source of π flux, much like an electron going around a solenoid. In the long wavelength continuum limit, a vison can therefore be approximated as a point vortex located at the origin. This readily maps the scattering problem to the famous Aharonov-Bohm effect, but for gapless Dirac particles. Due to the underlying gauge theory, we have the freedom to choose a convenient gauge to describe the 'vector potential' field of the vison. We find that it is most convenient to work in a singular gauge where the vison imposes an anti-periodic boundary condition on the free Majorana wavefunctions. Since the effect of scattering has been encoded into the wavefunction boundary conditions, we can make use of the circular symmetry of the free Dirac Hamiltonian, and solve it using polar coordinates (r, θ), choosing the vison position as origin:

$$\tilde{H}_{\boldsymbol{K}} = v_m \begin{pmatrix} 0 & ie^{i\theta}\left(\partial_r + \frac{i}{r}\partial_\theta\right) \\ ie^{-i\theta}\left(\partial_r - \frac{i}{r}\partial_\theta\right) & 0 \end{pmatrix}. \tag{5.3}$$

The wavefunctions can be obtained in the angular momentum basis, resulting in Bessel functions $J_l(kr)$ of half-integer orders:

$$\phi_{s,l,k}(r) = \begin{cases} \sqrt{\frac{k}{4\pi}} \begin{pmatrix} \sqrt{s}\, J_{-l+\frac{1}{2}}(kr) e^{i(l-\frac{1}{2})\theta} \\ -\sqrt{s}\, i\, J_{-l-\frac{1}{2}}(kr) e^{i(l+\frac{1}{2})\theta} \end{pmatrix}, & l \leq 0 \\ \sqrt{\frac{k}{4\pi}} \begin{pmatrix} \sqrt{s}\, J_{l-\frac{1}{2}}(kr) e^{i(l-\frac{1}{2})\theta} \\ \sqrt{s}\, i\, J_{l+\frac{1}{2}}(kr) e^{i(l+\frac{1}{2})\theta} \end{pmatrix}, & l > 0 \end{cases}, \tag{5.4}$$

where $s = \pm 1$ labels the positive and negative energy states respectively The case of $l = 0$ is special. The wave function weakly diverges at the origin as $r^{-\frac{1}{2}}$ and thus is a quasi-localized state[100, 101]. This wavefunction is plotted in Fig. 5.1b, obtained for a finite sized system.

The well-known scattering cross-section can then be obtained as (See Appendix C, Ref.[102] and [103] for details.)

Scattering cross-section

$$\frac{d\sigma}{d\varphi} = \frac{1}{2\pi k \sin^2 \varphi}, \qquad \varphi \neq 0, \tag{5.5}$$

where φ is the angle between incoming and outgoing wave vectors. This rather familiar result is peculiar due to its momentum dependence; the cross-section diverges for small momenta, $k \to 0$, as well as for forward-scattering ($\phi = 0$). This singular scattering cross-section reflects the long ranged nature of the vison. In fact, if one chooses a uniform circularly symmetric gauge to express the flux of a vison, the vector potential would have a $\frac{1}{r}$ dependence. This divergent cross-section is what makes a vison qualitatively different from usual heavy particles we encounter in standard impurity problems, treated as point scatterers [104].

5.3 Semi-classical Boltzmann Approach

The standard way to calculate the mobility of a heavy particle in a gapless bath is to derive its effective action by integrating out the bath [105, 106]. This procedure is however complicated in our case due to the singular nature of Majorana-vison scattering and the underlying gauge theory (projection is necessary). Instead, we use the insight that a vison is much heavier (or slower) than the linearly dispersing Majoranas, in the limit of weak perturbations. At a given temperature $T \ll K$, the typical momentum transfer from Majoranas to a vison is given by $|\Delta \boldsymbol{p}| \sim T/v_m$. the typical momentum of a vison near its band bottom is given by $p_v \sim \sqrt{T/W_v} \gg |\Delta \boldsymbol{p}|$. Therefore the momentum transfer from a single scattering event will be much smaller compared to the typical momentum of the vison. This key insight helps us to reformulate the problem in terms of a diffusion in momentum space. As we shall see, this approach provides a much more intuitive understanding and better analytical control.

Before we begin, it is important to examine the validity of a semi-classical approach for a phase of matter that is ‘as quantum as’ one could get. For this, we must compare the mean free path of a vison, l_v, with its wavelength, λ_v. In the limit of a slowly moving vison, we can use the relation $l_v \sigma n_m = 1$ (this basically is the definition of the scattering cross-section), where $\sigma \sim 1/k \sim 1/T$ is the scattering cross section, and $n_m \sim T^2$ is the density of thermally excited Majoranas. This gives the scaling of the mean free path to be $l_v \sim 1/T$. The wavelength of a slowly moving vison with a quadratic band bottom scales as $\lambda_v \sim 1/\sqrt{T}$. Since we are working at temperatures smaller than the vison gap (so that vison-vison and Majorana-Majorana interactions can be neglected), $l_v \gg \lambda_v$. Hence our semi-classical approach is justified in the low T limit.

Consider the momentum distribution function of a vison $f_{\boldsymbol{p}} = f^0_{\boldsymbol{p}} + \delta f_{\boldsymbol{p}}$, where $f^0_{\boldsymbol{p}} = ce^{-\beta E^v_{\boldsymbol{p}}}$ is the equilibrium Boltzmann distribution and $\delta f_{\boldsymbol{p}}$ encodes the small deviations induced by scattering processes. c is the normalization constant that will cancel out in the final result. Denoting the total force acting on the vison by $\boldsymbol{F}$, the distribution function obeys the linearized Boltzmann equation

$$\boldsymbol{v}\cdot\boldsymbol{F}\frac{\partial f^0_{\boldsymbol{p}}}{\partial E^v_{\boldsymbol{p}}} = \left(\frac{\partial f_{\boldsymbol{p}}}{\partial t}\right)_{scat} = \int \tilde{M}_{\boldsymbol{p}\boldsymbol{p}'}\delta f_{\boldsymbol{p}'}\frac{d^2p'}{4\pi^2}, \tag{5.6}$$

where $\boldsymbol{v} = \frac{\partial E^v_{\boldsymbol{p}}}{\partial \boldsymbol{p}}$ is the velocity of the vison obtained from its band structure, $\tilde{M}_{\boldsymbol{p}\boldsymbol{p}'}$ is the scattering rate from momentum $\boldsymbol{p}$ to $\boldsymbol{p}'$. $\tilde{M}_{\boldsymbol{p}\boldsymbol{p}'}$ can be obtained from the microscopic transition rates $W_{\boldsymbol{k},\boldsymbol{k}'}$ that describe the scattering of Majorana fermions from the vison:

$$M_{\boldsymbol{p},\boldsymbol{p}'} = \int \frac{d^2k}{(2\pi)^2}\frac{d^2k'}{(2\pi)^2}W^{\boldsymbol{p}}_{\boldsymbol{k},\boldsymbol{k}'}\, n^0_k(1-n^0_{k'})\delta(\boldsymbol{k}+\boldsymbol{p}-\boldsymbol{k}'-\boldsymbol{p}')\delta(\varepsilon_{\boldsymbol{k}}+E^v_{\boldsymbol{p}'}-\varepsilon_{\boldsymbol{k}'}-E^v_{\boldsymbol{p}}), \tag{5.7}$$

with $\tilde{M}_{\boldsymbol{p}\boldsymbol{p}'} = M_{\boldsymbol{p}\boldsymbol{p}'} - \delta(\boldsymbol{p}-\boldsymbol{p}')\int M_{\boldsymbol{p}'\boldsymbol{p}}d^2p'$, where the second term describes the out-scattering from $\boldsymbol{p}$ to an arbitrary momentum $\boldsymbol{p}'$. Here, by using the Fermi distribution $n^0_{\boldsymbol{k}}$, we have implicitly assumed that the Majoranas which are the *fast* degrees of freedom thermalize much faster than the slow moving visons. The energy dispersion of the Majorana fermions is given by $\varepsilon_{\boldsymbol{k}} = v_k k$.

We can now expand the distribution function as $\delta f_{\boldsymbol{p}} = (\partial f_0/\partial E^v_{\boldsymbol{p}})\phi_{\boldsymbol{p}}$, where $\phi_{\boldsymbol{p}}$ is a slowly varying function in momentum $\boldsymbol{p}$ and obtain.

$$\boldsymbol{F}\cdot\boldsymbol{v}^v_{\boldsymbol{p}} = \int \tilde{M}_{\boldsymbol{p}\boldsymbol{p}'}e^{\beta(E^v_{\boldsymbol{p}}-E^v_{\boldsymbol{p}'})}\phi_{\boldsymbol{p}'}\frac{d^2p'}{(2\pi)^2} \tag{5.8}$$

This expression is still no easy task to solve. However, we notice that when the perturbations are weak, the vison is a slow (or heavy) particle. For example, in the case of a Γ perturbation, vison mass M_v and its velocity $\boldsymbol{v}_{\boldsymbol{k}}$ follows $1/M_v, \boldsymbol{v}_{\boldsymbol{k}} \propto \Gamma$ for an FM Kitaev model and $1/M_v, \boldsymbol{v}_{\boldsymbol{k}} \sim \Gamma^2$ for an AFM model. The momentum transfer Δp from massless Majoranas to the vison is small at low T, $\Delta p = |\boldsymbol{p} - \boldsymbol{p}'| \sim k_B T / v_m$. Therefore, we can Taylor expand the above equation to leading order in Δp to obtain

$$\boldsymbol{v}^{v}_{\boldsymbol{p}} \cdot \boldsymbol{F} \approx \int \tilde{M}_{\boldsymbol{p}\boldsymbol{p}'} e^{-\beta \boldsymbol{v}^{v}_{\boldsymbol{p}} \cdot (\boldsymbol{p}' - \boldsymbol{p})} \left(\phi_{\boldsymbol{p}} + (\boldsymbol{p}' - \boldsymbol{p}) \cdot \nabla_{\boldsymbol{p}} \phi_{\boldsymbol{p}} \quad + \frac{(p'_i - p_i)(p'_j - p_j)}{2} \partial_{p_i} \partial_{p_j} \phi_{\boldsymbol{p}} \right) \frac{d^2 p'}{(2\pi)^2}. \tag{5.9}$$

Since we consider a single isolated vison, we have particle conservation built in, which implies $\int \tilde{M}_{\boldsymbol{p},\boldsymbol{p}'} \phi_{\boldsymbol{p}} \frac{d^2 p}{4\pi^2} = 0$. Total momentum conservation forces the second term to vanish in the limit of small vison velocity, $v_{\boldsymbol{p}} \to 0$. Thus, we need to expand the exponential to linear order in $v_{\boldsymbol{p}}$.

Carrying out the expansion to leading order, we arrive at the expression

$$\partial_t \phi_{\boldsymbol{p}} + \boldsymbol{v}^{v}_{\boldsymbol{p}} \cdot \boldsymbol{F} \approx D_p \nabla^2_{\boldsymbol{p}} \phi_{\boldsymbol{p}} + \gamma \boldsymbol{v}^{v}_{\boldsymbol{p}} \cdot \boldsymbol{\nabla}_{\boldsymbol{p}} \phi_{\boldsymbol{p}}, \tag{5.10}$$

where we have defined a diffusion constant in momentum space $D_{\boldsymbol{p}}$ and a constant γ, anticipating friction, as it couples to the velocity. Although it is possible to derive the temperature dependence of $D_{\boldsymbol{p}}$ and γ, it turns out their ratio follows directly from demanding particle number conservation for arbitrary $\phi_{\boldsymbol{p}}$.

In thermal equilibrium and the absence of an external force, particle conservation demands,

$$D_p \nabla^2_{\boldsymbol{p}} \phi_{\boldsymbol{p}} + \gamma \boldsymbol{v}^{v}_{\boldsymbol{p}} \cdot \boldsymbol{\nabla}_{\boldsymbol{p}} \phi_{\boldsymbol{p}} = 0. \tag{5.11}$$

Multiplying the equation with $f^0_{\boldsymbol{p}}$ and integrating by parts results in the following equality for arbitrary $\phi_{\boldsymbol{p}}$.

$$\int D_p \, (\nabla_{\boldsymbol{p}} f^0_{\boldsymbol{p}}) \, (\nabla_{\boldsymbol{p}} \phi_{\boldsymbol{p}}) \, d\boldsymbol{p} = -\gamma \int f^0_{\boldsymbol{p}} \boldsymbol{v}_{\boldsymbol{p}} \cdot \nabla \phi_{\boldsymbol{p}} d\boldsymbol{p}. \tag{5.12}$$

Using $\nabla_{\boldsymbol{p}} f^0_{\boldsymbol{p}} = \frac{\partial f^0_{\boldsymbol{p}}}{\partial E^{v}_{\boldsymbol{p}}} \cdot v_{\boldsymbol{p}}$ and $\frac{\partial f^0_{\boldsymbol{p}}}{\partial E^{v}_{\boldsymbol{p}}} = -\beta f^0_{\boldsymbol{p}}$, we obtain,

$$\gamma = -\frac{D_p}{T}. \tag{5.13}$$

This simple relation is one of the many forms in which the fluctuation-dissipation theorem, one of the most fundamental equations in statistical physics, shows up in the dynamics of particles coupled to a bath: in thermal equilibrium, noise necessarily accompanies dissipation.

With this, Eq. (5.10) transforms into the following drift-diffusion equation

Drift-Diffusion Equation

$$\partial_t \phi_{\boldsymbol{p}} + \boldsymbol{v}^{v}_{\boldsymbol{p}} \cdot \boldsymbol{F} \approx D_p \left(\nabla^2_{\boldsymbol{p}} \phi_{\boldsymbol{p}} - \frac{1}{T} \boldsymbol{v}^{v}_{\boldsymbol{p}} \cdot \boldsymbol{\nabla}_{\boldsymbol{p}} \phi_{\boldsymbol{p}} \right), \tag{5.14}$$

Let us take a moment to appreciate the above equation and recall the proverbial pollen grain. For readers who have been exposed to basic statistical physics, this equation may look familiar. Physically, it describes the venerable Brownian motion. The scattering from massless Majoranas not only acts as a source of noise, resulting in diffusion but also generates a frictional force proportional to $-\boldsymbol{v}_{\boldsymbol{p}}$ for the vison.

5.3.1 Diffusion constant in momentum space

The reader may wonder if we have lost all the 'quantumness' in the problem and derived a fully classical Brownian motion. This is not true; D_p holds information about the underlying quantum processes - scattering from gapless Majoranas. It is by definition, independent of the vison dispersion, as clear from Eq. (5.9). The transition rates $W_{\boldsymbol{k},\boldsymbol{k}'}$ and the differential scattering cross section are directly related as [107]

$$\frac{d^2p'}{(2\pi)^2}\frac{d^2k'}{(2\pi)^2} W_{\boldsymbol{k},\boldsymbol{k}'} (2\pi)^2 \delta(\boldsymbol{k} + \boldsymbol{p} - \boldsymbol{k}' - \boldsymbol{p}') 2\pi \delta(\varepsilon_{\boldsymbol{k}} - \varepsilon_{\boldsymbol{k}'}) \approx v_m d\theta_{\boldsymbol{k},\boldsymbol{k}'} \frac{d\sigma(k, \theta_{\boldsymbol{k},\boldsymbol{k}'})}{d\theta_{\boldsymbol{k},\boldsymbol{k}'}}. \tag{5.15}$$

Using Eq. (5.5), we obtain

$$D_p = v_m \int \frac{d^2k}{(2\pi)^2} d\theta_{\boldsymbol{k},\boldsymbol{k}'} k^2 \left(1 - \cos\theta_{\boldsymbol{k},\boldsymbol{k}'}\right) \frac{d\sigma(k, \theta_{\boldsymbol{k},\boldsymbol{k}'})}{d\theta_{\boldsymbol{k},\boldsymbol{k}'}} n(\varepsilon_k)(1 - n_{\varepsilon_{k'}}) = \frac{T^3}{6v_m^2}. \tag{5.16}$$

In hindsight, the temperature dependence of D_p could have been be guessed from dimensional arguments alone. The diffusion constant in momentum space is obtained from $D_p \sim (\delta k)^2/\tau$. $\delta k \sim T/v_m$ is the typical momentum transfer and the scattering time τ is obtained from $\sigma v_m \tau n_m \sim 1$. This gives the power law in temperature T^3 as expected from the derivation above. However, obtaining the pre-factor requires an explicit calculation, as detailed in Appendix D.

5.4 Results for Mobility - FM Kitaev

After solving the DDE, Eq. (5.14), for $\phi_{\boldsymbol{p}}$, we can obtain the mobility using Eq. (5.1) and the expression

$$\langle \boldsymbol{v}^{v}_{\boldsymbol{p}} \rangle = \frac{1}{N_v} \int \frac{d^2p}{(2\pi)^2} \boldsymbol{v}^{v}_{\boldsymbol{p}} \frac{\partial f_0}{\partial E^{v}_{\boldsymbol{p}}} \phi_{\boldsymbol{p}},$$

with normalization $N_v = \int f^0_{\boldsymbol{p}} \frac{d^2p}{(2\pi)^2}$.

First, we present results for the case where the vison dynamics is induced by the Γ term in a ferromagnetic (FM) Kitaev model. Recalling the dispersion relation from Chapter 4,

$$E^{v}(\boldsymbol{p}) \approx -1.45\Gamma \sum_{i=1}^{6} \cos\left(\boldsymbol{p}\cdot\boldsymbol{\delta}^{nnn}_{i}\right) \tag{5.17}$$

where $\boldsymbol{\delta}^{nnn}_{i}$ denotes the next-nearest-neighbour lattice vectors of the triangular lattice.

5.4.1 Low T limit: Universal mobility

Due to the inverse temperature dependence of the drift term, we can solve the DDE analytically in both $T \ll W_v$ and $T \gg W_v$ limits, where $W_v \approx 10|\Gamma|$ is the vison bandwidth. In the low-T limit, the drift term dominates and the solution is easily obtained as

$$\phi_{\boldsymbol{p}} \approx -\frac{T}{D_p} \boldsymbol{F}\cdot\boldsymbol{p}, \tag{5.18}$$

which leads us to the result

Universal mobility

$$\mu(T) \approx \frac{T}{D_p} = \frac{6v_m^2}{T^2}, \qquad \text{for} \qquad T \ll W_v. \tag{5.19}$$

This is a remarkable result due to the following reasons. (i) Mobility diverges in the limit $T \to 0$ which implies that, despite the presence of a gapless fermions that scatter strongly, the vison is a coherent particle in the zero temperature limit. (ii) The mobility and thus the diffusion constant are completely independent of the perturbation which caused it to move in the first place (Γ, in this case). The mobility at low temperatures is a fully universal quantity. Therefore, in a generic Kitaev spin liquid, the dynamics of single visons is universal at low-T as long as the non-Kitaev terms are small. The origin of this effect can be traced back to the scale invariance property of Dirac fermions and the universal cross-section from flux scattering. It is worth noting that similar results exists for vortices in d-wave superconductors with different pre-factors. However, for such systems, long range Coloumb interactions and Goldstone modes add non-trivial corrections.

5.4.2 High T limit

At temperatures larger than the bandwidth $W_v \sim \Gamma$, we can neglect the drift term and obtain the solution to the DDE by twice integrating over the momentum.

$$\phi_{\boldsymbol{p}} \approx F \int \frac{d\boldsymbol{p}}{(2\pi)^2} \frac{E^v_{\boldsymbol{p}}}{D_p}. \tag{5.20}$$

Carrying out the integration and imposing periodic boundary conditions lead to the high temperature mobility of the form

High T mobility

$$\mu(T) \approx \frac{3\, t_\Gamma^2 D_p}{T} = \frac{18\, t_\Gamma^2 v_m^2}{T^4}, \qquad \text{for} \qquad T \gg W_v., \tag{5.21}$$

where $t_\Gamma \approx -1.45\Gamma$ is the previously calculated hopping amplitude of the vison. In this high-T regime, the vison has a strongly suppressed mobility due to the strong scattering from Majorana fermions.

5.4.3 Numerical Solution to DDE

Having extracted the asymptotically exact mobilities analytically, we can solve the DDE numerically over the whole temperature range. Due to the momentum dependence of the drift term, we solve the equation by first Fourier transforming to the position space, and then inverse the kernel to obtain $\phi_{\boldsymbol{p}}$. The details are relegated to Appendix D. The resulting mobility $\mu(T)$ is plotted in Fig. 5.2 as a function of temperature.

Although, for concreteness, we focused on the dynamics induced by a Γ term for $K < 0$, the same universal low T mobility and high T power law are expected as long as (i) the vison bandwidth is small compared to the Majorana bandwidth, (ii) their dispersion is quadratic at the bottom of the band, and (iii) the Majorana dispersion can be described by a Dirac equation. Thus, in the case of magnetic field, the formula for the mobility is only valid for temperatures large compared to the field induced gap in the Majorana spectrum.

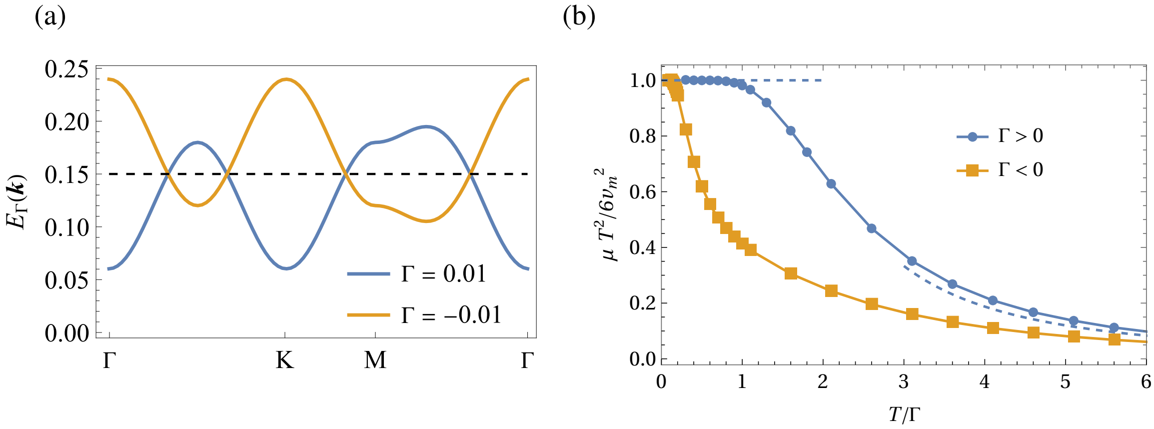

Fig. 5.2 **Mobility of a vison: FM Kitaev** (a.) Band dispersions of a vison in the ferromagnetic Kitaev model perturbed by a Γ term. (b.) Vison mobility $\mu(T)$, normalized to its low-T universal value $(6v_m^2/T^2)$, plotted as function of $T/|\Gamma|$ both for $\Gamma > 0$ and $\Gamma < 0$. Deviations from the universal low-T mobility are more pronounced for $\Gamma < 0$ at low T due to flat regions in the band structure close to the band minimum as shown in (a). The dashed lines indicate the low-T and high-T asymptotic power-laws, see Eq. (5.19).

5.5 Majorana-assisted Dynamics

Above, we saw how a coherently propagating vison becomes diffusive and is dampened by friction, due to scattering from thermal Majoranas; mobility μ decreases with temperature. In an anti-ferromagnetic Kitaev model, vison hopping is fully suppressed at linear order in Γ and magnetic field h (in the limit $\kappa \to 0$), due to interference effects (Recall Chapter 3.). Coherent hopping is only possible at second or higher orders in perturbation theory. However, scattering from Majoranas can disturb this perfect destructive interference and help the vison move. However, this will be a result of random scattering events that are thermally averaged and thus, incoherent. Such a hopping rate will typically increase with temperature as there are more Majoranas to scatter from at higher temperatures. Such processes should be taken into account when discussing vison dynamics in the AFM Kitaev model, as they can occur at second order in Γ or h, as we will describe now. We use a combination of analytical limits and low-energy approximations to compute this incoherent, *Majorana assisted* hopping rate in the low-T limit.

The incoherent hopping rate of a vison from position $\boldsymbol{R}_b$ to $\boldsymbol{R}_a$ is given by Fermi's golden rule formula when the perturbation ΔH is weak:

$$W^{ab}(T) = 2\pi \sum_n |\langle \boldsymbol{R}_a, m|\, \Delta H\, |\boldsymbol{R}_b, n\rangle|^2 \delta(E_m - E_n). \tag{5.22}$$

Here, $|\boldsymbol{R}_a, n\rangle$ denotes the many-particle eigenstates of Majorana fermion system labelled by n with energy E_n, in the presence of a single vison at $\boldsymbol{R}_a$. The golden rule formula thus describes a vison hopping between two sites by elastically scattering off Majorana fermions.

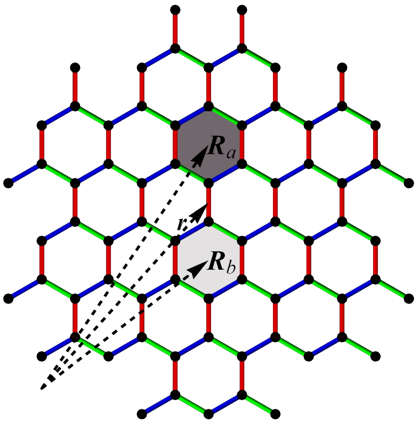

Fig. 5.3 **Majorana assisted hopping of visons.** Due to scattering from thermally excited Majoranas, a vison incoherently hops from $\boldsymbol{R}_a$ to $\boldsymbol{R}_b$ in the presence of a Γ term.

Let us, for concreteness, consider the Γ term, $\Delta H = \Delta H_\Gamma = \Gamma(\sigma^x_{\boldsymbol{r},A}\sigma^y_{\boldsymbol{r},B} + \sigma^y_{\boldsymbol{r},A}\sigma^x_{\boldsymbol{r},B})$, with $\boldsymbol{r}$ being the coordinate of the center of the z-bond. This term induces hopping of a vison along a z bond as shown in the Fig. 5.3. Note that in the AFM Kitaev model, this matrix element between ground states vanishes due the interference effect. Expanding ΔH_Γ in terms of the gauge and matter fermions gives us

$$\Delta H_\Gamma = \Gamma\left[b^x_{\boldsymbol{r},A} b^y_{\boldsymbol{r},B}\left(c^A_{\boldsymbol{r}} - ic^B_{\boldsymbol{r}}\right)\left(c^A_{\boldsymbol{r}} + ic^B_{\boldsymbol{r}}\right)\right], \tag{5.23}$$

where we fixed the gauge variables $ib^z_{\boldsymbol{r},A} b^z_{\boldsymbol{r},B} = 1$ for the two single-vison states. The b-fermions only affect the gauge fields and realize hopping of the bare vison and can thus be contracted in the matrix element calculation as shown in Chapter 3. We end up with matrix elements that involve only the matter Majoranas, thereby reducing our task to that of calculating the following matrix element, for arbitrary excited states m and n.

$$\tilde{w}^{ab}(m;n) = \langle M_n(\boldsymbol{R}_a)|\left(c^A_{\boldsymbol{r}} - ic^B_{\boldsymbol{r}}\right)\left(c^A_{\boldsymbol{r}} + ic^B_{\boldsymbol{r}}\right)|M_m(\boldsymbol{R}_b)\rangle\,. \tag{5.24}$$

The states appearing above can, in principle, have arbitrary number of Majorana excitations which makes it hard to gain any analytical control. However, as we are only interested in the low T limit, $\frac{T}{K} \ll 1$, we can use the fact that the Majorana density of states vanishes in the $T \to 0$ limit. This enables us to restrict the initial and final states to those with a single Majorana mode above the ground state. States with higher number of Majoranas will contribute to the hopping rate at sub-leading orders in temperature. Furthermore, the low energy Dirac equation and its exact solutions obtained in Eq.(5.4) allow us to make significant analytical progress.

We begin by rewriting the Majorana operators in terms of the continuum fields $\psi(\boldsymbol{r})$ that vary smoothly in the scale of lattice constant:

$$c^A_{\boldsymbol{r}} = \int d^2 r' \lambda(\boldsymbol{r}') e^{\pm i \frac{\pi}{4}} \psi_A(\boldsymbol{r}' + \boldsymbol{r}) + h.c. \tag{5.25}$$

$\lambda(\boldsymbol{r})$ is similar in spirit to a Wannier function, defining an effective cut-off of the low-energy theory. The unit cell position is parametrized by $\boldsymbol{r} = \boldsymbol{R}_a + \boldsymbol{\delta} = \boldsymbol{R}_b - \boldsymbol{\delta}$, which means that the vison hops by the vector $2\boldsymbol{\delta}$, as shown in Fig. 5.3. In the next step, we expand the field operators in terms of the eigenmodes as follows

$$\begin{aligned} &\psi_{A/B}(\boldsymbol{r} - \boldsymbol{R}_a) = \\ &\qquad \sum_l \int \frac{dk}{2\pi} \sqrt{\pi k} \left(a_{+,k,l} - i a_{-,k,l}\right) \left(f^{A/B}_{l,k}(\boldsymbol{r} - \boldsymbol{R}_a)\right)^* . \end{aligned} \tag{5.26}$$

The single-particle excited states are labelled by $n = \{s, l, k\}$ where quantum number $s = \pm$ labels particle/hole, $l \in \mathbb{Z}$ the angular momentum, and energy $\varepsilon(k) = \pm v_m k$. Here $a_{+,k,l}(a_{-,k,l})$ denote the eigenmodes with $\varepsilon_k > 0$ ($\varepsilon_k < 0$) and

$$\begin{aligned} f^A_{l,k}(\boldsymbol{r}) &= \begin{cases} J_{-l+\frac{1}{2}}(kr) e^{(l-\frac{1}{2})\theta} e^{i\boldsymbol{K}\cdot\boldsymbol{r}} & l \le 0 \\ J_{l-\frac{1}{2}}(kr) e^{(l-\frac{1}{2})\theta} e^{i\boldsymbol{K}\cdot\boldsymbol{r}} & l > 0, \end{cases} \\ f^B_{l,k}(\boldsymbol{r}) &= \begin{cases} J_{-l-\frac{1}{2}}(kr) e^{(l+\frac{1}{2})\theta} e^{i\boldsymbol{K}\cdot\boldsymbol{r}} & l \le 0 \\ J_{l+\frac{1}{2}}(kr) e^{(l+\frac{1}{2})\theta} e^{i\boldsymbol{K}\cdot\boldsymbol{r}} & l > 0. \end{cases} \end{aligned} \tag{5.27}$$

Note that the low-energy wavefunctions are half-integer Bessel functions naturally arising in fractional vortex-scattering problems, leading to interesting power laws [103, 106]. The excitations above the ground state (all negative energy states filled), are described by particle and hole operators which can be easily defined as

$$A^\dagger_+ \equiv a^\dagger_+, \quad A^\dagger_- \equiv a_- \quad \text{with} \quad A_\pm |M_0(\boldsymbol{R}_a)\rangle = 0. \tag{5.28}$$

Similarly, we denote by B the corresponding operators using scattering states with a vison centered at position $\boldsymbol{R}_b$.

Expanding the matrix element, Eq. (5.24), results in a sum of various scattering events described terms of the form $\sim A^\dagger B$, $AB^\dagger$, $A^\dagger B^\dagger$ and AB. The matrix element therefore involves computing overlaps of two-particle states which is quite cumbersome. However, looking closely we realize that terms of the form $A^\dagger B$ describe processes where both initial and final states contain a single excited Majorana particle and would contribute at the leading order in temperature. In contrast, the term $AB^\dagger$, for example, acting on initial and final states with single excitations results in the overlap of vison states with two excitations each. These terms therefore only contribute at higher orders in temperature which becomes clear from the calculations in Appendix E. We therefore focus on the $A^\dagger B$ term which admits a straightforward (but still tedious) analytical calculation shown in its full details in Appendix E. Here, I will outline the main steps required to arrive at the final result.

Starting from an initial state $n_0 = \{s_0, k_0, l_0\}$, the transition rate is obtained by summing over all the final states under the constraint of energy conservation

$$\tilde{W}^{ab}(s_0,k_0,l_0) \approx \Gamma^2 \left|\langle M_0(\boldsymbol{R}_a)|M_0(\boldsymbol{R}_b)\rangle\right|^2 \left(S_{s_0+}(k_0,l_0) + S_{s_0-}(k_0,l_0)\right), \tag{5.29}$$

where the overlap of the ground-state wave functions $\langle M_0(\boldsymbol{R}_a)|M_0(\boldsymbol{R}_b)\rangle$ is calculated numerically for finite size systems and extrapolated to the thermodynamics limit. We use the shorthand notation $S_{s_0\pm}(k_0,l_0)$ to denote the overlap of singly excited states. For example, for a particle excitation in the initial state labelled by $s_0 = +$, we obtain

$$\begin{aligned} S_{++}(k_0,l_0) = \frac{2\pi}{v_m}\sum_l \int \frac{dk}{2\pi}\Bigg|\sum_{l_1,l_2}\int d^2r_1 d^2r_2 \lambda(\boldsymbol{r}_1-\boldsymbol{\delta})\lambda(\boldsymbol{r}_2+\boldsymbol{\delta})\times \\ \int \frac{dk_1 dk_2}{(2\pi)^2}\pi\sqrt{k_1k_2}\left[\eta^+_{k_1,l_1}(\boldsymbol{r}_1)\eta^{-*}_{l_2,k_2}(\boldsymbol{r}_2)\right](2\pi)^2\delta(k_0-k_1)\delta(k-k_2)\delta_{l_0,l_1}\delta_{l,l_2}\Bigg|^2 \delta(k_0-k), \end{aligned}$$

where we further introduce the notations

$$\eta^{\pm *}_{k,l}(\boldsymbol{r}) = e^{i\frac{\pi}{4}} f^{A*}_{k,l}(\boldsymbol{r}) \pm e^{-i\frac{\pi}{4}} f^{B*}_{k,l}(\boldsymbol{r}). \tag{5.30}$$

S_{+-} are obtained by simply replacing η^- by η^+ in Eq. (5.30). As we saw in Eq. (5.27), $f^{A/B}_{k,l}(\boldsymbol{r})$ are essentially half-integer Bessel functions. The localized Wannier functions $\lambda(\boldsymbol{r})$ can be approximated by delta functions in the long wavelength limit.

Next, we make a crucial observation that the dominant contribution to Eq. (5.30) arises from the angular momentum $l = 0$ since in the low momentum limit $k_0\delta \ll 1$, $f^B_{l,k_0}(r) \sim (k_0 r)^{-l-\frac{1}{2}}$. This leads to the leading contribution to $\tilde{W}^{ab}$ given by

$$S_{ss'}(k_0,l_0) \approx \frac{\Omega_0^2\pi^2}{v_m} k_0^2 \left(k_0\delta + \frac{1}{k_0\delta}\right)^2, \tag{5.31}$$

where $\Omega_0 = a^2/2$ is area of the real space unit cell. The total incoherent hopping rate as a function of temperature can be then obtained using the Fermi distribution $n^0_{k_0,l_0}$ to sum over all initial states.

$$W^{ab}(T) \approx \int \frac{dk_0}{2\pi} \sum_{s_0=\pm,\, l_0} n_{k_0,l_0} \tilde{W}^{ab}(s_0,k_0,l_0) \approx \Gamma^2 \pi^3 \left(\frac{0.17\, a^2 k_B T}{32\, v_m^2} + \frac{3.04\, a^4 (k_B T)^3}{16\, v_m^4} \right) + \mathscr{O}(T^5). \tag{5.32}$$

The leading term is linear in T and the sub-leading corrections arise at order T^3.

To obtain the diffusion constant, we assume a random walk of the vison on the triangular lattice with a hopping rate $W^{ab}(T)$. This leads to a diffusion constant linear in T and a temperature independent mobility.

Majorana-Assisted Hopping (AFM Kitaev)

$$\mu(T) = \frac{D(T)}{T} \sim \frac{\Gamma^2 a^2}{v_m^2}, \qquad \text{for} \qquad K \gg T \gg \sqrt{\Gamma K}. \tag{5.33}$$

Let us now examine the temperature range of validity of the above result. Although the hopping amplitude of a vison in the AFM model vanishes at linear order in Γ, coherent hopping can occur at higher orders. Assuming that the vison gets a dispersion at second order in Γ, with a bandwidth $W_v^{(2)} \sim \Gamma^2/K$, in the $T \to 0$ limit, we are back in the universal mobility regime, as in the FM model (Eq. (5.19)). Therefore, to estimate the temperature range where the assisted hopping dominates, we must compare the high-T mobility in Eq. (5.19) and Eq. (5.33). Thus, we obtain the crossover temperature $T^* \approx \sqrt{\Gamma K}$, the lower bound in Eq. (5.33). The upper bound is the vison gap $\sim K$, in order to ensure that we are in the dilute vison limit, as usual.

5.6 Summary and Discussion

Friction is a universal phenomenon, and its microscopic description typically relies on coupling to a gapless bath, that disturbs the moving particle's coherence. In this chapter, we described how scattering from thermally excited Majorana fermions leads to frictional forces on the vison, endowing it with a finite mobility $\mu(T)$. We expect this to be a rather general phenomenon in gauge theories with gapless matter. In the limit of weak perturbations (equivalently, heavy vison limit), we analytically obtained the exact temperature dependence of its mobility. In the limit of weak perturbations, using that the visons are much heavier than the Majoranas, we were able to formulate the dynamics as a drift-diffusion process in momentum space. Remarkably, when temperature T is much smaller than the vison bandwidth, the mobility is fully universal and is entirely determined by the Kitaev interaction strength K. This effect emerges due to a conspiracy between the singular scattering from the gauge flux and the scale invariance property of the low energy Majorana modes. In fact, one can arrive at this universal result by purely

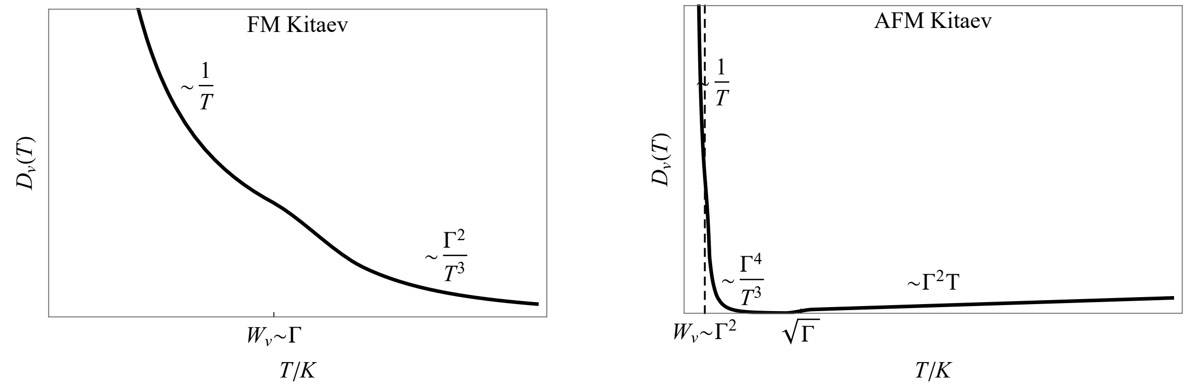

Fig. 5.4 **Temperature evolution of vison mobility in a Kitaev model perturbed by a weak Γ term.** Diffusion constant of a vison depends on the temperature and is sensitive to the sign of the Kitaev coupling $K = \pm 1$. Power laws are indicated (pre-factors are not exact). AFM model has a large temperature regime where Majorana assisted hopping dominates the dynamics. In all cases, vison mobility diverges in the $T \to 0$ limit demonstrating that it is a coherently propagating quasiparticle.

dimensional arguments, where the key input is the scale invariance of a Dirac system. At temperatures larger than the vison bandwidth, a different power-law ($\mu \sim T^{-4}$) takes over, with non-universal pre-factors.

That said, the gapless Majorana fermions are not always a vison's enemies that dampen its motion. Incoherently scattering off Majoranas can give random kicks to a vison that otherwise struggles to move. This effect is more pronounced in the AFM Kitaev model, since coherent vison hopping is strongly suppressed due to interference effects. Although in the $T \to 0$ limit, the mobility is universal, assisted hopping takes over rather quickly in an intermediate temperature range (Eq. 5.33) and results in a T-independent mobility. The low energy quasi-localized modes with wavefunctions $\psi(r) \sim \frac{1}{\sqrt{r}}$ dominate this short range hopping of the visons. In Fig. 5.4, we have sketched the main results of this chapter showing the different qualitative behaviour of the vison diffusion constant in FM and AFM Kitaev models.

What are the implications of our results? One upshot is that, in the gapless phase, visons essentially behave like random walkers with a low-T universal mobility. This determines its transport and equilibration properties. Consider a thermal quench experiment on a pure Kitaev model. From a high energy state with a finite density of visons and Majoranas, the system will relax by quasiparticle collisions and annihilations. The matter Majorana fermions are fast (velocity $\sim K$) whereas the visons are static and hence the system cannot get rid of them. This changes drastically in a generic Kitaev liquid. Visons are now diffusive and can thus collide with each other and annihilate. Given that they are much slower than the Majoranas, the long time relaxation bottleneck is set by the diffusion constant. This follows directly from a simple diffusion-annihilation model of Brownian walkers, where the density of the walkers follow the well known power-law decay [108].

$$n_v(t) \sim \frac{\log(t)}{D_v t} \tag{5.34}$$

Any physical observable that is sensitive to the density of visons will therefore exhibit such a long-time behaviour. For example, in the ferromagnetic Kitaev model under an external magnetic field of strength h, a vison at the band minimum has a kinetic energy of $6t^h \propto h$, carrying a magnetization $6\hbar\frac{dt^h}{dh} \approx 3.6\hbar$, parallel to the external magnetic field which follows from Eq. (4.27). The total magnetization will then be proportional to the density of visons n_v, which could be tracked in real time using optical measurements [109]. A recent pump-probe experiment on $\alpha - \mathrm{RuCl_3}$ has in fact observed excitations two distinct relaxation time scales, above the ordering temperature [110].

Thus in a material hosting the Kitaev spin liquid phase, long time tails in relaxation experiments may be a promising signature to look for. Such experiments have been incredibly successful in proving the existence of emergent magnetic monopoles in spin ice materials. The effect of disorder and pinning on visons should also be taken into account to make realistic predictions, where one may speculate the emergence of glassy dynamics [111], as the pinned visons will require thermal activation to hop. In this case, however, one also has to consider the effect of disorder on the Majorana fermions as well.

Chapter 6

2D to 3D: Multilayer Spin Liquids

A defining aspect of the Kitaev quantum spin liquid is its two-dimensional nature. However, we live in a three-dimensional (3D) world and so do real materials. For example, α-RuCl$_3$ is composed of layers of two-dimensional (2D) honeycomb lattices stacked on top of each other, weakly coupled by van der Waals interaction. Experimentally, there is strong evidence that the interlayer interactions are sizeable and they influence the magnetic properties of the materials [112, 113]. However, this important aspect is often ignored in theoretical considerations. There have been some recent numerical studies on bilayer Kitaev models, that have provided insights into phase transitions induced by the interlayer coupling [114, 115]. The pair tunnelling of Majorana fermions across layers was studied by Werman et al. in Ref.[116]. In a broader context, in Ref. [117], Devakul *et al.* showed that 2D topological phases that exist in layered systems should exhibit a divergence in the ratio of in-plane and out-of-plane resistivity.

Besides its relevance to materials, multilayer topological models have been used to build more exotic *fractonic* phases matter, where the emergent quasi-particles display highly restricted mobility or even complete immobility [118–120]. However, such constructions are often complicated and involve interactions of more than two spins. In an unrelated development, it has been discovered that stacking multiple 2D materials on top of each other can lead to unprecedented control over the electronic and magnetic properties allowing us to tune the through exotic phases including superconductivity and fractionalized phases [121]. Therefore it is both timely and important to investigate the effects of stacking multiple layers on a 2D spin liquid system and its emergent gauge fields.

To make progress, we will consider simple 3D models where Kitaev layers are stacked on top of each other in different stacking arrangements commonly seen in materials, weakly coupled by a Heisenberg interaction. Like any other perturbation, the interlayer coupling makes the static gauge fields of the monolayers dynamic. It is, therefore, natural to ask: (i) What are the low-energy dynamical excitations of the gauge field? (ii) How do they propagate throughout the full 3D system? Even within such a simple construction, rich dynamical behaviours, some of which are reminiscent of exotic fractons [119], emerge from residual conservation laws.

This chapter is based on the article published as npj quantum materials ***9****, 62(2024), co-authored by Achim Rosch. The contents of the chapter closely follow the publication and figures are mainly reproduced from the paper.*

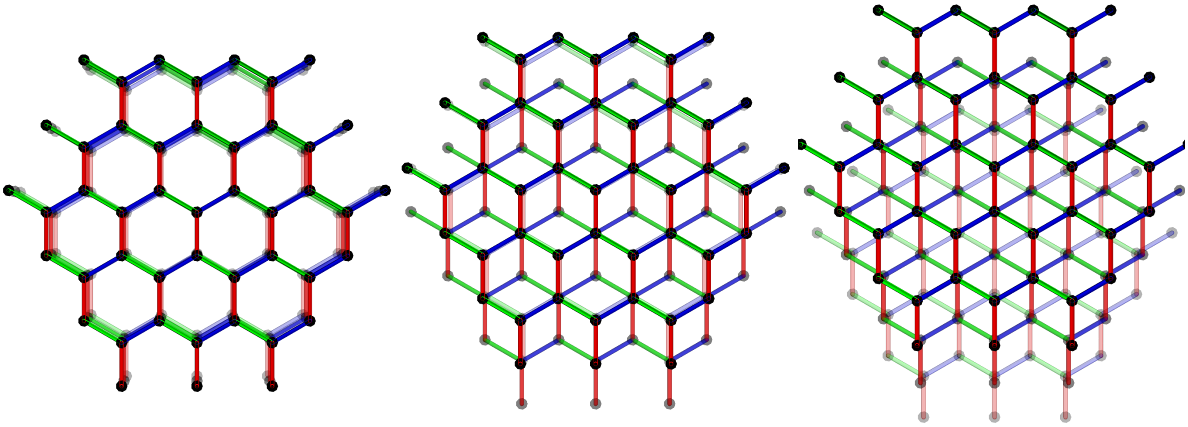

Fig. 6.1 **Stacking Kitaev spin liquid layers.** Top view of multilayer systems of Kitaev spin models stacked on top of each other in an AA, AB and ABC fashion (darker shaded layers lie above the lighter shaded ones). For AB stacking every second layer is shifted by $(0,a)$ where a is the nearest-neighbour distance. For ABC stacking, each layer is shifted by $(0,a)$ relative to the one below it which results in a three-layer periodic structure in the stacking direction as $(0,3a)$ is a lattice vector. The spins that sit directly above (or below) each other interact with a weak Heisenberg interlayer coupling. The coloured bonds denote the type of Kitaev interactions between the sites (x-blue, y-green and z-red).

6.1 The Model

There are different ways of stacking honeycomb lattices. Here we consider three main variants; AA, AB and ABC stacking patterns. The coupling between the layers is described by a nearest-neighbour Heisenberg interaction.

AA stacking. The simplest one is the AA stacking where every site is translated by a distance $d_\perp$ along the z axis which is taken to be the stacking direction perpendicular to the plane. The interlayer coupling is then expressed as

$$\Delta H_\perp^{AA} = J_\perp \sum_l \sum_{\langle ij\rangle_\perp} \boldsymbol{\sigma}_{i,l} \cdot \boldsymbol{\sigma}_{j,l+1}. \tag{6.1}$$

AB stacking. For AB stacking, however, adjacent layers obtain an extra in-plane shift compared to the AA stacking, such that atoms on the A sublattice in even layers and atoms of the B sublattice in odd layers are on top of each other:

$$\Delta H_{\perp}^{AB} = J_{\perp} \sum_{l} \sum_{\substack{\langle ij \rangle_{\perp} \\ i\in A, j\in B}} \boldsymbol{\sigma}_{i,2l} \cdot (\boldsymbol{\sigma}_{j,2l+1} + \boldsymbol{\sigma}_{j,2l-1}). \tag{6.2}$$

ABC stacking. Adjacent layers are all shifted by a lattice constant relative to each other in the same direction for ABC stacking. See Fig. 6.1. A spin in layer l on the A sublattice interacts with a spin in layer $l+1$ on the B sublattice directly above its position. In contrast, a spin in layer l on the B sublattice interacts with a spin in layer $l-1$ on the A sublattice directly below its position:

$$\Delta H_{\perp}^{ABC} = J_{\perp} \sum_{l} \sum_{\substack{\langle ij \rangle_{\perp} \\ i\in A, j\in B}} \boldsymbol{\sigma}_{i,l} \cdot \boldsymbol{\sigma}_{j,l+1}. \tag{6.3}$$

In all the above expressions, $\langle ij \rangle_{\perp}$ denotes nearest neighbour sites separated by interlayer spacing $d_{\perp}$ along the stacking axis direction.

The total Hamiltonian of the multilayer system is given by

Multilayer Kitaev model

$$H = \sum_{l} H_K^l + \Delta H_{\perp}, \tag{6.4}$$

where $H_K^l = \sum_{\langle ij \rangle_{\alpha}} K_{\alpha} \sigma_{i,l}^{\alpha} \sigma_{j,l}^{\alpha}$ is the familiar Kitaev Hamiltonian for the layer l, and $\Delta H_{\perp}$ depends on the stacking. In the limit of $J_{\perp} \to 0$, the model reduces to many decoupled Kitaev layers that can be solved exactly. Our approach is to carry out a perturbative analysis of dynamics of gauge field excitations, in the limit of weak $J_{\perp}$.

6.2 Conservation Laws

The single layer Kitaev model is exactly solvable due to the extensive number of conserved plaquette operators. It was this conservation law that prohibited the motion of visons. Adding further interactions spoils this property as we have seen in the previous chapters. Naturally, an interlayer coupling also breaks this conservation law. Nevertheless, there exist residual conserved quantities in the multilayer system we consider here. These conservation laws, although not sufficient to make the system integrable, govern the dynamics of quasiparticles in the 3D space.

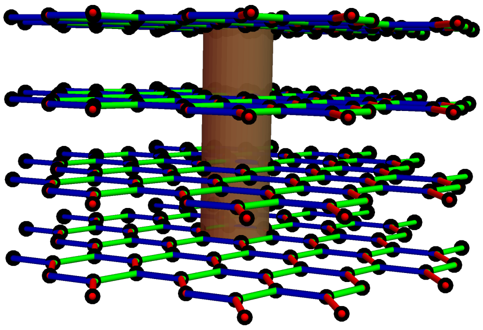

Fig. 6.2 **Conserved vison-stacks in an AA stacked Kitaev model.** In an system where Kitaev models are stacked in an AA fashion and coupled by Heisenberg interaction, products of plaquette operators $\hat{W}_{p,l}$ along a vertical stack (brown tube) is conserved. Single visons therefore cannot move out of the stack.

6.2.1 AA stacking: Vison stacks

In an AA stacked Kitaev model, the parity of visons in a hexagonal vertical column is conserved. We define vison *stack* operator X_p as the product of plaquette operators that lie directly on top of each other, as illustrate in Fig. 6.2.

$$X_p = \prod_l W_{p,l}, \tag{6.5}$$

where the product is over the layer index l. This quantity is conserved within our model.

This implies that a single vison in a given layer cannot move without creating extra visons in other layers to preserve the parity of the vison stacks. Moreover, the fact that in each layer, the vison parity is conserved due to the identity $\prod_p W_{p,l} = 1$ (assuming periodic boundary in the layer), a single vison cannot tunnel between layers. Therefore, the vison stack conservation law is sufficient to completely restrict the motion of a single vison. This conservation law was already pointed out in Ref. [122] and [114]. All the X_p operators are mutually commuting, resulting in 2^{L^2} conserved quantities for a system with (linear) layer dimension L.

6.2.2 AB and ABC stacking: Sheet operators

For AB and ABC types of stacking, however, such a local conservation law cannot be defined due to the relative shift between the layers. Nevertheless, we identify a novel set of global conservation laws. Consider the following operators

Conserved sheets

$$S_m^{\alpha\beta} = \prod_l L_{m,l}^{\alpha\beta} = \prod_l \left(\prod_{\langle ij \rangle \in \mathscr{C}_{m,l}^{\alpha\beta}} \hat{K}_{\langle ij \rangle}^l \right), \tag{6.6}$$

where $\hat{K}_{\langle ij \rangle}^l = \sigma_{i,l}^\alpha \sigma_{j,l}^\alpha$ are the Kitaev terms on the bond $\langle ij \rangle$. $\mathscr{C}_{m,l}^{\alpha\beta}$ label a zig-zag chain made of α and β type bonds in layer l that wraps around the torus (periodic boundary conditions are assumed) as shown by the thick lines in Fig. 6.3. $m = 1, \ldots, L$ indexes the position of the chain within the layer.

Since the operator $S_m^{\alpha\beta}$ is a product of Wilson loops, $L_{m,1}^{\alpha\beta}$, that are parallel to each other along the stacking direction, they form a sheet. Every sheet commutes with the Hamiltonian and is, hence, a conserved quantity. For AB stacking the sheets are perpendicular to the layer plane but are tilted for the ABC stacking as shown in the lower panel of Fig. 6.3. S_m^{xy}, S_m^{yz} and S_m^{xz} do not commute with each other but the product $S_{m_1}^{\alpha\beta} S_{m_2}^{\alpha\beta}$ commutes with all other operators. This results in the number of commuting operators scaling with $\frac{2^{3L}}{8}$. This number is lower compared to the AA stacking case where it was found to be 2^{L^2}. Nevertheless, how do they affect the dynamics of the gauge excitations?

Single visons are immobile Let us start with a single vison, which was immobile in the AA stacked model due to the local conservation law of vison stacks. Analysing its dynamics in AB and ABC stacks is more subtle due to the sheet conservation laws. Moving a single vison in layer l, within the layer, must be induced by an open string of spin operators, C^1, which must arise from the interlayer coupling at some order n in perturbation theory. i.e, $C^1 \sim \Delta H_\perp^n$. However, such a string will inevitably cross a Wilson loop $L_{l,m}^{\alpha\beta}$ for some m and flip its parity. The conservation of $S_m^{\alpha\beta}$ will force a Wilson loop in another layer, that is part of the sheet, to flip its parity and ultimately lead to the creation of visons in that layer. Therefore, it is impossible to move a single vison across a sheet without creating extra visons in other layers. Together, the three sheets around a given plaquette effectively trap a single vison and completely localize it.

How do we describe the dynamics of the gauge field then? The strategy is to look for composite excitation of visons that are mobile due to the inter-layer coupling. We start with pairs of visons, as they form the lowest energy excitations above single visons. It turns out that there exists a rich zoo of vison-pairs which exhibit exotic dynamics due to the interplay of conservation laws and topology. We will now explore them one by one.

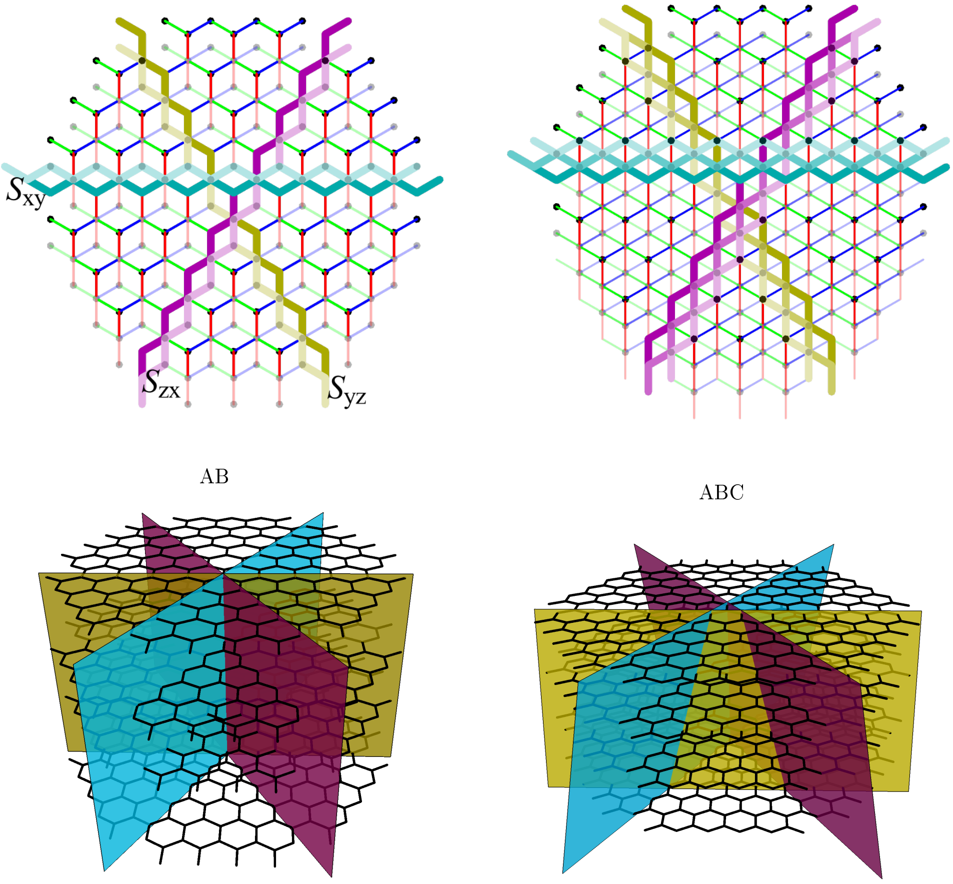

Fig. 6.3 **Conserved sheet operators.** Conservation laws in AB (left) and ABC (right) stacked Kitaev models are shown for a bilayer and trilayer respectively (darker shaded layers are above the lighter shaded ones.). A single sheet operator is defined as the product of Kitaev terms along a thick coloured chain. This defines three types of sheets formed by x and y bonds (cyan), y and z bonds (yellow), and, x and z bonds (violet). The full 3D representations for the sheet operators are shown in the lower panels. For ABC stacking the sheets are tilted.

6.3 Intra-layer Vison Pair: AA Stacking

We will first focus on the AA stacking to elucidate the dynamic properties of mobile vison-pairs. We define an *intra-layer vison pair*, vp_α, as a localized pair of visons sharing an $\alpha = x, y, z$ type link in a single layer. The vison stack conservation law, $\hat{X}_p$, prohibits their motion within the layer. However, the action of $\Delta H_\perp^\alpha$ on a state with a single vp_α excitation effectively hops it to an adjacent layer directly above or below. This is illustrated in Fig. 6.4 b. This leads to an effective one dimensional motion of a given intra-layer pair along the z axis. The hopping

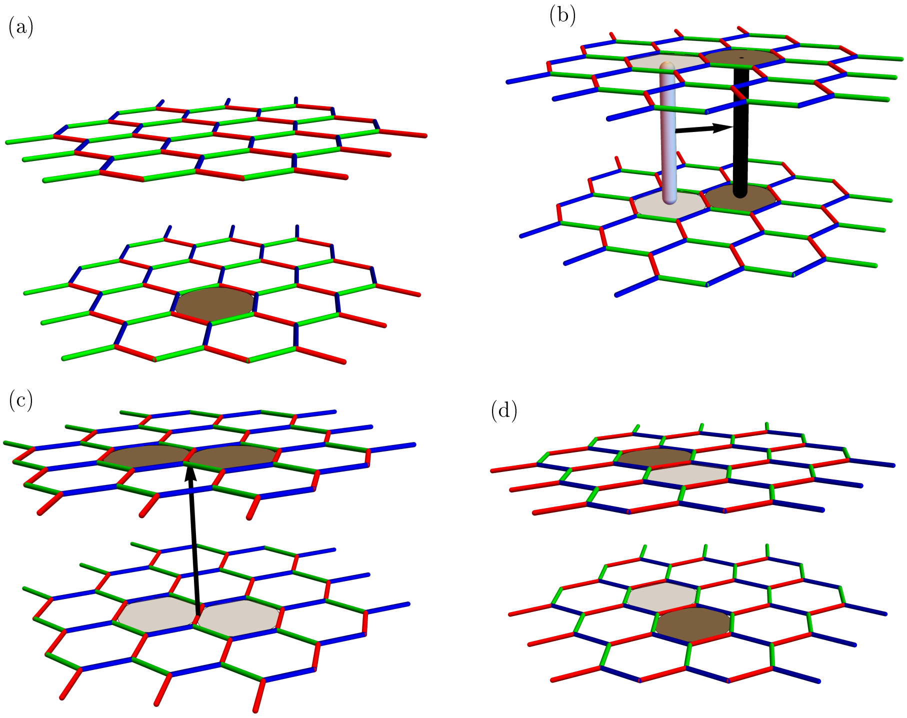

Fig. 6.4 **Visons in an AA stacked Kitaev model.** (a) A single vison (shaded plaquette) excitation is immobile. (b) An inter-layer vison pair vp_I can hop in a plane parallel to the layers. (c) An intra-layer vison pair vp_α ($\alpha = x,\ y,\ z$) can only hop between layers along the stacking direction. (d) Another inter-layer pair vp_I', flips between two states by exchanging the vison positions. In (b), (c) and (d), the inter-layer coupling induces transitions between the light- and dark-shaded plaquette pairs.

amplitude for a vp_z can be computed using

$$\begin{aligned}\frac{t_{vp_z}}{J_\perp} &= \Big(\big\langle\Phi_0^2(\emptyset)\big|\otimes\big\langle\Phi_0^1(\boldsymbol{R},\boldsymbol{R}+\boldsymbol{\eta}_z)\big|\Big)\Delta H_\perp\Big(\big|\Phi_0^1(\emptyset)\big\rangle\otimes\big|\Phi_0^2(\boldsymbol{R},\boldsymbol{R}+\boldsymbol{\eta}_z)\big\rangle\Big)\\ &=\Big|\big\langle\Phi_0^1(\boldsymbol{R},\boldsymbol{R}+\boldsymbol{\eta}_z)\big|\,\sigma^z_{i,1}\,\big|\Phi_0^1(\emptyset)\big\rangle\Big|^2+\Big|\big\langle\Phi_0^1(\boldsymbol{R},\boldsymbol{R}+\boldsymbol{\eta}_z)\big|\,\sigma^z_{j,1}\,\big|\Phi_0^1(\emptyset)\big\rangle\Big|^2,\end{aligned}\tag{6.7}$$

where $\boldsymbol{R}$ is the position vector of a vison in the given layer and $\boldsymbol{\eta}_z$ is a unit vector perpendicular to the z-link. The states appearing in the above expression are the eigenstates of the multilayer system in the $J_\perp = 0$ limit. These are simply the tensor products of the single layer wavefunctions. As already described in Chapter 3, the single layer wavefunction can in turn be decomposed into a direct product of the matter fermion (c_i) and gauge sector (b_i).

Using the Pfaffian method described in Chapter 4, we numerically evaluate the matrix element. Fig. 6.5 shows the hopping rate of the vison-pair as a function of system size. The value extrapolates to zero in the thermodynamic limit implying that there is no coherent hopping at linear order in $J_\perp$. This surprising result can be rationalized by analysing the vison-pair wavefunction. It was pointed out in previous works [48, 47] that when one compares the ground-state wave functions in the presence and absence of a vison pair, they have different matter-Majorana

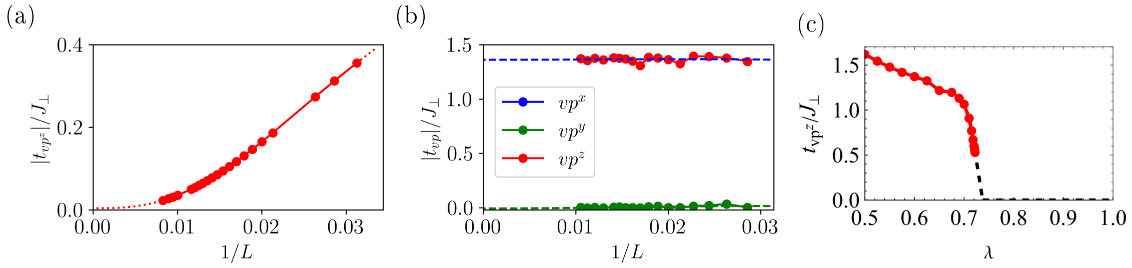

Fig. 6.5 **Hopping of intra-layer vison pairs in the AA stacked model.** (a) Inter-layer hopping amplitude t_{vp_z} of intra-layer vison pairs, as a function of inverse system size at the isotropic point, $\lambda = 1$. In the thermodynamic limit, t_{vp_z} vanishes. (b) For anisotropic Kitaev couplings, $\lambda = 0.6$, the vison pair vp_z obtains a finite hopping amplitude while vp_x and vp_y do not. (c) Hopping amplitude of vp_z as a function of anisotropy λ for linear system size $L = 70$. The dashed lines are guides to the eye.

parity. Thus, the only way to create or destroy a vison pair, is to simultaneously change the Majorana parity. Technically, in the calculation of Eq. (6.7) this is accomplished by occupying the lowest-energy Majorana state. In the gapless phase, this mode is delocalized and hence the tunnelling of such an extended object (vison pair + fermion) vanishes in the thermodynamic limit. While Eq. (6.7) is only valid to linear order in $\Delta H_\perp$, the 'parity-obstruction argument' applies to all orders in $\Delta H_\perp$ as long as the Kitaev phase is stable.

6.3.1 Effect of anisotropy

One of the important parameters of the Kitaev model is the anisotropy of couplings, parametrized by $\lambda = K_x/K_z = K_y/K_z$. For $\lambda < 0.5$, the matter fermions are gapped out and the model undergoes a phase transition to a gapped Z_2 spin liquid which is adiabatically connected to the toric code phase. As we are interested in the gapless spin liquid phase and moreover, a strong anisotropy of $\lambda \sim 0.5$ is perhaps not experimentally relevant for real materials, we stay in the regime $\lambda > 0.5$. Although the ground states are not affected by tuning λ, the dynamics of excitations are qualitatively modified as we describe below.

As shown in Fig. 6.5b and c, the vison pair vp_z obtains a finite hopping matrix element in the thermodynamic limit when $\lambda \lesssim 0.72$. In contrast, the other two types of vison pairs vp_x and vp_y are still not able to hop coherently. This sudden change in the nature of the vison-pair can be rationalized by observing that the matter-fermion parity of the *physical* vison-pair state changes abruptly at $\lambda \approx 0.72$. For $\lambda \gtrsim 0.72$, the physical vison-pair state has an odd matter fermionic parity, making its wavefunction extended due to the extra matter Majorana mode added. However, for $\lambda \lesssim 0.72$, the extra matter Majorana is no more required and the wavefunctions is therefore localized. An interesting consequence of this effect is that the lowest energy vison-pair changes from a fermionic ($\lambda \gtrsim 0.72$) to a bosonic excitation ($\lambda \lesssim 0.72$). Only the boson can hop coherently as discussed in detail later. This is consistent with the

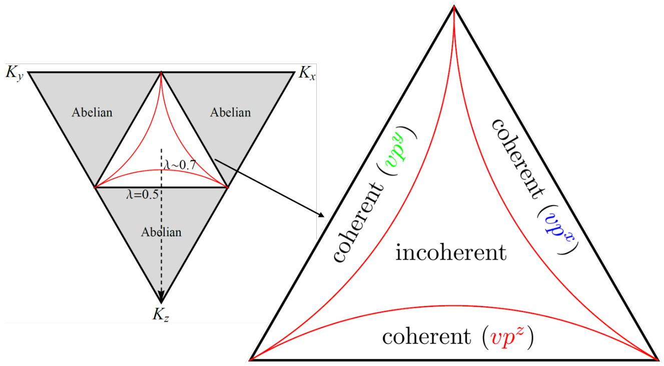

Fig. 6.6 **Effect of anisotropy on interlayer tunnelling.**. Within the gapless phase of the pure Kitaev model (unshaded triangle), the intra-layer tunnelling is strongly influenced by the Kitaev anisotropy λ. This defines regions, within the gapless phase, separated by the red arcs, exhibiting an incoherent tunnelling and a coherent hopping behaviour of vison-pair excitations. The coherent excitations are denoted in colours.

principle that only a topologically trivial (vacuum sector) excitation can move between layers. This change of quantum numbers of an excited state is sometimes called a ‘dynamical quantum phase transition’ (DQPT) as at this point, time-dependent correlation functions change their qualitative properties. This was, in fact pointed out in some previous works that calculated the dynamical response of the Kitaev model [47, 48, 123].

6.3.2 Majorana-assisted hopping

In the isotropic limit (or, $\lambda \gtrsim 0.72$), we showed that the interlayer hopping of a vison pair (vp_α) is always accompanied by the creation (or destruction) of Majorana modes in the two layers. Although this leads to vanishing coherent hopping rate at zero-temperature, incoherent Majorana-assited hopping processes are allowed at finite temperature. Such a hopping rate can be computed using Fermi’s golden rule formula

$$\Gamma^z_\perp = \frac{2\pi}{\hbar} \sum_{m,n} |\langle \Psi_m(\boldsymbol{R}_l)| \Delta H |\Psi_n(\boldsymbol{R}_{l+1})\rangle|^2 e^{-\beta E_n} \delta(E_m - E_n). \tag{6.8}$$

The states $|\Psi(\boldsymbol{R}_l)_m\rangle = |\Phi_{m_1}(\boldsymbol{R}_l)\rangle |\Phi_{m_2}(\emptyset)\rangle$ are constructed by populating the Majorana states of layer l and $l+1$ labelled by m_l and m_{l+1}, respectively, with $m = \{m_l, m_{l+1}\}$.

It turns out that in the low energy (equivalently low T) limit, one can neglect the scattering of Majorana fermions from the vison pair. We can confirm this by calculating the full Green’s function of the Majoranas in the presence of a vison-pair, which approaches the free particle Green’s function as $\omega \to 0$. See Appendix F for details (also Ref. [124]). In this limit, using the Lehmann representation approximately transforms the above expression into a convolution of two local Majorana spectral functions $C_{\alpha\beta}(\omega, 0) \propto |\omega|$ in each layer. (Due to the lengthy

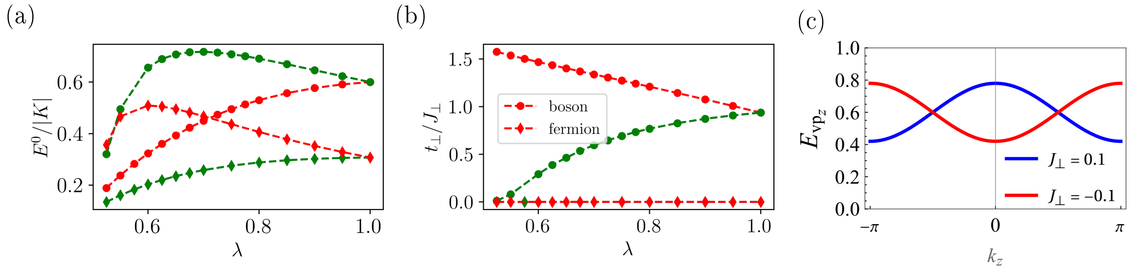

Fig. 6.7 **Ising anyon pairs - AA stacking.** (a) The energy of intra-layer vison pairs (Ising anyon pairs) in the non-abelian phase (for $\kappa = 0.1,\ J_\perp = 0$) as a function of the anisotropy λ. The colours label the type of bond shared by the anyons - vp_x and vp_y vison-pairs (green) have the same energy, the vp_z pair is colored in red. Circles and diamonds denote bosonic and fermionic vison pairs, respectively. A level crossing between the fermionic and bosonic vison-pairs occurs at $\lambda \approx 0.72$. (b) Inter-layer hopping amplitudes of the vison pairs. Only pairs that belong to the vacuum sector (i.e, bosons) can coherently hop. (c) The one dimensional dispersion of the bosonic vp_z along the z direction for $\lambda = 1$ and $\kappa = 0.1$ for different signs of $J_\perp$.

expressions and overwhelming number of indices, the derivation is relegated to Appendix F). This leads to an inter-layer diffusion constant for the intra-layer pairs

Interlayer diffusion

$$D_\perp = \Gamma^z_\perp d^2_\perp \sim \frac{J^2_\perp d^2_\perp T^3}{K^4}, \tag{6.9}$$

where $d_\perp$ is the inter-layer separation. The Majorana-assisted hopping of vison pairs is, therefore, possible, but strongly suppressed at low temperatures.

6.3.3 Non-abelian phase and anyon tunneling

Adding an external magnetic field can transform the gapless spin liquid into a gapped chiral gapped spin liquid with a Majorana gap Δ_m. As detailed in the Chapter 3, the visons in this phase are Ising anyons with localized Majorana zero modes attached to them. The intra-layer vison-pairs (anyon pairs) now carry a localized fermion mode with energy ε_0, where $\Delta_m > \varepsilon_0 > 0$, arising from the hybridization of the Majorana modes of the two visons that are now close to each other. This mid-gap mode can be occupied or empty, defining two types of intra-layer vison pairs. In the language of topological field theories, the Ising anyons can fuse in two different ways, $\sigma \times \sigma = \mathbb{1}$ or $\sigma \times \sigma = \psi$. An anyon pair that is created by any physical operator out of vacuum is a boson whereas a pair that fuses to release a fermion (ψ) is fermionic in nature. The energies of these vison pairs in $J_\perp \to 0$ limit are shown in Fig. 6.7a. The two types of pairs have different total fermionic parity and do not hybridize with each other, signifying that they belong to different superselection sectors.

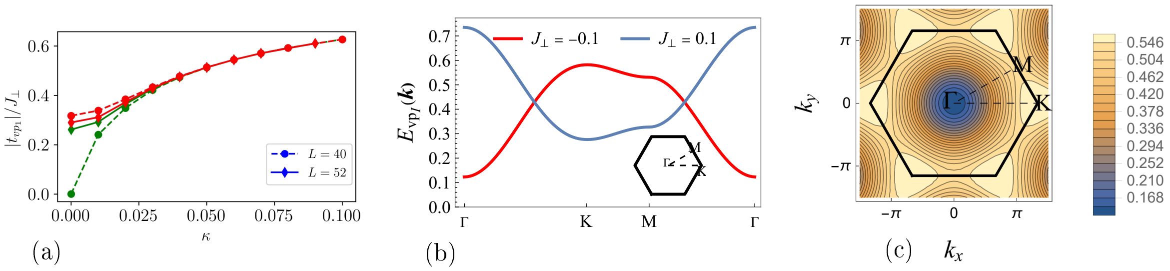

(a) (b) (c)

Fig. 6.8 **Dynamics of inter-layer vison pairs - AA stacking.** In Figure (a), the hopping amplitude of the interlayer-vison pair, vp_I, is plotted as a function of Majorana mass κ for the AA stacked model. The corresponding 2D dispersion of the vp_I is shown in (b) and (c). The dispersions are obtained for $\kappa = 0.05$.

We can now calculate the hopping rates of the two different intra-layer vison pairs to linear order in $J_\perp$ which is shown in Fig. 6.7b. At $T = 0$, only the bosonic pair can tunnel between the layers (to arbitrary order in $J_\perp$), whereas the fermionic pair requires assistance from thermally excited Majorana fermions which are gapped in the non-abelian phase.

The level crossing between the fermionic and bosonic vp_z pair at $\lambda \approx 0.72$ shown in Fig. 6.7 has important physical consequences in the $\kappa \to 0$ limit, when the gap closes. It explains our previous finding from Fig. 6.5c that the nature of a vison-pair changes suddenly at this point in a so-called ‘dynamical quantum phase transition’.

When κ and therefore the Majorana gap is reduced, the fermionic bound state grows in size. Thus, for $\kappa \to 0$, only the vison pair without a fermion bound to it (the lower energy state) remains as a point-like particle. Therefore, the ‘physical’ vp_z pair at $\kappa = 0$ changes its statistics and ability to tunnel at $\lambda \approx 0.72$. In contrast, the vp_x and vp_y pairs do not tunnel in this limit.

Note that, we expect that the critical value, $\lambda \approx 0.72$ calculated above in the $J_\perp \to 0$ limit, will be shifted to larger values upon increasing $J_\perp$ as the bosonic vison gains extra kinetic energy by inter-layer tunnelling.

6.4 Inter-layer Vison Pair: AA Stacking

A second kind of dynamical excitation, an *inter-layer vison pair*, vp_I, is made of two visons from adjacent layers, as shown in Fig. 6.4b for an AA stacked model. We will see later that it can also be defined in AB and ABC stacked models. An inter-layer vison pair is always confined to move in a plane (as the vison parity of a given plane cannot change) but can hop between nearest neighbour plaquettes within each layer due to the inter-layer perturbation $\Delta H_\perp$. The vp_I pair thus moves on a triangular lattice formed by the plaquettes of the honeycomb lattice.

We can now calculate the hopping matrix elements of an inter-layer pair across an α-bond, $t^{\alpha}_{vp_I}$, induced by $\Delta H^{AA}_{\perp}$ to leading order in $J_\perp$. For a vison pair in the layers 1 and 2 hopping across the z bonds, we find

$$\begin{aligned}\frac{t^{z}_{vp_I}}{J_\perp} &= \left\langle \Phi^2_0(\boldsymbol{R})\right| \otimes \left\langle \Phi^1_0(\boldsymbol{R})\right| \Delta H^z_\perp \left|\Phi^1_0(\boldsymbol{R}')\right\rangle \otimes \left|\Phi^2_0(\boldsymbol{R}')\right\rangle \\ &= \left\langle \Phi^1_0(\boldsymbol{R})\right| \sigma^z_{i,1} \left|\Phi^1_0(\boldsymbol{R}')\right\rangle^2 + \left\langle \Phi^1_0(\boldsymbol{R})\right| \sigma^z_{j,1} \left|\Phi^1_0(\boldsymbol{R}')\right\rangle^2 ,\end{aligned} \tag{6.10}$$

where i and j refer to the sites sharing a z-link. The second equality is due to the decoupled nature of the layers in the unperturbed limit. The hopping amplitude is thus directly related to a magnetic field induced hopping rate of a vison in a monolayer Kitaev model. The single vison hopping rate was calculated in [85, 125] and it was found that in the gapless phase, for a single vison hopping due to a σ^{α} operator, a quasi-bound Majorana state leads to strong finite size effects. To avoid this issue, we open a small gap κ in the Majorana spectrum by adding a time reversal symmetry breaking *nnn* hopping. The calculation for one layer is done using periodic boundary conditions in a finite size system of width L. Thus, we are forced to consider two visons per layer at a distance of approximately $L/2$. For $\kappa \to 0$ the results depends sensitively on L, the precise location of the two visons and the direction of hopping as the quasi-bound Majorana states of the two vison pairs overlap. No such problem exist for sufficiently large κ as shown in Fig. 6.8a. At a small $\kappa \approx 0.02K$, the hopping amplitude can be read off from the plot as

$$t^{x}_{vp_I} = t^{y}_{vp_I} = t^{z}_{vp_I} \approx 0.35\, J_\perp \tag{6.11}$$

Using this, we can calculate the dispersion of vp_I as shown in Fig. 6.8b. The excitation gap evolves as $\Delta_{vp_I} \approx E^0_{vp_I} - 6\,|t_{vp_I}|$ for $J < 0$ with a band minimum at the Γ point. For $J > 0$, the gap is given by $\Delta_{vp_I} \approx E^0_{vp_I} - 3\,|t_{vp_I}|$ with multiple band minima at the K points of the Brillouin zone.

It is interesting to point out that the dynamics of the inter-layer vison pair induced by the inter-layer Heisenberg coupling $J_\perp$ is strikingly different from the dynamics of a single vison induced by an external magnetic field (See Chapter 4). In both cases the same type of σ^z matrix elements $A_i = \left\langle \Phi^1_0(\boldsymbol{R})\right| \sigma^z_{i,1} \left|\Phi^1_0(\boldsymbol{R}')\right\rangle$ needs to be calculated. The single vison hopping is then determined by $A_i + A_j$ while the hopping rate of the pair arises from $(A_i)^2 + (A_j)^2$. For $K > 0$ one has $A_i = -A_j$ and thus a destructive interference prohibits field-induced single vison hopping [85, 125]. This effect is absent for the inter-layer pair hopping. For antiferromagnetic Kitaev coupling, $K > 0$ and finite κ, the single-vison band is topological as has been shown in Ref. [85, 125]. Again this effect is absent for the inter-layer pair.

However, an interesting situation arises when a ferromagnetic Kitaev model is coupled to an antiferromagnetic model. In this case, the hopping amplitude vanishes in the limit $\kappa \to 0$ due to the destructive interference arising from the AFM layer. This would mean that such an alternate stacking pattern would be more stable to inter-layer pair softening induced instabilities. It has been shown that field induced phases are qualitatively different for FM and AFM Kitaev models which seems to be strongly related to the strikingly different vison dynamics [89, 69, 126]. It is tempting to speculate that novel topological phases may exist for an FM-AFM Kitaev bilayer for an intermediate $J_\perp$. In fact, Ref. [115] has presented numerical exact diagonalization results roughly consistent with this argument.

Inter-layer vison pair - type 2 There exists a second type of inter-layer vison pair, shown in Fig 6.4d which also acquires dynamics due to $\Delta H_\perp$. This excitation is bound to a bilayer and does not de-localize in space. However, it has an internal dynamics arising from the coupling (linear in $J_\perp$) between two states that differ by their vison positions as shown in Fig 6.4d. Solving a two-level problem for this mode gives the energy levels,

$$E_{vp'_I} = E^0_{2v} \pm J_\perp t_{vp_I} \tag{6.12}$$

6.5 Inter-layer Vison Pairs: AB Stacking

Let us now look at the AB stacked model. The strikingly different conservation laws for AA and AB models directly translates to qualitatively different vison-pair dynamics in the two models. While for AA stacking, the vison stack operators, Eq. (6.5), are conservation laws, for AB stacking, sheet operators, Eq. (6.6), are conserved instead. Let us see how this profoundly influences the dynamics of inter-layer vison pairs and their quantum numbers.

The sheet conservation laws help define three species of inter-layer pairs, as illustrated in Fig. 6.9b. Remarkably, a given inter-layer pair is restricted to move along a one-dimensional channel within the 2D plane! The 1D channel is essentially the sheet operator of the bilayer and thus the three species vp^{AB}_{xy}, vp^{AB}_{yz} and vp^{AB}_{zx} propagate along the sheets S^{xy}_m, S^{yz}_m and S^{zx}_m respectively for a given index m. This *sub-dimensional mobility* is a direct consequence of the conservation laws (Eq. (6.6)) which prevent single visons from crossing a sheet.

The hopping amplitudes are evaluated using the same methods as in the AA case leading to the relation

$$t_{vp^{AB}_{\alpha\beta}} = J_\perp \left\langle \Phi^1_0(\boldsymbol{R}) \right| \sigma^\gamma_{i,1} \left| \Phi^1_0(\boldsymbol{R}') \right\rangle \left\langle \Phi^2_0(\boldsymbol{R}) \right| \sigma^\gamma_{j,2} \left| \Phi^2_0(\boldsymbol{R}') \right\rangle \tag{6.13}$$

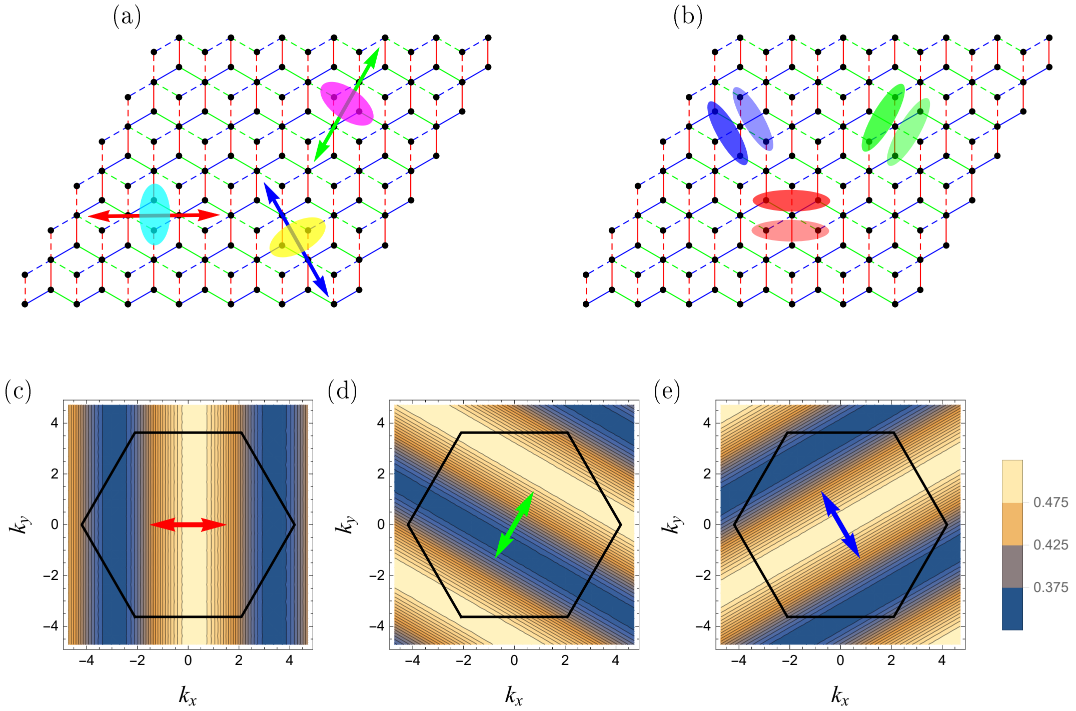

Fig. 6.9 **Dynamics of vison pairs - AB stacking.** (a) Inter-layer vison pairs are illustrated for an AB stacked bilayer using ellipses that cover the centers of the two visons (one from each layer). Each of the three species, vp_{xy}^{AB} (cyan), vp_{yz}^{AB} (yellow) and vp_{zx}^{AB} (violet)), is forced to move along the corresponding sheet operator (shown in Fig. 6.3), indicated by the arrows. Figure (b) illustrates intra-layer vison pairs that can only move out of plane along the z axis. The interlayer coupling induces hopping between the lightly shaded visons in the lower layer (dashed lines) and the darker shaded pair in the upper layer (solid lines), thus tracing a zig-zag path along the z axis. Lower panel shows dispersions of the three inter-layer vison pairs, vp_{xy}^{AB}-(c), vp_{zx}^{AB}-(d) and vp_{yz}^{AB}-(e). The black solid line shows the first Brillouin zone. The one-dimensional nature of the excitations is highlighted by the colored arrows consistent with (a). The plots are obtained for $J_\perp = .1|K|$ and $\kappa = 0.05$.

where $i \in$ sublattice A, $j \in$ sublattice B and $\alpha \neq \beta \neq \gamma$. The magnitude of the hopping rate is exactly half of that of the AA-model computed in Eq. (6.11),

$$|t_{vp_{\alpha\beta}^{AB}}| = \frac{|t_{vp_I}^{\gamma}|}{2}. \tag{6.14}$$

The factor of $\frac{1}{2}$ relating the AA and AB stacked models simply arises from the fact that only one out of the two sublattices of a given monolayer unit cell contributes to the interlayer coupling in the AB model while both the sublattices additively contribute to the hopping in the AA case.

The corresponding dispersions are plotted in Fig. 6.9 showing their 1D nature which is to be contrasted with the fully 2D dispersion of inter-layer vison pairs in the AA model (Fig. 6.8c).

6.6 Intra-layer vison pair - AB stacking

Similar to the AA case, intra-layer vison pairs in the AB model, vp^{AB}_{α}, sharing an α bond in a layer can only hop across layers. In-plane motion of such pairs are forbidden by the sheet conservation laws discussed earlier. This hopping process is illustrated for a bilayer in Fig. 6.9b, where three different species of intra-layer vison pairs that share x, y and z bonds are shown. As in the AA case, near the isotropic point $\lambda \gtrsim 0.72$, the excitations can only incoherently tunnel via Majorana assisted hopping with a diffusion constant

$$D^{AB}_{\perp} = \frac{D_{\perp}}{2} \tag{6.15}$$

For $\lambda \lesssim 0.72$, however, the intra-layer vison pair vp^{AB}_{z} can coherently hop with a hopping amplitude

$$t_{vp^{AB}_{\alpha}} = \frac{t_{vp_{\alpha}}}{2} \tag{6.16}$$

The factor of $\frac{1}{2}$ relating the AA and AB stacked models has already been discussed above. While the dispersions of the AA and AB intra-layer pairs are one-dimensional in the z axis, the vp^{AB}_{z} traces a zig-zag path in real space.

The dynamics of intra-layer vison pairs (Ising anyon pairs) in the chiral spin liquid phase was also discussed for the AA model. It turns out that all the results are also applicable to the AB stacked model (up to the extra factor of $\frac{1}{2}$ in the hopping amplitudes).

6.7 Dynamics in ABC Stacked Model

For ABC stacking, a simple observation makes our life easier. A pair of neighbouring layers in the ABC model is (up to translations) equivalent to a bilayer in the AB model. The dynamics of inter-layer vison pairs in an ABC stacked model is therefore identical to that of the AB model. For an inter-layer vison pair in a given bilayer, the sheet conservation law restricts its motion to a 1D channel along the line obtained by projecting the sheet on to the bilayer. At linear order in $J_{\perp}$, the hopping is induced by the coupling between the two layers.

$$t_{vp^{ABC}_{\alpha\beta}} = t_{vp^{AB}_{\alpha\beta}} \tag{6.17}$$

This similarity of AB and ABC models, however, does not translate directly to the intra-layer pairs. It is affected qualitatively by the ABC stacking. In this case, the sheet operators are tilted. For a given intra-layer pair, there are two relevant sheet operators which cut the pair into half.

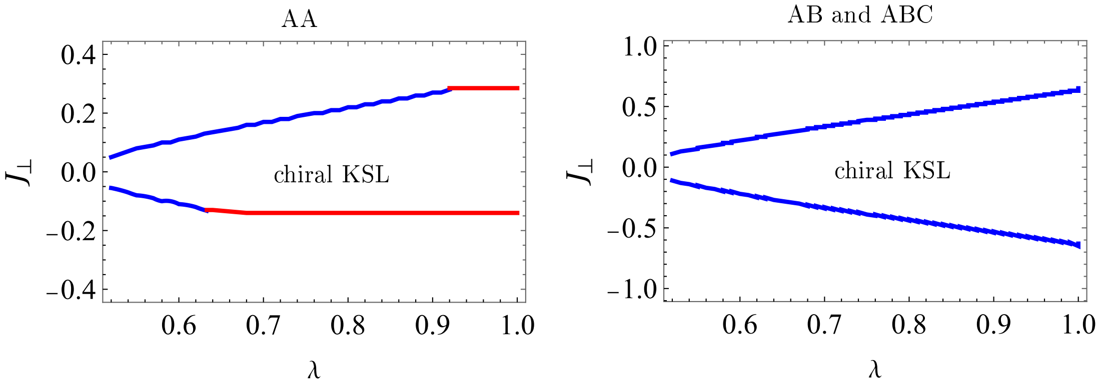

Fig. 6.10 **Inter-layer coupling induced instabilities.** Gap closing instabilities of the chiral KSL as a function of the anisotropy λ and the inter-layer Heisenberg coupling $J_\perp$. The left panel applies to AA stacking, the right panel to both AB and ABC stacking. Vison-pair excitations become gapless when crossing the solid lines (estimated from perturbation theory linear in $J_\perp$). Across blue lines, the intra-layer pairs close the gap while the red lines indicate the gap closing due to inter-layer pairs (vp_I.). This plot is obtained for $\kappa = 0.05$.

Sheet-operator conservation then enforces that the pair moves parallel to these two sheets. Thus it can only move along the line obtained by the crossing of the two sheets shown in Fig. 6.3.

Importantly, three types of intra-layer pairs (vp_x^{ABC}, vp_y^{ABC} and vp_y^{ABC}) now move in three different directions, $(0, \sqrt{3}a, 3d_\perp), (-\frac{\sqrt{3}}{2}a, -\frac{3}{2}a, 3d_\perp), (\frac{\sqrt{3}}{2}a, -\frac{3}{2}a, 3d_\perp)$, where $d_\perp$ is the distance of layers, see Fig. 6.3. The hopping amplitude is however identical to that in the AB model due to the same arguments discussed above.

$$t_{vp_\alpha^{ABC}} = t_{vp_\alpha^{AB}} \tag{6.18}$$

6.8 Instabilities

An important consequence of the gauge excitations acquiring dynamics is the possibility of vison proliferation when the energy of the excitations become negative. Assuming our perturbation theory is still valid, we can estimate the critical strength of $J_\perp$ where such an instability may arise. As we saw that the Kitaev coupling anisotropy also has a strong influence on the dynamics, we can compute a stability region for the Kitaev spin liquid in the $\lambda - J_\perp$ parameter space. The resulting estimate for the locations of the phase transitions is shown in Fig. 6.10 where we assumed a small but finite Majorana gap, $\kappa = 0.05$, to avoid large finite-size effects.

The calculation proceeds as follows. First, we determine, for $J_\perp = 0$, the energy of the vison pair. Second, one obtains its hopping rate and thus the correction to the dispersion E_k linear in $J_\perp$. Solving for $E_k = 0$ at the band minimum allows to determine the critical $J_\perp$. As shown in Fig. 6.10, the instability occurs at relatively small values of $J_\perp$ and thus likely in a parameter regime where our perturbative approach is approximately valid.

An interesting detail in this diagram is the nature of the excitation that softens. The color in Fig. 6.10 encodes the type of vison pair which drives the instability. For isotropic Kitaev couplings, $\lambda = 1$, the leading instability for both AB and ABC stacking arises from the motion of intra-layer vison pairs while for AA stacking it is dominated by inter-layer pairs. This is because only for AA stacking do the inter-layer pairs have a two-dimensional dispersion and thus gain much more kinetic energy. For large anisotropies (smaller λ) in the AA stacked model, one can also find regimes, where the 1D motion of intra-layer pairs can trigger phase transitions. The sub-dimensional nature of inter-layer excitations in AB and ABC is likely to result in a qualitatively different phase compared to the AA model when they proliferate.

6.9 Summary and Discussion

Although we considered three simplest 3D constructions by stacking Kitaev layers, we obtained a rich zoo of dynamical gauge field excitations. The effect of stacking on the conservation laws and thus the dynamics of the system was rather surprising. We identified novel sheet conservation laws reminiscent of certain fracton models in AB and ABC stacked models. Although still under debate, $\alpha-\mathrm{RuCl}_3$ is believed to have an ABC or AB type stacking, depending on the temperature regime. Our results may therefore be relevant to $\alpha-\mathrm{RuCl}_3$ although with additional perturbations taken into consideration.

Intra-layer perturbations In the three simplified models considered in this chapter, we completely neglected perturbations within the layers, so that we could isolate the effect of interlayer interactions. However, when looking for experimental signatures arising from the rich dynamics of vison-pairs, it is essential to include the effect of additional intra-layer perturbations which are at least as strong as the interlayer coupling. Foremost, they make single visons mobile as they violate the conservation laws. This effect was comprehensively studied in the previous two chapters. Moreover, they can give rise to in-plane motion of intra-layer vison pairs which was studied by Zhang. et. al. in a contemporary work [67]. For inter-layer pairs, intra-layer perturbations can induce motion only at second order in perturbation theory since two visons in two different layers have to be moved simultaneously. For example, the hopping amplitude of an inter-layer pair induced by a Γ term would be $\sim \Gamma^2/\varepsilon^b_{vp_I}$, where $\varepsilon^b_{vp_I}$ is the binding energy of the inter-layer pair.

Experimental Signatures We saw that an intricate interplay of conservation laws and topology gives rise to sub-dimensional excitations whose dynamics is strongly influenced by the

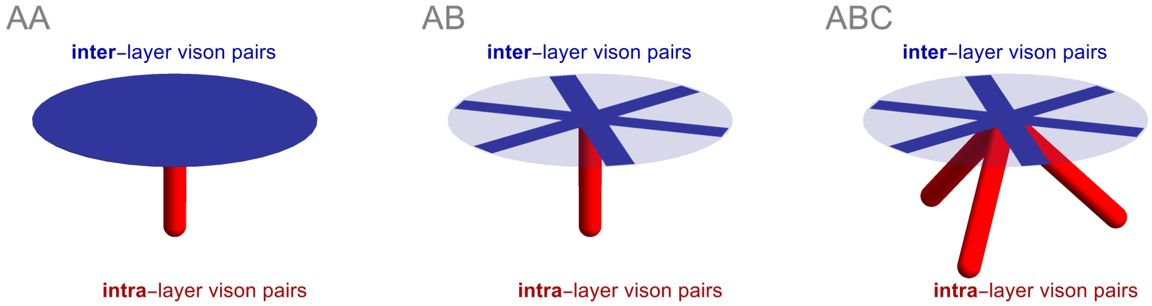

Fig. 6.11 **Dimensionality of vison-pairs in a layered Kitaev model.** Schematic illustration of the propagation of vison-pair excitations after a spot on the surface of a crystal is heated by a laser pulse. The laser pulse creates locally a high density of vison excitations. Vison pairs are mobile and move in a pattern characteristic of the dimensionality of their motion. (Illustration by Achim Rosch.)

stacking pattern. The additional spatial dimension introduced thus has a surprising effect on the nature and motion of the fractional quasiparticles. One way to probe this rich and peculiar dynamics is to investigate the relaxation dynamics of a layered Kitaev material. In a typical pump-probe setup, one would shine a laser beam to the top layer which excites a large number of Majoranas, visons and vison-pairs. While the interlayer-pairs will diffuse within the layer plane according to their dimensionality, the intra-layer pairs will penetrate into the bulk. This may be detected using local optical measurements [109]. Fig. 6.11 shows a sketch of this dynamics for the three different stacking patterns. Although the conservation laws may be broken by a generic Kitaev model, the key principle that only vison pairs can diffuse in the stacking direction is a robust consequence of the topology. This can be used as a guiding principle to design experiments to track the diffusion and annihilation of visons in layered spin liquid materials. The coherent propagation of anyon pairs in the out-of-plane direction in the chiral spin liquid phase may be probed using a momentum dependent inelastic neutron spectroscopy. This should result in a sharp signature in the $(0,0,1)$ direction [127]. However, here one has to carefully separate the multi-particle continuum arising due to the presence of intra-layer perturbations which are of similar or larger strength compared to inter-layer couplings.

Fusion rules of anyon pairs In the chiral spin liquid phase, visons are Ising anyons. This immediately begs the question what is the statistics of the vison-pairs discussed in this chapter. The intra-layer vison pairs can either be bosonic or fermionic as we saw above. However, an inter-layer anyon pair now has two Majorana zero modes (one in each layer) which makes their quantum dimension 2. This gives rise to a rich set of fusion rules if two vison-pairs of the same bilayer meet. Consider AA stacking for example. For a pair, vp_I in the bilayer $(l,l+1)$, one finds four different fusion outcomes, $vp_I \times vp_I = \mathbb{1} + \psi_l + \psi_{l+1} + \psi_l \psi_{l+1}$, where ψ_l denotes a fermionic excitation in layer l. Now imagine a pair in the bilayer $(l-1,l)$ meets a pair in the bilayer $(l,l+1)$. Their fusion leads to single visons in layer $l-1$ and $l+2$, possibly releasing a fermion in layer l. For AB stacking, let us consider for simplicity only the case when an inter-layer vison pair $vp^{AB}_{xy,l}$ meets a $vp^{AB}_{yz,l}$ in the same bilayer l. Due to the relative offset of the visons in the bilayer, only two of the four visons can fuse either in layer l or $l+1$, leaving behind an intra-layer pair vp^{AB}_{y}, able to move in the z direction and either one or no Majorana modes; $vp^{AB}_{xy,l} \times vp^{AB}_{yz,l} = vp^{AB}_{y}(\mathbb{1}+\psi_l) + vp^{AB}_{y}(\mathbb{1}+\psi_{l+1})$. The same applies to the ABC model, the only difference being that the intra-layer pair vp^{ABC}_{y} moves in a direction oblique to the z axis.

Fractons? A recent and perhaps the most exotic addition to the zoo of topological excitations are fractons. These are quasiparticle excitations of certain 3D topological phases which are immobile when they are isolated but become mobile when in pairs. In certain sub-class of fractonic phases (called type-II), excitations are constrained to move in a sub-dimensional manifold[120]. In the multilayer systems studied here, single visons are immobile and vison-pairs may have strongly constrained one-dimensional dynamics strikingly similar to fractons. However, the crucial difference from true fractons is that these properties are not robust to general symmetry allowed perturbations as discussed above. Although model specific conservation laws (sheets) were necessary to obtain the sub-dimensional mobilities of the inter-layer pairs, that the simplest 3D constructions using 2D spin liquid layers led to fracton-like dynamics is fascinating by itself. The proliferation of these 'approximate fractons' might be a route towards truly fractonic phases and other 3D topological phases [128, 129]. Our results may also suggest that Kitaev materials might also provide a platform to realize highly exotic fractonic phases by engineering interlayer couplings. The connection of our results to layer construction models of fractons studied in Ref. [130] is perhaps an interesting direction for future research.

Part III

Experimental Signatures

Chapter 7

Raman Spectroscopy of Visons

Arguably, spectroscopy is the go-to technique for probing quasiparticle properties in condensed matter systems. In this approach, photons, electrons, or neutrons are directed at a sample material, and the scattered signal is detected. The incident particles excite the system at a given frequency before scattering out, and resulting spectrum carries crucial information about the energy, spin and lifetimes of the underlying quasiparticles.

In magnetic systems, neutron scattering (with a wavelength $\sim .1$ nm) can induce local spin flips, thereby detecting spin-spin correlations. In a magnetically ordered phase, neutron scattering can create single magnons leading to a resonant peak in the spectrum at the energy corresponding to the magnon. However, in a spin liquid, spectroscopic experiments are generally expected to observe a broad continuum response in energy. This broad response is characteristic of fractionalization, where a single spin flip produces multiple quasiparticles that can propagate independently. Indeed, neutron spectroscopy on some Kitaev materials provided the first glimpses of a liquid-like state[75, 131, 132].

Nonetheless, a broad feature in spectroscopy can also arise from more ‘trivial’ sources, such as disorder scattering or interactions between conventional quasiparticles. Therefore, it is a pressing question how to distinguish between these two scenarios in an experimental setting.

In this context, optical Raman spectroscopy has emerged as a complementary tool for probing the excitations of fractionalized phases [133, 134]. Its main advantage lies in the ability of long wavelength optical light to probe a variety of excitations, including the ones with $S = 0$ quantum numbers (e.g. a pair of magnons), which is ideal for fractionalized excitations. In contrast, conventional neutron scattering primarily probe spin flip ($S = 1$) excitations. Furthermore, the signal intensity in neutron scattering is often limited by the physical sample volume. Raman scattering also offers the ability to control the polarization of light which can be used to detect time-reversal or inversion symmetry-breaking orders and even reveal information about Berry curvature effects [135].

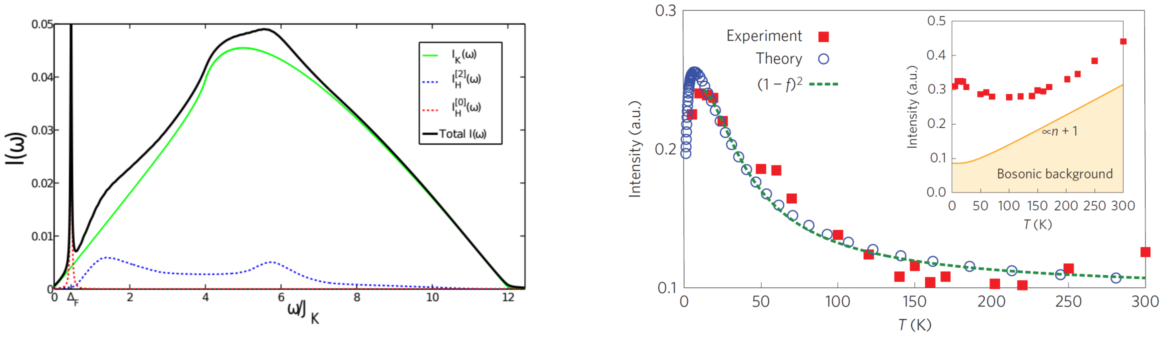

Fig. 7.1 **Raman response of a pure Kitaev model and experimental data in zero-magnetic field.** (a.) In the gapless phase, matter Majoranas are created in pairs and thus contribute a continuum response. The sharp peak results from the Heisenberg term creating four visons which are gapped. Figure adapted from Ref. [1]. (b.) Experimental result of Ref. [76] showing the temperature evolution of the Raman intensity fit with the pure Kitaev model calculations. (f denotes the Fermi distribution function)

The interaction between optical light and Mott-Hubbard systems has been extensively studied in early works by Elliot, Loudon and Fleury [136, 137], as well as by Shasthry and Shairman[138]. This typically leads to a Raman operator, that describes the light-spin coupling, proportional to the spin exchange Hamiltonian itself. Motivated by intriguing recent experiments conducted on the Kitaev material $\alpha-\mathrm{RuCl}_3$[139, 140], we compute the Raman response from the Ising anyons of a weakly perturbed ferromagnetic Kitaev chiral spin liquid.

At the time of writing this thesis, a manuscript based on this chapter is being prepared, to be submitted for publication. "Raman response from anyons in Kitaev materials." A P Joy and Achim Rosch, in preparation.

7.1 Raman Response of the Kitaev Model: Review

The Raman response of the Kitaev model was first studied by Knolle *et al.* [1]. The authors considered a pure Kitaev model with a weak Heisenberg perturbation. Within the Loudon-Fleury theory, the Raman operator has a similar form to the exchange Hamiltonian.

$$\mathscr{R}_{LF} = (\boldsymbol{e}_{in}\cdot\boldsymbol{d}_{\langle ij\rangle_\alpha})(\boldsymbol{e}_{out}\cdot\boldsymbol{d}_{\langle ij\rangle_\alpha})(K_R\sigma_i^\alpha\sigma_j^\alpha + J_R\boldsymbol{\sigma}_i\cdot\boldsymbol{\sigma}_j) \tag{7.1}$$

where $\boldsymbol{d}_{\langle ij\rangle_\alpha}$ is the vector connecting the two sites. Crucially, previous theoretical studies assumed that the visons remain static, neglecting corrections from the Heisenberg term in the Hamiltonian. Recall the spin-Majorana mapping: the Kitaev term ($\sim -i\,u_{\langle ij\rangle}c_ic_j$) commutes with the gauge field and only couples to the matter fermions. The Heisenberg term, however, excites both the matter fermions and the four adjacent visons. See Fig.7.3b. In the gapless phase, the main result is a broad continuum, reflecting the Majorana density of states, alongside

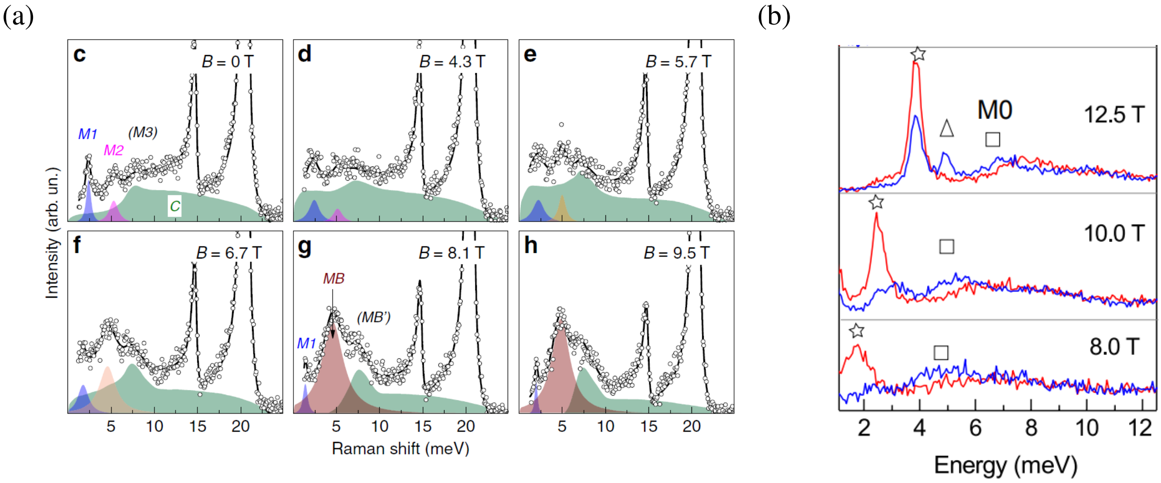

Fig. 7.2 **Raman response of $\alpha-$RuCl$_3$ in the field induced phase.** When an external magnetic field suppresses the magnetic order, $\alpha-$RuCl$_3$ seems to enter into a disordered phase possibly described by a perturbed Kitaev model. The Raman response in this regime features both multi-particle continua as well as sharp peaks. (a.) Figure adapted from Ref. [140] shows sharp modes which were attributed to bound-states of anyons. (b) Figure adapted from Ref. [139] shows the polarization dependence of the Raman response, specifically in cross-circularly polarized geometries. Red (blue) corresponds to $LR(RL)$ polarization channels. Ref. [139] identifies the M0 mode in (b.) with the MB mode of (a.).

a sharp peak at the four-vison energy gap, as shown in Fig. 7.1a. The response from the Kitaev term was found to be polarization-independent, whereas the Heisenberg contribution exhibits a weak polarization dependence.

In this chapter, we consider a scenario that may be more relevant to the magnetic field-induced spin liquid phases suspected to exist in Kitaev materials. We will argue that, in a generic Kitaev liquid, Raman processes naturally couple to dynamical visons[1] (or equivalently, the Ising anyons) allowing for the direct probing of the emergent gauge sector.

7.2 Raman Experiments on $\alpha-$RuCl$_3$

As a concrete example, we review some of the main results of Raman spectroscopy experiments done on $\alpha-$RuCl$_3$. Early works of Nasu *et al.*. [76] and Sandilands *et al.*. [133] analysed the Raman response at zero external magnetic field. Since $\alpha-$RuCl$_3$ magnetically orders below ~ 7 K, the study was conducted at higher temperatures to access the putative proximate spin liquid regime. The temperature evolution of the spectrum was found to be consistent with the presence of fermionic quasiparticles which was suggested as evidence for the existence of matter Majorana fermions in the system. (see Fig. 7.1b.) This was further supported by the

---

[1] Since visons become Ising anyons in the chiral phase, the terms 'vison' and 'anyon' are used interchangeably in this chapter.

theoretical claim that the Raman operators in a pure Kitaev model (essentially the Kitaev term), exclusively excite the matter Majorana fermions, as discussed above.

More recently, Raman spectroscopy experiments were done in a finite magnetic field, probing the intermediate field regime where a half-quantized thermal Hall effect was observed in $\alpha-\mathrm{RuCl}_3$. However, the interpretation of these results is more involved. In all the studies, both a continuum and multiple sharp peaks were observed, with the modes displaying strong polarization dependence. In a study by Wulferding *et al.*. [140], a sharp mode was detected in the field range of 7-8 T which was attributed to bound-states of anyons (MB in Fig.7.2a). This experiment employed a configuration where the incident wave was right-circularly polarized and the scattered light was detected in left-circularly polarized channel (*RL* configuration). Intriguingly, a more detailed polarization-resolved study by Sahasrabudhe *et.al.* [139] found that this mode indeed does not show up in an *LR* configuration. Furthermore, they found other sharp peaks that only emerge in certain polarization geometries.

This discussion raises important questions about the nature of excitations in the intermediate field regime of $\alpha-\mathrm{RuCl}_3$. It is important to clarify if the features in Raman response arise from relatively trivial (partially) polarized state or if they are indeed signatures of the fractionalized quasiparticles characteristic of the chiral spin liquid. Given that the magnetic field ranges used in Ref. [139] and [140] coincide with the regime where the half-quantized THE was been observed by Kasahara*et al.* [42] (although on different samples), a detailed calculation of Raman response from a realistic model is necessary. In this chapter, we develop a low-energy effective model for a generic Kitaev liquid, based on the insights from previous chapters and study the Raman response from dynamical visons.

We consider a hierarchy of energy levels as sketched in Fig. 7.4a. The Majorana spectrum has a gap Δ_m which we assume to be much larger than the vison gap E_v^0. The single anyon band structure is determined by the static vison gap Δ_v and the hopping rates. The relation between Δ_m and Δ_v in the pure Kitaev model is shown in Fig. 7.4b. For reasonably large values of Δ_m (e.g, $\Delta_m \approx |K|$), the vison gap is well below the Majorana gap. Once dynamical, they acquire dispersion, further lowering the vison gap. In this framework, within the chiral spin liquid phase of the Kitaev type, visons are the low-energy bulk degrees of freedom that dominate the Raman response.

7.3 Light-Vison Coupling

To calculate the Raman response, we first need to understand how optical light interacts with visons. At first glance, it is not obvious how the emergent gauge field interacts with the real electromagnetic (gauge) field. At the most fundamental level, electromagnetic fields couple to the electrons of the magnetic atoms [137, 141], leading to virtual electron hopping between them, assisted by photons. This process, in turn, generates spin-spin couplings that are described by Raman operators.

In the conventional approach, developed by Loudon and Fleury [137], Raman operators arise from super-exchange processes similar to those that give rise to the spin Hamiltonian itself. The only difference is that the exchange is photon-assisted, and therefore comes with polarization-dependent prefactors. However, in a notable recent study, Yang, Li, Rousochatzakis and Perkins demonstrated that the presence of multiple exchange paths between the magnetic ions, mediated by ligands, can induce extra contributions beyond the Loudon-Fleury theory [141]. They derived the most general form of Raman operators for Kitaev magnets, including α-RuCl$_3$. A full derivation of these operators starting from the underlying Hubbard model is beyond the scope of this thesis, and I refer the reader to Ref. [141] for a detailed discussion.

Following Yang *et al.*, the full Raman operator for a $J-K-\Gamma$ model can be written as

$$\mathscr{R}(\boldsymbol{e}_{in},\boldsymbol{e}_{out}) = \sum_{\langle ij\rangle_\alpha} \mathscr{R}^K + \mathscr{R}^\Gamma + \mathscr{R}^J + \mathscr{R}^h \tag{7.2}$$

where

$$\begin{aligned} \mathscr{R}^J &= \sum_{\langle ij\rangle_\alpha} P^J_{ij} \boldsymbol{\sigma}_i \cdot \boldsymbol{\sigma}_j, & \mathscr{R}^K &= \sum_{\langle ij\rangle_\alpha} P^K_{ij} \sigma_i^\alpha \sigma_j^\alpha \\ \mathscr{R}^\Gamma &= \sum_{\langle ij\rangle_\alpha} P^\Gamma_{ij} (\sigma_i^\beta \sigma_j^\gamma + \sigma_j^\beta \sigma_i^\gamma), & \mathscr{R}^h &= \sum_{\langle ij\rangle_\alpha} P^h_{ij} (\sigma_i^\alpha + \sigma_j^\alpha). \end{aligned} \tag{7.3}$$

$\boldsymbol{e}_{in}$ and $\boldsymbol{e}_{out}$ are the polarization vectors of the incident and reflected light respectively.

The Kitaev-like term $\mathscr{R}^K \sim iu_{ij}c_ic_j$ does not excite the visons and only couple to the matter Majoranas. Within our approach, the Majoranas have a large energy gap compared to the visons. Therefore, we omit the Kitaev term in our calculations, which is justified in the low-energy limit. While the off-diagonal term, $\mathscr{R}^\Gamma$, and the magnetic field-like term $\mathscr{R}^h$ create pairs of nearest neighbour and next-nearest neighbour visons respectively, the Heisenberg term, $\mathscr{R}^J$, generates four visons, which is a higher-energy process. This is illustrated in Fig. 7.3b. Consequently, the lowest energy Raman processes are primarily contributed by $\mathscr{R}^\Gamma$ and $\mathscr{R}^h$, and we will focus on these terms in the remainder of this chapter.

The coefficients P_{ij} encode the polarization dependence for a given link $\langle ij\rangle$. We use the expressions for these geometric factors as derived in Ref. [141].

$$\begin{aligned} P^\Gamma_{\langle ij\rangle_\alpha} &= -\frac{\Gamma_R}{2} \boldsymbol{e}_{in} \cdot \boldsymbol{d}_{\langle ij\rangle_\alpha}\, \boldsymbol{e}_{out} \cdot \boldsymbol{d}_{\langle ij\rangle_\alpha}, \\ P^h_{\langle ij\rangle_\alpha} &= -i\frac{h_R}{2} (\boldsymbol{e}_{in} \cdot \boldsymbol{d}^\perp_{\langle ij\rangle_\alpha}\, \boldsymbol{e}_{out} \cdot \boldsymbol{d}_{\langle ij\rangle_\alpha} - \boldsymbol{e}_{in} \cdot \boldsymbol{d}_{\langle ij\rangle_\alpha}\, \boldsymbol{e}_{out} \cdot \boldsymbol{d}^\perp_{\langle ij\rangle_\alpha}), \end{aligned} \tag{7.4}$$

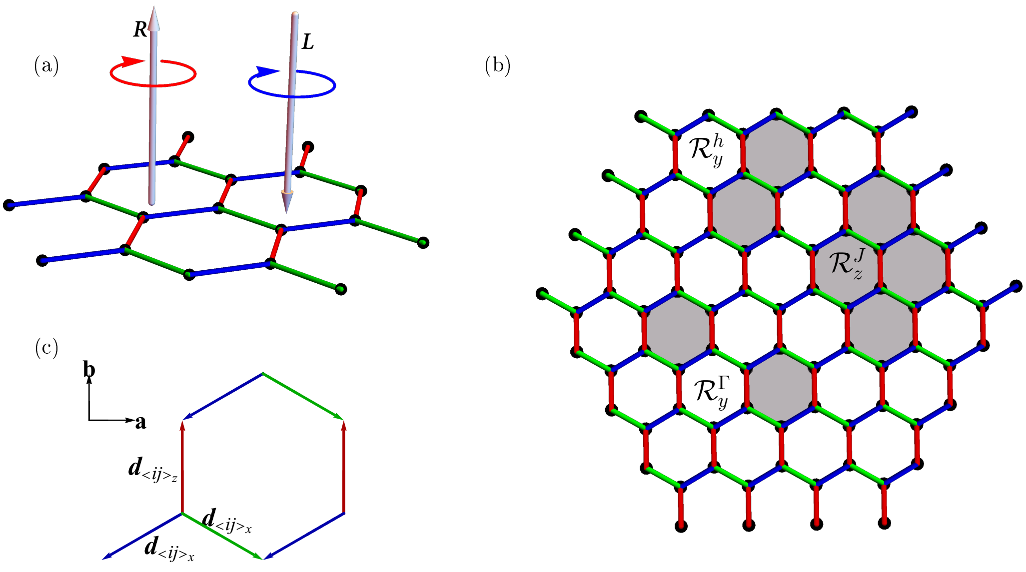

Fig. 7.3 **Experimental geometry and coordinate vectors.**(a) An incident left-circularly polarized light (L) is incident on the sample perpendicular to the honeycomb plane. The reflected light is detected in the right-circular polarization channel (R). (b) Illustration of vison creation/annihilation by different Raman operators defined in Eq. (7.3). A given term in $\mathscr{R}^\Gamma$ and $\mathscr{R}^h$ creates pairs of visons while a term in $\mathscr{R}_J$ creates four visons. (c.) Definition of lattice vectors used in the polarization factors of Raman operators.

where $\boldsymbol{d}_{\langle ij\rangle_\alpha}$ is the vector (from sublattice A to B) corresponding to α-type bond and $\boldsymbol{d}^\perp_{\langle ij\rangle_\alpha}$ is the vector perpendicular to it. (See Fig. 7.3a for the definitions.) Γ_R and h_R define the strengths of the Raman couplings, whose values are material specific, requiring microscopic details.

7.3.1 Experimental geometry

We have the following experimental geometry in mind. The 2D honeycomb plane lies in the xy plane, as shown in Fig. 7.3. The incoming light has a wave-vector $\boldsymbol{k}_{in} = -|k_z|\hat{z}$ perpendicular to the plane, and the outgoing light is detected in the $-\hat{z}$ direction. The polarization vectors of the incident light $\boldsymbol{e}_{in}$ and reflected light $\boldsymbol{e}_{out}$, therefore, lie in the xy plane, and are expressed in terms of the crystallographic axes $\boldsymbol{a} = (1,0)$ and $\boldsymbol{b} = (0,1)$. Linear polarization channels are defined by choosing $\boldsymbol{e}_{in}$ and $\boldsymbol{e}_{out}$ to be parallel to $\boldsymbol{a}$ or $\boldsymbol{b}$. Right (Left) circular polarized light has a polarization vector defined in the complex plane as $\boldsymbol{a}+i\boldsymbol{b}$ $(\boldsymbol{a}-i\boldsymbol{b})$, where the imaginary part encodes the $\pi/2$ phase difference that defines circular polarization. For example, in the LR polarization channel, shown schematically in Fig. 7.3a, $\boldsymbol{e}_{in} = (\boldsymbol{a}-i\boldsymbol{b})/\sqrt{2}$ and $\boldsymbol{e}_{out} = (\boldsymbol{a}+i\boldsymbol{b})/\sqrt{2}$.

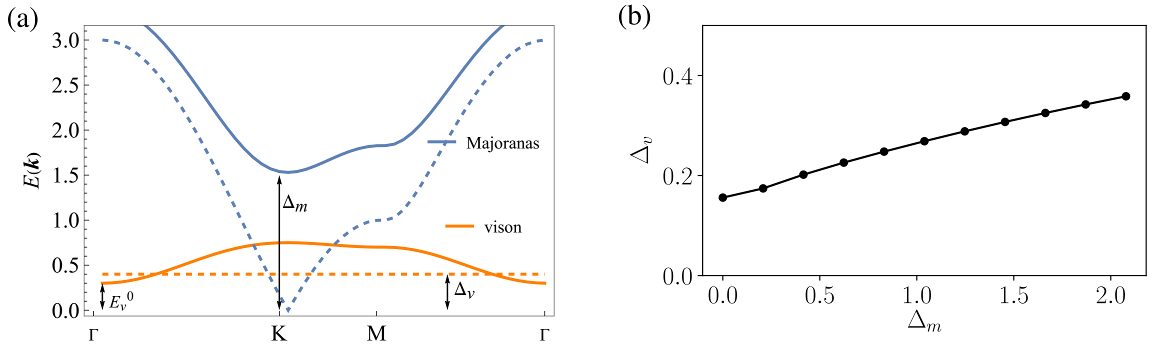

Fig. 7.4 **Hierarchy of excitations in the chiral spin liquid.** (a) Schematic band structures of Majorana fermions (blue) and visons (orange) in a perturbed Kitaev's chiral liquid considered in this chapter. The pure Kitaev model has a flat vison band and a gapless Majorana dispersion (dashed lines). In the chiral phase, Majoranas acquire a gap Δ_m and the visons acquire a finite dispersion (solid lines). We consider the scenario where $\Delta_m \gg E_v^0$, making the low-energy bulk degrees of freedom primarily mobile visons. (b) Vison gap as a function of Δ_m computed for the pure Kitaev model.

7.4 Raman response

At zero temperature ($T = 0$), the Raman intensity can be calculated using linear response theory,

$$I(t) = \langle\Psi_0|\mathscr{R}_{2v}(t)\mathscr{R}_{2v}(0)|\Psi_0\rangle = \langle\Psi_0|e^{-iHt}\mathscr{R}_{2v}(0)e^{iHt}\mathscr{R}(0)|\Psi_0\rangle \tag{7.5}$$

where we have approximated the full Raman operator with the low-energy part within the two-vison sector defining $\mathscr{R}_{2v} = \mathscr{R}^{\Gamma} + \mathscr{R}^{h}$. $|\Psi_0\rangle$ is the ground state of the system described by a perturbed ferromagnetic Kitaev chiral spin liquid Hamiltonian H. Within our model, the Majorana fermions are gapped out and the visons obtain a band structure with energy gap E_v^0. (See Fig. 7.4 for a schematic). The ground state therefore has no visons. $\mathscr{R}_{2v}$ acting on $|\Psi_0\rangle$ creates states with a pair of visons which then evolve according to the unitary operator $e^{iHt/\hbar}$.

Fourier transforming to frequency space, and using Lehman representation, we can rewrite the above expression yielding the golden rule formula,

$$I(\omega) = \frac{2\pi}{\hbar}\sum_n |\langle n|\mathscr{R}_{2v}|\Psi_0\rangle|^2 \delta(\omega - (E_n - E_0)) \tag{7.6}$$

where $|n\rangle$ corresponds to the eigenstates of the Hamiltonian projected on to the two-vison subspace. E_n is the energy of $|n\rangle$ and E_0 is the ground state energy which will be assumed to be zero. Our task now is to find $|n\rangle$ which amounts to solving the Hamiltonian of a pair of visons in a perturbed Kitaev chiral liquid.

7.5 Two-particle effective model

In the previous chapters, we showed that in a generic perturbed ferromagnetic Kitaev model, anyons are mobile and can be described by a tight-binding model on the dual triangular lattice. In principle, the hopping amplitudes are determined by the weak non-Kitaev terms (as detailed in Chapter 3. However, here we set aside these microscopic details and treat the hopping rates as unknown parameters.

In the non-interacting limit, the Hamiltonian of a system of two particles, with coordinates $\boldsymbol{r}_1$ and $\boldsymbol{r}_2$ hopping on the triangular lattice is given by

$$H^0 = \sum_{j=1,2} \sum_{\boldsymbol{r}_j,i} \left(t_{nn}(\boldsymbol{\delta}_i^{nn}) \left|\boldsymbol{r}_j\right\rangle \left\langle \boldsymbol{r}_j + \boldsymbol{\delta}_i^{nn}\right| + t_{nnn}(\boldsymbol{\delta}_i^{nnn}) \left|\boldsymbol{r}_j\right\rangle \left\langle \boldsymbol{r}_j + \boldsymbol{\delta}_i^{nnn}\right| \right) + \text{h.c}, \tag{7.7}$$

where $\boldsymbol{\delta}_i^{nn}$ and $\boldsymbol{\delta}_i^{nnn}$ denote the six nearest (*nn*) and next-nearest neighbour vectors (*nnn*). In the absence of interactions, the dynamical response will therefore be simply given by the two-anyon continuum, specified by the dispersion

$$E_{2v}(\boldsymbol{K}) = E_v(\boldsymbol{q}) + E_v(\boldsymbol{K} - \boldsymbol{q}), \tag{7.8}$$

where the single-particle dispersion

$$E_v(\boldsymbol{q}) = E_v^0 + \sum_i 2t_{nn} \cos\left(\boldsymbol{q} \cdot \boldsymbol{\delta}_i^{nn}\right) + 2t_{nnn} \cos\left(\boldsymbol{q} \cdot \boldsymbol{\delta}_i^{nnn}\right). \tag{7.9}$$

For a given total momentum $\boldsymbol{K}$, there is a continuum of energy levels corresponding to the values of $\boldsymbol{q}$.A standard approach for studying two-body problems is to utilize relative and center of mass (COM) coordinates. However, applying this in a lattice model requires some care.

Due to the overall translation symmetry, the total momentum $\boldsymbol{K}$ is a good quantum number. We can thus use the plane wave basis defined by

$$\left|\boldsymbol{K}, \boldsymbol{r}\right\rangle = \frac{1}{L} \sum_{\boldsymbol{R}} e^{i\boldsymbol{K}\cdot(\boldsymbol{R}+\frac{\boldsymbol{r}}{2})} \left|\boldsymbol{R}, \boldsymbol{R}+\boldsymbol{r}\right\rangle, \tag{7.10}$$

where $\boldsymbol{R} = \frac{(\boldsymbol{r}_1+\boldsymbol{r}_2)}{2}$ is the COM position and $\boldsymbol{r} = \boldsymbol{r}_1 - \boldsymbol{r}_2$ is the relative coordinate. L is the linear system size required for normalization. The action of H_0 on this state does not change the total momentum $\boldsymbol{K}$, allowing us to derive the following Hamiltonian in the relative coordinate space.

$$H^0_{rel} = \sum_{\boldsymbol{r},i} \left(\tilde{t}_{nn}(\boldsymbol{\delta}_i^{nn}) \left|\boldsymbol{r}\right\rangle \left\langle \boldsymbol{r} + \boldsymbol{\delta}_i^{nn}\right| + \tilde{t}_{nnn}(\boldsymbol{\delta}_i^{nnn}) \left|\boldsymbol{r}\right\rangle \left\langle \boldsymbol{r} + \boldsymbol{\delta}_i^{nnn}\right| \right) + \text{h.c} \tag{7.11}$$

where $\tilde{t}_{nn}(\boldsymbol{\delta}_i^{nn}) = 2\, t_{nn}(\boldsymbol{\delta}_i^{nn}) \cos\left(\frac{\boldsymbol{K}\cdot\boldsymbol{\delta}_i^{nn}}{2}\right)$ and $\tilde{t}_{nnn}(\boldsymbol{\delta}_i^{nnn}) = 2\, t_{nnn}(\boldsymbol{\delta}_i^{nnn}) \cos\left(\frac{\boldsymbol{K}\cdot\boldsymbol{\delta}_i^{nnn}}{2}\right)$.

For a given total momentum $\boldsymbol{K}$, the relative coordinate Hamiltonian thus reduces to a tight-binding model with modified hopping amplitudes dependent on $\boldsymbol{K}$. In this chapter, we will focus exclusively on the case where the total momentum $\boldsymbol{K} = 0$. This condition is satisfied because Raman scattering typically involves zero momentum transfer. Consequently, we will set $\tilde{t}_{nn} = 2\, t_{nn}$ and $\tilde{t}_{nnn} = 2\, t_{nnn}$ for the rest of this chapter.

In the absence of interactions, the eigenstates of the system can be labeled by the total momentum $\boldsymbol{K}$ and the relative momentum $\boldsymbol{q}$:

$$|\Psi_{2v}(\boldsymbol{K},\boldsymbol{q})\rangle = \frac{1}{L}\sum_{\boldsymbol{R}} e^{i\boldsymbol{K}\cdot\boldsymbol{R}} \sum_{\boldsymbol{r}} e^{i\boldsymbol{q}\cdot\boldsymbol{r}}\, |\boldsymbol{R},\boldsymbol{r}\rangle\,. \tag{7.12}$$

However, this independent vison approximation is rather incomplete due to the presence of both long-range and short range-interactions, which we will discuss now.

7.5.1 Long-range statistical interaction

We now remind ourselves that in the non-Abelian phase under consideration, visons are Ising anyons characterized by a statistical exchange interaction. For two Ising anyons created out of the ground state, with coordinates $\boldsymbol{r}_1$ and $\boldsymbol{r}_2$, the total wavefunction $\Psi(\boldsymbol{r}_1,\boldsymbol{r}_2)$ transforms non-trivially under exchange.

$$\Psi(\boldsymbol{r}_1,\boldsymbol{r}_2) = e^{i\frac{\pi}{8}}\Psi(\boldsymbol{r}_2,\boldsymbol{r}_1), \tag{7.13}$$

provided $|\boldsymbol{r}_1 - \boldsymbol{r}_2| \gg \xi$, where $\xi \propto \frac{1}{\Delta_m}$ is the localization length of the Majorana mode attached to each particle. This was already discussed in Chapter 2. Exchanging them twice is topologically equivalent to moving one particle around the other. By analogy to the well-known Aharonov-Bohm effect, a single anyon perceives the other as a source of $\frac{\pi}{4}$ flux. This insight can be used to represent the anyonic nature as a 'magnetic' flux attached to each particle. This *flux-attachment* process is a powerful tool for understanding anyons in a variety of systems [142, 143]. In the following, we will employ this technique to solve the dynamics of a pair of anyons.

7.5.2 Short-range interaction

When the visons are at a finite separation, the Majorana modes attached to them can overlap, leading to a splitting of the two zero energy modes. This results in an effective interaction between two anyons that depends on their relative distance. Several early works on the Kitaev

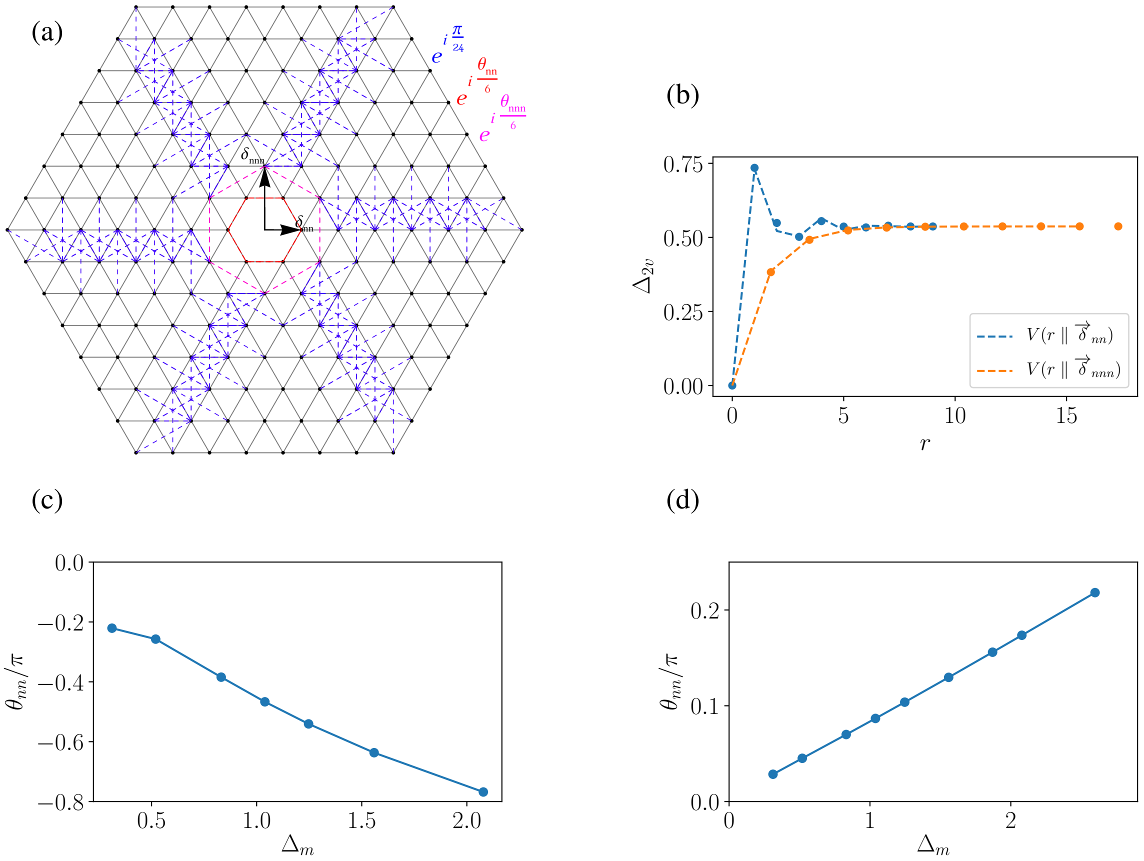

Fig. 7.5 **Two-particle effective model of anyon pair dynamics.** (a) Relative coordinate space of a pair of Ising anyons in the Kitaev model form a triangular lattice. The effective Hamiltonian is mapped to a tight-binding model on this triangular lattice with *nn* and *nnn* hopping. Absence of hopping to the origin implements the hardcore condition. Away from the origin, universal non-trivial statistics of the anyons enforce a phase change $\theta = \frac{\pi}{4}$, when one particle loops around the other (implemented as Peierls phase factors multiplying the hopping amplitudes shown in blue). Near the origin, anyon-pairs acquire local Berry phases θ_{nn} (red) and θ_{nnn} (magenta) for a *nn* and *nnn* pair respectively. Their values, as a function of Δ_m, are shown in (c) and (d). (b) (Physical) Ground state energy of a pair of anyons as a function of their relative separation ($\Delta_m = 1.03, N = 34 \times 34$). The numerically obtained data (points) can be excellently fitted by the analytical form of Eq. (7.14) (dashed). The plot is obtained for $\Delta_m = 1.0\ |K|$.

model have thoroughly studied this effect [144–146]. Fig. 7.5b shows the ground state energy of a two-anyon system (relative to the anyon free ground state) as a functions of their separation r. The anyons belong to the vacuum sector, created locally by a single spin flip acting on the ground state. In the pure Kitaev model with a Majorana gap Δ_m, the numerical values can be excellently fitted to an analytical form derived from previous studies

$$V(\boldsymbol{r}) = \Delta_{2v}(r \to \infty) - \Delta_{2v}(r \to \infty) \cos\left(\frac{\boldsymbol{K}_D \cdot \boldsymbol{r}}{2}\right) e^{-r/\xi}. \tag{7.14}$$

Here, $\xi \approx \frac{1.43}{\Delta_m}$ (obtained from the fit) denotes the localization length of the Majorana zero modes, and $\boldsymbol{K}_D = (\frac{4\pi}{3\sqrt{3}}, 0)$ is the Dirac point in momentum space. As a side note, when calculating the ground state energy for a given vison pair configuration numerically, one has to implement the projection operator to obtain the correct physical quantities. This interaction is short-ranged and can be neglected when they anyons are well separated. However, as Fig.7.5 shows, there is a sizeable next-nearest neighbour attractive potential of approximately 0.3 Δ_m which may induce bound states in some cases, as we will see later.

Within our model, anyons are treated as hardcore particles, meaning they cannot occupy the same site. In fact, two visons at the same site is equivalent to no visons by their $\mathbb{Z}_2$ nature, which would take the system out of the two-particle subspace.

Berry phases of anyon pairs

The universal exchange phase of $\theta = \frac{\pi}{8}$ is strictly valid only when the anyons are well separated ($r \gg \xi$). When anyons are close to each other, both the energy splitting and the hopping amplitudes are modified. We account for this short-range effect by explicitly calculating the hopping matrix elements for nearest-neighbor (nn) and next-nearest-neighbor (nnn) pairs. In the relative coordinate space, this leads to a different Berry flux near the origin different than the universal $\frac{\pi}{4}$. This is illustrated in Fig. 7.5a, where an *nn*-pair taken around the origin acquires a phase θ_{nn} (red lies) while an *nnn*-pair acquires a Berry phase θ_{nnn} (magneta lines). Fig.7.5 c and d show the values of these phases as a function of the Majorana gap Δ_m. Beyond *nnn* separation, universal value $\frac{\pi}{4}$ is implemented.

7.6 Raman Intensity Calculation

We will now use the two-particle model derived above to compute the Raman response. The total Hamiltonian of the two-anyon system can be decoupled into center of mass (COM) and relative coordinate frames. Given the discrete translational symmetry of the system, the COM motion corresponds to that of a free-particle on a triangular lattice with momentum denoted by $\boldsymbol{K}$. The relative part of the Hamiltonian is governed by the effective model we derived in the previous section. (See Fig. 7.5.)

Effective Hamiltonian

$$H_{rel} = \sum_{\boldsymbol{r},i} \tilde{t}_{nn}(\boldsymbol{r}, \boldsymbol{\delta}_i^{nn}) \left|\boldsymbol{r}\right\rangle \left\langle \boldsymbol{r} + \boldsymbol{\delta}_i^{nn}\right| + \tilde{t}_{nnn}(\boldsymbol{r}, \boldsymbol{\delta}_i^{nnn}) \left|\boldsymbol{r}\right\rangle \left\langle \boldsymbol{r} + \boldsymbol{\delta}_i^{nnn}\right| + \sum_{\boldsymbol{r}} V(\boldsymbol{r}) + \text{h.c}, \quad (7.15)$$

where $\tilde{t}_{nn}(\boldsymbol{r},\boldsymbol{\delta}_i^{nn})$ and $\tilde{t}_{nnn}(\boldsymbol{r},\boldsymbol{\delta}_i^{nnn})$ are position dependent hopping amplitudes. $\tilde{t}_{nn}(0,\boldsymbol{\delta}_i^{nn}) = 0$ and $\tilde{t}_{nnn}(0,\boldsymbol{\delta}_i^{nnn}) = 0$ encode the hardcore condition. The hopping amplitudes are generally complex and incorporate the Peierls phase factors which account for the non-trivial exchange statistics θ as well as the local Berry phases θ_{nn} and θ_{nnn}. We diagonalize this Hamiltonian on a finite triangular lattice to obtain the full spectrum and eigenfunctions.

There is, however, an important caveat. Since we model the exchange phase of anyons using a flux attachment process, we must first define their statistics before attaching the flux. Here, we choose bosonic statistics, which requires the wavefunctions to be symmetric, restricting the angular momentum quantum numbers to even values. Technically, we implement this by diagonalizing the Hamiltonian in the even angular momentum sectors. For a triangular lattice with symmetry group C_6, the allowed angular momenta are $l = 0, \pm 2$. The Hamiltonian can be efficiently diagonalized in these sectors for system sizes of the order 10^4 sites.

The real space wave-functions corresponding to the n^{th} eigenstate can be written as

$$\left|\phi_n^{2v}\right\rangle = \sum_{\boldsymbol{r}} \chi_n(\boldsymbol{r})\,|\boldsymbol{R},\boldsymbol{r}\rangle \tag{7.16}$$

where $|\boldsymbol{R},\boldsymbol{r}\rangle$ denotes the two vison state parametrized by the COM position $\boldsymbol{R}$ and relative coordinate $\boldsymbol{r}$. The energy E_{2v}^n, and amplitudes $\chi_n(\boldsymbol{r})$ are obtained numerically. Including the center of mass dynamics, we can express the full set of eigenstates labelled by COM momentum $\boldsymbol{K}$ and the index n

$$\left|\Psi^{2v}(\boldsymbol{K},n)\right\rangle = \frac{1}{L}\sum_{\boldsymbol{R}} e^{i\boldsymbol{K}\cdot\boldsymbol{R}}\left|\phi_n^{2v}\right\rangle \tag{7.17}$$

We can now substitute $\left|\Psi^{2v}(\boldsymbol{K},n)\right\rangle$ in Eq. (7.6) to evaluate the Raman spectrum.

$$I(\omega) = \sum_n \frac{2\pi}{\hbar}\int \frac{d\boldsymbol{K}}{(2\pi)^2}\left|\sum_{\boldsymbol{R},\boldsymbol{r}} \frac{e^{-i\boldsymbol{K}\cdot\boldsymbol{R}}}{L}\chi_n^*(\boldsymbol{r})\,\langle\boldsymbol{r},\boldsymbol{R}|\sum_{\boldsymbol{R}'}\left(\mathscr{R}^h(\boldsymbol{R}') + \mathscr{R}^\Gamma(\boldsymbol{R}')\right)|\Psi_0\rangle\right|^2 \delta(\omega - E^r{}_n - E^{\text{COM}}(\boldsymbol{K})) \tag{7.18}$$

where the total energy of a state $|n,\boldsymbol{K}\rangle$ is given by the sum of the COM kinetic energy $E^{\text{COM}}(\boldsymbol{K})$ and eigen-energies E_n^r.

We now parametrize the sum within the Raman operator (over $\boldsymbol{R}'$) using the COM and relative coordinates. $\mathscr{R}^h(\boldsymbol{R},\boldsymbol{\delta}_i^{nn})$ creates a nearest neighbour pair of visons separated by $\boldsymbol{\delta}_i^{nn}$ and center of mass positioned at $\boldsymbol{R}+\boldsymbol{\delta}_i^{nn}/2$, as illustrated in Fig. 7.6. $\mathscr{R}^\Gamma(\boldsymbol{R})$ creates a next-nearest neighbour pair of visons separated by $\boldsymbol{\delta}_i^{nnn}$, with the center of mass at $\boldsymbol{R}+\boldsymbol{\delta}_i^{nnn}/2$. From the

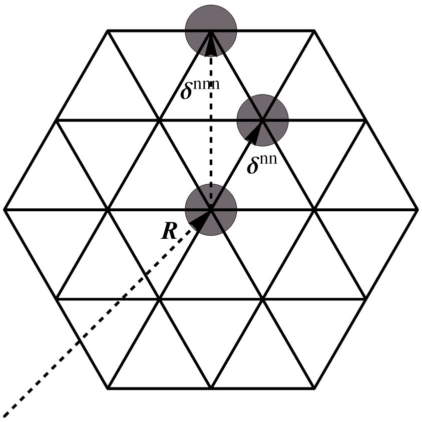

Fig. 7.6 **Parametrization of Raman operator in the lattice.** Raman operator $\mathscr{R}^h(\boldsymbol{R},\delta_{nn})$ creates a pair of visons at $\boldsymbol{R}$ and $\boldsymbol{R}+\boldsymbol{\delta}_{nn}$ while $\mathscr{R}^\Gamma(\boldsymbol{R},\boldsymbol{\delta}_{nnn})$ creates a pair at $\boldsymbol{R}$ and $\boldsymbol{R}+\boldsymbol{\delta}_{nnn}$. See main text.

orthogonality of different flux sectors, it follows that

$$\langle \boldsymbol{r},\boldsymbol{R}|\mathscr{R}^h(\boldsymbol{R}',\boldsymbol{\delta}_i^{nn})\,|\Psi_0\rangle \;\propto\; \delta\left(\boldsymbol{R}-\boldsymbol{R}'-\frac{\boldsymbol{\delta}_i^{nn}}{2}\right)\delta(\boldsymbol{\delta}_i^{nn}-\boldsymbol{r}). \tag{7.19}$$

Using the above relations, and carrying out the sums in Eq.(**??**), we obtain a concise expression for the Raman intensity

$$I(\omega)=\frac{2\pi}{\hbar}\sum_n |M_n^h+M_n^\Gamma|^2\delta(\omega-E_n^r-E_0^{\rm COM}) \tag{7.20}$$

where $E_0^{\rm COM}=E^{\rm COM}(\boldsymbol{K}=0)$ gives only a constant shift to the onset of the spectrum. In the following, we fix this to zero for convenience. The matrix elements for pair creation are given by

$$M_n^h=\sum_i \chi_n^*(\boldsymbol{\delta}_i^{nn})\,\langle 0,\boldsymbol{\delta}_i^{nn}|\mathscr{R}^h(0,\boldsymbol{\delta}_i^{nn})\,|\Psi_0\rangle\,,\qquad M_n^\Gamma=\sum_i \chi_n^*(\boldsymbol{\delta}_i^{nnn})\,\langle 0,\boldsymbol{\delta}_i^{nnn}|\mathscr{R}^\Gamma(0,\boldsymbol{\delta}_i^{nnn})\,|\Psi_0\rangle \tag{7.21}$$

where the sum is over the *nn* and *nnn* bonds around the origin. These matrix elements can be evaluated numerically using the Pfaffian approach. The fact that the COM momenta $\boldsymbol{K}$ does not appear in the response is consistent with the fact that Raman scattering is a zero momentum transfer process. The absence of the center of mass momentum $\boldsymbol{K}$ in the response is consistent with the nature of Raman scattering as a zero momentum transfer process.

Remark on the superselection sector Note that we have fixed the anyon-free initial state $|\Psi_0\rangle$ to be the ground state of the matter sector. This automatically fixes the superselection sector to be the vacuum, consequently fixing the value of θ to $\frac{\pi}{8}$. To create an anyon-pair in the fermionic sector, with $\theta=-3\pi/8$, the anyon free initial state must have an extra matter fermion. However, due to the large Majorana gap Δ_m, this process typically requires a finite temperature.

7.7 Warm-up: Non-interacting Anyons

Before delving into the Ising anyons of the Kitaev liquid, it is helpful to first examine simpler models of dynamical anyons. By doing so, we can gain insight into certain universal features in spectroscopy, particularly those that arise when considering free anyons that interact solely through their statistical exchange phase

7.7.1 Power-law onset: Band with a single minimum

In a significant contribution, Morampudi *et al.* [147] predicted that the statistical phase of abelian anyons leads to a characteristic power-law onset in their dynamical response. While visons are non-abelian anyons, within our effective two-particle model, they behave like abelian anyons with an exchange phase $\theta = \frac{\pi}{8}$. Drawing from the insights of Ref. [147], we anticipate observing similar a power-law behaviour in Raman spectrum. Let us briefly review the reasoning behind this.

Consider a tight-binding dispersion of a single anyon $E(\boldsymbol{k})$, which exhibits a single minimum at the Γ point ($\boldsymbol{k} = 0$). Near the band bottom, the Hamiltonian of a pair of non-interacting abelian anyons, characterized an exchange phase $\phi = 2\pi\alpha$, can be expanded and analyzed using relative and COM coordinates.

In the relative coordinate space, the problem reduces to a free particle of mass $\mu = m/2$ moving in the presence of a "magnetic" flux $\phi = 2\pi\alpha$ located at the origin. Here, the mass of the particle is defined at the band bottom by $m = (\frac{\partial^2 E(\boldsymbol{k})}{\partial \boldsymbol{k}^2})^{-1}$ evaluated at $\boldsymbol{k} = 0$. All interactions between the particles including their long-range statistical phase, manifest solely in the relative coordinate frame. The dynamics of the center of mass, on the other hand, is that of a free-particle with mass $2m$. The total Hamiltonian can be expressed as

$$H = \frac{K^2}{4m} + \frac{k_r^2}{m} + \frac{(l-\alpha)^2}{mr^2}, \tag{7.22}$$

where $\boldsymbol{K}$ is the COM momentum, k_r is radial component of the relative momentum $\boldsymbol{k}$, and $l \in 0, 2, 4, \ldots$ is the angular momentum quantum number of two particle system. Notice the shift in angular momentum by α, a direct consequence of the statistical phase.

The solution to the corresponding Schrödinger equation are given by Bessel functions of fractional order :

$$\psi_{k,l}(\boldsymbol{r}) \sim \sqrt{\frac{k}{L^3}} J_{|l+\alpha|}(kr). \tag{7.23}$$

where $\sqrt{\frac{k}{L^3}}$ is a normalization factor. Next, we consider a local operator $\mathscr{R}(\boldsymbol{\delta})$ that creates a pair of anyons separated by a distance $\boldsymbol{\delta}$, which is approximately a few lattice constants. The intensity at zero net momentum transfer ($\boldsymbol{K} = 0$) can be calculated by following the same steps as in the previous section, resulting in the response:

$$I(\omega, \boldsymbol{K} = 0) \sim \sum_l \int dk |\langle \psi_{k,l} | \mathscr{R}(\boldsymbol{\delta}) |0\rangle|^2 \delta(\omega - E^0_{2v} - k^2/2\mu). \tag{7.24}$$

At low frequencies near the band gap, i.e. $\omega \to E^0_{2v}$, the response will be dominated by $l = 0$ eigenstate. In this limit where $k\delta \ll 1$, the Bessel functions can be approximated by $J_{|\alpha|}(k\delta) \sim (k\delta)^\alpha$. This leads to a power law dependence of the intensity

Power-law onset

$$I(\omega, \boldsymbol{K} = 0) \sim (\omega - E^0_{2v})^\alpha. \tag{7.25}$$

For example, for semions (e and m particles of the toric code [30]), $\alpha = 0.5$, and $\alpha = 1$ for fermions. This effect can also be understood as a generalized exclusion principle, most familiar in the case of fermions. While multiple bosons can occupy the same quantum state, fermions exclude each other completely. Anyons are somewhere in between.

Corrections from hardcore constraint

It was noted in Ref.[147] that, for bosons $\alpha = 0$, short range repulsive interactions, such as those imposed by the hardcore constraint, significantly alter the power law onset, resulting in a logarithmic rather than a sharp onset. In our analysis, we extend this discussion to consider the effect of hardcore constraint on a general abelian phase. We find that the corrections get increasingly important as α gets below $\frac{1}{2}$. Hardcore condition in the relative coordinates translates into an infinite potential for $r < a$, where a is the lattice constant

$$I(\omega) \propto \frac{1}{1 + \tan^2(\delta_\alpha)} |J_\alpha(\sqrt{\omega}) - \tan(\delta_\alpha) Y_\alpha(\sqrt{\omega})|^2 \sim c_1(\omega - E^0_{2v})^\alpha + c_2(\omega - E^0_{2v})^{2\alpha}. \tag{7.26}$$

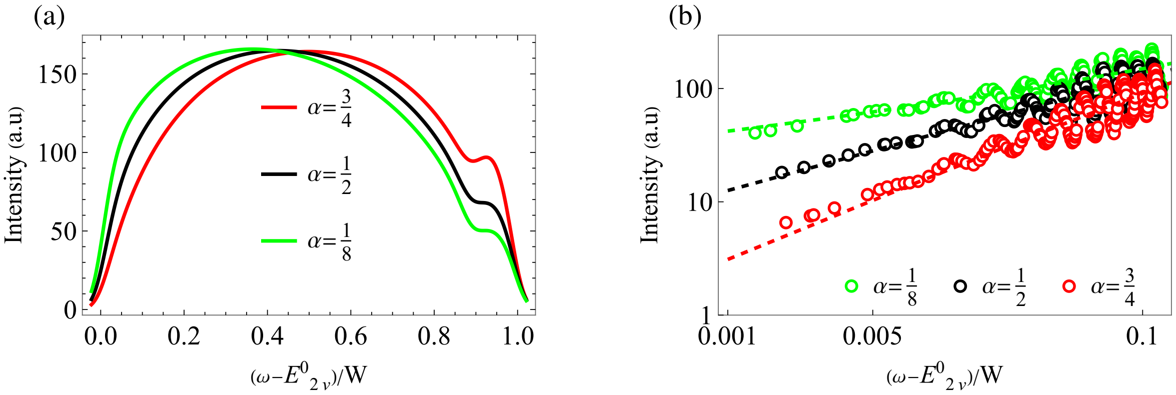

Fig. 7.7 **Raman spectrum for free anyons and the power law onset.** (a.) Raman spectra obtained for a pair of free (hardcore) anyons on a triangular lattice with exchange parameter α. E^0_{2v} denotes the gap to the two-particle continuum and W denotes the width of the continuum. (b.) Log-Log plot of the low energy onset. The dashed lines show the power law fits predicted by Eq. (7.26). The plots are obtained for a finite size triangular lattice with linear system size $L = 100$ sites. A Gaussian broadening of $\delta = 0.01$ is used in (a.). A smaller value, $\delta = 0.005$ is used to resolve the power-law in (b.)

Here, the phase shift δ_α is defined by $\tan(\delta_\alpha) = J_\alpha(a\sqrt{\omega})/Y_\alpha(a\sqrt{\omega})$, with Y_l being the Bessel function of the second kind. The above expressions recover the power-law ω^α with a leading correction $\sim \omega^{2\alpha}$.

Strictly speaking, we consider the Raman response and not the dynamical structure factor (probed by inelastic neutron scattering for example), as discussed in Ref. [147]. However, the pair production process should share similar physics and reflect the generalized exclusion principle. Fig. 7.7 shows the Raman spectra for anyons with three different values of α. Different power-law behaviours can be seen with the curves getting steeper as α decreases, as expected from Eq.(7.26).

Angular momentum selection rules and circular polarization

One feature that makes Raman scattering a versatile experimental probe is its polarization degree of freedom. Information about spatial symmetries of excitations can be accessed using light waves with different polarization vectors.Additionally, the chirality, or handedness, of excitations can be probed using circularly polarized light. This is best understood by looking at the angular momentum of the wavefunctions.

Left (Right)-circularly polarized light carries a quantum of angular momentum $+\hbar(-\hbar)$ [148, 149]. When the incident and reflected light possess the same angular momentum, there is no net angular momentum transfer to the system. This implies that the anyon-pair states that are involved in such a scattering process should have angular momentum $l = 0$. However, when the incident light is left (right)-circularly polarized and the reflected light is of the opposite

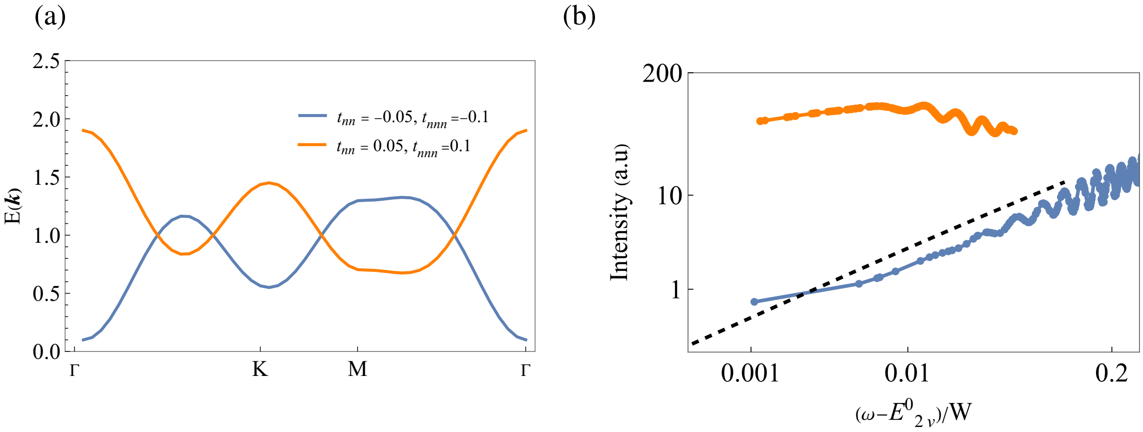

Fig. 7.8 **Multiple band-minima and power-law onset.** (a.) Two single-particle band structures on a triangular lattice with nearest and next-nearest-neighbour hopping rates shown. The anyons have an exchange parameter $\alpha = \frac{3}{4}$. In (b.), the expected power-law $(\omega - E^0_{2v})^{\frac{3}{4}}$ behaviour (dashed line) is observed for the case with a single band minima (blue), but not for multiple degenerate minima (orange). See main text for more details.

polarization, there is a net transfer of angular momentum $\Delta l = \pm 2\hbar$. Therefore, such a process couples only to states with $l = \pm 2$ depending on the incident polarization.

From the derivation above, it is clear that the power-law onset originates from the $l = 0$ states. Therefore, we naturally expect it to be most pronounced in the parallel polarization channel (*RR* or *LL*). Indeed we have used an *LL* channel in Fig. 7.7 to confirm this. Conversely, in the cross polarized channel (either *LR* or *RL*), only wavefunctions with a finite angular momenta ($l = \pm 2$) contribute and will lead to different power-laws, as we will see shortly.

7.7.2 Bands with multiple minima

Intuitively, the power-law onset results from the statistical repulsion of a pair of anyons arising from their exchange phase. Extending this argument, if there are multiple degenerate minima in the single-particle band structure, one may create two anyons close to each other locally but at different points in the momentum space. This may affect the power-law onset.

It is instructive to consider the case of fermions. If the band bottom is at the Γ point, the above described power-law is valid, since a Raman process can only create a pair with momenta $\boldsymbol{q}$ and $-\boldsymbol{q}$ near Γ. In the limit $\boldsymbol{q} \to 0$, we thus follow the derivation above and obtain the power-law $I(\omega) \sim \omega$. Now imagine that the band $E(\boldsymbol{k})$ has two degenerate minima at $\boldsymbol{K}_0$ and $-\boldsymbol{K}_0$ in the first Brillouin zone. One can create fermions at the two distinct minima with momenta $\boldsymbol{K}_0 + \boldsymbol{q}$ and $-\boldsymbol{K}_0 - \boldsymbol{q}$. In the limit of $\boldsymbol{q} \to 0$, or $\omega \to 2E(\boldsymbol{K}_0)$, the Raman matrix element for creating a pair, separated by $\boldsymbol{\delta}$, in Eq. (7.21) is finite and proportional to $|K_0||\boldsymbol{\delta}|$. This results in a significant deviation from the power-law onset.

In Fig. 7.8, we confirm this by comparing two band structures: one with a single band minimum (blue) and another with multiple band-minima (orange). The corresponding low-energy Raman onset for $\alpha = 3/4$ is shown as an example. The band with single minima shows the expected power-law $\sim (\omega - E^0_{2v})^{\frac{3}{4}}$ (dashed line), whereas the band with multiple minima shows a much flatter curve, qualitatively different from the power-law behaviour.

7.8 Results: Ising Anyons

Finally, we will now present the results for the Ising anyons in the ferromagnetic Ktaev model.

7.8.1 Parameter space

Our effective Hamiltonian Eq. (7.15) has several parameters that are, in principle, determined by the microscopic exchange couplings. Due to a lack of conclusive estimates, we do the following to keep the parameter space under control. In the effective two-anyon model, we consider the following independent parameters: (i.) Anyon hopping amplitudes, t_{nn} and t_{nnn}, (ii.) Majorana mass gap Δ_m that fixes the static vison gap Δ^0_v, as shown in Fig. 7.4b. The values of local Berry fluxes θ_{nn} and θ_{nnn} are computed explicitly and are determined by Δ_m, as shown in Fig. 7.5. We will also restrict ourselves to the case where $t_{nn} < 0$, assuming that the dominant contribution to the nearest neighbour hopping comes from the magnetic field, which always gives a negative hopping rate (See Section 4.4).

The Raman response calculation also involves the parameters h_R and Γ_R, which should also be, in principle, determined by the microscopic model of the material in question. However, in our model, only the ratio h_R/Γ_R is relevant (See Eq. (7.18)). The absolute values only affect the overall magnitude of the response.

7.8.2 Continuum response

When the hopping amplitudes are much larger than the interaction scale, the spectrum of hardcore anyons exhibits a continuum of energy levels, associated with creating the anyon pairs with equal and opposite momenta.

We consider six polarization channels in relation with the experimental discussion presented earlier. In $aa(ab)$ channel, the incident light is polarized along the crystallographic axis $\boldsymbol{a}$, while the reflected light is detected with polarization along $\boldsymbol{a}(\boldsymbol{b})$. In addition, we also consider circularly polarized channels where the incident and reflected light waves can be left or right circularly polarized defining four channels: LL, RR (parallel-circularly polarization) and LR, RL (cross-circularly polarization).

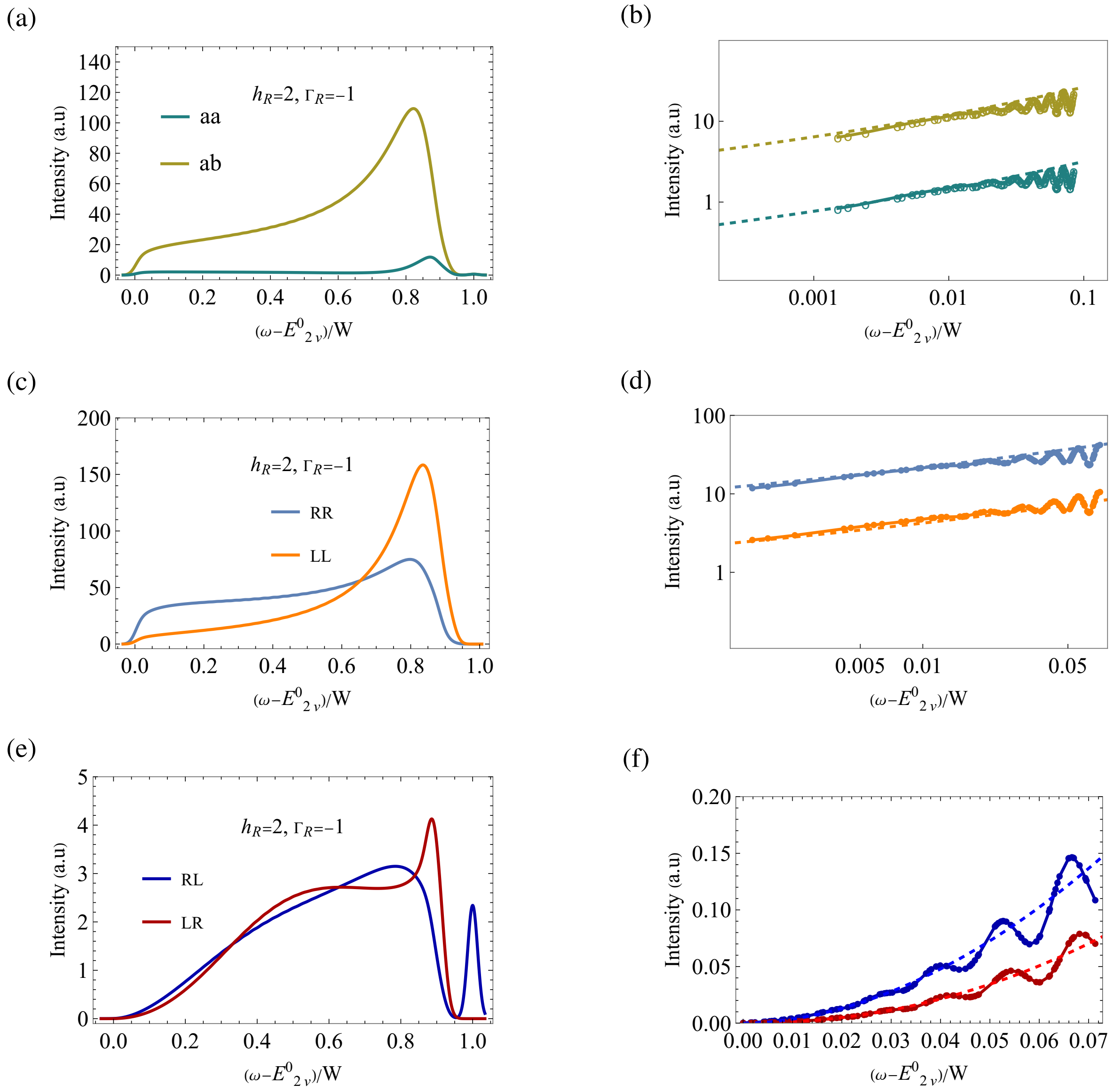

Fig. 7.9 **Continuum response and power-law onset.** Raman spectra showing the two-particle continuum obtained in (a) linear and (b) parallel-circular polarization, and (c) cross-circularly polarized channels. The dashed lines in the lower panels (d,e) show the predicted power-law onset $I(\omega) \sim (\omega - E^0_{2v})^{.125}$ arising from topological spin $\theta = \frac{\pi}{8}$ (Eq. 7.26). In (c) and (f), the cross-circularly polarized channels only couple to states with finite angular momenta, resulting in leading power-law behaviours $(\omega - E^0_{2v})^{1.875}$ (blue) and $(\omega - E^0_{2v})^{2.125}$ (red). The results are obtained for hopping amplitudes $t_{nn} = -0.075$, $t_{nnn} = -0.01$ and Majorana gap $m = 2$, all expressed in units of the static vison-pair energy gap $2\Delta_v = |K|$ (K is the Kitaev coupling). The effective model is diagonalized on a lattice of linear size $L = 100$ (see Fig. 7.5). To calculate the Raman spectrum, a Gaussian approximation for the Dirac-delta function with width $\delta = .02$ is used for the left panel, and $\delta = .005$ is used for the right panel to accurately resolve the power-laws.

Fig. 7.9 shows the Raman spectrum in different polarization channels for the effective model parameters $\Delta_m = 2, t_{nn} = -0.075$ and $t_{nnn} = -0.01$, which are expressed in units of the static vison-pair energy $2\Delta_v = |K|$. The low energy regime is dominated by the two-anyon continuum. The predicted power-law onset with an exponent $\frac{1}{8}$ is shown in the log-log plot on the right panel.

Comparing to the non-interacting case (see Fig. 7.7), we find that the short range interaction between anyons only affects the high energy behaviour, while the low-energy onset remains robust. The large difference in the overall magnitude of the Raman intensity in cross-circularly polarized channels is due to the vanishing of the Raman operator $\mathscr{R}^h$ in LR, RL channels. The two Raman operators obey the following transformation rules.

$$\begin{aligned} P^{\Gamma}(\boldsymbol{e}_L, \boldsymbol{e}_L) = P^{\Gamma}(\boldsymbol{e}_R, \boldsymbol{r}_R), \qquad P^h(\boldsymbol{e}_L, \boldsymbol{e}_L) = -P^h(\boldsymbol{e}_R, \boldsymbol{r}_R) \\ P^{\Gamma}(\boldsymbol{e}_R, \boldsymbol{e}_L) = P^*_{\Gamma}(\boldsymbol{e}_L, \boldsymbol{e}_R), \qquad P^h(\boldsymbol{e}_R, \boldsymbol{e}_L) = P^h(\boldsymbol{e}_L, \boldsymbol{e}_R) = 0, \end{aligned} \tag{7.27}$$

Interestingly, an anti-bound state emerges above the continuum which is detected only in the *RL* polarization channel. A general discussion on bound states is given below.

Circular polarization and power-law onset

As argued in the previous section, circular polarization channels can be used to efficiently probe the statistical parameter α. Fig. 7.9 (b) and (e) show the Raman spectra in parallel-circularly polarized channels *LL* and *RR*, which couple only to $l = 0$ eigenstates, resulting in the power-law onset consistent with the prediction of Eq. (7.26). In contrast, cross-circularly polarized channels *RL* and *LR* couple to states with $l = 2$ and $l = -2$ respectively. Here, as shown in Fig. 7.9f, the low energy onsets are consistent with the power-laws (dashed lines) $(\omega - E^0_{2v})^{2-\alpha}$ and $(\omega - E^0_{2v})^{2+\alpha}$. This follows directly from the derivation outlined in Section 7.7, where the wavefunctions with finite angular momenta scale like $(kr)^{2\pm\alpha}$. The anti-bound state above the continuum has an angular momentum quantum number $l = 2$ and thus only couples to the cross-circularly polarized *RL* channel.

7.8.3 Low-energy bound states

The short-range interaction between anyons, as shown in Fig. 7.5b, although exponentially small in separation, results in a next-nearest-neighbour attractive interaction. Depending on the bandwidth of the anyons, this may induce bound states below the continuum.

In Fig. 7.10a, we present the numerically obtained energy spectrum of the effective model (black) for parameters $t_{nn} = -0.025, t_{nnn} = 0.01, \Delta = 1.0$, superimposed on the non-interacting continuum (red) plotted as a function of center of mass momentum. Three bound states emerge below the continuum. Real space (radial) profiles of these wavefunctions plotted in Fig. 7.10b show that the bound states correspond to next-nearest-neighbour pairs of anyons, consistent with the *nnn* attractive interaction. Indeed, the bound states appear as sharp peaks in the Raman

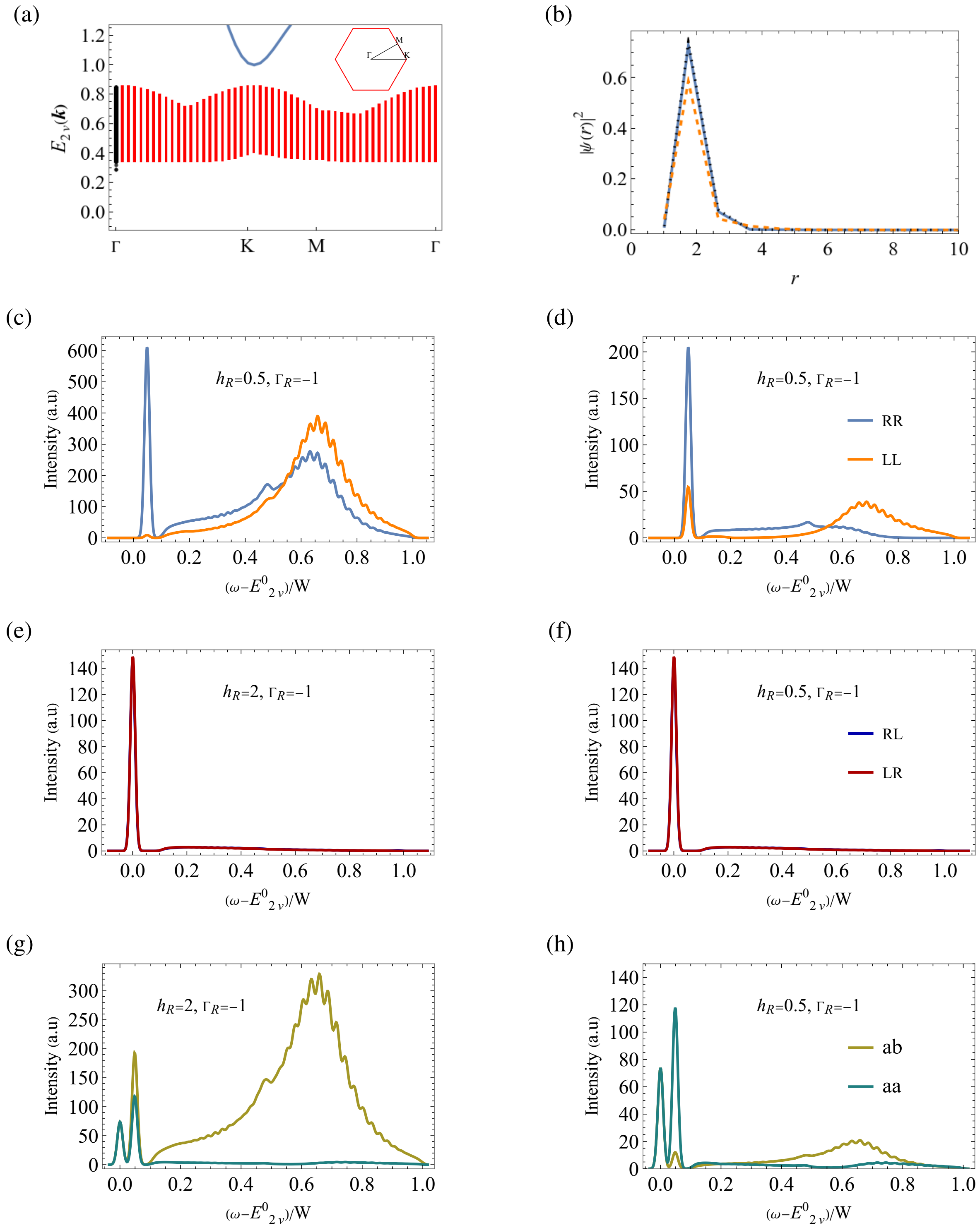

Fig. 7.10 **Sharp peaks from anyon bound states.** Raman spectrum for effective model parameters $\Delta_m = 1, t_{nn} = -0.025, \text{and} t_{nnn} = 0.015$, shown for two values of $\frac{h_R}{\Gamma_R}$. (a.) Red points are obtained from the non-interacting two-particle continuum, plotted as a function of the COM momentum. Black points are obtained by diagonalizing the interacting problem. Three bound states emerge below the continuum. (b.) Probability amplitudes of the three bound-states plotted as function of the relative radial coordinate r. While all three bound states are visible in linear polarization channels, (g,h), they show strong sensitivity to circular polarizations. $LR(RL)$ channel selectively couples to $l = +2(-2)$ states, (e,f), while only the $l = 0$ state is visible in LL and RL channels, (c,d). The value of $\frac{h_R}{\Gamma_R}$ influences the response in linear and parallel-circularly polarized channels.

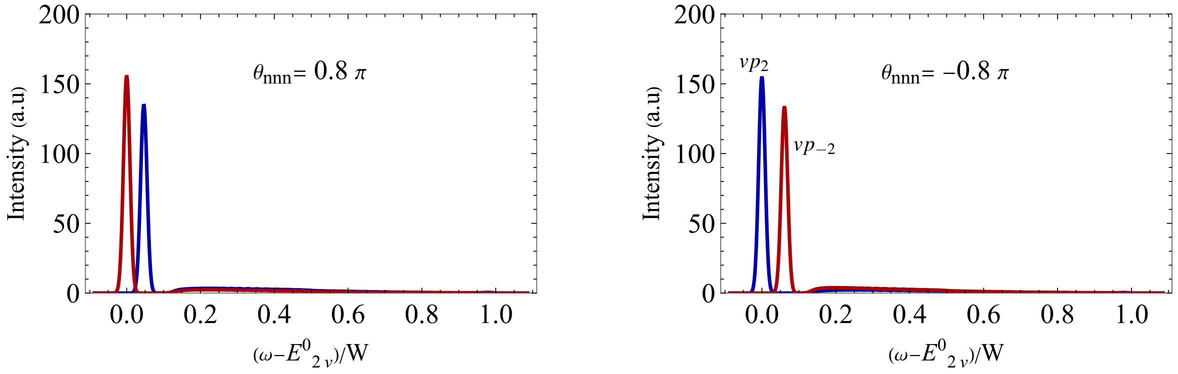

Fig. 7.11 **Berry phase effect on helicity dependence.** Raman response in the cross-circularly polarized channel from two bound states vp_2 and vp_{-2}. The energy splitting between the states and there relative Raman intensity is controlled by the Berry flux θ_{nnn}. Color code: blue - *RL* and red - *LR*.

spectra. In light of the experimental results mentioned before, it is worthwhile to investigate the polarization dependence of these bound state peaks.

Helicity selectivity and Berry phase effects

For the specified parameter values, there are three low-energy bound states, denoted by vp_{-2}, vp_{+2}, vp_0, where the subscripts label their angular momentum quantum numbers. All states are visible in linear polarization channels *aa* and *ab*. In the case of circularly polarized channels, vp_0 is only visible in the parallel polarization channels *LL* and *RR*. The relative intensity in these two channels is a controlled by the quantity h_R/Γ_R. This follows directly from the transformation rules given by Eq. (7.27). In the *LL* channel, the Ramana matrix element is proportional to $\mathscr{R}^\Gamma + \mathscr{R}^h$, while it is proportional to $\mathscr{R}^\Gamma - \mathscr{R}^h$ in the *RR* channel.

However, the case of cross-circular polarization is more interesting. As $\mathscr{R}^h = 0$ in this configuration, any difference in the *LR* and *RL* spectrum should arise from the intrinsic chirality of the wavefunctions themselves. While vp_{-2} couples only to the *RL* channel, response from vp_{+2} only appears in the *LR* channel. However, they are almost degenerate, making it difficult to distinguish them in the spectrum. Interestingly, the energy splitting between the vp_{-2} and vp_{+2} states depend strongly on the value of θ_{nnn}. This is again consistent with the fact that the bound state corresponds to a next-nearest pair.

Intuitively, this could be understood by considering the bound-state as a particle on a hexagonal ring threaded by a flux θ_{nnn}. For the parameters used to obtain the results of Fig. 7.10, $\theta_{nnn} = 0.1\pi$, which is rather small. However, if we allow this to be an independent parameter, the splitting can be made larger and the response in *LR* and *RL* channels will be strongly asymmetric. Fig. 7.11 shows the spectrum for different values of θ_{nnn}, with other parameters held the same as in Fig. 7.10.

7.9 Summary and Discussion

Raman spectroscopy is a versatile tool used to study the fundamental excitations in quantum materials. In fractionalized systems, Raman spectrum is generally expected to show a continuum response due to the constraint that excitations must always be created in pairs. In Kitaev materials, Raman experiments have provided valuable insights into the underlying degrees of freedom, but they have also presented several puzzles. For example, in $\alpha - \mathrm{RuCl}_3$, the zero-field intermediate temperature regime shows a broad continuum consistent with fractionalization, while sharp peaks appear in the field-induced regime relevant to the half-quantized thermal Hall experiments.

In this chapter, based on the insights developed in Part I, we considered a simplified model of a chiral spin liquid with dynamical Ising anyons. In the low-energy limit, where only a single anyon-pair is created, we derived a two-particle effective model that takes into account the long-range exchange interaction as well as the short range interaction due to the overlap of Majorana modes. Within this two-anyon subspace, the exchange statistics is fully determined by the topological spin of the anyons, $\theta = \frac{\pi}{8}$. Raman operators derived by Yang *et al.* [141] were used to obtain the response arising from the creation and annihilation processes of anyon pairs induced by light.

We find that the Raman response can be qualitatively different depending on the microscopic parameters that determine the anyon dynamics. When the kinetic energy of the anyons dominate over the short range interaction between them, a two-particle continuum results. When the anyon band structure has a single minimum, the low-energy onset of the spectrum exhibits a characteristic power-law behaviour, given by $I(\omega) \sim \omega^{\alpha}$, where $\alpha = \frac{1}{8}$, reflecting the topological spin of an Ising anyon - a universal property of the chiral spin liquid. This is a direct consequence of the anyons exhibiting a statistical repulsion due to their exchange phase. However, when the band structure exhibits multiple minima, this power law is modified, as anyons can be created at two different minima, thereby circumventing the statistical repulsion. Consequently, the observability of this power-law thus strongly depends on the details of the anyon band structure. Additionally, the experimental resolution required to accurately determine the exponent is an important consideration that needs to be investigated.

The interaction between anyons, although exponentially small in their separation, may induce bound-states in certain parameter regimes, contributing sharp peaks in the Raman response. A robust signature of low-energy bound states was found in the cross-circularly polarized channel. Two of the lowest energy bound states couple selectively to *RL* or *LR* channels due to angular momentum selection rules.

Our analysis was restricted to the zero temperature limit. At finite temperature, we anticipate two main effects. First, the gapped continuum will further broaden as the gap gets filled due to thermally excited visons. Second, thermally excited Majorana fermions will allow for the production of anyon pairs that belong to the fermionic superselection sector. For example, starting from state with a thermally excited matter fermion at the Dirac point $\boldsymbol{K}$ with energy Δ_m, a pair of anyons with energy $E_v(\boldsymbol{K}+\boldsymbol{q})$ and $E_v(\boldsymbol{K}-\boldsymbol{q})$ can be created with arbitrary momentum $\boldsymbol{q}$. However, this signal will be suppressed by the factor $e^{-\beta\Delta_m}$. The reverse process, involving annihilation of a pair of thermally excited anyons to release a matter fermion, may also occur, but will be suppressed by a factor $e^{-\beta(E_v(\boldsymbol{K}-\boldsymbol{q})+E_v(\boldsymbol{q}))}$.

What do our results mean for the experiments on $\alpha-\mathrm{RuCl}_3$? Although the microscopic Hamiltonian parameters of $\alpha-\mathrm{RuCl}_3$ are currently unknown, our simplified model is generally consistent with the existing Raman experiments. Within our effective model, bound states that show strong polarization dependence naturally emerge. However, for a more quantitative comparison to experiments, a better understanding of the microscopic parameters is necessary. It is also important to investigate more trivial scenarios where the sharp peaks may arise from magnons or magnon bound-states in a partially polarized phase. A simple linear spin-wave theory was employed (not included in this thesis) to calculate the Raman response for such a model, but the results were inconsistent with the experimental data. Higher order spin-wave theory may be necessary to fully characterize the Raman spectrum in such a phase.

Another obvious, yet perhaps ambitious goal would be to go beyond the two-anyon subspace, which will necessarily make non-abelian braiding effects more significant and visible. For instance, one could trap a single anyon in the sample using a scanning tunnelling microscope [150] or a vacancy [151, 100, 152] before conducting the Raman experiment. The response would then include processes where the created pair braids around the trapped anyon, changing its superselection sector. This may lead to a marked difference in the response compared to the scenario without any trapped anyons. A related idea was recently applied to predict non-linear pump-probe relaxation rates in anyonic systems in Ref. [153]. Here, a pump laser pulse creates a pair of anyons, followed by a probe pulse creating another pair. The long-range statistical interactions between the two pair was found to result in an anomalous relaxation rate.

In a broader context, recent works have proposed circularly polarized light scattering as a direct probe of the chirality of excitations. In Ref. [135], Boström *et al.* argued that magnetic circular dichroism arising from two-magnon Raman scattering could be used to detect the Berry curvature of topological magnons. This mechanism is, in a certain sense, similar to our discussion on the Berry phase-controlled polarization selectivity of anyon bound states (Fig.7.11). In this regard, one could also ask if the chirality of the matter Majoranas may be visible in Raman spectroscopy. In fractional quantum Hall systems, it was recently proposed that a similar circular polarized Raman scattering experiment could detect a chiral neutral collective mode of a quantum Hall droplet, resembling many similarities to a "graviton"[154]. This has, in fact, been observed experimentally [155]. Given the many similarities between quanutm Hall systems and chiral spin liquids, it is intriguing to investigate these connections in depth.

A natural extension of our analysis to the AFM Kitaev model is possible. Given that the band structure of anyons is strikingly different compared to an FM Kitaev model, we expect qualitative differences in Raman signatures for an AFM model. In particular, the Berry curvature of single-vison bands could produce a strong signature in the helicity dependence of the spectrum, typically detected through magnetic circular dichroism. This expectation follows from recent proposals for detecting magnon band topology using circularly polarized Raman scattering[135]. Here, unlike magnons, which are bosons, the anyonic statistics of visons might lead to interesting features.

Chapter 8

Thermal Hall Effect

A smoking-gun signature of a chiral spin liquid is its quantized thermal Hall conductivity. In Chapter 3, we saw how a weak magnetic field gaps out the Majorana fermions, endowing the bands with finite Chern numbers. A remarkable physical consequence of this is the half-quantized thermal Hall effect. An equivalent description of this Hall effect exist at the edge of a system. The chiral spin liquid is characterized by a gapless, propagating Majorana mode along the edges of the sample. This edge mode is protected from backscattering, such as from disorder, due to its topological nature, which is responsible for the quantization.

This theory, however, neglects the gauge field completely. At temperatures, much below the vison energy gap, $T \ll \Delta_v$, this simplification is well justified, as the density of gauge field excitations will be exponentially suppressed: $n_v \sim e^{-\frac{\Delta_v}{k_B T}}$. This was also the basis for Kitaev's perturbative treatment of the magnetic field, which leads to the chiral phase in the first place. However, in real systems that always operate at small but finite temperatures, it is important to understand the role of visons in thermal Hall experiments. In this chapter, we present the details of a novel thermal Hall effect arising from dynamical visons.

8.1 Thermal Hall effect of visons

A striking result of Chapter 4 was the prediction of Chern bands of single visons (Ising anyons) in an AFM Kitaev model under a weak $[111]$ magnetic field. What are the physical consequences of this? The Berry curvature of bands can lead to Hall effects, even in the non-interacting limit [156]. This naturally predicts a novel thermal Hall effect originating from the gauge degrees of freedom of the Kitaev spin liquid. In the non-interacting single-particle picture-valid when the vison density is small- the thermal conductivity can be directly calculated from the Berry curvature as follows.

$$\kappa_{xy}(T) = -\frac{1}{T}\int_0^\infty d\varepsilon\,\varepsilon^2\,\sigma_{xy}(\varepsilon)\frac{\partial n_v(\varepsilon)}{\partial\varepsilon}, \tag{8.1}$$

where $n(\varepsilon)$ describes the thermal occupation of the particle as function of their energy and $\sigma_{xy}(\varepsilon)$ is computed from

$$\sigma_{xy}(\varepsilon) = -\sum_\alpha \int \frac{d^2k}{(2\pi)^2}\boldsymbol{\Omega}_{\alpha\boldsymbol{k}}\Theta\left(\varepsilon - E^v_{\alpha\boldsymbol{k}}\right) \tag{8.2}$$

where $\alpha = 1,2$ labels the two vison bands. The above formula for Hall conductivity of general non-interacting quasiparticles has been derived by various authors using a variety of approaches. Interested readers may consult Ref. [156].

An important feature that distinguishes the vison Hall effect from those of other (bosonic) quasiparticles, such as phonons or magnons, is due to their anyonic nature. Although at the single particle level, statistics is irrelevant, the non-trivial quantum dimension of Ising anyons, $d = \sqrt{2}$, however, is important. This encodes the degeneracy arising from the zero-energy fermion mode shared by a pair of well-separated visons in the chiral spin liquid. This results in an extra entropic factor to the Boltzmann distribution function describing a non-interacting vison.

$$n_v(E^v_{\alpha,\boldsymbol{p}}) \approx \exp\left(-\frac{E^v_{\alpha,\boldsymbol{p}} - T\ln\sqrt{2}}{T}\right) \tag{8.3}$$

Within our approach, visons in an AFM Kitaev model attain nearest neighbour hopping $t^h \propto h$ and a next-nearest neighbour $t^\Gamma \propto \Gamma$ (for a fixed κ). This leads to the following Hamiltonian for a single vison on a triangular lattice.

$$\begin{aligned} H^v(\boldsymbol{p}) &= \Delta_v^0\mathbb{1} - \boldsymbol{h}(\boldsymbol{p})\cdot\boldsymbol{\sigma} \\ \boldsymbol{h}(\boldsymbol{p}) &= 2t^h\begin{pmatrix}\sin(\boldsymbol{p}\cdot\boldsymbol{\eta}_1)\\ \cos(\boldsymbol{p}\cdot\boldsymbol{\eta}_2)\\ \sin(\boldsymbol{p}\cdot\boldsymbol{\eta}_3)\end{pmatrix} + 2t^\Gamma\begin{pmatrix}\sin(\boldsymbol{p}\cdot(\boldsymbol{\eta}_1+\boldsymbol{\eta}_3))\\ \cos(\boldsymbol{p}\cdot(\boldsymbol{\eta}_2+\boldsymbol{\eta}_3))\\ \sin(\boldsymbol{p}\cdot(\boldsymbol{\eta}_2-\boldsymbol{\eta}_1))\end{pmatrix} \end{aligned} \tag{8.4}$$

with $\eta_1 = (\frac{1}{2},\frac{\sqrt{3}}{2})$,$\eta_2 = (\frac{1}{2},-\frac{\sqrt{3}}{2})$ and $\eta_3 = (1,0)$. The corresponding energy bands are given by $E^v_{\pm,\boldsymbol{p}} = \Delta_v^0 \pm |\boldsymbol{h}(\boldsymbol{p})|$. Using the energy dispersion and Eq. (3.38) of Chapter 3, we can compute the thermal Hall conductivity of a visons.

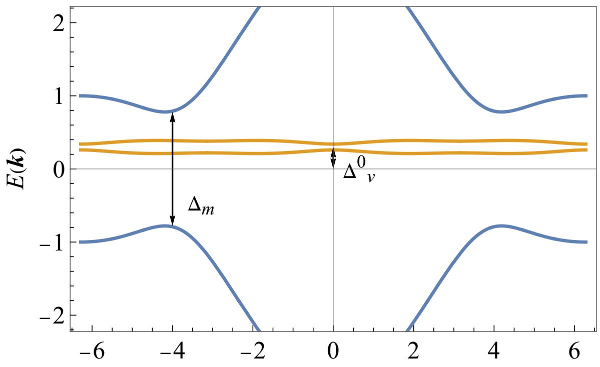

Fig. 8.1 **Majorana and vison bands in an AFM Kitaev liquid.**A likely arrangement of energy bands of visons and Majoranas in a chiral spin liquid adiabatically connected to the AFM Kitaev model. The Majoranas are gapped out, making visons the low energy degrees of freedom in the bulk. Predictions for thermal Hall effect in such a scenario are presented in Fig. 8.2

8.2 Prediction for AFM Kitaev Materials

Having established that not only the Majorana fermions, but visons also contribute to the thermal Hall effect, the natural question is how it may show up in Kitaev materials that are adiabatically connected to an AFM Kitaev model. Here, one can have several scenarios distinguished by the energy hierarchy of Majoranas and visons. The precise values of κ, E_v^0, t^h and t^Γ that determine the band structures depend on the microscopic exchange couplings. For most Kitaev materials including $\alpha-\mathrm{RuCl}_3$ these parameters are still not established. However, looking at the thermal Hall experiments [42, 43], it is likely that in a field-induced spin liquid regime, the Majorana gap (Δ_m) has to be sizeable to observe the quantization. This insight may be used to consider the likely scenario where the vison bands lie within a large Majorana gap as shown in Fig. 8.1. In such a scenario, the vison thermal Hall effect will be added on top of the half-quantized Hall effect of Majorana fermions. Since the visons are still gapped, their contribution will follow a temperature activated behaviour preserving the half-quantized plateau at very low temperatures, $T \ll \Delta_v^0$. However, the temperature dependence of the thermal Hall signal of the whole system will be qualitatively modified.

An important factor here is the relative sign of the Majorana and vison Hall contributions. We find that the vison hopping amplitude is *not* affected by the sign of the Majorana mass gap κ. Within our perturbation theory linear in h, the sign of the Chern number of the lowest vison band is determined by the flux acquired by the vison when it hops along a triangular loop, using hopping processes triggered by h_x, h_y and h_z. This results in the Chern number $C_V = -\mathrm{sgn}(h_x h_y h_z)$ for the lowest vison band. This has to be compared to the Chern number of the Majorana band [40, 43], $C_m = \mathrm{sgn}(\kappa)$ which leads to $C_m = \mathrm{sgn}(h_x h_y h_z)$ for a Kitaev model solely perturbed by $\boldsymbol{h} = (h_x, h_y, h_z)$ [40]. As the signs are opposite, the vison Hall effects of Majorana fermions and visons are subtractive.

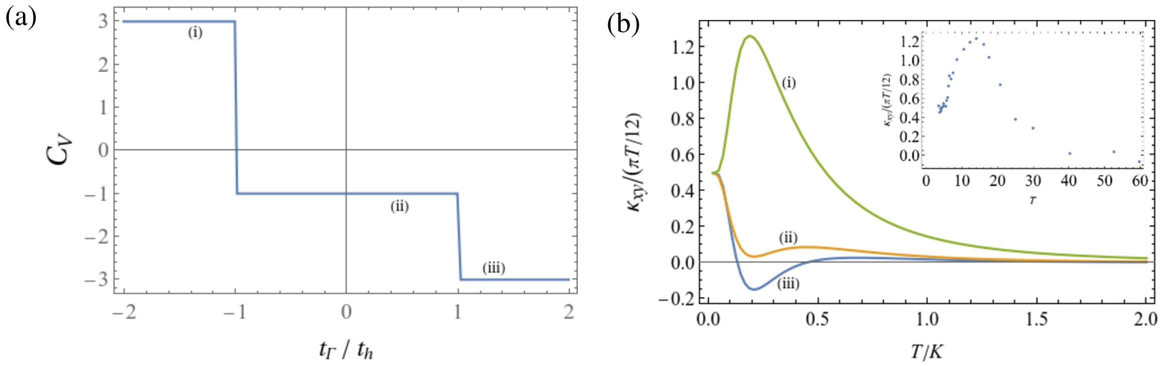

Fig. 8.2 (a). Chern number of the lowest vison band in the AFM Kitaev model as a function of the ratio of t_Γ and t_h. (b). Thermal Hall conductivity of an AFM Kitaev spin liquid with both matter Majorana and vison contributions. Different curves are obtained for lowest Majorana band having Chern number +1 and lowest vison band with Chern number (+3,-1,-3) as marked in (a). We assume that the vison bands lie within a large Majorana gap κ. (See Fig.8.1) The curves in sub-figure (b) are calculated with the following parameters: (i)$\Delta_v^0 = 0.6K, \kappa = 0.25K, t^h = 0.05K, t^\Gamma = -0.08K$,(ii) $\Delta_v^0 = 0.6K, \kappa = 0.25K, t^h = 0.1K, t^\Gamma = 0.05K$, (iii)$\Delta_v^0 = 0.6K, \kappa = 0.25K, t^h = 0.05K, t^\Gamma = 0.07K$. Inset: Experimentally obtained κ_{xy} for α-RuCl$_3$ (reproduced from Ref.[43]). The material however, likely has a ferromagnetic Kitaev coupling.

We find that if the Majorana gap κ arises solely at cubic order in the magnetic field i.e, $\kappa \propto h^3$, then the lowest vison band has the Chern number -1 - opposite sign as that of the lowest Majorana band. As shown in Fig. 8.2.a, the situation changes when one adds the effect of t_Γ. Depending on the sign and size of t_Γ, the Chern number of the lowest vison band takes the values 3, -1, or -3. Remarkably, the vison band gets a large Chern number $+3$ when $t_\Gamma/t_h < -1$.

Here we considered a magnetic field in (111) direction, perpendicular to the plane. When the field is rotated, the sign of the Hall effect (for both the plateau and the peak) in α-RuCl$_3$ is approximately given by $\mathrm{sgn}(h_x h_y h_z)$ [43]. This is consistent with theory, as the Majorana mass Δ_m (and thus the Majorana Hall effect) is proportional to $h_x h_y h_z$ [40] in the h field-perturbed Kitaev model. The Chern number of the vison band, arising from t_h, is determined by the sign of the flux enclosed by a triangle, which is also determined by the product $h_x h_y h_z$. Furthermore, we find that $t_\Gamma \to t_\Gamma^*$ for $\kappa \to -\kappa$ which results, within our approximations, in a jump in the sign of the vison Chern number simultaneously with that of the Majorana bands.

8.3 Comparison to Experiments

Experimentally, one can expect either a characteristic dip or a peak in the Hall signal depending on whether the Chern number of the lowest vison band is negative or positive as shown schematically in Fig. 8.2.

If we take the half-quantized THE experiments as evidence for the chiral spin liquid [42, 43], how does our prediction fit into this framework? First of all, a disclaimer is necessary. Within our approximations, only an AFM Kitaev coupling or a phase with the same symmetry fractionalization pattern as that of the AFM model can show the vison Hall effect. Nevertheless, an intriguing observation in α-RuCl$_3$, a characteristic peak above a half-integer quantized plateau [42, 43], is intriguing. Fig. 8.2 b shows the experimental data in the inset for comparison. This suggests that the system hosts additional chiral excitations on top of the Majorana fermions. As the amplitude of the peak is very large, almost twice the plateau value, the experimental result is consistent with the presence of a gapped excitation with a Chern number larger than 1. It is tempting to associate this feature with a vison Hall effect. While it has been suggested early on [157] that α-RuCl$_3$ has an antiferromagnetic Kitaev coupling, experimental evidence is in favour of a ferromagnetic Kitaev coupling, see, e.g., Ref. [72].

An alternate explanation comes from phonons, the dominant energy carriers in any solid state system. Although electrically neutral and hence no direct coupling to magnetic fields, phonons have been shown to exhibit thermal Hall effects in a variety of materials[158, 55]. Several mechanisms have been proposed to explain this including coupling to magnons [159], skew-scattering from impurities [160, 161] and charge puddles [158]. It was shown in two contemporary works by Winkler and Rosch [56], and Ye et. al. [57] that phonons were necessary to observe the Majorana Hall effect in a chiral spin liquid. Moreover, Winkler and Rosch predicted that phonons will also contribute to the thermal Hall effect due to the Berry phase imprinted on them by the chiral Majoranas. However, this contribution is way too small to explain the observed peak in $\alpha-\mathrm{RuCl}_3$ It is perhaps fair to say that a theory that explains the anomalously large thermal Hall effects in several Mott insulating materials is urgently needed.

To end this section on an optimistic note, it is encouraging to see the recent reports of materials with a dominant AFM Kitaev interaction [162, 163]. The detection of a vison thermal Hall effect in these materials would help establish the presence of emergent dynamical gauge fields and anyons.

Chapter 9

Conclusions and Outlook

In modern condensed matter physics, the emergence of gauge theories and topological excitations not only define new paradigms for quantum matter but also has far-reaching implications for future technologies. Quantum spin liquids offer an exciting platform to realize this physics in real materials. Among the numerous models theoretically proposed, perhaps the most attractive model-thanks to its exact solubility-is the Kitaev spin liquid, which realizes an exotic phase with fractionalized excitations and an emergent gauge field. This model has become increasingly relevant as there is a large class of materials, known as Kitaev materials, that show great promise in realizing the spin-spin interactions necessary to support it. However, a conclusive evidence for fractionalization and the emergent gauge fields in Kitaev materials is still lacking, primarily due to the presence of undesirable perturbations inevitable in real materials. Recent experimental observation of a half-quantized thermal Hall conductivity, a smoking-gun signature of the Kitaev spin liquid, has generated significant excitement among researchers. However, strong sample dependence and conflicting experimental results call for a better understanding of models and materials alike. In this thesis, we explored this gap between the pure Kitaev model and real material candidates. Our focus was on the nature of the emergent $\mathbb{Z}_2$ gauge field, strongly coupled to Majorana fermions. Static in the pure model, the gauge field acquires dynamics when perturbations are present. To study this, we focused on the elementary excitations of the gauge field - visons. In this regard, we distinguish between the pure Kitaev model and a generic Kitaev liquid by developing a comprehensive theory of dynamical visons of the latter and predicting novel experimental signatures.

The first and foremost question concerns the coherence of the vison as a quantum particle, which is not guaranteed *a priori* in the Kitaev spin liquid. The gauge flux of π carried by the vison is seen as a singular scattering potential by the gapless Majoranas, as indicated by the diverging scattering cross section. We described a vison as a quasiparticle dressed by a cloud of scattered Majorana fermions. To capture its dynamics, we employed a controlled degenerate perturbation theory, which involved calculating the hopping matrix elements of an isolated vison. Although this sounds straightforward, the computation of matrix elements was complicated by the implementation of projection operation (enforced by the gauge theory) and selection of appropriate basis states to represent the Majorana many-body wavefunctions.

We used a Pfaffian method, derived from many-body path integrals to calculate wavefunction overlaps between different ground states of the fermionic system. Considering a weak off-diagonal Γ term and an external magnetic field (h), we obtained the dispersion of a vison. A surprising result was the profound influence of the sign of Kitaev coupling (K) in determining the vison dynamics. While in an FM Kitaev model ($K < 0$), single visons acquire dispersion linear in these perturbations, all processes linear in Γ and h are suppressed by a destructive interference in an AFM Kitaev model ($K > 0$). This effect was found to hinge on the symmetries of the system and revealed a more fundamental property of the topological phase - symmetry fractionalization. The visons of the AFM model carry fractional crystal momentum, resulting in an enhanced periodicity in their dispersion.

When a [111] magnetic field opens up a gap in the Majorana spectrum, the system becomes a chiral spin liquid, with the visons transforming into Ising anyons in the bulk. Here, a remarkable consequence of the non-trivial symmetry fractionalization in the AFM Kitaev model is the emergence of Chern bands of visons. Vison bands were found to carry Chern numbers $+3, +1, -1, -3$, determined by the relative strengths of the magnetic field h and Γ term. As a result, a novel experimental signature, thermal Hall effect from thermally excited visons could be predicted within our theory. However, detecting this would require a material with an AFM Kitaev coupling. Although most materials currently being investigated are believed to posses FM Kitaev interactions, recent reports of AFM Kitaev interactions in materials like $Na_3Co_2SbO_6$ and $Na_2Co_2TeO_6$ are encouraging [164].

In Chapter 5, we investigated the effects of scattering from gapless Majoranas on a moving vison. This was essential to answer the question about the coherent propagation of the vison. There are two important effects arising from scattering of Majoranas - friction and diffusion, a classic manifestation of the fluctuation-dissipation theorem. When a vison moves according to its band dispersion, its motion is dampened by the scattering of Majorana fermions which are much faster and lighter than the vison. By expressing this problem as a drift-diffusion equation in momentum space, we extracted the temperature dependence of the vison mobility.

In a ferromagnetic Kitaev liquid, where the vison is highly mobile (velocity linear in perturbations), this leads to a decreasing mobility as the temperature increases. Remarkably, in the low-T limit, the vison mobility was found to be universally given by $\mu(T) \approx \frac{v_m^2}{6\,T^2}$, completely determined by the Majorana velocity $v_m \propto |K|$. At higher temperatures, the power law is modified to $\mu(T) \sim \frac{18\,t_v^2 v_m^2}{T^4}$, which depends on the hopping rate t_v of the vison. A diverging mobility in the $T \to 0$ limit confirms the notion that a vison is indeed a coherent quasiparticle despite the its gauge flux. In hindsight, this result is the consequence of a interplay between the diverging scattering cross-section and scale invariance property of the Majorana fermions.

An initially immobile vison can hop incoherently by scattering from Majorana fermions. In an AFM Kitaev model, where interference effects strongly suppress vison motion, such an assisted hopping may become the dominant mechanism for vison dynamics. By solving the Dirac equation in the presence of a vison, we obtained the vison hopping rates by analytically calculating the golden rule transition rates. Here, a quasi-localized Majorana mode was found to give the dominant contribution to the hopping rate at low temperatures. Although in the limit $T \to 0$, the universal mobility remains valid due to higher-order coherent vison hopping processes, we identified an intermediate temperature regime where a T-independent mobility dominates the dynamics, driven by Majorana-assisted processes. This is reminiscent of Ohmic friction typically found in metals, which arises from entirely different mechanisms, such as Landau damping.

Next, motivated by the three-dimensional (layered) nature of Kitaev materials, we took a step toward understanding the effects of a third-dimension on a 2D emergent gauge field. In Chapter 6, we investigated three simple models of multilayer Kitaev spin liquids. We stacked pure Kitaev models on top of each other, in AA, AB and ABC stacking patterns, weakly coupled by a nearest neighbour Heisenberg interaction. Interplay of topological order and model-specific conservation laws led to a rich dynamics of the gauge field in these models.

We identified novel conservation laws in AB and ABC stacked models, which could be visualized as 2D sheets of operators crisscrossing the multilayer system. While topological order prohibited single visons from tunnelling between layers, these conservation laws prevented their in-plane motion, completely immobilizing single visons! This forced them to form pairs in order to become mobile. We identified two types of excitations: inter-layer and intra-layer pairs. They were found to exhibit qualitatively different dynamics, governed by the conservation laws specific to each stacking pattern.

In AB and ABC stacked systems, inter-layers pairs were constrained by the sheet conservation laws to move in 1-D channels, while in the AA model, they enjoy a fully 2D mobility. Intra-layer pairs, however, could move between layers, with their direction of motion determined by the conservation laws. Additionally, depending on the anisotropy of Kitaev interactions, an intra-layer pair could hop either coherently or incoherently. In the chiral spin liquid phase, we identified two types of intra-layer vison pairs: bosonic and fermionic ones. Only a bosonic intra-layer pair was able to coherently tunnel between layers, while the fermionic one could not. This rich zoo of dynamical vison-pairs could be probed through their characteristic dimensionality of motion.

In Chapter 7, we explored how traditional Raman scattering could be used to probe vison dynamics in a generic chiral Kitaev spin liquid. Motivated by recent experiments on the Kitaev material $\alpha - \mathrm{RuCl}_3$, we computed the Raman spectrum of a ferromagnetic Kitaev spin liquid in the chiral phase. We assumed a plausible experimental scenario where the Majorana fermions are gapped out by a magnetic field, and the low-energy degrees of freedom are mobile Ising anyons. Since low-energy Raman processes primarily create pairs of anyons, we first derived an effective two-particle Hamiltonian for a pair of Ising anyons. The effective model included the universal long range statistical phase as well as the short range interacting arising from the localized Majorana zero modes. Using Raman operators derived by Yang. *et al* [141], we calculated the zero temperature Raman response.

When the vison bandwidth, or equivalently the hopping amplitudes, are large, the spectrum exhibits a two-particle continuum, a hallmark of fractionalization. Existing literature predicts that dynamical correlation functions could display signatures of anyonic statistics. Indeed, we found that the universal parameter $\alpha = 1/8$, characterising the chiral spin liquid, could be detected in the scaling of the Raman intensity as $I(\omega) \sim (\omega - E^0_{2v})^{\alpha}$, where E^0_{2v} is the two-particle gap. However, in order to observe this power-law, the anyon band structure must have a single minimum, which depends sensitively on the strength and signs of non-Kitaev interactions.

In some parameter regimes, the interaction between anyons was found to induce multiple bound states. We computed the Raman response from these bound states and analysed their sensitivity to circularly polarized light. Robust sharp peaks arising from anyon bound states were found to appear only in specific polarization channels, determined by the angular momentum quantum number of the wavefunctions. Such helicity-selective modes have been observed in recent experiments on $\alpha - \mathrm{RuCl}_3$, in the purported field-induced spin liquid regime[139]. Although our calculations were restricted to the two-anyon sector and zero temperature, it provides a controlled calculation of Raman response from anyons in the Kitaev liquid beyond the integrable limit.

9.1 Outlook

As with all scientific endeavours, this thesis raises more questions than it has answered. We have already presented detailed discussions on the limitations and open questions pertaining to the respective chapters. Here, I will take a step back and make an attempt to gather some thoughts on a few odds and ends.

An obvious question concerns the experimental signatures of dynamical gauge fields in Kitaev materials. The consequences of the diffusive motion of visons in relaxation experiments were discussed in detail in Chapter 5. By combining insights from Chapter 6, one could propose a universal signature of topological excitations in quasi-2D layered spin liquid systems. With Roman Lange, we have recently explored a simple model of visons diffusing in a layered system, which has shown novel corrections to relaxation times of a purely 2D model. Here a concrete experimental proposal needs to be developed with the microscopic details taken into account.

The softening of the vison gap and the resulting instabilities of the spin liquid phase require a much deeper understanding. Our perturbative approach was able to give a rough estimate of the critical points where the gaps close but is incapable of describing the phase transitions (if any). What is the resulting state when the visons proliferate? To the best of my knowledge, this remains an open problem. A major obstacle is the non-abelian nature of the particles, which prohibits a description in terms of a confinement-deconfinement type transition well understood in $\mathbb{Z}_2$ gauge theories [98, 165]. Phase transitions induced by the condensation of bosonic bound states of visons or vison-Majorana composites have been explored [166, 67, 167].

What is the edge theory corresponding to the topological vison bands that we have discovered in the AFM Kitaev liquid? The edge modes will be Ising anyons themselves, and their stability is an interesting question, as they may scatter from the gapless Majorana edge modes. A channel of propagating Ising anyons at the boundary may also have direct implications for topological quantum computing. For example, one could consider utilising these edge states for braiding.

An exciting recent development is the emergence of noisy intermediate-scale quantum (NISQ) devices, comprising a few (10-100) qubits, realized on a variety of hardware platforms. While nature has been hard on us in the real materials front, physicists have turned to these devices to simulate and study exotic many-body phases. An interesting question is how to describe and detect the dynamics of topological excitations in these simulated phases. Unlike a real material described by a Hamiltonian, quantum devices employ discrete quantum gates and measurement protocols to realize exotic states.

These are just a few of the many exciting questions that have crossed my mind throughout the course of this thesis. I believe the work presented here will not only contribute to our current understanding but also guide future experiments and theoretical advances in our search for dynamical emergent gauge fields, one of the most extraordinary predictions of modern condensed matter physics. That said, we shall remind ourselves to keep an open mind, for science has an uncanny way of surprising us in the most unexpected ways.

References

[1] J. Knolle, Gia-Wei Chern, D. L. Kovrizhin, R. Moessner, and N. B. Perkins. Raman scattering signatures of kitaev spin liquids in $A_2\mathrm{iro}_3$ iridates with $a =$ Na or li. *Phys. Rev. Lett.*, 113:187201, Oct 2014.

[2] On the theory of phase transitions. In D. TER HAAR, editor, *Collected Papers of L.D. Landau*, pages 193–216. Pergamon, 1965.

[3] Kenneth G. Wilson. The renormalization group: Critical phenomena and the kondo problem. *Rev. Mod. Phys.*, 47:773–840, Oct 1975.

[4] Leo P. Kadanoff. Scaling laws for ising models near T_c. *Physics Physique Fizika*, 2:263–272, Jun 1966.

[5] P. W. Anderson, G. Yuval, and D. R. Hamann. Exact results in the kondo problem. ii. scaling theory, qualitatively correct solution, and some new results on one-dimensional classical statistical models. *Phys. Rev. B*, 1:4464–4473, Jun 1970.

[6] Franz J. Wegner and Anthony Houghton. Renormalization group equation for critical phenomena. *Phys. Rev. A*, 8:401–412, Jul 1973.

[7] Michael E. Fisher. The renormalization group in the theory of critical behavior. *Rev. Mod. Phys.*, 46:597–616, Oct 1974.

[8] Lev Davidovich Landau. On the Theory of the Fermi Liquid. *J. Exp. Theor. Phys.*, 35, 1958.

[9] V. L. Ginzburg and L. D. Landau. *On the Theory of Superconductivity*, pages 113–137. Springer Berlin Heidelberg, Berlin, Heidelberg, 2009.

[10] John Bardeen, Leon N Cooper, and Robert Schrieffer. Theory of superconductivity. *Physical Review*, 108(5):1175–1204, 1957.

[11] Nobel prize in physics, https://www.nobelprize.org/prizes/physics/2016/press-release/, 2016.

[12] K. v. Klitzing, G. Dorda, and M. Pepper. New method for high-accuracy determination of the fine-structure constant based on quantized hall resistance. *Phys. Rev. Lett.*, 45:494–497, Aug 1980.

[13] JP Eisenstein and HL Stormer. The fractional quantum hall effect. *Science*, 248(4962):1510–1516, 1990.

[14] L. Saminadayar, D. C. Glattli, Y. Jin, and B. Etienne. Observation of the $e/3$ fractionally charged laughlin quasiparticle. *Phys. Rev. Lett.*, 79:2526–2529, Sep 1997.

[15] R. B. Laughlin. Anomalous quantum hall effect: An incompressible quantum fluid with fractionally charged excitations. *Phys. Rev. Lett.*, 50:1395–1398, May 1983.

[16] Daniel Arovas, J. R. Schrieffer, and Frank Wilczek. Fractional statistics and the quantum hall effect. *Phys. Rev. Lett.*, 53:722–723, Aug 1984.

[17] B. I. Halperin. Statistics of quasiparticles and the hierarchy of fractional quantized hall states. *Phys. Rev. Lett.*, 52:1583–1586, Apr 1984.

[18] Subir Sachdev. *Fractionalization and emergent gauge fields I*, page 151–152. Cambridge University Press, 2023.

[19] Chetan Nayak, Steven H. Simon, Ady Stern, Michael Freedman, and S. Das Sarma. Non-abelian anyons and topological quantum computation. *Reviews of Modern Physics*, 80(3):1083–1159, 2008.

[20] B. I. Halperin, Patrick A. Lee, and Nicholas Read. Theory of the half-filled landau level. *Phys. Rev. B*, 47:7312–7343, Mar 1993.

[21] David Tong. Gauge theory. *Lecture notes, DAMTP Cambridge*, 10:8, 2018.

[22] Steven T Bramwell and Michel JP Gingras. Spin ice state in frustrated magnetic pyrochlore materials. *Science*, 294(5546):1495–1501, 2001.

[23] Lin Lin, YL Xie, JJ Wen, Shuai Dong, ZB Yan, and JM Liu. Experimental observation of magnetoelectricity in spin ice dy2ti2o7. *New Journal of Physics*, 17(12):123018, 2015.

[24] David Jonathan Pryce Morris, David Alan Tennant, Santiago Andres Grigera, B Klemke, C Castelnovo, R Moessner, C Czternasty, M Meissner, KC Rule, J-U Hoffmann, et al. Dirac strings and magnetic monopoles in the spin ice dy2ti2o7. *Science*, 326(5951):411–414, 2009.

[25] K Matsuhira, Y Hinatsu, and T Sakakibara. Novel dynamical magnetic properties in the spin ice compound dy2ti2o7. *Journal of Physics: Condensed Matter*, 13(31):L737, 2001.

[26] Carley Paulsen, Martin James Jackson, Elsa Lhotel, Benjamin Canals, D Prabhakaran, K Matsuhira, SR Giblin, and ST Bramwell. Far-from-equilibrium monopole dynamics in spin ice. *Nature Physics*, 10(2):135–139, 2014.

[27] Kate A. Ross, Lucile Savary, Bruce D. Gaulin, and Leon Balents. Quantum excitations in quantum spin ice. *Phys. Rev. X*, 1:021002, Oct 2011.

[28] P.W. Anderson. Resonating valence bonds: A new kind of insulator? *Materials Research Bulletin*, 8(2):153 – 160, 1973.

[29] Ady Stern. Anyons and the quantum hall effect—a pedagogical review. *Annals of Physics*, 323(1):204–249, 2008.

[30] A Yu Kitaev. Fault-tolerant quantum computation by anyons. *Annals of physics*, 303(1):2–30, 2003.

[31] Franz J Wegner. Duality in generalized ising models and phase transitions without local order parameters. *Journal of Mathematical Physics*, 12(10):2259–2272, 1971.

[32] Xiao-Gang Wen. Quantum orders and symmetric spin liquids. *Phys. Rev. B*, 65:165113, Apr 2002.

[33] Zohar Nussinov and Gerardo Ortiz. Autocorrelations and thermal fragility of anyonic loops in topologically quantum ordered systems. *Physical Review B—Condensed Matter and Materials Physics*, 77(6):064302, 2008.

[34] Benjamin J Brown, Daniel Loss, Jiannis K Pachos, Chris N Self, and James R Wootton. Quantum memories at finite temperature. *Reviews of Modern Physics*, 88(4):045005, 2016.

[35] Satoshi Yamashita, Yasuhiro Nakazawa, Masaharu Oguni, Yugo Oshima, Hiroyuki Nojiri, Yasuhiro Shimizu, Kazuya Miyagawa, and Kazushi Kanoda. Thermodynamic properties of a spin-1/2 spin-liquid state in a κ-type organic salt. *Nature Physics*, 4(6):459–462, 2008.

[36] Minoru Yamashita, Norihito Nakata, Yoshinori Senshu, Masaki Nagata, Hiroshi M Yamamoto, Reizo Kato, Takasada Shibauchi, and Yuji Matsuda. Highly mobile gapless excitations in a two-dimensional candidate quantum spin liquid. *Science*, 328(5983):1246–1248, 2010.

[37] Tian-Heng Han, Joel S Helton, Shaoyan Chu, Daniel G Nocera, Jose A Rodriguez-Rivera, Collin Broholm, and Young S Lee. Fractionalized excitations in the spin-liquid state of a kagome-lattice antiferromagnet. *Nature*, 492(7429):406–410, 2012.

[38] Tokuro Shimokawa, Ken Watanabe, and Hikaru Kawamura. Static and dynamical spin correlations of the $s = \frac{1}{2}$ random-bond antiferromagnetic heisenberg model on the triangular and kagome lattices. *Phys. Rev. B*, 92:134407, Oct 2015.

[39] Matthias Punk, Debanjan Chowdhury, and Subir Sachdev. Topological excitations and the dynamic structure factor of spin liquids on the kagome lattice. *Nature Physics*, 10(4):289–293, 2014.

[40] Alexei Kitaev. Anyons in an exactly solved model and beyond. *Annals of Physics*, 321(1):2 – 111, 2006. January Special Issue.

[41] G. Khaliullin and G. Jackeli. Mott insulators in the strong spin-orbit coupling limit: From heisenberg to a quantum compass and kitaev models. *Physical Review Letters*, 102(1), 2009/01/06/.

[42] Y. Kasahara, T. Ohnishi, Y. Mizukami, O. Tanaka, Sixiao Ma, K. Sugii, N. Kurita, H. Tanaka, J. Nasu, Y. Motome, T. Shibauchi, and Y. Matsuda. "Majorana quantization and half-integer thermal quantum Hall effect in a Kitaev spin liquid". *Nature*, 559(7713), 2018.

[43] T. Yokoi, S. Ma, Y. Kasahara, S. Kasahara, T. Shibauchi, N. Kurita, H. Tanaka, J. Nasu, Y. Motome, C. Hickey, S. Trebst, and Y. Matsuda. Half-integer quantized anomalous thermal Hall effect in the Kitaev material candidate α-RuCl$_3$. *Science*, 373(6554), 2021.

[44] Michael Tinkham. *Introduction to Superconductivity*. Dover Publications, 2 edition, 2004.

[45] Alexander Altland and Ben D Simons. *Condensed matter field theory*. Cambridge university press, 2010.

[46] Jean-Paul. Blaizot and Georges. Ripka. Quantum theory of finite systems. MIT Press, 1986///.

[47] Fabio L. Pedrocchi, Stefano Chesi, and Daniel Loss. Physical solutions of the kitaev honeycomb model. *Phys. Rev. B*, 84:165414, Oct 2011.

[48] Matthias Vojta and Fabian Zschocke. Physical states and finite-size effects in kitaev's honeycomb model: Bond disorder, spin excitations, and nmr line shape. *Physical Review B*, 92(1), 2015/07/06/.

[49] Matthew P. A. Fisher and T. Senthil. Z_2 gauge theory of electron fractionalization in strongly correlated systems. *Physical Review B*, 62(12), 2000/09/15/.

[50] Saptarshi Mandal, R. Shankar, and G. Baskaran. Exact results for spin dynamics and fractionalization in the kitaev model. *Physical Review Letters*, 98(24), 2007/06/11/.

[51] Hong Yao and Steven A. Kivelson. Exact chiral spin liquid with non-abelian anyons. *Phys. Rev. Lett.*, 99:247203, Dec 2007.

[52] Elliott H. Lieb. Flux phase of the half-filled band. *Phys. Rev. Lett.*, 73:2158–2161, Oct 1994.

[53] Tim Eschmann, Petr A. Mishchenko, Kevin O'Brien, Troels A. Bojesen, Yasuyuki Kato, Maria Hermanns, Yukitoshi Motome, and Simon Trebst. Thermodynamic classification of three-dimensional kitaev spin liquids. *Phys. Rev. B*, 102:075125, Aug 2020.

[54] F. D. M. Haldane. Model for a quantum hall effect without landau levels: Condensed-matter realization of the "parity anomaly". *Phys. Rev. Lett.*, 61:2015–2018, Oct 1988.

[55] É. Lefrançois, G. Grissonnanche, J. Baglo, P. Lampen-Kelley, J.-Q. Yan, C. Balz, D. Mandrus, S. E. Nagler, S. Kim, Young-June Kim, N. Doiron-Leyraud, and Louis Taillefer. Evidence of a phonon hall effect in the kitaev spin liquid candidate $\alpha-$rucl$_3$. *Phys. Rev. X*, 12:021025, Apr 2022.

[56] Yuval Vinkler-Aviv and Achim Rosch. Approximately Quantized Thermal Hall Effect of Chiral Liquids Coupled to Phonons. *Phys. Rev. X*, 8:031032, Aug 2018.

[57] Mengxing Ye, Gábor B. Halász, Lucile Savary, and Leon Balents. Quantization of the Thermal Hall Conductivity at Small Hall Angles. *Phys. Rev. Lett.*, 121:147201, Oct 2018.

[58] M Leinaas and J Myrheim. On the theory of identical particles. ii nuovo cimento 37b. *Nuovo Cimento B (1971-1996)*, 1977.

[59] Frank Wilczek. Quantum mechanics of fractional-spin particles. *Phys. Rev. Lett.*, 49:957–959, Oct 1982.

[60] James Nakamura, Shuang Liang, Geoffrey C Gardner, and Michael J Manfra. Direct observation of anyonic braiding statistics. *Nature Physics*, 16(9):931–936, 2020.

[61] Jiannis K. Pachos. *Introduction to Topological Quantum Computation*. Cambridge University Press, USA, 1st edition, 2012.

[62] Nevill F Mott. The basis of the electron theory of metals, with special reference to the transition metals. *Proceedings of the Physical Society. Section A*, 62(7):416, 1949.

[63] Kliment I Kugel and Daniel I Khomskii. Crystal-structure and magnetic properties of substances with orbital degeneracy. *Zh. Eksp. Teor. Fiz*, 64:1429–1439, 1973.

[64] Simon Trebst and Ciarán Hickey. Kitaev materials. *Physics Reports*, 950:1–37, 2022.

[65] Jeffrey G. Rau, Eric Kin-Ho Lee, and Hae-Young Kee. Generic spin model for the honeycomb iridates beyond the kitaev limit. *Phys. Rev. Lett.*, 112:077204, Feb 2014.

[66] Subhro Bhattacharjee, Roderich Moessner, and Johannes Knolle. Dynamics of a quantum spin liquid beyond integrability: The kitaev-heisenberg-Γ model in an augmented parton mean-field theory. *Physical Review B*, 97(13), 2018/04/30/.

[67] Shang-Shun Zhang, Gábor B. Halász, Wei Zhu, and Cristian D. Batista. Variational study of the kitaev-heisenberg-gamma model. *Phys. Rev. B*, 104:014411, Jul 2021.

[68] Ruben Verresen, Roderich Moessner, Frank Pollmann, and Matthias Gohlke. Dynamics of the kitaev-heisenberg model. *Physical Review Letters*, 119(15), 2017/10/12/.

[69] Ciarán Hickey and Simon Trebst. Emergence of a field-driven u (1) spin liquid in the kitaev honeycomb model. *Nature Communications*, 10(1).

[70] Xue-Yang Song, Yi-Zhuang You, and Leon Balents. Low-energy spin dynamics of the honeycomb spin liquid beyond the kitaev limit. *Phys. Rev. Lett.*, 117:037209, Jul 2016.

[71] Maria Hermanns, Itamar Kimchi, and Johannes Knolle. Physics of the kitaev model: Fractionalization, dynamic correlations, and material connections. *Annual Review of Condensed Matter Physics*, 9(1):17–33, 2018.

[72] P. A. Maksimov and A. L. Chernyshev. Rethinking $\alpha-$rucl$_3$. *Phys. Rev. Res.*, 2:033011, Jul 2020.

[73] P. Lampen-Kelley, S. Rachel, J. Reuther, J.-Q. Yan, A. Banerjee, C. A. Bridges, H. B. Cao, S. E. Nagler, and D. Mandrus. Anisotropic susceptibilities in the honeycomb kitaev system $\alpha-$rucl$_3$. *Phys. Rev. B*, 98:100403, Sep 2018.

[74] Kejing Ran, Jinghui Wang, Wei Wang, Zhao-Yang Dong, Xiao Ren, Song Bao, Shichao Li, Zhen Ma, Yuan Gan, Youtian Zhang, J. T. Park, Guochu Deng, S. Danilkin, Shun-Li Yu, Jian-Xin Li, and Jinsheng Wen. Spin-wave excitations evidencing the kitaev interaction in single crystalline $\alpha-$rucl$_3$. *Phys. Rev. Lett.*, 118:107203, Mar 2017.

[75] Arnab Banerjee, Jiaqiang Yan, Johannes Knolle, Craig A Bridges, Matthew B Stone, Mark D Lumsden, David G Mandrus, David A Tennant, Roderich Moessner, and Stephen E Nagler. Neutron scattering in the proximate quantum spin liquid α-rucl3. *Science*, 356(6342):1055–1059, 2017.

[76] Joji Nasu, Johannes Knolle, Dima L Kovrizhin, Yukitoshi Motome, and Roderich Moessner. Fermionic response from fractionalization in an insulating two-dimensional magnet. *Nature Physics*, 12(10):912–915, 2016.

[77] Kumpei Imamura, Shota Suetsugu, Yuta Mizukami, Yusei Yoshida, Kenichiro Hashimoto, Kenichi Ohtsuka, Yuichi Kasahara, Nobuyuki Kurita, Hidekazu Tanaka, Pureum Noh, et al. Majorana-fermion origin of the planar thermal hall effect in the kitaev magnet α-rucl3. *Science advances*, 10(11):eadk3539, 2024.

[78] K. W. Plumb, J. P. Clancy, L. J. Sandilands, V. Vijay Shankar, Y. F. Hu, K. S. Burch, Hae-Young Kee, and Young-June Kim. $\alpha-$rucl$_3$: A spin-orbit assisted mott insulator on a honeycomb lattice. *Phys. Rev. B*, 90:041112, Jul 2014.

[79] Jan A. N. Bruin, Raphael Claus, Yoshimitsu Matsumoto, Nobuyuki Kurita, Hidekazu Tanaka, and Hidenori Takagi. Robustness of the thermal hall effect close to half-quantization in α-rucl$_3$. *Nature Physics*, 18:401–405, 2022.

[80] Peter Czajka, Tong Gao, Max Hirschberger, Paula Lampen-Kelley, Arnab Banerjee, Jiaqiang Yan, David G Mandrus, Stephen E Nagler, and NP Ong. Oscillations of the thermal conductivity in the spin-liquid state of α-rucl3. *Nature Physics*, 17(8):915–919, 2021.

[81] O Tanaka, Y Mizukami, R Harasawa, K Hashimoto, K Hwang, N Kurita, H Tanaka, S Fujimoto, Y Matsuda, E-G Moon, et al. Thermodynamic evidence for a field-angle-dependent majorana gap in a kitaev spin liquid. *Nature Physics*, 18(4):429–435, 2022.

[82] Gaoting Lin, Jaehong Jeong, Chaebin Kim, Yao Wang, Qing Huang, Takatsugu Masuda, Shinichiro Asai, Shinichi Itoh, Gerrit Günther, Margarita Russina, et al. Field-induced quantum spin disordered state in spin-1/2 honeycomb magnet na2co2teo6. *Nature communications*, 12(1):5559, 2021.

[83] Jinwu Ye and Subir Sachdev. Coulomb interactions at quantum hall critical points of systems in a periodic potential. *Phys. Rev. Lett.*, 80:5409–5412, Jun 1998.

[84] Aprem P. Joy. *Dynamics of visons in perturbed Kitaev models, Master's thesis*. 2020.

[85] Aprem P. Joy and Achim Rosch. Dynamics of visons and thermal hall effect in perturbed kitaev models. *Phys. Rev. X*, 12:041004, Oct 2022.

[86] L. M. Robledo. Sign of the overlap of hartree-fock-bogoliubov wave functions. *Physical Review C*, 79(2), 2009/02/20/.

[87] M. Wimmer. Algorithm 923: Efficient numerical computation of the pfaffian for dense and banded skew-symmetric matrices. *ACM Trans. Math. Softw.*, 38(4), August 2012.

[88] Maissam Barkeshli, Parsa Bonderson, Meng Cheng, and Zhenghan Wang. Symmetry fractionalization, defects, and gauging of topological phases. *Phys. Rev. B*, 100:115147, Sep 2019.

[89] Niravkumar D. Patel and Nandini Trivedi. Magnetic field-induced intermediate quantum spin liquid with a spinon fermi surface. *Proceedings of the National Academy of Sciences*, 116(25):12199–12203, 2019.

[90] Jeffrey G. Rau, Eric Kin-Ho Lee, and Hae-Young Kee. Generic Spin Model for the Honeycomb Iridates beyond the Kitaev Limit. *Phys. Rev. Lett.*, 112:077204, Feb 2014.

[91] Ji ří Chaloupka, George Jackeli, and Giniyat Khaliullin. Zigzag Magnetic Order in the Iridium Oxide Na$_2$IrO$_3$. *Phys. Rev. Lett.*, 110:097204, Feb 2013.

[92] Hyun-Yong Lee, Ryui Kaneko, Li Ern Chern, Tsuyoshi Okubo, Youhei Yamaji, Naoki Kawashima, Yong Baek Kim, Ryui Kaneko, Li Ern Chern, Tsuyoshi Okubo, Youhei Yamaji, Naoki Kawashima, Yong Baek Kim, Ryui Kaneko, Li Ern Chern, Tsuyoshi Okubo, Youhei Yamaji, Naoki Kawashima, and Yong Baek Kim. Magnetic field induced quantum phases in a tensor network study of Kitaev magnets. *Nature Communications*, 11(1).

[93] Matthias Gohlke, Li Ern Chern, Hae-Young Kee, and Yong Baek Kim. Emergence of nematic paramagnet via quantum order-by-disorder and pseudo-Goldstone modes in Kitaev magnets. *Phys. Rev. Research*, 2:043023, Oct 2020.

[94] Ravi Yadav, Nikolay A. Bogdanov, Vamshi M. Katukuri, Satoshi Nishimoto, Jeroen van den Brink, and Liviu Hozoi. Kitaev exchange and field-induced quantum spin-liquid states in honeycomb αRuCl$_3$. *Scientific Reports*, 6(1).

[95] Stephen M. Winter, Ying Li, Harald O. Jeschke, and Roser Valentí. Challenges in design of Kitaev materials: Magnetic interactions from competing energy scales. *Phys. Rev. B*, 93:214431, Jun 2016.

[96] Y. S. Hou, H. J. Xiang, and X. G. Gong. Unveiling magnetic interactions of ruthenium trichloride via constraining direction of orbital moments: Potential routes to realize a quantum spin liquid. *Phys. Rev. B*, 96:054410, Aug 2017.

[97] Yejin Huh, Matthias Punk, and Subir Sachdev. Vison states and confinement transitions of $\mathbb{Z}_2$ spin liquids on the kagome lattice. *Phys. Rev. B*, 84:094419, Sep 2011.

[98] Simon Trebst, Philipp Werner, Matthias Troyer, Kirill Shtengel, and Chetan Nayak. Breakdown of a topological phase: Quantum phase transition in a loop gas model with tension. *Phys. Rev. Lett.*, 98:070602, Feb 2007.

[99] Andrew M. Essin and Michael Hermele. Spectroscopic signatures of crystal momentum fractionalization. *Phys. Rev. B*, 90:121102, Sep 2014.

[100] Wen-Han Kao, Johannes Knolle, Gábor B. Halász, Roderich Moessner, and Natalia B. Perkins. Vacancy-induced low-energy density of states in the kitaev spin liquid. *Phys. Rev. X*, 11:011034, Feb 2021.

[101] Johannes Knolle, Roderich Moessner, and Natalia B. Perkins. Bond-Disordered Spin Liquid and the Honeycomb Iridate H$_3$LiIr$_2$O$_6$: Abundant Low-Energy Density of States from Random Majorana Hopping. *Phys. Rev. Lett.*, 122:047202, Feb 2019.

[102] Y. Aharonov and D. Bohm. Significance of Electromagnetic Potentials in the Quantum Theory. *Phys. Rev.*, 115:485–491, Aug 1959.

[103] Sriram Ganeshan, Manas Kulkarni, and Adam C. Durst. Quasiparticle scattering from vortices in d-wave superconductors. ii. berry phase contribution. *Phys. Rev. B*, 84:064503, Aug 2011.

[104] Achim Rosch. Quantum-coherent transport of a heavy particle in a fermionic bath. *Advances in Physics*, 48(3), 1999/05/01.

[105] Achim Rosch. Quantum-coherent transport of a heavy particle in a fermionic bath. *Advances in Physics*, 48(3), 1999.

[106] Predrag Nikolić and Subir Sachdev. Effective action for vortex dynamics in clean d-wave superconductors. *Phys. Rev. B*, 73:134511, Apr 2006.

[107] Reif, F. (1965). Fundamentals of statistical and thermal physics. New York: McGraw-Hill.

[108] John Cardy. Reaction-diffusion processes. *A+ A*, 100(26):13–19, 2006.

[109] Julian Wagner, Anuja Sahasrabudhe, Rolf Versteeg, Zhe Wang, Vladimir Tsurkan, Alois Loidl, Hamoon Hedayat, and Paul H. M. van Loosdrecht. Nonequilibrium dynamics of α-rucl$_3$ – a time-resolved magneto-optical spectroscopy study. *arXiv*, 2022.

[110] Haochen Zhang, Subin Kim, Young-June Kim, Hae-Young Kee, and Luyi Yang. Ultrafast spin dynamics in the proximate quantum spin liquid $\alpha - \text{RuCl}_3$. *Phys. Rev. B*, 110:L081111, Aug 2024.

[111] Wassilios Papawassiliou, Nicolas Lazaridis, Eunice Mumba Mpanga, Jonas Koppe, Nikolaos Panopoulos, Marina Karagianni, Lydia Gkoura, Romain Berthelot, Michael Fardis, Andrew J. Pell, and Georgios Papavassiliou. The role of quantum metastability and the perspective of quantum glassiness in kitaev fractional spin dynamics: An nmr study. *arXiv.2407.14663*, 2024.

[112] C. Balz, L. Janssen, P. Lampen-Kelley, A. Banerjee, Y. H. Liu, J.-Q. Yan, D. G. Mandrus, M. Vojta, and S. E. Nagler. Field-induced intermediate ordered phase and anisotropic interlayer interactions in $\alpha{-}\text{rucl}_3$. *Phys. Rev. B*, 103:174417, May 2021.

[113] Lukas Janssen, Stefan Koch, and Matthias Vojta. Magnon dispersion and dynamic spin response in three-dimensional spin models for $\alpha{-}\text{rucl}_3$. *Phys. Rev. B*, 101:174444, May 2020.

[114] Urban F. P. Seifert, Julian Gritsch, Erik Wagner, Darshan G. Joshi, Wolfram Brenig, Matthias Vojta, and Kai P. Schmidt. Bilayer kitaev models: Phase diagrams and novel phases. *Phys. Rev. B*, 98:155101, Oct 2018.

[115] Aayush Vijayvargia, Urban F. P. Seifert, and Onur Erten. Topological and magnetic phase transitions in the bilayer kitaev-ising model. *Phys. Rev. B*, 109:024439, Jan 2024.

[116] Yochai Werman, Shubhayu Chatterjee, Siddhardh C. Morampudi, and Erez Berg. Signatures of fractionalization in spin liquids from interlayer thermal transport. *Phys. Rev. X*, 8:031064, Sep 2018.

[117] Trithep Devakul, S. L. Sondhi, S. A. Kivelson, and Erez Berg. Floating topological phases. *Phys. Rev. B*, 102:125136, Sep 2020.

[118] Michael Pretko, Xie Chen, and Yizhi You. Fracton phases of matter. *International Journal of Modern Physics A*, 35(06):2030003, 2020.

[119] Kevin Slagle and Yong Baek Kim. Fracton topological order from nearest-neighbor two-spin interactions and dualities. *Phys. Rev. B*, 96:165106, Oct 2017.

[120] Andrey Gromov and Leo Radzihovsky. Colloquium: Fracton matter. *Rev. Mod. Phys.*, 96:011001, Jan 2024.

[121] Cécile Repellin. The twisted material that splits the electron. *Nature*.

[122] Hiroyuki Tomishige, Joji Nasu, and Akihisa Koga. Low-temperature properties in the bilayer kitaev model. *Phys. Rev. B*, 99:174424, May 2019.

[123] J. Knolle, D. L. Kovrizhin, J. T. Chalker, and R. Moessner. Dynamics of a two-dimensional quantum spin liquid: Signatures of emergent majorana fermions and fluxes. *Phys. Rev. Lett.*, 112:207203, May 2014.

[124] Aaditya Panigrahi, Piers Coleman, and Alexei Tsvelik. Analytic calculation of the vison gap in the kitaev spin liquid. *Phys. Rev. B*, 108:045151, Jul 2023.

[125] Chuan Chen and Inti Sodemann Villadiego. Nature of visons in the perturbed ferromagnetic and antiferromagnetic kitaev honeycomb models. *Phys. Rev. B*, 107:045114, Jan 2023.

[126] Christoph Berke, Simon Trebst, and Ciarán Hickey. Field stability of majorana spin liquids in antiferromagnetic kitaev models. *Phys. Rev. B*, 101:214442, Jun 2020.

[127] Masanori Kohno, Oleg A Starykh, and Leon Balents. Spinons and triplons in spatially anisotropic frustrated antiferromagnets. *Nature Physics*, 3(11):790–795, 2007.

[128] Lukas Schamriß, Lea Lenke, Matthias Mühlhauser, and Kai Phillip Schmidt. Quantum phase transitions in the k-layer ising toric code. *Phys. Rev. B*, 105:184425, May 2022.

[129] Kyusung Hwang. Anyon condensation and confinement transition in a kitaev spin liquid bilayer. *Phys. Rev. B*, 109:134412, Apr 2024.

[130] Gábor B. Halász, Timothy H. Hsieh, and Leon Balents. Fracton topological phases from strongly coupled spin chains. *Phys. Rev. Lett.*, 119:257202, Dec 2017.

[131] Seung-Hwan Do, Sang-Youn Park, Junki Yoshitake, Joji Nasu, Yukitoshi Motome, Yong Seung Kwon, DT Adroja, DJ Voneshen, Kyoo Kim, T-H Jang, et al. Majorana fermions in the kitaev quantum spin system α-rucl3. *Nature Physics*, 13(11):1079–1084, 2017.

[132] Arnab Banerjee, Paula Lampen-Kelley, Johannes Knolle, Christian Balz, Adam Anthony Aczel, Barry Winn, Yaohua Liu, Daniel Pajerowski, Jiaqiang Yan, Craig A Bridges, et al. Excitations in the field-induced quantum spin liquid state of α-rucl3. *npj Quantum Materials*, 3(1):8, 2018.

[133] Luke J. Sandilands, Yao Tian, Kemp W. Plumb, Young-June Kim, and Kenneth S. Burch. Scattering continuum and possible fractionalized excitations in $\alpha-\mathrm{rucl}_3$. *Phys. Rev. Lett.*, 114:147201, Apr 2015.

[134] Dirk Wulferding, Youngsu Choi, Wonjun Lee, and Kwang-Yong Choi. Raman spectroscopic diagnostic of quantum spin liquids. *Journal of Physics: Condensed Matter*, 32(4):043001, 2019.

[135] Emil Viñas Boström, Tahereh Sadat Parvini, James W. McIver, Angel Rubio, Silvia Viola Kusminskiy, and Michael A. Sentef. Direct optical probe of magnon topology in two-dimensional quantum magnets. *Phys. Rev. Lett.*, 130:026701, Jan 2023.

[136] RJ Elliott and R Loudon. The possible observation of electronic raman transitions in crystals. *Physics Letters*, 3(4):189–191, 1963.

[137] P. A. Fleury and R. Loudon. Scattering of light by one- and two-magnon excitations. *Phys. Rev.*, 166:514–530, Feb 1968.

[138] B. Sriram Shastry and Boris I. Shraiman. Theory of raman scattering in mott-hubbard systems. *Phys. Rev. Lett.*, 65:1068–1071, Aug 1990.

[139] Anuja Sahasrabudhe, Mikhail A. Prosnikov, Thomas C. Koethe, Philipp Stein, Vladimir Tsurkan, Alois Loidl, Markus Grüninger, Hamoon Hedayat, and Paul H. M. van Loosdrecht. Chiral excitations and the intermediate-field regime in the kitaev magnet $\alpha-\mathrm{rucl}_3$. *Phys. Rev. Res.*, 6:L022005, Apr 2024.

[140] Dirk Wulferding, Youngsu Choi, Seung-Hwan Do, Chan Hyeon Lee, Peter Lemmens, Clément Faugeras, Yann Gallais, and Kwang-Yong Choi. Magnon bound states versus anyonic majorana excitations in the kitaev honeycomb magnet α-rucl3. *Nature communications*, 11(1):1603, 2020.

[141] Yang Yang, Mengqun Li, Ioannis Rousochatzakis, and Natalia B Perkins. Non-loudon-fleury raman scattering in spin-orbit coupled mott insulators. *Physical Review B*, 104(14):144412, 2021.

[142] J. K. Jain. Composite-fermion approach for the fractional quantum hall effect. *Phys. Rev. Lett.*, 63:199–202, Jul 1989.

[143] Frank Wilczek. *Fractional statistics and anyon superconductivity*, volume 5. World scientific, 1990.

[144] Ville Lahtinen, Andreas W. W. Ludwig, Jiannis K. Pachos, and Simon Trebst. Topological liquid nucleation induced by vortex-vortex interactions in kitaev's honeycomb model. *Phys. Rev. B*, 86:075115, Aug 2012.

[145] Meng Cheng, Roman M. Lutchyn, Victor Galitski, and S. Das Sarma. Splitting of majorana-fermion modes due to intervortex tunneling in a $p_x + ip_y$ superconductor. *Phys. Rev. Lett.*, 103:107001, Aug 2009.

[146] Ville Lahtinen, Graham Kells, Angelo Carollo, Tim Stitt, Jiri Vala, and Jiannis K Pachos. Spectrum of the non-abelian phase in kitaev's honeycomb lattice model. *Annals of Physics*, 323(9):2286–2310, 2008.

[147] Siddhardh C. Morampudi, Ari M. Turner, Frank Pollmann, and Frank Wilczek. Statistics of fractionalized excitations through threshold spectroscopy. *Phys. Rev. Lett.*, 118:227201, May 2017.

[148] Lifa Zhang and Qian Niu. Chiral phonons at high-symmetry points in monolayer hexagonal lattices. *Phys. Rev. Lett.*, 115:115502, Sep 2015.

[149] Yuki Tatsumi, Tomoaki Kaneko, and Riichiro Saito. Conservation law of angular momentum in helicity-dependent raman and rayleigh scattering. *Phys. Rev. B*, 97:195444, May 2018.

[150] Masafumi Udagawa, Shintaro Takayoshi, and Takashi Oka. Scanning tunneling microscopy as a single majorana detector of kitaev's chiral spin liquid. *Phys. Rev. Lett.*, 126:127201, Mar 2021.

[151] Santhosh G., V. Sreenath, Arul Lakshminarayan, and Rajesh Narayanan. Localized zero-energy modes in the kitaev model with vacancy disorder. *Phys. Rev. B*, 85:054204, Feb 2012.

[152] A. J. Willans, J. T. Chalker, and R. Moessner. Disorder in a quantum spin liquid: Flux binding and local moment formation. *Phys. Rev. Lett.*, 104:237203, Jun 2010.

[153] Max McGinley, Michele Fava, and S. A. Parameswaran. Signatures of fractional statistics in nonlinear pump-probe spectroscopy. *Phys. Rev. Lett.*, 132:066702, Feb 2024.

[154] Shiuan-Fan Liou, F. D. M. Haldane, Kun Yang, and E. H. Rezayi. Chiral gravitons in fractional quantum hall liquids. *Phys. Rev. Lett.*, 123:146801, Sep 2019.

[155] Jiehui Liang, Ziyu Liu, Zihao Yang, Yuelei Huang, Ursula Wurstbauer, Cory R Dean, Ken W West, Loren N Pfeiffer, Lingjie Du, and Aron Pinczuk. Evidence for chiral graviton modes in fractional quantum hall liquids. *Nature*, 628(8006):78–83, 2024.

[156] Lifa Zhang. Berry curvature and various thermal hall effects. *New Journal of Physics*, 18(10):103039, 2016.

[157] Heung-Sik Kim, Vijay Shankar V., Andrei Catuneanu, and Hae-Young Kee. Kitaev magnetism in honeycomb rucl$_3$ with intermediate spin-orbit coupling. *Phys. Rev. B*, 91:241110, Jun 2015.

[158] Rohit Sharma, Mahasweta Bagchi, Yongjian Wang, Yoichi Ando, and Thomas Lorenz. Phonon thermal hall effect in charge-compensated topological insulators. *Phys. Rev. B*, 109:104304, Mar 2024.

[159] Li Ern Chern, Emily Z. Zhang, and Yong Baek Kim. Sign structure of thermal hall conductivity and topological magnons for in-plane field polarized kitaev magnets. *Phys. Rev. Lett.*, 126:147201, Apr 2021.

[160] Haoyu Guo and Subir Sachdev. Extrinsic phonon thermal hall transport from hall viscosity. *Phys. Rev. B*, 103:205115, May 2021.

[161] Léo Mangeolle, Leon Balents, and Lucile Savary. Phonon thermal hall conductivity from scattering with collective fluctuations. *Phys. Rev. X*, 12:041031, Dec 2022.

[162] Chaebin Kim, Jaehong Jeong, Gaoting Lin, Pyeongjae Park, Takatsugu Masuda, Shinichiro Asai, Shinichi Itoh, Heung-Sik Kim, Haidong Zhou, Jie Ma, et al. Antiferromagnetic kitaev interaction inj eff= 1/2 cobalt honeycomb materials na3co2sbo6 and na2co2teo6. *Journal of Physics: Condensed Matter*, 34(4):045802, 2021.

[163] Yusuke Sugita, Yasuyuki Kato, and Yukitoshi Motome. Antiferromagnetic kitaev interactions in polar spin-orbit mott insulators. *Phys. Rev. B*, 101:100410, Mar 2020.

[164] Chaebin Kim, Jaehong Jeong, Gaoting Lin, Pyeongjae Park, Takatsugu Masuda, Shinichiro Asai, Shinichi Itoh, Heung-Sik Kim, Haidong Zhou, Jie Ma, Je-Geun Park, Jaehong Jeong, Gaoting Lin, Pyeongjae Park, Takatsugu Masuda, Shinichiro Asai, Shinichi Itoh, Heung-Sik Kim, Haidong Zhou, Jie Ma, and Je-Geun Park. Antiferromagnetic kitaev interaction inj. *Journal of Physics: Condensed Matter*, 34(4).

[165] S. Mandal, Subhro Bhattacharjee, K. Sengupta, R. Shankar, and G. Baskaran. Confinement-deconfinement transition and spin correlations in a generalized kitaev model. *Phys. Rev. B*, 84:155121, Oct 2011.

[166] Shang-Shun Zhang, Gábor B Halász, and Cristian D Batista. Theory of the kitaev model in a [111] magnetic field. *Nature Communications*, 13(1):399, 2022.

[167] Inti Sodemann. Private communication.

Appendix A

Overlap of BCS Vacua: Path Integrals

In this appendix, we derive the Pfaffian formula to calculate the overlap between two Bogoliubov vacua. This was first introduced by Robledo to calculate nuclear matrix elements inside a nucleus [86]. We begin by introducing some of the important properties of Pfaffians which will aid us along the derivation. The pfaffian of a 2N dimensional anti-symmetric matrix M is defined as

$$\mathrm{Pf}(M) = \frac{1}{n!2^n} \sum_{\{P\}} \varepsilon(P) M_{i_1,i_2} M_{i_3,i_4} \dots M_{i_2n-1,i_2n} \tag{A.1}$$

where $\{P\}$ is the set of all possible permutations of $(i_1, i_2 \dots i_2n)$ and $\varepsilon(P) = \pm 1$ for even (odd) permutations. Some of the useful properties of Pfaffian are

$$\mathrm{Pf}(S^T MS) = \det(S) Pf(M) \tag{A.2}$$

$$\mathrm{Pf}\begin{pmatrix} 0 & M \\ -M^T & 0 \end{pmatrix} = (-1)^{N(N-1)/2} \det(M) \tag{A.3}$$

$$|\mathrm{Pf}(M)| = |\sqrt{\det(M)}| \tag{A.4}$$

Consider two BdG Hamiltonians H_1 and H_2 in fermion operators f which are diagonalized by Bogoliubov transformations $X^{(1)}, Y^{(1)}$ and $X^{(2)}, Y^{(2)}$ respectively. Let the corresponding quasiparticle operators be $a^{(1)}$ and $a^{(2)}$ respectively.

$$X_{ij}^{(l)} f_j^\dagger + Y_{ij}^{(l)} f_j = a_i^{(l)\dagger} \tag{A.5}$$

Using Thouless parametrization we can express the Bogoliubov vacua (ground state) as

$$\left|\psi^{l}\right\rangle = |\mathscr{N}_l| \exp\left\{-\frac{1}{2}\sum_{i<j}^{N} Z_{ij}^{(l)} f_i^\dagger f_j^\dagger\right\} |0_f\rangle \tag{A.6}$$

where l takes values 1 or 2 corresponding to the labels. The total dimension of the single particle Hilbert space is N. $\left|0_f\right\rangle$ denotes the vacuum of the f fermions - $f\left|0_f\right\rangle = 0$. Note that we have implicitly fixed the phase of the wavefunction by taking the modulus of the normalization factor $N^{(l)}$. $Z^{(l)}$ is a $N \times N$ anti-symmetric matrix given by

$$Z^{(l)} = ((X^{(l)})^{-1} Y^{(l)})^* \tag{A.7}$$

The overlap between the two vacua is given by

$$\left\langle \psi^{(1)} \middle| \psi^{(2)} \right\rangle = \langle 0_f | \, e^{\frac{1}{2} Z_{ij}^{(1)*} f_i f_j} e^{-\frac{1}{2} Z_{ij}^{(2)} f_i f_j} \left|0_f\right\rangle \tag{A.8}$$

Introducing fermion coherent states $|z\rangle$ which have the corresponding anti-commuting Grassmann variables z_k and z_k^* obeying the following properties

$$f_k |z\rangle = z_k |z\rangle \qquad\qquad \langle z| f_k^\dagger = z_k^* \langle z| \tag{A.9}$$

we can insert the identity operator defined as

$$\mathbb{1} = \int \prod (dz_k dz_k^* e^{-z_k^* z_k}) |z\rangle \langle z| \tag{A.10}$$

into the overlap expression to obtain

$$\begin{aligned} \left\langle \psi^{(1)} \middle| \psi^{(2)} \right\rangle &= \int (\prod dz_k^* dz_k) \langle 0_f | \, e^{\frac{1}{2} Z_{kk'}^{(1)*} f_k f_{k'}} e^{-z_k^* z_k} |z\rangle \langle z| \, e^{-\frac{1}{2} Z_{kk'}^{(2)} f_k^\dagger f_{k'}^\dagger} \left|0_f\right\rangle \\ &= \int (\prod dz_k^* dz_k) e^{\frac{1}{2} Z_{kk'}^{(1)*} z_k z_{k'}} e^{-z_k^* z_k} e^{-\frac{1}{2} Z_{kk'}^{(2)} z_k^* z_{k'}^*} \end{aligned} \tag{A.11}$$

The integration is Grassmann variables can be carried out using conventional methods. But in order to carefully track the sign of the overlap, we introduce some intermediate steps. The terms that appear in the exponents can be written in a compact form using a bipartite skew-symmetric matrix.

$$\mathbb{Z}^{(12)} = \begin{pmatrix} -Z^{(2)} & -\mathbb{1} \\ \mathbb{1} & Z^{(1)*} \end{pmatrix} \tag{A.12}$$

and a Grassmann vector $z_\mu = (z_k^*, z_k)$ to give

$$\left\langle \psi^{(1)} \middle| \psi^{(2)} \right\rangle = \int (\prod dz_k^* dz_k) e^{\frac{1}{2} z_\mu \mathbb{Z}^{(12)}_{\mu\mu'} z_{\mu'}} \tag{A.13}$$

The skew-symmetric matrix $\mathbb{Z}^{(12)}$ can always be transformed to a canonical form by unitary transformation U.

$$U^T \mathbb{Z}^{(12)} U = \mathbb{Z}_c = \begin{pmatrix} 0 & B \\ -B & 0 \end{pmatrix} \tag{A.14}$$

where B is an N dimensional diagonal matrix with $B_{ii} = \beta_i$ which are real and positive. In terms of the canonical Grassmann variable $\eta_\mu = U_{\mu'\mu} z'_\mu$,

$$\left\langle \psi^{(1)} \middle| \psi^{(2)} \right\rangle = \int (\prod d\eta_k^* d\eta_k) e^{\Sigma_{k=1}^N \beta_k \eta_k^* \eta_k} \det\{(U)\} \tag{A.15}$$

where $det(U)$ is the Jacobian of the transformation. The overlap can now be easily calculated since $\int d\eta^* d\eta e^{\beta\eta^*\eta} = -\beta$. With the help of Eqn. A.3

$$\left\langle \psi^{(1)} \middle| \psi^{(2)} \right\rangle = (-1)^N \det(U) \prod_{k=1}^{N} \beta_k \tag{A.16}$$

The product of β can be precisely expressed as the Pfaffian of $\mathbb{Z}_c$ using its very definition A.1 as $\prod_{k=1}^N \beta_k = (-1)^{N(N-1)/2} \mathrm{Pf}(\mathbb{Z}_c)$. Using Eqn. A.2, we can finally express the Pfaffian formula of the overlap with the correct sign as

$$\left\langle \psi^{(1)} \middle| \psi^{(2)} \right\rangle = (-1)^{N(N+1)/2} \mathrm{Pf}(\mathbb{Z}^{(12)}) \tag{A.17}$$

Appendix B

Diagonalizing the Majorana Hamiltonian

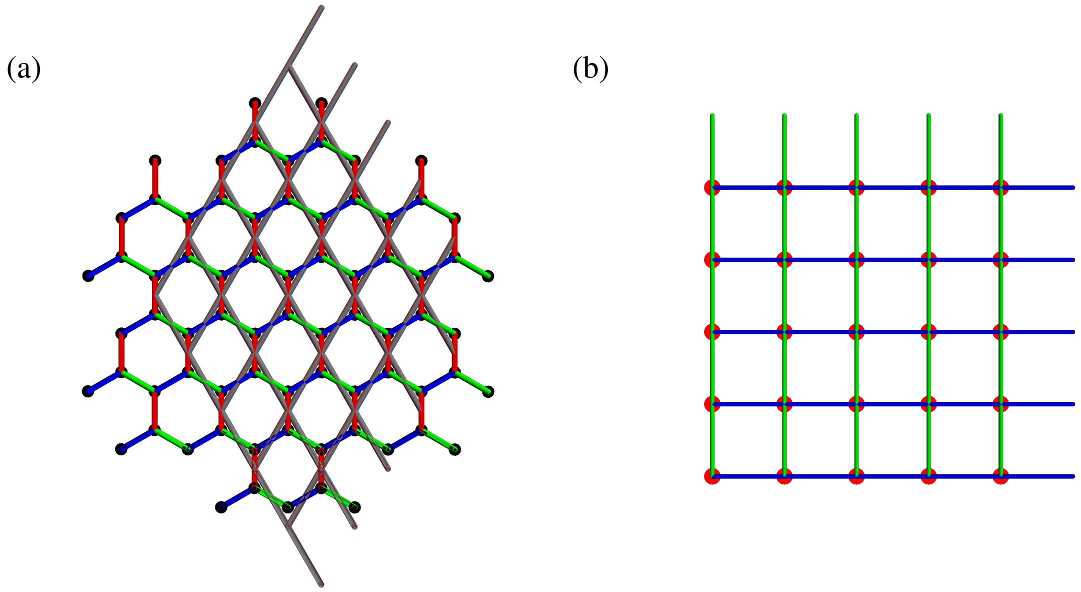

Fig. B.1 (a.) Honeycomb lattice with bond dependent interactions. (b.) The z bonds are mapped on to the sites of a square lattice, where a unit cell of the honeycomb lattice resides.

In this appendix I will describe how the numerical diagonalization is setup for the Majorana fermions for different vison positions. Let us start with the vison free sector. The fermion Hamiltonian on the honeycomb lattice is mapped to an effective square lattice by shrinking one of the bonds to a point (say z bond) as shown in Fig. B.1, resulting in a square lattice with linear size $L_1\boldsymbol{a}_1$ and $L_2\boldsymbol{a}_2+M\boldsymbol{a}_1$. M, termed as the 'twist factor', determines how the two edges are joined to form a periodic boundary. Indexing the sites of the new square lattice according to the periodic boundary conditions, the x and y couplings of the Kitaev Hamiltonian can be encoded as couplings between the sites and the z type couplings as the diagonal elements. The Kitaev

Hamiltonian has the form

$$H = \left(c_1^A, c_2^A, .., c_N^A\right) \begin{pmatrix} D & iM \\ -iM & -D \end{pmatrix} \begin{pmatrix} c_1^B \\ c_2^B \\ . \\ . \\ c_N^B \end{pmatrix} \tag{B.1}$$

The matrices obtained in this definition can be easily manipulated as described in the Chapter 2 to obtain the corresponding Hamiltonian of the complex fermion operators f and $f^\dagger$.

$$M_{ki} = K^x u_{k_A i_B} \qquad M_{ij} = K^y u_{i_A j_B} \qquad M_{ii} = K^z u_{i_A i_B}$$

where $i_{A(B)}$ labels the $A(B)$ sublattice sites in the i^{th} unit cell, defined at every site of the square lattice. Next-nearest neighbour hopping enters via

$$D_{ik} = K^x u_{i_A j_B} u_{j_B k_A}$$

which was defined in Chapter 2. Visons can be added by flipping a string of $u_{\langle ij \rangle}$. Due to periodic boundary conditions we can only add visons in pairs. In our calculations we add a pair of visons by flipping a chain of $u_{\langle ij \rangle_y}$ where the chain is parallel to the x axis of the (reduced) square lattice.

Appendix C

Scattering Cross-section of a vison

In this appendix, we reproduce the well known result for Aharonov-Bohm scattering of Dirac fermions from a localized point flux. Due to its π flux, we choose a gauge where the vison is implemented as an anti-periodic boundary condition for the wavefunctions. This is equivalent to a singular gauge where the vison is a semi-infinite branch cut in space.

An incoming wave in this gauge can be written in the coordinate space (r,φ)

$$\psi_{in}(\boldsymbol{r}) = e^{-i\frac{\varphi}{2}} e^{i\boldsymbol{k}\cdot\boldsymbol{r}} \begin{pmatrix} e^{-i\frac{\theta}{2}} \\ e^{i\frac{\theta}{2}} \end{pmatrix} \tag{C.1}$$

where the factor $e^{-i\frac{\varphi}{2}}$ implements the singular gauge that we are working with. We therefore look for a solution of the scattering problem which has an asymptotic form

$$\tilde{\psi}(kr) \xrightarrow{kr>>1} e^{-i\frac{\varphi}{2}} e^{ikr\cos\varphi} \begin{pmatrix} e^{-i\frac{\theta}{2}} \\ e^{i\frac{\theta}{2}} \end{pmatrix} + f(k,\varphi)\frac{e^{ikr}}{\sqrt{r}} \begin{pmatrix} e^{-i\frac{\phi}{2}} \\ e^{i\frac{\phi}{2}} \end{pmatrix} \tag{C.2}$$

The second term is the scattered wave and $f(k,\varphi)$ gives the scattering amplitude. Below, I focus on the first spinor component and extract the scattering amplitude to avoid clutter.

General solution to the Dirac equation with antiperiodic boundary condition is given by Eq.C.2

$$\tilde{\psi}_{s,l,k}(r) = \begin{pmatrix} i^{-l+\frac{1}{2}} J_{-l+\frac{1}{2}}(kr) e^{i(l-\frac{1}{2})\theta} \\ -s i^{-l-\frac{1}{2}} J_{-l-\frac{1}{2}}(kr) e^{i(l+\frac{1}{2})\theta} \end{pmatrix}, \qquad l \leq 0 \tag{C.3}$$

$$\begin{pmatrix} i^{l-\frac{1}{2}} J_{l-\frac{1}{2}}(kr) e^{i(l-\frac{1}{2})\theta} \\ s i^{l+\frac{1}{2}} J_{l+\frac{1}{2}}(kr) e^{i(l+\frac{1}{2})\theta} \end{pmatrix}, \qquad l > 0 \tag{C.4}$$

Using the following asymptotic form of Bessel functions we can expand the solutions and read off the pre-factor of the outgoing spherical wave.

$$J_l(kr) \approx \sqrt{\frac{2}{\pi kr}} \cos\left(kr - \frac{l\pi}{2} - \frac{\pi}{4}\right) \tag{C.5}$$

This gives the scattering amplitude

$$f(k,\varphi) = \frac{2}{\sqrt{\pi k}} \left(\sum_{l\leq 0} (-i) e^{il\varphi} + \sum_{l>0} e^{il\varphi} \right) \tag{C.6}$$

this sum can be carried out using analytic continuation of φ from the complex plane to the real axis. The scattering cross-section is then given by

$$\frac{d\sigma}{d\varphi} = |f(k,\varphi)|^2 = \frac{1}{2\pi k \sin^2\varphi} \tag{C.7}$$

for $\varphi \neq 0$

Appendix D

Solving the drift-diffusion equation

Here, I outline the details of numerically solving the drift-diffusion equation Eq. (5.14). Due to the momentum dependence of the drift term, we use Fourier transformation to write the equation in a matrix form. For simplicity, we can assume the force $\boldsymbol{F}$ is in the x direction, denoted by superscript '(1)'. In steady state, using $\phi_{\boldsymbol{p}} = \sum_{\boldsymbol{r}} e^{-i\boldsymbol{p}\cdot\boldsymbol{r}} \phi_{\boldsymbol{r}}$,

$$F^{(1)} \sum_{\boldsymbol{r}} \boldsymbol{v}_{\boldsymbol{r}}^{(1)} e^{-i\boldsymbol{p}\cdot\boldsymbol{r}} = D_p \left(-\sum_{r} r^2 \phi_{\boldsymbol{r}} e^{-i\boldsymbol{p}\cdot\boldsymbol{r}} + i \sum_{\boldsymbol{r},\boldsymbol{r}'} \boldsymbol{r}' \cdot v_{\boldsymbol{r}} \phi_{\boldsymbol{r}'} e^{-i\boldsymbol{p}\cdot(\boldsymbol{r}'+\boldsymbol{r})} \right) \tag{D.1}$$

Here, the sum $\sum_{\boldsymbol{r}}$ is taken over real space, which is discretized on a triangular lattice. For each Fouroer component, this leads to a matrix equation

$$\boldsymbol{v}_{\boldsymbol{r}_0}^{(1)} \delta_{\boldsymbol{r},\boldsymbol{r}_0} = \left(-r^2 \delta_{\boldsymbol{r},\boldsymbol{r}_0} + i \sum_{r} \boldsymbol{v}_{\boldsymbol{r}+\boldsymbol{r}_0} \cdot \boldsymbol{r} \right) \phi_{\boldsymbol{r}} \tag{D.2}$$

This can be written as a matrix equation

$$V = K\boldsymbol{\Phi} \tag{D.3}$$

in the discretized real space lattice of linear size L. Inverting this gives the solution to Φ. While solving the linear equation, an important subtlety is that the $\boldsymbol{r}_0 = 0$ component of the equation results in a singular matrix K as $v_{\boldsymbol{r}_0} = 0$. We fix this by defining $K_{0,0} = 1$, which does not affect the final solution. The obtained $\phi_{\boldsymbol{r}}$ is then Fourier transformed back to the momentum space. At low-T, it is also important to include sufficiently many Fourier modes (real space points) since the solution $\phi_{\boldsymbol{p}}$ develops features of order $\sqrt{T}$. Fig. D.1 shows this finite size effect which is more pronounced for smaller number lattice points.

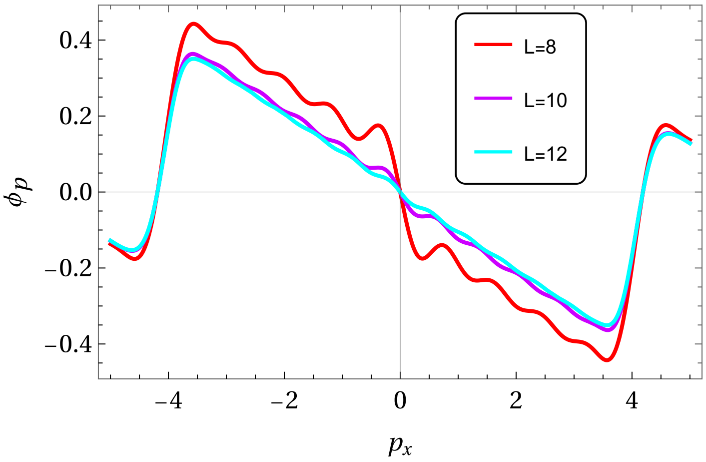

Fig. D.1 Numerical solution to the drift-diffusion equation at $D/T = 0.1$ and $\Gamma = -1$ for various number of Fourier modes used. The matrix equation Eq. (D.3) is diagonalized on a lattice of L linear size. Features of width $\sqrt{T}$ develops for small L.

D.0.1 Calculation of the Diffusion constant

In this subsection, we provide the details of the calculation of the momentum space diffusion constant of the vison. In the heavy vison limit, we can approximate the scattering cross-section with that of a single vison. For the vison, the transition rate between two momentum states $\boldsymbol{p}$ ans $\boldsymbol{p}'$ due to scattering from Majoranas is given by

$$M_{\boldsymbol{p},\boldsymbol{p}'} = \int \frac{d^2k}{4\pi^2}\frac{d^2k'}{4\pi^2} W_{\boldsymbol{k},\boldsymbol{k}'} n_k (1-n_{k'}) \delta(\boldsymbol{k}+\boldsymbol{p}-\boldsymbol{k}'-\boldsymbol{p}') \delta(\varepsilon_{\boldsymbol{k}}-\varepsilon_{\boldsymbol{k}'}). \tag{D.4}$$

Here, an incoming Majorana fermion with momentum $\boldsymbol{k}$ is scattered into a state with momentum $\boldsymbol{k}'$, by the vison potential, with the scattering rate determined by $W_{\boldsymbol{k},\boldsymbol{k}'}$. n_k denotes the Fermi function specifying the occupation of the Majoranas. The delta functions implement the total momentum and energy conservation. Note that within our approximation, we have neglected the recoil energy of the vison and assume an elastic scattering.

$W_{\boldsymbol{k},\boldsymbol{k}'}$. n_k is directly related to the scattering cross-section:

$$\frac{d^2p'}{4\pi^2}\frac{d^2k'}{4\pi^2} W_{\boldsymbol{k},\boldsymbol{k}'} (2\pi)^2 \delta(\boldsymbol{k}+\boldsymbol{p}-\boldsymbol{k}'-\boldsymbol{p}') 2\pi\delta(\varepsilon_{\boldsymbol{k}}-\varepsilon_{\boldsymbol{k}'}) \approx v_F d\theta_{\boldsymbol{k},\boldsymbol{k}'} \frac{d\sigma(k,\theta_{\boldsymbol{k},\boldsymbol{k}'})}{d\theta_{\boldsymbol{k},\boldsymbol{k}'}}. \tag{D.5}$$

Using this, we can derive an analytical expression for the diffusion constant D_p

$$\begin{aligned} D_p =& \int \frac{d^2p'}{4\pi^2}\frac{d^2k}{4\pi^2}\frac{d^2k'}{4\pi^2}\left|\boldsymbol{p}'-\boldsymbol{p}\right|^2 W_{\boldsymbol{k},\boldsymbol{k}'} n_k(1-n_{k'})(2\pi)^2\delta(\boldsymbol{k}+\boldsymbol{p}-\boldsymbol{k}'-\boldsymbol{p}')2\pi\delta(\varepsilon_{\boldsymbol{k}}-\varepsilon_{\boldsymbol{k}'}) \\ =& v_F \int \frac{d^2k}{4\pi^2} d\theta_{\boldsymbol{k},\boldsymbol{k}'} k^2 \left(1-\cos\theta_{\boldsymbol{k},\boldsymbol{k}'}\right)\frac{d\sigma(k,\theta_{\boldsymbol{k},\boldsymbol{k}'})}{d\theta_{\boldsymbol{k},\boldsymbol{k}'}} n(\varepsilon_k)(1-n_{\varepsilon_k}) \\ =& v_F \int \frac{dk}{2\pi} k^3 \sigma_{tr}(k) n(v_F k)\left(1-n(v_F k)\right) \\ =& \frac{1}{2\pi^2 v_F^2}\int \varepsilon^2 n(\varepsilon)\left(1-n(\varepsilon)\right) d\varepsilon \\ =& \frac{1}{2\pi^2 v_F^2 \beta^3}\int_0^\infty x^2 n(x)\left(1-n(x)\right) dx \end{aligned} \tag{D.6}$$

where we used $\sigma_{tr} = \frac{1}{\pi k}$, defined as the transport scattering cross-section, which neutralises the divergent forward scattering. Solving the integral gives the diffusion constant given in the main text.

Appendix E

Majorana assisted hopping of single visons

In this appendix, I will present the detailed expressions required to obtain the Majorana assisted hopping rate in Eq. (5.33). We start with the following expression in the main text (Eq. (5.29))

$$\frac{\tilde{W}^{(1)}(s,k_0,l_0)}{\Gamma^2\left|\langle 0_A|0_B\rangle\right|^2} = \sum_s \left(S_{s+}(k_0,l_0) + S_{s-}(k_0,l_0)\right) \tag{E.1}$$

$$\tag{E.2}$$

$$S(k_0,l_0)_{++} = \frac{2\pi}{v_F}\sum_l \int \frac{dk}{2\pi}\left|\sum_{l_1,l_2}\int d^2r_1 d^2r_2 \varepsilon(\boldsymbol{r}_1-\boldsymbol{\delta})\varepsilon(\boldsymbol{r}_2+\boldsymbol{\delta})\int \frac{dk_1dk_2}{4\pi^2}\pi\sqrt{k_1k_2}\left[\eta^{+}_{k_1,l_1}(\boldsymbol{r}_1)\eta^{-*}_{l_2,k_2}(\boldsymbol{r}_2)\right]4\pi^2\delta(k_0-k_1)\delta(k-k_2)\delta_{l_0,l_1}\delta_{l,l_2}\right|^2\delta(k_0-k) \tag{E.3}$$

$$S(k_0,l_0)_{+-} = \frac{2\pi}{v_F}\sum_l \int \frac{dk}{2\pi}\left|\sum_{l_1,l_2}\int d^2r_1 d^2r_2 \varepsilon(\boldsymbol{r}_1-\boldsymbol{\delta})\varepsilon(\boldsymbol{r}_2+\boldsymbol{\delta})\int \frac{dk_1dk_2}{4\pi^2}\pi\sqrt{k_1k_2}\left[\eta^{+}_{k_1,l_1}(\boldsymbol{r}_1)\eta^{+}_{l_2,k_2}(\boldsymbol{r}_2)\right]4\pi^2\delta(k_0-k_1)\delta(k-k_2)\delta_{l_0,l_1}\delta_{l,l_2}\right|^2\delta(k_0-k) \tag{E.4}$$

$$\eta^{\pm *}_{k,l}(\boldsymbol{r}) = e^{i\frac{\pi}{4}} f^{A*}_{k,l}(\boldsymbol{r}) \pm e^{-i\frac{\pi}{4}} f^{B*}_{k,l}(\boldsymbol{r}) \tag{E.5}$$

We now approximate the smoothing function to a delta function centred around the unit cell $\varepsilon(\boldsymbol{r}) \approx \Omega_0\delta^2(0)$ where $\boldsymbol{r}$ is measured from the unit cell position. This approximation can be verified to ensure the commutation relations of the Majorana operators.

$$S(k_0,l_0)_{++} = \frac{\Omega_0^2\pi^2}{v_F}k_0^2\left|\eta^{+}_{k_0,l_0}(-\boldsymbol{\delta})\right|^2\left[\sum_l\left|\eta^{-*}_{k_0,l}(\boldsymbol{\delta})\right|^2\right] \tag{E.6}$$

where $\pm\boldsymbol{\delta} = (\delta, \pm\frac{\pi}{2})$.

Since we are in the low energy long wavelength limit, we can approximate the Bessel functions with their small argument forms. $J_l(\rho) \approx \rho^l$. Since $k_0\delta << 1$. The most diverging contribution in the above sum thus comes from the $l = 0$ angular momentum channel. Similarly,

$$S(k_0,l_0)_{++} \approx \frac{\Omega_0^2\pi^2}{v_F}k_0^2\left|\eta^{+}_{k_0,l_0}(-\boldsymbol{\delta})\right|^2\left|i\sqrt{k_0\delta}-\frac{1}{\sqrt{k_0\delta}}\right|^2 = \frac{\Omega_0^2\pi^2}{v_F}k_0^2\left|\eta^{+}_{k_0,l_0}(-\boldsymbol{\delta})\right|^2\left(k_0\delta+\frac{1}{k_0\delta}\right) \tag{E.7a}$$

$$S(k_0,l_0)_{+-} \approx \frac{\Omega_0^2\pi^2}{v_F}k_0^2\left|i\eta^{+}_{k_0,l_0}(-\boldsymbol{\delta})\right|^2\left(k_0\delta+\frac{1}{k_0\delta}\right) \tag{E.7b}$$

$$S(k_0,l_0)_{-+} \approx \frac{\Omega_0^2\pi^2}{v_F}k_0^2\left|-i\eta^{-*}_{k_0,l_0}(-\boldsymbol{\delta})\right|^2\left(k_0\delta+\frac{1}{k_0\delta}\right) \tag{E.7c}$$

$$S(k_0,l_0)_{--} \approx \frac{\Omega_0^2\pi^2}{v_F}k_0^2\left|\eta^{-*}_{k_0,l_0}(-\boldsymbol{\delta})\right|^2\left(k_0\delta+\frac{1}{k_0\delta}\right) \tag{E.7d}$$

The full transition rate can be therefore calculated by carrying out a thermal average over the initial states. The dominant contribution is

$$\begin{aligned} W^{(1)} &\approx \int \frac{dk_0}{2\pi}\sum_{l_0} n_{k_0,l_0}\tilde{W}^{(1)}(k_0,l_0) \\ &= \frac{\mathcal{N}\Gamma^2\Omega_0^2\pi^2}{2\delta v_F}\int \frac{dk_0}{2\pi}(1+e^{\beta v_F k_0})^{-1} \\ &= \frac{\mathcal{N}\Gamma^2\Omega_0^2\pi^3}{32\beta\delta^2 v_F^2}\int du\frac{1}{1+e^u} \end{aligned} \tag{E.8}$$

Appendix F

Majorana assisted hopping of intra-layer vison pairs

Here, we calculate the Golden-rule transition rate of a (fermionic) vison pair in the gapless phase for the isotropic Kitaev model. As described in the main text, the assisted hopping rate $\Gamma_\perp$ (Eq. (6.8) in the main text) calculation can be carried out analytically in the low T limit. Let us look at the transition rate from layer l to layer $l+1$

$$\Gamma_\perp = \sum_{m,m',n,n'} e^{-\beta(E_n^l + E_{n'}^{l+1})} \left\langle \Phi_m^l(\boldsymbol{R}) \right| \left\langle \Phi_{m'}^{l+1}(\emptyset) \right| \Delta H \left| \Phi_n^l(\emptyset) \right\rangle \left| \Phi_{n'}^{l+1}(\boldsymbol{R}) \right\rangle \delta(E_m^l + E_{m'}^{l+1} - E_n^l - E_{n'}^{l+1}) \tag{F.1}$$

where the many body wavefunctions of layer l with quantum number n is given by

$$\left| \Phi_n^l(\boldsymbol{R}) \right\rangle = \hat{P}_l \left| \mathscr{G}(\boldsymbol{R}) \right\rangle_l \left| M(\mathscr{G}(\boldsymbol{R})) \right\rangle_l, \tag{F.2}$$

and we denote by $\left| \Phi_n^l(\emptyset) \right\rangle$ the wave function without any vison pair.

We now explain why in the low energy limit, vison pair-Majorana scattering can be neglected and one may replace the scattering states with free Majorana wavefunctions.

Scattering from a vison-pair is described by the full Green's function of the Majorana fermions in the presence of a potential term $V = -2Kic_ic_j$ at a single link $\langle ij \rangle_z$. This can be calculated using the Dyson equation.

$$G(\boldsymbol{k},\boldsymbol{k}';i\omega) = G_0(\boldsymbol{k},\boldsymbol{k}';i\omega) + \int d\boldsymbol{k}_1 d\boldsymbol{k}_2 G_0(\boldsymbol{k},\boldsymbol{k}_1;i\omega) V_{\boldsymbol{k}_1,\boldsymbol{k}_2} G(\boldsymbol{k}_2,\boldsymbol{k}';i\omega) \tag{F.3}$$

with the scattering potential in the momentum space $V_{\boldsymbol{k}_1,\boldsymbol{k}_2} = -4K\tau^y$ where $\boldsymbol{\tau} = (\tau^x, \tau^y, \tau^z)$ denotes the Pauli matrices in the sublattice basis. Integrating over $\boldsymbol{k}$ and $\boldsymbol{k}'$ on both sides of the Dyson equation gives us the self consistent equation for the dressed local Green's function $g(i\omega) = \int d\boldsymbol{k}d\boldsymbol{k}' G(\boldsymbol{k},\boldsymbol{k}';i\omega)$

$$g(i\omega) = g_0(i\omega) - 4K\tau^y g_0(i\omega)g(i\omega) \tag{F.4}$$

which gives

$$g(i\omega) = g_0(i\omega)(1+4K\tau^y g_0(i\omega))^{-1} \tag{F.5}$$

The local bare Green's function is given by is

$$g_0(i\omega) = \int \frac{d\boldsymbol{k}}{(2\pi)^2} \frac{1}{i\omega - v_m \boldsymbol{\tau}\cdot\boldsymbol{k}} \tag{F.6}$$

Analytically continuing by $i\omega \to \omega + i\delta sign(\omega)$, we get, in the low ω limit,

$$\begin{aligned} g_0(\omega) &= \frac{1}{2\pi}\int_0^{\Lambda} dk \frac{1}{\omega - v_m\boldsymbol{\tau}\cdot\boldsymbol{k} + isign(\omega)\delta} \\ &= \frac{\omega}{2\pi}\log\left(\frac{\omega^2}{v_m^2\Lambda^2}\right) + i\frac{|\omega|}{2v_m} \end{aligned} \tag{F.7}$$

where Λ is a high energy cut-off defining out low energy limit. The above equation reproduces the linear density of states for Dirac particles. Plugging this into Eq. F.5, we can see that in the $\omega \to 0$ limit, the full Green's function approaches the bare one. Hence we replace the scattered states with the free particle states as $|\Psi_{m_l}(\boldsymbol{R}_l)\rangle = \hat{P}_l\,|\mathscr{G}(\boldsymbol{R}_l)\rangle_l\,|M_{m_l}(\emptyset)\rangle_l$ where m_l labels the many-body eigenstates of the matter fermions. While this is not valid for Majorana states at high energy, it is approximately valid at low energies.

Expanding the interlayer Hamiltonian in terms of the Majorana fermions $\Delta H^z_\perp(i) = -b^z_{i,l}b^z_{i,l+1}c_{i,l}c_{i,l+1}$ and contracting the gauge fermions we get

$$\begin{aligned} \Gamma_\perp &\approx J_\perp^2 \sum_{\substack{m,m'\\ n,n'}} e^{-\beta(E^l_n+E^{l+1}_{n'})} \left| \left\langle M^l_m(\emptyset)\right| \left\langle M^{l+1}_{m'}(\emptyset)\right| c_{i,l}c_{i,l+1} + c_{j,l}c_{j,l+1} \left|M^l_n(\emptyset)\right\rangle \left|M^{l+1}_{n'}(\emptyset)\right\rangle \right|^2 \delta(E^l_m + E^{l+1}_{m'} - E^l_n - E^{l+1}_{n'}) \\ &= J_\perp^2 \sum_{\substack{p,q=\{i,j\}\\ m,m'\\ n,n'}} e^{-\beta(E^l_n+E^{l+1}_{n'})} \left\langle M^l_m(\emptyset)\right| c_{p,l} \left|M^l_n(\emptyset)\right\rangle \left\langle M^l_n(\emptyset)\right| c_{q,l} \left|M^l_m(\emptyset)\right\rangle \\ &\qquad \times \left\langle M^{l+1}_{m'}(\emptyset)\right| c_{p,l+1} \left|M^{l+1}_{n'}(\emptyset)\right\rangle \left\langle M^{l+1}_{n'}(\emptyset)\right| c_{q,l+1} \left|M^{l+1}_{m'}(\emptyset)\right\rangle \delta(E^l_m + E^{l+1}_{m'} - E^l_n - E^{l+1}_{n'}) \end{aligned} \tag{F.8}$$

which can be identified as a convolution of Majorana spectral functions on each layer.

$$\Gamma_{\perp}(\beta) \approx J_{\perp}^{2} \sum_{\alpha,\beta=A,B} \int_{-\infty}^{\infty} \Big[C_{\alpha,\beta}(\omega,\boldsymbol{r}=0)C_{\alpha,\beta}(-\omega,\boldsymbol{r}=0)\Big]d\omega \tag{F.9}$$

where $C(\omega,\boldsymbol{r}=0) = -2\,n_f(\omega)\,\mathrm{Im}\int \frac{d^2k}{4\pi^2}G^R(\omega,\boldsymbol{k})$ is the spectral function of the matter Majorana fermions obtained from the free particle (retarded) Green's function written in the sublattice basis (A,B). In the low energy Dirac description of the Majoranas, the Green's function is

$$G(i\omega,\boldsymbol{k}) = \frac{1}{i\omega - v_m\boldsymbol{k}\cdot\boldsymbol{\tau}} \tag{F.10}$$

where, $\boldsymbol{\tau} = (\tau_x,\tau_y)$ are the Pauli operators. This leads to a linear density of states, characteristic of Dirac fermions, reflected in the spectral function.

$$C_{\alpha,\beta}(\omega,0) = n_f(\omega)\frac{|\omega|}{v_m^2}\delta_{\alpha,\beta} \tag{F.11}$$

Plugging this into the equation for $\Gamma_{\perp}$, we get

$$\Gamma_{\perp}(T) \approx J_{\perp}^{2}\frac{2\,\pi}{\hbar}\int_{\infty}^{\infty} n_f(\omega)(1-n_f(\omega))\frac{\omega^2}{v_m^4}d\omega = \frac{2\pi T^3}{\hbar v_m^4} \tag{F.12}$$

While the prefactor of this formula is not exact (we neglected the effect of scattering of high-energy Majorana states from the vison pair), the T dependence is expected to be exact in the low-T limit.